A Search For Electron Antineutrino Disappearance with the Double Chooz Far Detector

Matthew H. Toups

Submitted in partial fulfillment of the
requirements for the degree
of Doctor of Philosophy
in the Graduate School of Arts and Sciences

COLUMBIA UNIVERSITY

2012

ABSTRACT

A Search For Electron Antineutrino Disappearance with the Double Chooz Far Detector

Matthew H. Toups

We present a search for electron antineutrino disappearance at the Chooz nuclear power plant in Chooz, France. Using the Double Chooz far detector and 101.5 days of detector run time, we measure $\sin^2(2\theta_{13}) = 0.086 \pm 0.041$ (stat.) ± 0.030 (syst.) from a rate and shape fit. A combined analysis of T2K and Double Chooz data finds that $\sin^2(2\theta_{13}) = 0$ is excluded at the 3σ level.

Table of Contents

List of Figures

List of Tables

Acknowledgments

First and foremost, I would like to thank my Ph.D. adviser, Prof. Mike Shaevitz, for his wisdom, insight, and guidance during my years at Columbia. I am grateful for the opportunity we have had to work together and hope to collaborate again in the near future.

To all my Columbia neutrino group colleagues, both past and present: thank you for creating such a hospitable and stimulating work environment. In particular I thank my post-doc, Camillo Mariani, for his leadership, mentorship, and friendship these past several years. I thank Leslie Camilleri for his counsel and his great example of dedication to physics. I also thank my fellow Columbia University graduate student, Double Chooz colleague, and office mate, Arthur Franke, for his collegiality, hard work, and professionalism, which have made him a pleasure to work with. Finally, I thank my fellow graduate student Gary Cheng for his entertaining lunchtime and van ride conversations, his inquisitiveness, and his cooperation in sharing computing resources.

To all of the Nevis staff: thank you for making Nevis Labs such a special place to work. In particular, I thank Bill Sippach for his patience in teaching me about digital electronics and how to program FPGAs. I also thank Bill Seligman for helping me become a better programmer and a better systems administrator.

I also thank all of my Double Chooz collaborators, whose hard work and combined effort made these Double Chooz first results possible.

I express my deepest gratitude and thanks to Renee Rakel for her constant love and support, which has inspired and sustained me this past year.

Finally, I thank my parents, Bill Toups and Leann Logsdon, who have always believed in me and encouraged me to chase my dreams.

Chapter 1

Introduction

In a now famous letter to a group of physicists gathered in Tuebingen in December 1930, Pauli postulated the existence of a light, neutral spin 1/2 particle, which is emitted together with the electron in radioactive β decay. If such a particle existed, he argued, it could explain the continuous β decay energy spectrum while preserving the law of conservation of energy. In 1934, Fermi incorporated the neutrino in his theory of β decay, which laid the theoretical foundation for studying the properties of the neutrino [1].

The neutrino was first detected by F. Reines and C. Cowan at the Hanford nuclear reactor in 1956 using the inverse β-decay (IBD) reaction $\bar{\nu}_e + p \rightarrow e^+ + n$ [2]. In 1962, the muon neutrino produced from the decay in flight of pions via $\pi^\pm \rightarrow \mu^\pm + \nu_\mu(\bar{\nu}_\mu)$ was discovered by a Columbia group led by Lederman, Schwartz, and Steinberger [3]. The third generation neutrino was first anticipated after the discovery of the tau charged lepton in 1975 [4], and direct detection of the tau neutrino was finally achieved by the DONUT experiment in 2000 [5].

As early as 1957—shortly after the neutrino was first detected—Pontecorvo proposed the idea of neutrino $\nu \leftrightarrow \bar{\nu}$ oscillations in analogy with $K^0 \leftrightarrow \bar{K}^0$ oscillations [6]. In 1962, Maki, Nakagawa, and Sakata suggested that neutrino flavor transitions or "oscillations" could occur if neutrinos had mass [7]. This provided a theoretical framework to interpret the results reported by Ray Davis in 1968, in which fewer electron neutrinos were detected from the sun than predicted by theory [8]. Davis's experiment began a close to half-century long program of neutrino experiments, which have probed structure of neutrino

flavor change. These experiments have established that neutrinos have mass and have validated the neutrino oscillation hypothesis.

This thesis describes a search for $\bar{\nu}_e$ disappearance with the Double Chooz (DC) experiment. Apparent $\bar{\nu}_e$ disappearance occurs in the DC detector as a result of neutrino oscillations. DC is only sensitive to electron flavor antineutrinos via the familiar IBD reaction pioneered by Reines and Cowan [2]. Therefore, neutrino flavor transitions from $\bar{\nu}_e$ to $\bar{\nu}_\mu$ or $\bar{\nu}_\tau$ appear as a deficit of IBD events in the DC detector with respect to the no oscillation expectation. The aim of the $\bar{\nu}_e$ disappearance search is to measure θ_{13}, a fundamental parameter of the Standard Model of particle physics,[1] the theory which describes all fundamental particles and their interactions[2].

This rest of this thesis is structured as follows. In Ch. 2 we explore extensions to the standard electroweak theory describing neutrino interactions to include neutrino mass. The neutrino oscillation formalism is introduced, and the oscillation results from the last decade are reviewed. We introduce the DC experiment in Ch. 3 and provide details of its design principles and operation. In Ch. 4 we describe the $\bar{\nu}_e$ reactor flux prediction, which is crucial a piece of the $\bar{\nu}_e$ disappearance analysis. In Ch. 5, we discuss the detector Monte Carlo (MC) simulation and energy calibration. We give an account of the IBD candidate event selection and efficiency estimation in Ch. 6. In Ch. 7, we describe the backgrounds to the IBD candidate selection and explain how they are estimated from the data. We present the $\bar{\nu}_e$ disappearance analysis based on a χ^2 fit in Ch. 8. Finally, in Ch. 9 we compare the DC $\bar{\nu}_e$ disappearance result with the results of other contemporaneous experiments.

[1] We will describe how to adapt the Standard Model to include neutrino masses in Ch. 2.

[2] The gravitational force is not included in the Standard Model

Chapter 2

Neutrino Mass, Mixing, and Flavor Change

We present a brief introduction to the theoretical foundation for including neutrino mass in the Standard Model of particle physics[1]. Next, we introduce the neutrino mixing formalism and derive the phenomenon of neutrino oscillations. We give a survey of neutrino oscillation results from the last two decades and describe how all the data can be described by the mixing of the three neutrino flavors ν_e, ν_μ, and ν_τ. Finally, we describe ongoing neutrino oscillation searches which aim to further our understanding of neutrino mixing and flavor change.

2.1 Neutrinos in the Standard Model

Neutrinos in the Standard Model (SM) are described by the electroweak (EW) theory developed by Glashow, Salam, and finally Weinberg in the 1960s [9–11]. The theory is written as a Lorentz-invariant, local quantum field theory with an $SU(2) \times U(1)$ gauge symmetry. The $SU(2)$ and $U(1)$ gauge symmetries are called weak isospin and weak hypercharge respectively. The particle content of the theory is specified in terms of chiral left- and right-handed fermionic fields ψ_L and ψ_R, respectively. These can be constructed from the chiral

[1]Natural units $\hbar = c = 1$ are assumed unless otherwise noted.

projection operators $P_L = \frac{1}{2}(1 - \gamma_5)$ and $P_R = \frac{1}{2}(1 + \gamma_5)$ in terms of the Dirac spinor field ψ as $P_L\psi = \psi_L$ and $P_R\psi = \psi_R$, where $\gamma_5 = i\gamma^0\gamma^1\gamma^2\gamma^3$.

The spin-1/2 matter fields consist of two quarks, one charged lepton, and one neutrino, repeated in three generations. Both chiral left- and right-handed fields are included for each particle with the exception of the neutrino, for which only a chiral left-handed field is included. In addition, a spin-0 field ϕ called the Higgs is also included in the theory. These fields are arranged into multiplets of weak isospin and their quantum number assignments are given in Table 2.1.

Quantum Numbers					Generation		
S	T	T_3	Y	$Q = T_3 + Y/2$	1	2	3
1/2	1/2	1/2	1/3	2/3	u_L^0	c_L^0	t_L^0
1/2	1/2	-1/2	1/3	-1/3	d_L^0	s_L^0	b_L^0
1/2	1/2	1/2	-1	0	$(\nu_e)_L^0$	$(\nu_\mu)_L^0$	$(\nu_\tau)_L^0$
1/2	1/2	-1/2	-1	-1	e_L^0	μ_L^0	τ_L^0
1/2	0	0	4/3	2/3	u_R^0	c_R^0	t_R^0
1/2	0	0	-2/3	-1/3	d_R^0	s_R^0	b_R^0
1/2	0	0	-2	-1	e_R^0	μ_R^0	τ_R^0
0	1/2	1/2	1	1	ϕ^+		
0	1/2	-1/2	1	0	ϕ^0		

Table 2.1: Summary of the spin (S), the weak isospin (T, T_3), and weak hypercharge (Y) quantum number assignments for each of the spin-1/2 and spin-0 matter fields in the electroweak theory. Q refers to the electromagnetic charge and L and R subscripts denote chiral left- and right-handed fields, respectively.

The electroweak Lagrangian is the most general, renormalizable Lagrangian consistent with the particle content and internal symmetries of the theory. Most notably, weak isospin invariance precludes the possibility of writing down a Dirac mass term in the EW Lagrangian because

$$-\mathcal{L}_{M_\psi} = m\overline{\psi}\psi = m(\overline{\psi_L}\psi_R + \overline{\psi_R}\psi_L) \tag{2.1}$$

is not invariant under weak isospin gauge transformations for any fermion ψ. Instead, fermion masses are acquired from the Higgs via spontaneous symmetry breaking (SSB). Consider the Yukawa interaction of the leptons with the Higgs, which is invariant under weak isospin gauge transformations. The term in the EW Lagrangian is given by

$$-\mathcal{L}_y = h^e(\overline{e_L^0}, \overline{\nu_L^0})\begin{pmatrix}\phi^+\\ \phi^0\end{pmatrix}e_R^0 + h.c. \tag{2.2}$$

After the Higgs acquires a vacuum expectation value $\langle\phi\rangle = \binom{0}{v/\sqrt{2}}$, $v \sim 246$ GeV, the Yukawa interaction includes a term

$$-\mathcal{L}_y \supset h^e\frac{v}{\sqrt{2}}(\overline{e_L^0}e_R^0 + \overline{e_R^0}e_L^0) = h^e\frac{v}{\sqrt{2}}\overline{e^0}e^0, \tag{2.3}$$

where $e^0 = e_L^0 + e_R^0$. This is a Dirac mass term for the electron with the mass given by $h^e v/\sqrt{2}$. This mass term is constructed out of both chiral left- and right-handed electron fields. The omission of a chiral right-handed neutrino field in the standard EW theory means that no such Yukawa term gives rise to neutrino mass after SSB. Therefore, neutrinos in the Standard Model are massless.

2.1.1 Models of Neutrino Mass

To accommodate the discovery of neutrino mass, a natural approach is to add a chiral right-handed neutrino field to the particle content of the standard EW theory. In order for this field to generate a mass for the neutrino, this field is required to be a weak isospin singlet and have $Y = 0$. Adding such a field will generate a Dirac mass for the neutrino after SSB given by

$$-\mathcal{L}_{D_\nu} = h^\nu\frac{v}{\sqrt{2}}\overline{\nu^0}\nu^0. \tag{2.4}$$

However, there are two issues with the mass term constructed in this way. The first has to do with the smallness of neutrino masses with respect to the other fermions. This can be phrased in terms of the neutrino Yukawa couplings to the Higgs. Direct searches have placed an upper limit on the neutrino mass to be < 2 eV [12, 13]. Therefore, we estimate that $h^\nu < 10^{-11}$. The next lightest fermion is the electron, for which $h^e \sim 10^{-6}$, at least 5 orders of magnitude larger.

The second issue has to do with the generality of the Dirac mass term for the neutrino. Once ν_R^0 has been added to the theory, a second renormalizable mass term can now also be written down as

$$-\mathcal{L}_{Maj} = \frac{m_R}{2}\left(\overline{(\nu_R^0)^c}\ (\nu_R^0) + (\overline{\nu_R^0})\ (\nu_R^0)^c\right) \tag{2.5}$$

where $(\nu_R^0)^c$ is the charge conjugate of ν_R^0 and has the opposite chirality. $\mathcal{L}_{Maj}$ is the so-called Majorana mass term for the neutrino. $\mathcal{L}_{Maj}$ can be rewritten in terms of the mass eigenstate $(\nu_R^0 + (\nu_R^0)^c)$ as

$$-\mathcal{L}_{Maj} = \frac{m_R}{2}\overline{(\nu_R^0 + (\nu_R^0)^c)}\ (\nu_R^0 + (\nu_R^0)^c) = \frac{m_R}{2}\bar{\nu}\nu. \tag{2.6}$$

Eq. 2.6 illustrates the fact that a Majorana fermion is its own antiparticle and violates lepton number conservation. $\mathcal{L}_{Maj}$ is unique to the neutrino because the neutrino is the only neutral fermion in the SM.

If we assume both Dirac and Majorana mass terms are present, then after SSB the neutrino mass term in the Lagrangian is

$$\begin{aligned} -\mathcal{L}_{M_\nu} &= \frac{m_R}{2}\ \overline{(\nu_R^0)^c}\ \nu_R^0 - m_D\ \overline{\nu_R^0}\ \nu_L^0 + h.c. \\ &= \frac{1}{2}\left(\overline{(\nu_L^0)^c},\ \overline{(\nu_R^0)}\right)\begin{pmatrix} 0 & m_D \\ m_D & m_R \end{pmatrix}\begin{pmatrix} \nu_L^0 \\ (\nu_R^0)^c \end{pmatrix} + h.c. \\ &= \frac{1}{2}\overline{(\eta_L^0)^c}\ M_\nu\ \eta_L^0 + h.c., \end{aligned} \tag{2.7}$$

where $(\eta_L^0)^T = \left(\nu_L^0,\ (\nu_R^0)^c\right)$. M_ν can be diagonalized by a unitary matrix Z so that Eq. 2.7 becomes

$$\begin{aligned} -\mathcal{L}_{M_\nu} &= \frac{1}{2}\overline{(\eta_L)^c}D_\nu\eta_L + h.c. \\ &= \frac{1}{2}\bar{\eta}D_\nu\eta, \end{aligned} \tag{2.8}$$

where $\overline{(\eta_L^0)^c}Z^* = \overline{(\eta_L)^c}$, $\eta_L = Z^\dagger\eta_L^0$, $Z^*D_\nu Z^\dagger = M_\nu$, and $\eta = \eta_L + (\eta_L)^c$.

2.1.2 The See-saw Mechanism

One important feature of the Majorana mass term given in Eq. 2.6 is that it does not originate from electroweak symmetry breaking. Therefore, there is no reason for m_R to be

at the EW symmetry-breaking scale. If we assume the Dirac neutrino mass—which does originate from EW SSB—is roughly the same size as a typical quark mass $m_D \sim m_q$ but that $m_R >> m_D$, then in terms of $\eta = \binom{\nu}{N}$, Eq. 2.8 is given by

$$-\mathcal{L}_{M_\nu} \simeq \frac{1}{2}\left(\overline{\nu}, \overline{N}\right)\begin{pmatrix} m_D^2/m_R & 0 \\ 0 & m_R \end{pmatrix}\binom{\nu}{N} \tag{2.9}$$

Therefore, instead of obtaining one Dirac neutrino, by adding a Majorana mass term we now have a pair of Majorana neutrinos, one with $m_\nu \simeq m_D^2/m_R$ and one with $m_N \simeq m_R$. This is the see-saw mechanism [14]. If we do this for all three generations of neutrinos and identify the light neutrinos with the ones we observe in nature, the assuming $m_D \sim m_{top}$, we must have $m_N \sim 10^{15}$ GeV. Therefore, the smallness of neutrino masses is related to lepton number violating physics at a very high energy scale, which is tantalizingly close to the scale of some grand unified theories [15].

2.2 Neutrino Mixing and Flavor Change

In the SM, neutrinos interact through the weak charged and neutral currents, e.g.

$$\mathcal{L}_{CC} = \frac{g}{\sqrt{2}} W_\lambda^- \ \overline{e_L^0} \ \gamma^\lambda \ (\nu_e)_L^0 + h.c. \tag{2.10}$$

$$\mathcal{L}_{NC} = \frac{g}{2\cos_{\theta_W}} Z_\lambda \ \overline{(\nu_e)_L^0} \ \gamma^\lambda \ (\nu_e)_L^0 \tag{2.11}$$

However, if neutrinos have mass, the well-defined flavor eigenstates, in terms of which Eq. 2.10 and Eq. 2.11 are written may not be the same as the mass eigenstates of the propagation Hamiltonian. Let us define the neutrino flavor eigenstates $\nu_\alpha,\ \alpha = e, \mu, \tau$ as the neutrino states which are produced in association with the charged lepton $l_\alpha,\ l_e = e,\ l_\mu = \mu,\ l_\tau = \tau$ in a weak charged-current interaction. In general, the flavor eigenstates ν_α are related to the mass eigenstates ν_i by a unitary transformation U[2]:

$$|\nu_\alpha >= \sum_i U_{\alpha i} |\nu_i > \tag{2.12}$$

In other words, a neutrino ν_α produced in association with a charged lepton l_α will propagate as a linear superposition of neutrino mass eigenstates given by equation Eq. 2.12.

[2]Sterile neutrinos are not considered in the following discussion.

Or alternatively, a neutrino mass eigenstate ν_i will participate in a weak charged current interaction as a linear superposition of flavor eigenstates ν_α according to

$$|\nu_i >= \sum_\alpha U^*_{\alpha i}|\nu_\alpha > \tag{2.13}$$

Neutrino oscillations arise as a manifestation of this mixing as the flavor content of a neutrino changes when it propagates from the point of production to the point of detection. To see this, consider the propagation of a neutrino mass eigenstate ν_i with momentum p_i over a distance L in a time T in the lab frame. In a plane wave approximation, ν_i evolves according to

$$|\nu_i(L,T) >= e^{-i(E_iT-p_iL)}|\nu_i(0) > \tag{2.14}$$

Therefore, the probability that a neutrino ν_α produced in a charged-current interaction is detected some time later as a ν_β is

$$P(\nu_\alpha \to \nu_\beta) = | < \nu_\beta|\nu_\alpha(L,T) > |^2 = |\sum_i U^*_{\beta i}e^{-i(E_iT-p_iL)}U_{\alpha i}|^2 = \sum_{ij} U_{\beta j}U^*_{\alpha j}e^{-i\phi_{ij}}U^*_{\beta i}U_{\alpha i} \tag{2.15}$$

where ϕ_{ij} encodes the interference of the neutrino mass eigenstate ν_i with the neutrino mass eigenstate ν_j and is given by

$$\phi_{ij} = (E_i - E_j)T - (p_i - p_j)L = (E_i - E_j)\left[T - \frac{E_i + E_j}{p_i + p_j}L\right] + \frac{m_i^2 - m_j^2}{p_i + p_j}L \tag{2.16}$$

In the ultra-relativistic limit, $T \cong L$ up to corrections of $\mathcal{O}(\frac{m^2_{i,j}}{E^2_{i,j}})$, and the first term in Eq. 2.16 can be neglected relative to the second term, giving

$$\phi_{ij} \cong \frac{m_i^2 - m_j^2}{2p}L \cong \frac{\Delta m^2_{ij}L}{2E} \tag{2.17}$$

where $p = (p_i + p_j)/2$, $\Delta m^2_{ij} = m_i^2 - m_j^2$, and the dependence of $p_{i,j}$ on $m_{i,j}$ can be neglected in the denominator, so that $p^{-1} \cong E^{-1}$ [16].

To simplify the expression in Eq. 2.15, we add the term $\delta_{\alpha\beta} - \sum_{ij} U_{\beta j}U^*_{\alpha j}U^*_{\beta i}U_{\alpha i}$ which is identically zero by the unitarity of U. The transition probability can then be expressed

as

$$\begin{aligned} P(\nu_\alpha \to \nu_\beta) &= \delta_{\alpha\beta} - \sum_{ij} U_{\beta j} U^*_{\alpha j} U^*_{\beta i} U_{\alpha i} \left(1 - e^{-i\frac{\Delta m^2_{ij} L}{2E}}\right) \\ &= \delta_{\alpha\beta} - 4\sum_{i>j} \Re[U_{\beta j} U^*_{\alpha j} U^*_{\beta i} U_{\alpha i}] \sin^2\left(\frac{\Delta m^2_{ij} L}{4E}\right) \\ &\quad + 2\sum_{i>j} \Im[U_{\beta j} U^*_{\alpha j} U^*_{\beta i} U_{\alpha i}] \sin\left(\frac{\Delta m^2_{ij} L}{2E}\right) \end{aligned} \tag{2.18}$$

The flavor change phenomena expressed by Eq. 2.18 are called neutrino oscillations, because of the sinusoidal dependence of the transition probability as a function of $\frac{\Delta m^2_{ij} L}{E}$. Note that the above expression implies that the phenomenon of neutrino oscillations requires flavor mixing, i.e. $U \neq I$ and the existence of at least two non-degenerate neutrino mass eigenstates. In the case of three non-degenerate neutrino mass eigenstates, the oscillation formula depends on the three mass-squared splittings, Δm^2_{21}, Δm^2_{31}, and Δm^2_{32}. However, only two of these are independent since $\Delta m^2_{32} + \Delta m^2_{21} = \Delta m^2_{31}$.

A complex U can lead to the CP violation $P(\nu_\alpha \to \nu_\beta) \neq P(\bar{\nu}_\alpha \to \bar{\nu}_\beta)$ for $\alpha \neq \beta$. To see this, note that the oscillation probability for anti-neutrinos can be written in terms of the oscillation probability for neutrinos assuming CPT invariance: $P(\bar{\nu}_\alpha \to \bar{\nu}_\beta) \xrightarrow{CPT} P(\nu_\beta \to \nu_\alpha)$. From Eq. 2.18 above, we see that $P(\nu_\beta \to \nu_\alpha; U) = P(\nu_\alpha \to \nu_\beta; U^*)$, so that $P(\bar{\nu}_\alpha \to \bar{\nu}_\beta; U) = P(\nu_\alpha \to \nu_\beta; U^*)$.

In general, an $N \times N$ unitary matrix can be described by $n(n-1)/2$ real mixing angles and $n(n+1)/2$ complex, CP-violating phases [17]. If neutrinos are Dirac-type fermions, then $2n-1$ of the complex phases can be absorbed into redefinitions of the neutrino and charged lepton fields, so that only $(n-1)(n-2)/2$ of these phases are physical. If, on the other hand, the neutrinos are Majorana-type fermions, then only n of the complex phases can be absorbed into redefinitions of the charged lepton fields, so that $n(n-1)/2$ of the phases are physical. In the case of 3 neutrino mixing, U is a 3×3 matrix and is parameterized by 3 mixing angles $(\theta_{12}, \theta_{13}, \theta_{23})$ and 3 CP-violating phases $(\delta, \alpha_1, \alpha_2)$. The phases α_1 and α_2 are called the Majorana CP-violating phases because they are only physical if the neutrinos are Majorana-type fermions. Similarly, δ is called the Dirac CP-violating phase. A standard choice for the parametrization of the lepton mixing matrix U in terms of these quantities

is given by [16]

$$U = \begin{bmatrix} c_{12}c_{13} & s_{12}c_{13} & s_{13}e^{-i\delta} \\ -s_{12}c_{23} - c_{12}s_{23}s_{13}e^{i\delta} & c_{12}c_{23} - s_{12}s_{23}s_{13}e^{i\delta} & s_{23}c_{13} \\ s_{12}s_{23} - c_{12}c_{23}s_{13}e^{i\delta} & -c_{12}s_{23} - s_{12}c_{23}s_{13}e^{i\delta} & c_{23}c_{13} \end{bmatrix} \times \mathrm{diag}\left(1, e^{i\alpha_1/2}, e^{i\alpha_2/2}\right) \tag{2.19}$$

where $s_{ij} \equiv \sin\theta_{ij}$ and $c_{ij} \equiv \cos\theta_{ij}$. By plugging Eq. 2.19 into the oscillation probability given in Eq. 2.18, we see that both α_1 and α_2 drop out of the equation. Neutrino oscillations are therefore not sensitive to the Majorana CP-violating phases and so can be neglected in our oscillation formulae.

The parametrization in Eq. 2.19 also highlights that in order for the Dirac CP-violating phase δ to be physical, we must have $\theta_{13} \neq 0$. In fact there is nothing special about the mixing angle θ_{13}. If any of the $U_{\alpha i} = 0$, then U can be parameterized by only two real mixing angles. Thus, all three mixing angles θ_{ij} must be nonzero in order for δ to be observable. This can also be shown explicitly by computing $P(\bar{\nu}_\alpha \to \bar{\nu}_\beta) - P(\nu_\alpha \to \nu_\beta)$ using the expression for U given in Eq. 2.19. However, both θ_{12} and θ_{23} are known to be nonzero, whereas only an upper limit exists for θ_{13}[3]. Therefore, establishing whether or not θ_{13} is nonzero is a crucial step towards determining whether neutrino oscillations can be used to measure CP violation in the neutrino sector.

2.2.1 Two-flavor mixing

In the case of two-flavor mixing, the oscillation formulae simplify considerably. Based on the analysis of the previous section, the lepton mixing matrix U is a 2×2 unitary matrix parametrized by one mixing angle and no Dirac CP-violating phases. Therefore, it is customary to define

$$U = \begin{pmatrix} \cos\theta & \sin\theta \\ -\sin\theta & \cos\theta \end{pmatrix}. \tag{2.20}$$

[3]In Ch. 9 we discuss recent evidence for nonzero θ_{13}.

In terms of this matrix, Eq. 2.15 reduces to

$$P(\nu_\alpha \to \nu_\beta) = \begin{cases} 1 - \sin^2(2\theta_\alpha)\sin^2(\frac{\Delta m^2 L}{4E}) & \alpha = \beta \\ \sin^2(2\theta_{\alpha\beta})\sin^2(\frac{\Delta m^2 L}{4E}) & \alpha \neq \beta \end{cases} \tag{2.21}$$

The two-flavor oscillation formula given in Eq. 2.21 is a good approximation of the full three-flavor oscillation formula in certain cases. For example, if the mass-squared splittings of the neutrino mass eigenstates are hierarchical, i.e. if $\Delta m^2_{21} << \Delta m^2_{32} \sim \Delta m^2_{31} \sim \Delta m^2$, then the oscillation formula for an experiment with $\Delta m^2 L/4E \sim \mathcal{O}(1)$ is given by

$$P(\nu_\alpha \to \nu_\beta) = \begin{cases} 1 - 4T_\alpha(1 - T_\alpha)\sin^2(\Delta m^2 L/4E) & \alpha = \beta \\ S_{\alpha\beta}\sin^2(\Delta m^2 L/4E) & \alpha \neq \beta \end{cases} \tag{2.22}$$

where $S_{\alpha\beta} = 4|U_{\alpha 3}U^*_{\beta 3}|^2$ and $T_\alpha = |U_{\alpha 3}|^2$ [18]. Thus, $\sin^2 2\theta_\alpha$ and $\sin^2 2\theta_{\alpha\beta}$ in Eq. 2.21 can be identified with $4T_\alpha(1 - T_\alpha)$ and $S_{\alpha\beta}$ in Eq. 2.22, respectively.

Another instance in which the two-flavor oscillation formula is a good approximation of the full three-flavor oscillation formula is for ν_e oscillations in the limit $|U_{e3}|^2 = \sin^2\theta_{13} \to 0$. In this case,

$$|\nu_e> = \cos\theta_{12}|\nu_1> + \sin\theta_{12}|\nu_2> \tag{2.23}$$

and therefore only two neutrino mass eigenstates participate in the neutrino propagation. Thus, Eq. 2.21 is valid for oscillations between ν_e and the orthogonal flavor combination ν_x given by

$$|\nu_x> = -\sin\theta_{12}|\nu_1> + \cos\theta_{12}|\nu_2> . \tag{2.24}$$

An important consequence of Eq. 2.21 is that two-flavor neutrino oscillations in vacuum are not sensitive to the sign of Δm^2. In terms of Eq. 2.23, exchanging the roles of the two mass eigenstates (and therefore the sign of Δm^2_{21}) is equivalent to making the substitution $\theta \to \frac{\pi}{2} - \theta$. Thus, we have the choice of labeling ν_1 and ν_2 in terms their flavor content (e.g. ν_1 is the mass eigenstate comprised of more ν_e than ν_2) or in terms of their relative masses (e.g. $m_{\nu_2} > m_{\nu_1}$).

2.2.2 Mass Hierarchy

In the full three-flavor model of neutrino mixing, we take a hybrid approach to labeling the neutrino mass eigenstates. The mass-squared splittings are known to be hierarchical (see

Sec. 2.4.3), therefore we can define ν_3 as the neutrino mass eigenstate whose mass is very different from the masses of the other two mass eigenstates (either much larger or much smaller), i.e. $|\Delta m^2_{21}| << |\Delta m^2_{32}| \sim |\Delta m^2_{31}| \sim |\Delta m^2|$. Effectively, this definition specifies the flavor content of ν_3 (short-baseline reactor experiments tell us that $|U_{e3}|^2 < 4\%$, for example), but does not specify the mass hierarchy, i.e. whether $m_3 > m_{1,2}$ or $m_3 < m_{1,2}$. Therefore, the sign of Δm^2_{31} (and Δm^2_{32}) can be either positive or negative. If $\Delta m^2_{31} > 0$, this is called the "normal" mass hierarchy. If however, $\Delta m^2_{31} < 0$, this is called the "inverted" mass hierarchy.

It is more convenient, on the other hand, to label the other two mass eigenstates in terms of their masses. Without loss of generality, we set $m_{\nu_2} > m_{\nu_1}$. In Sec. 2.2.4 we will see how solar matter effects allow us to then distinguish between $\theta_{12} < \frac{\pi}{4}$ (ν_1 is comprised of more ν_e than ν_2) and $\theta_{12} > \frac{\pi}{4}$ (ν_1 is comprised of less ν_e than ν_2). In a similar way, matter effects from accelerator neutrino beams passing through the earth can be used to determine the mass hierarchy (see Sec. 2.2.3).

2.2.3 Matter Effects in the Earth

The equations given above were derived for neutrino propagation through vacuum. In the presence of matter, neutrino oscillations are modified because the coherent forward scattering of neutrinos off of atomic electrons is different for ν_e than for ν_μ and ν_τ [19].

To see how the neutrino propagation is modified in the presence of matter, we first write down the vacuum propagation Hamiltonian in terms of the flavor basis as

$$\begin{aligned} H^{vac}_{\alpha\beta} &= \langle \nu_\alpha | H^{vac} | \nu_\beta \rangle \\ &= \sum_{ij} \langle \nu_i | U^*_{\alpha i} H^{vac} U_{\beta j} | \nu_j \rangle \\ &= \sum_i E_i U^*_{\alpha i} U_{\beta i} \end{aligned} \tag{2.25}$$

If we work in the two-flavor basis, in which both Eq. 2.23 and Eq. 2.24 are expressed

$(\alpha,\ \beta =\ \mathrm{e},\ x)$, the vacuum propagation Hamiltonian becomes

$$\begin{aligned} H^{vac}_{\alpha\beta} &= \frac{\Delta E}{2}\begin{pmatrix} -\cos 2\theta & \sin 2\theta \\ \sin 2\theta & \cos 2\theta \end{pmatrix} + \frac{E_2+E_1}{2}\begin{pmatrix} 1 & 0 \\ 0 & 1 \end{pmatrix} \\ &= \tilde{H}^{vac}_{\alpha\beta} + \lambda I, \end{aligned} \tag{2.26}$$

where E_i is the energy of the neutrino mass eigenstate i, and $\Delta E = E_2 - E_1 \sim \Delta m^2/2E$ in the ultra-relativistic approximation. Because neutrino oscillations depend only on the relative differences in the propagation of the two neutrino eigenstates, we can safely ignore the multiple of the identity matrix in Eq. 2.26, which just represents an overall energy shift.

The Hamiltonian governing neutrino propagation through matter is then $H^M = \tilde{H}^{vac} + V_W + V_Z$, where $\tilde{H}^{vac}$ is the Hamiltonian given in Eq. 2.26 and V_W and V_Z are the charged current and neutral current interaction potential energies for neutrinos propagating through matter, respectively. If we assume a constant matter density, then in the same basis used in Eq. 2.26 H^M can be expressed as

$$\begin{aligned} H^M_{\alpha\beta} &= \tilde{H}^{vac}_{\alpha\beta} + \tilde{V}_W\begin{pmatrix} 1 & 0 \\ 0 & 0 \end{pmatrix} + \tilde{V}_Z\begin{pmatrix} 1 & 0 \\ 0 & 1 \end{pmatrix} \\ &= \tilde{H}^{vac}_{\alpha\beta} + \frac{\tilde{V}_W}{2}\begin{pmatrix} 1 & 0 \\ 0 & -1 \end{pmatrix} + \lambda' I \\ &= \tilde{H}^M_{\alpha\beta} + \lambda' I \end{aligned} \tag{2.27}$$

where $\tilde{V}_W$ is given in terms of the electron density N_e and the Fermi coupling constant G_F as $\tilde{V}_W = \sqrt{2}G_F N_e$. After again neglecting a multiple of the identity matrix, the effective propagation Hamiltonian in matter can be recast in terms of $x = \frac{2\sqrt{2}G_f N_e E}{\Delta m^2}$ as

$$\begin{aligned} \tilde{H}^M_{\alpha\beta} &= \frac{\Delta m^2_M}{4E}\begin{pmatrix} -(\cos 2\theta - x) & \sin 2\theta \\ \sin 2\theta & (\cos 2\theta - x) \end{pmatrix} \\ &= \frac{\Delta m^2_M}{4E}\begin{pmatrix} -\cos 2\theta_M & \sin 2\theta_M \\ \sin 2\theta_M & \cos 2\theta_M \end{pmatrix} \end{aligned} \tag{2.28}$$

where

$$\sin^2 2\theta_M = \frac{\sin^2 2\theta}{\sin^2 2\theta + (\cos 2\theta - x)^2} \tag{2.29}$$

and

$$\frac{\Delta m_M^2}{4E} = \frac{\Delta m^2}{4E}\sqrt{\sin^2 2\theta + (\cos 2\theta - x)^2}. \tag{2.30}$$

Thus, we see that both oscillation length and the mixing parameters are modified in the presence of matter. The effect is the result of an interplay between a neutrino's mass and its ν_e flavor content. Therefore, this effect can be used to determine the mass hierarchy, i.e. whether the neutrino mass eigenstate with the smallest ν_e flavor content (ν_3) has a larger or smaller mass than the other two mass eigenstates (see Sec. 2.4.1).

2.2.4 Matter Effects in the Sun

The sun is a pure source of ν_e, which are produced predominantly by the *pp* fusion chain in the core. In analogy with Eq. 2.27, we can write down the Hamiltonian for neutrinos propagating through the sun as

$$H_{\alpha\beta}^M = \tilde{H}_{\alpha\beta}^{vac} + \tilde{V}_W \begin{pmatrix} 1 & 0 \\ 0 & 0 \end{pmatrix} + \tilde{V}_Z \begin{pmatrix} 1 & 0 \\ 0 & 1 \end{pmatrix}. \tag{2.31}$$

For sufficiently high energy neutrinos or for sufficiently high electron densities N_e, the $\tilde{V}_W$ term will dominate over $\tilde{H}_{\alpha\beta}^{vac}$, so that ν_e is an approximate eigenstate of $H_{\alpha\beta}^M$ corresponding to the higher energy neutrino mass eigenstate. The electron density of the sun N_e changes as a function of radius so that $H_{\alpha\beta}^M$ evolves into $\tilde{H}_{\alpha\beta}^{vac}$ as a neutrino leaves the core and escapes from the sun. However, if the evolution of the propagation Hamiltonian from $H_{\alpha\beta}^M$ to $\tilde{H}_{\alpha\beta}^{vac}$ is adiabatic, then ν_e produced in the sun's interior will evolve into ν_2, which is defined such that $\nu_2 > \nu_1$. Evidence suggests that $> 90\%$ of ^8B ν_e produced in the sun's core evolve into ν_2 due to matter effects in the sun [20]. Therefore, to a first approximation, the ν_e flavor content of ^8B solar neutrinos reaching the earth is expected to be $|U_{e2}|^2 \sim \sin^2\theta_{12}$.

2.3 Status of Neutrino Oscillation Measurements

Evidence for neutrino oscillations comes from both natural and man-made sources of neutrinos covering a wide range of energies. All measurements made so far can be described in

the framework of neutrino oscillations among three active flavors[4].

2.3.1 Atmospheric ν_μ disappearance

The Super Kamiokande (Super-K) experiment gave some of the first concrete evidence for neutrino oscillations in the late 1990s by measuring ν_μ[5] produced from cosmic ray showers. These showers produce pions[6] in the upper atmosphere which decay to produce neutrinos according to

$$\pi \to \mu + \nu_\mu$$

$$\mu \to e + \nu_e + \nu_\mu$$

Using a 50 kT water Cherenkov detector, Super-K observed an energy-dependent deficit in the ratio of up-going ν_μ to ν_e with respect to the ratio down-going ν_μ to ν_e [24]. This is interpreted as ν_μ created in the atmosphere on the other side of the earth oscillating into ν_τ before reaching the detector. To first order, the ν_μ survival probability can be fit according to

$$P(\nu_\mu \to \nu_\mu) = 1 - \sin^2(2\theta_{atm}) \sin^2\left(\frac{\Delta m^2_{atm} L}{4E}\right). \tag{2.32}$$

with $\sin^2(2\theta_{atm}) \sim \sin^2 2\theta_{23}$ and $\Delta m^2_{atm} \sim \Delta m^2_{32} \sim \Delta m^2_{31}$ according to Eq. 2.22. The initial Super-K results gave $\sin^2(2\theta_{atm}) > 0.82$ and $5 \times 10^{-4} < |\Delta m^2_{atm}| < 6 \times 10^{-3}\text{eV}^2$ at 90% C.L. [24]

2.3.2 Long-baseline accelerator ν_μ disappearance

A relatively pure beam of ν_μ can be built by accelerating protons and colliding them on a fixed target. The resulting hadronic shower produces charged pions[7] which are then focused

[4]Reports of neutrino oscillations by the LSND collaboration [21] would have required the addition of a fourth neutrino. However, this result has subsequently been ruled out by the MiniBooNE collaboration [22] (though the situation is still not entirely clear [23]) and so it is not considered here.

[5]Super-K does not distinguish between neutrinos and antineutrino on an event by event basis, so we drop the distinction between particles and antiparticles in what follows.

[6]Kaons are also produced in cosmic ray showers, but are neglected here for simplicity.

[7]Kaons also make a non-negligible contribution to the beam composition, but are omitted from this discussion for clarity

towards a remote detector by a magnetic horn. Neutrinos are produced from the decay in flight of the pions and daughter muons in a way analogous to cosmic ray showers:

$$\pi^+(\pi^-) \rightarrow \mu^+(\mu^-) + \nu_\mu(\bar{\nu}_\mu)$$
$$\mu^+(\mu^-) \rightarrow e^+(e^-) + \nu_e(\bar{\nu}_e) + \bar{\nu}_\mu(\nu_\mu),$$

where the charge of the particles which are focused can be selected by changing the polarity of the magnetic horn. The MINOS experiment compares the unoscillated ν_μ flux in a near detector to the oscillated ν_μ flux in a far detector. Both detectors use magnetized tracking calorimeters consisting of alternating layers of steel and plastic scintillator optimized to track and measure muons.

Again, the survival probability can be fit to first order by Eq. 2.32. MINOS and several other long-baseline accelerator ν_μ disappearance measurements have now confirmed the mixing parameters found by Super-K [25–27]. A full, combined fit of atmospheric and long-baseline accelerator neutrino experiments gives $|\Delta m^2_{atm}| = 2.32^{+0.12}_{-0.08} \times 10^{-3}$ eV^2 and $\sin^2 2\theta_{atm} > 0.90$ at 90% C.L. [26] The corresponding confidence intervals are reproduced in Fig. 2.1.

2.3.3 Solar ν_e disappearance

According to the standard solar model (SSM), a large flux of ν_e is produced as a byproduct of the *pp* fusion chain and the *CNO* cycle in the sun. Fig. 2.2 illustrates the expected neutrino flux on earth based on SSM calculations due to John Bachall [28].

The first evidence for neutrino flavor change was given by Ray Davis and collaborators in 1968, when they observed a deficit of ν_e from the sun with respect to the predictions of the SSM [8]. A deficit was subsequently confirmed by several other experiments [29–32], though the magnitude of the deficit differed between them. This discrepancy between theory and experiment was called the "solar neutrino problem".

The solar neutrino problem was definitely put to rest by the Sudbury Neutrino Observatory (SNO) experiment in the 2000s. SNO was a heavy water Čerenkov detector capable

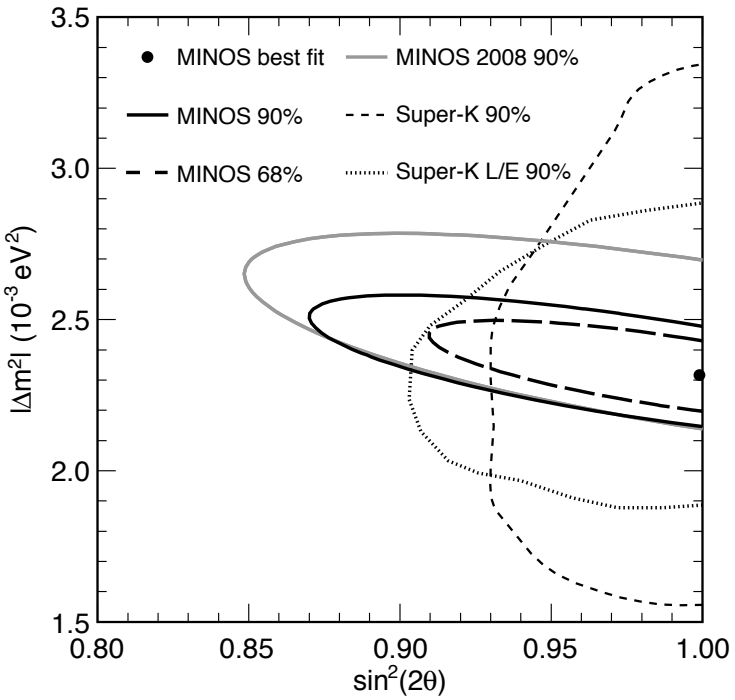

Figure 2.1: MINOS best fit ν_μ disappearance oscillation parameters and confidence intervals superimposed on Super-K allowed regions [26].

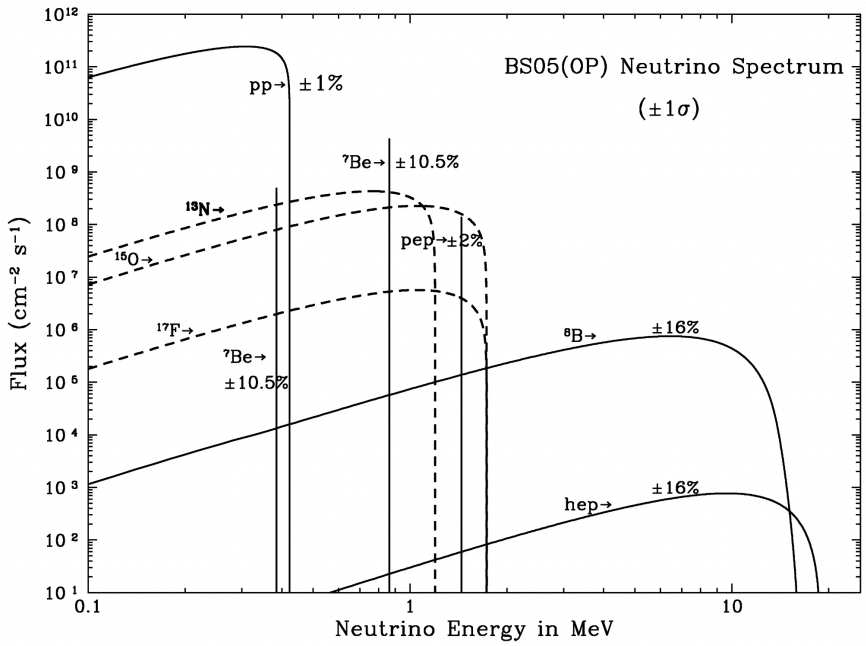

Figure 2.2: Solar ν_e flux from various branches of the *pp* fusion chain and *CNO* cycle in the the sun. Curves are given in $\mathrm{cm}^{-2}\mathrm{s}^{-1}\mathrm{MeV}^{-1}$ and the vertical lines are given in $\mathrm{cm}^{-2}\mathrm{s}^{-1}$ [28].

of detecting solar neutrinos through three independent processes

$\nu_e + d \rightarrow e^- + p + p$	Charged Current (CC) interaction
$\nu_\alpha + d \rightarrow \nu_\alpha + p + n$	Neutral Current (NC) interaction
$\nu_\alpha + e^- \rightarrow \nu_\alpha + e^-$	Elastic Scattering (ES) interaction

All neutrino flavors participate in the NC interaction equally and so this process gives a direct measure of the total solar neutrino flux. The ES interaction is sensitive to all neutrino flavors, but has a higher cross section for electron flavor neutrinos than muon and tau flavor neutrinos. The CC interaction, on the other hand, is only sensitive to electron flavor neutrinos. Therefore, the ν_e content of the solar neutrino flux can be determined in a model-independent way from measurements of these processes. In this way SNO measured a neutrino flux from NC interactions consistent with the SSM [28] and found [33]

$$\frac{\phi_{CC}}{\phi_{NC}} = 0.301 \pm 0.033, \tag{2.33}$$

which gave unambiguous evidence for neutrino flavor change. If the deficit in ν_e is inter-

preted in the context of neutrino oscillations according to Sec. 2.2.4, Eq. 2.33 constrains the ν_e flavor content of ν_2 as well as the value of Δm^2_{21}.

2.3.4 Reactor $\bar{\nu}_e$ disappearance

Nuclear power plants are an isotropic source of $\sim$ MeV $\bar{\nu}_e$ produced in the β-decay of the fission fragments of ^{235}U, ^{238}U, ^{239}Pu, and ^{241}Pu. The full, three flavor survival probability for $\bar{\nu}_e$ emitted from nuclear reactors is given by Eq. 2.18 as

$$\begin{aligned} P(\bar{\nu}_e \to \bar{\nu}_e) = 1 &- 4|U_{e2}|^2|U_{e1}|^2 \sin^2\left(\frac{\Delta m^2_{21} L}{4E}\right) \\ &- 4|U_{e3}|^2|U_{e1}|^2 \sin^2\left(\frac{\Delta m^2_{31} L}{4E}\right) \\ &- 4|U_{e3}|^2|U_{e2}|^2 \sin^2\left(\frac{\Delta m^2_{32} L}{4E}\right) \end{aligned} \tag{2.34}$$

Using the parametrization of Eq. 2.19, Eq. 2.34 can be expressed as

$$\begin{aligned} P(\bar{\nu}_e \to \bar{\nu}_e) = 1 &- \sin^2(2\theta_{13}) \sin^2(\Delta m^2 L/4E) \\ &- \cos^4\theta_{13} \sin^2 2\theta_{12} \sin^2(\Delta m^2_{21} L/4E) \end{aligned} \tag{2.35}$$

where

$$\sin^2(\Delta m^2 L/4E) = r \ \sin^2(\Delta m^2_{32} L/4E) + (1-r) \ \sin^2(\Delta m^2_{31} L/4E) \tag{2.36}$$

and

$$r = \frac{|U_{e2}|^2}{|U_{e2}|^2 + |U_{e1}|^2}. \tag{2.37}$$

2.3.4.1 Long baseline reactor $\bar{\nu}_e$ experiments

The KamLAND experiment measured the combined disappearance of reactor $\bar{\nu}_e$ emitted from several reactor cores at different nuclear power plants with a flux-weighted average distance from the detector of $\sim$ 180 km. The detector is a large liquid scintillator located in the Kamioka mine under 2700 meters water equivalent (m.w.e.) of overburden. Reactor $\bar{\nu}_e$ were detected using the IBD process $\bar{\nu}_e + p \to e^+ + n$ via the characteristic delayed coincidence of the prompt positron signal followed by the delayed neutron capture signal pioneered by Fred Reines and Clyde Cowan in the 1950s [2].

KamLAND measured an energy-dependent deficit of $\bar{\nu}_e$ with respect to the $\bar{\nu}_e$ flux predicted from the nuclear reactors. In the limit $\sin^2 2\theta_{13} \to 0$ the neutrino survival probability for KamLAND can be approximated by Eq. 2.15, with $\theta \sim \theta_{12}$ and $\Delta m^2 \sim \Delta m^2_{21}$.

The KamLAND experiment measured [34] $\Delta m^2_{21} = 7.58\ ^{+0.14}_{-0.13}\ (stat)\ ^{+0.15}_{-0.15}\ (sys) \times 10^{-5}$ eV^2 and $\tan^2\theta_{12} = 0.56\ ^{+0.10}_{-0.07}\ (stat)\ ^{+0.10}_{-0.06}\ (sys)$, which they then combined with solar neutrino data. The allowed regions for the solar neutrino experiments, the KamLAND experiment, and the combined fit are given in Fig. 2.3.

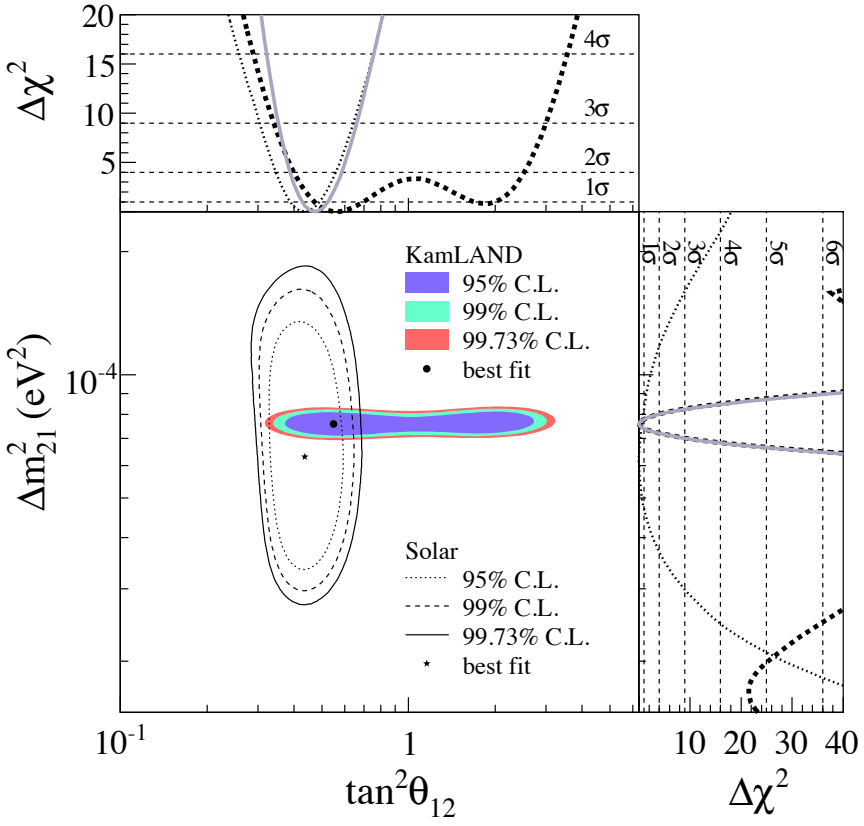

Figure 2.3: The allowed regions and $\Delta\chi^2$ contours for solar neutrino data, KamLAND $\bar{\nu}_e$ disappearance data, and the combined fit [34].

2.3.4.2 Short-baseline $\bar{\nu}_e$ disappearance

Several experiments have searched for the disappearance of reactor $\bar{\nu}_e$ with baselines of $10 - 1000$ m. Until recently[8], none has observed any significant deficit with respect to the $\bar{\nu}_e$ flux predicted from the reactors [35–42]. The best limit on $\sin^2 2\theta_{13}$ came from the CHOOZ experiment. The CHOOZ detector was a scintillation detector which measured $\bar{\nu}_e$ using IBD interactions similar to KamLAND. The $\bar{\nu}_e$ survival probability for such an experiment is given by Eq. 2.35, where the last term can be neglected if $\sin^2 2\theta_{13} > 0.02$[9] so that

$$P(\bar{\nu}_e \to \bar{\nu}_e) \cong 1 - \sin^2(2\theta_{13}) \sin^2(\Delta m^2 L/4E). \tag{2.38}$$

No significant deficit was observed and so an upper limit $\sin^2 2\theta_{13} < 0.15$ (90% C.L.) was established [16].

2.4 Measuring θ_{13}

The value of last mixing angle θ_{13} has remained unmeasured until only recently. As described in Sec. 2.2, measuring a nonzero value for θ_{13} is crucial to determining whether CP violation can be measured in neutrino oscillations.

There are two experimental approaches to measuring θ_{13}. Long-baseline accelerator experiments look for the appearance of ν_e in a $\sim$ GeV accelerator-based ν_μ beam over distances of several hundred kilometers. Short-baseline reactor experiments look for the disappearance of $\sim$ MeV $\bar{\nu}_e$ from nuclear reactors over a distance of ~ 1 km. Both have sensitivity to θ_{13}, but in different ways.

[8] In Ch. 9 we discuss recent evidence for nonzero θ_{13}.

[9] In this case the last term of Eq. 2.35 comprises less than 10% of the disappearance signal

2.4.1 Long-baseline accelerator experiments

The ν_e appearance probability in a purely ν_μ beam can be expanded in terms of the two small parameters $\Delta m^2_{21}/\Delta m^2_{31}$ and $\sin^2 2\theta_{13}$ as [18, 43]

$$P(\nu_\mu \to \nu_e) \cong \sin^2 2\theta_{13}\, T_1 - \alpha \sin 2\theta_{13}\, T_2 + \alpha \sin 2\theta_{13}\, T_3 + \alpha^2 T_4, \tag{2.39}$$

with

$$T_1 = \sin^2 \theta_{23} \frac{\sin^2[(1-x)\Delta]}{(1-x)^2}, \tag{2.40}$$

$$T_2 = \sin\delta \sin 2\theta_{12} \sin 2\theta_{23} \sin\Delta \frac{\sin(x\Delta)}{x} \frac{\sin[(1-x)\Delta]}{(1-x)}, \tag{2.41}$$

$$T_3 = \cos\delta \sin 2\theta_{12} \sin 2\theta_{23} \cos\Delta \frac{\sin(x\Delta)}{x} \frac{\sin[(1-x)\Delta]}{(1-x)}, \tag{2.42}$$

and

$$T_4 = \cos^2 \theta_{23} \sin^2 2\theta_{12} \frac{\sin^2(x\Delta)}{x^2}. \tag{2.43}$$

In the above equations $\Delta = \Delta m^2_{31}/4E$, $x = 2\sqrt{2} G_F N_e E/\Delta m^2_{31}$, G_F is the Fermi coupling constant, and N_e is the electron number density. In this expression the first term represents oscillations due to the atmospheric mass-squared splitting and the last term represents oscillations due to the solar mass-squared splitting. The second (third) term is the CP violating (conserving) interference term between the oscillations driven by the atmospheric and solar mass-squared splittings. The corresponding expression for antineutrinos can be obtained by reversing the sign of x and δ in Eq. 2.40- 2.43.

The above expression makes clear that long-baseline ν_e appearance experiments are sensitive not only to θ_{13} but also to δ and the sign of Δm^2_{31}. This makes a unambiguous measurement of θ_{13} impossible. However, if the value of θ_{13} can be determined by other means, then by comparing the probabilities for $\nu_\mu \to \nu_e$ and $\bar{\nu}_\mu \to \bar{\nu}_e$, long-baseline accelerator experiments may be able to determine the effects of CP violation and to determine whether the mass hierarchy is normal or inverted.

2.4.1.1 Hint of Nonzero θ_{13}

Two long-baseline accelerator experiments have performed ν_e appearance searches, which have given hints of a nonzero value of θ_{13}. The MINOS experiment recently reported a

best fit value of $2\sin^2\theta_{23}\sin^2(2\theta_{13}) = 0.041\ ^{+0.041}_{-0.031}$ ($0.079\ ^{+0.071}_{-0.053}$) for the normal (inverted) mass hierarchy at $\delta = 0$, but only disfavored $\sin^2 2\theta_{13} = 0$ at 89% C.L. [44] The T2K experiment also performed a search for ν_e appearance and found $0.03\ (0.04) < \sin^2 2\theta_{13} < 0.28\ (0.34)$ (90% C.L.) for the normal (inverted) mass hierarchy at $\delta_{CP} = 0$ with an indication of ν_e appearance at a significance of 2.5 σ [45]. Though both experiments show hints of nonzero θ_{13}, neither experiment has given conclusive results.

The T2K experiment is ongoing and will continue to update its ν_e appearance results as it accumulates more data. In addition, a third long-baseline accelerator experiment called Noνa should come on line in the summer of 2012. Noνa is not only sensitive to θ_{13}, but it also has sensitivity to the sign of Δm^2_{31} through matter effects (see Eq. 2.39) [46].

2.4.2 Short-baseline reactor experiments

The $\bar{\nu}_e$ survival probability measured by short-baseline reactor experiments at distances of roughly ~ 1 km from the reactor cores is given by Eq. 2.38. To improve on the CHOOZ limit, systematic uncertainties must be kept at the few percent level or lower. Three next-generation reactor experiments, Double Chooz [47], Daya Bay [48], and RENO [49], designed to have sensitivity $\sin^2(2\theta_{13})$ down to $0.01 - 0.03$ are currently taking data. If $\sin^2(2\theta_{13}) \sim 0.1$ as the combined fits of the results from T2K and MINOS suggest, then these experiments will make unambiguous measurements of $\sin^2(2\theta_{13})$ in 2012[10].

2.4.3 Looking Forward

Since Ray Davis first reported a deficit of solar neutrinos in the 1960s, we've come a long way in our understanding of neutrino mass, mixing, and flavor change. Much of the progress in measuring the mass-squared differences and the parameters of the lepton mixing matrix has come in the last two decades. The situation at the beginning of 2012 is best summarized

[10] In Ch. 9 we will see that this was in fact the case.

by neutrino mixing parameters given by the Particle Data Group [16]

$$\sin^2 2\theta_{12} = 0.861\ ^{+0.026}_{-0.022} \tag{2.44}$$

$$\Delta m^2_{21} = (7.50 \pm 0.21) \times 10^{-5}\ \text{eV}^2 \tag{2.45}$$

$$\sin^2 2\theta_{23} > 0.92\ (90\%\ \text{C.L.}) \tag{2.46}$$

$$|\Delta m^2_{32}| = (2.43 \pm 0.13) \times 10^{-3}\ \text{eV}^2 \tag{2.47}$$

$$\sin^2 2\theta_{13} < 0.15\ (90\%\ \text{C.L.}) \tag{2.48}$$

The hunt is on to measure θ_{13}, the last unknown angle of the lepton mixing matrix. Indications for a nonzero value of θ_{13} are given by the latest results from the long-baseline accelerator experiments MINOS and T2K. Next-generation reactor experiments capable of probing $\sin^2(2\theta_{13})$ down to $0.01-0.03$ are online and currently taking data. If θ_{13} is found to be > 0.01, then high intensity, conventional neutrinos beams may be able to probe the Dirac CP violating phase δ of the lepton mixing matrix. An observation of CP violation in lepton sector would be truly profound because the only known current source of CP violation in the SM comes from the quark mixing matrix [17, 50] and is too small to account for the observed matter/antimatter asymmetry in the universe [51]. CP violation in lepton sector may provide a clue to understanding what role neutrinos may have played in producing the matter/antimatter asymmetry in the universe [52]. Measuring θ_{13} is just the beginning.

Chapter 3

The Double Chooz Experiment

The Double Chooz experiment seeks to measure the value of $\sin^2(2\theta_{13})$ by looking for the disappearance of $\bar{\nu}_e$'s emitted from twin 4.25 GW_{th} pressurized water reactors (PWRs) at the Chooz nuclear power plant in Champagne-Ardenne region of France. Fig. 3.1 gives an aerial view of the Chooz nuclear power plant. In Sec. 3.1, we give an overview of the Double Chooz experimental concept and the $\bar{\nu}_e$ detection technique. In Sec. 3.2, we describe the Double Chooz detector in detail.

3.1 Experimental Concept

The survival probability for short-baseline reactor $\bar{\nu}_e$ disappearance experiments is derived in Ch. 2 and given by Eq. 2.38. The expression depends on two theoretical parameters which must be determined from experiment: Δm^2 and $\sin^2(2\theta_{13})$. It also depends on two parameters, L and E, which describe the neutrino propagation distance and energy, respectively. These are experimental parameters that are dictated by the experimental design. If L is measured in meters, E is measured in MeV, and Δm^2 is measured in eV^2, then the expression for the survival probability is given by

$$P(\bar{\nu}_e \to \bar{\nu}_e) \cong 1 - \sin^2(2\theta_{13}) \sin^2(1.267 \Delta m^2 L/E). \tag{3.1}$$

As a function of the neutrino propagation distance, the survival probability reaches its first minimum at $L \sim E/\Delta m^2$. The value of Δm^2 in this expression is precisely measured

Figure 3.1: An aerial view of the Chooz nuclear power plant in Champagne-Ardenne region of France. This is the site of the Double Chooz experiment.

by long-baseline ν_μ disappearance experiments and found to be $(2.43 \pm 0.13) \times 10^{-3}$ eV^2 [16]. Therefore, a detector measuring reactor $\bar{\nu}_e$ with energies of a few MeV will be most sensitive to $\sin^2(2\theta_{13})$ at a distance of ~ 1250 m from the reactor core for 3 MeV neutrinos.

3.1.1 $\bar{\nu}_e$ Disappearance

Nuclear reactors are copious, isotropic sources of $\bar{\nu}_e$'s (see Ch. 4). The Double Chooz experiment aims to determine $\sin^2(2\theta_{13})$ by measuring $\bar{\nu}_e$ disappearance at a distance of ~ 1 km from the twin Chooz reactor cores, Chooz B1 and Chooz B2. This can be done in one of two ways.

In the first approach, a single-detector measurement of the $\bar{\nu}_e$ flux at ~ 1 km can be compared to the $\bar{\nu}_e$ flux prediction given by simulations of the nuclear reactor cores. In this case the fission rates for each of the main fuel isotopes contributing to the $\bar{\nu}_e$ flux are determined from simulations. These are then multiplied by the corresponding $\bar{\nu}_e$ energy spectrum per fission to obtain the $\bar{\nu}_e$ flux prediction. This approach was taken by previous reactor $\bar{\nu}_e$ experiments and is limited by the $\sim 2\%$ precision with which the $\bar{\nu}_e$ flux can be

predicted.

In the second approach, two (or more) identical detectors are used to measure the $\bar{\nu}_e$ flux at different distances. The first ("near") detector is placed close to the reactor cores such that the $\bar{\nu}_e$ survival probability is ~ 1. The near detector therefore measures the unoscillated $\bar{\nu}_e$ reactor flux. The second ("far") detector is placed at ~ 1 km to maximize sensitivity to an oscillated $\bar{\nu}_e$ reactor flux. The disappearance probability can then be obtained by comparing the measured $\bar{\nu}_e$ flux at the near and far detectors after correcting for the $1/L^2$ dependence of the isotropic $\bar{\nu}_e$ flux, where L is the distance from the reactor. This approach is being taken by current reactor neutrino experiments. It overcomes the limitation associated with precisely predicting the reactor $\bar{\nu}_e$ flux. In general, multi-detector measurements are limited by uncertainty on the relative calibration between the detectors.

The Double Chooz near detector will be located a distance of ~ 400 meters from the reactor cores under ~ 120 meters of water equivalent (m.w.e.) flat overburden. The far detector is located a distance of ~ 1.05 km from the reactor cores under the side of a mountain providing ~ 300 m.w.e. of overburden. The overburden is crucial in reducing the muon-induced backgrounds described in Ch. 7. Table 3.1 gives further details of the experimental site.

Detector	Distance to Chooz B1	Distance to Chooz B2	Overburden
Far	1114.6 m	998.1 m	300 m.w.e.
Near	466 m	351 m	120 m.w.e.

Table 3.1: Summary of the distances of each detector to the two Chooz reactor cores. The distances for the far detector pit were surveyed by the CHOOZ experiment to an accuracy of 10 cm [53]. An uncertainty of 20 cm is used by DC to account for differences in the CHOOZ and DC detectors. The distances for the near detector are design distances.

The Double Chooz near detector is not expected to begin taking data until 2014. However, the Double Chooz far detector began taking data in December 2011. Therefore, the analysis described in this work uses the single-detector approach to measure the $\bar{\nu}_e$ disappearance probability at ~ 1 km in order to determine the value of $\sin^2(2\theta_{13})$.

3.1.2 Detection Technique

Double Chooz detects reactor $\bar{\nu}_e$'s via the inverse β-decay (IBD) interaction on free protons:

$$\bar{\nu}_e + p \rightarrow e^+ + n \tag{3.2}$$

Using the IBD interaction to detect reactor $\bar{\nu}_e$ was pioneered by Reines and Cowan in the 1950's. It was used for two main reasons. First, the charged current interaction has a larger interaction cross section for MeV $\bar{\nu}_e$ than any other process. Second, both final state particles can be detected in coincidence, which allows for a very efficient suppression of backgrounds associated with single interactions in the detector.

In the lab frame, the IBD energy threshold, $E_{\bar{\nu}_e}^{thr}$, is given by

$$E_{\bar{\nu}_e}^{thr} = \frac{(M_n + m_e)^2 - M_p^2}{2M_p} = 1.8 \text{ MeV}. \tag{3.3}$$

Above threshold, the energy of the incoming $\bar{\nu}_e$ energy $E_{\bar{\nu}_e}$ is related to the energy of the outgoing positron E_{e^+} according to

$$E_{\bar{\nu}_e} = \frac{2M_p E_{e^+} + M_n^2 - M_p^2 - m_e^2}{2M_p - 2E_{e^+} + 2\cos\theta_{e^+}\sqrt{E_{e^+}^2 - m_e^2}} \tag{3.4}$$

where M_p is the mass of the proton, M_n is the mass of the neutron, m_e is the mass of the electron, and θ_{e^+} is the angle of the outgoing positron momentum with respect to the incoming $\bar{\nu}_e$ direction. For reactor $\bar{\nu}_e$ with energies of a few MeV, Eq. 3.4 can be approximated as

$$E_{\bar{\nu}_e} \simeq (E_{e^+} + \Delta)(1 + E_{e^+}/M_p) + \frac{\Delta^2 - m_e^2}{M_p} \tag{3.5}$$

where $\Delta = M_n - M_p = 1.293$ MeV.

The IBD cross section is very well known. In the large nucleon mass limit, it can be written as $\sigma_{IBD}(E_e) = \kappa p_e E_e$, where $E_e = E_\nu - (M_n - M_p)$ and $p_e = \sqrt{E_e^2 - m_e^2}$ are the energy and momentum of the positron. The prefactor κ can be directly related to the neutron lifetime as $\kappa = \frac{2\pi^2/m_e^5}{f^R \tau_n} = 0.961 \times 10^{-43} \left(\frac{cm}{\text{MeV}}\right)^2$, where τ_n is the measured neutron lifetime [16] and f^R is the phase space factor for the β-decay of the free neutron [54]. Corrections to the IBD cross section have been computed to $\mathcal{O}(1/M)$ [55], where M is the average nucleon mass. Fig. 3.2 gives a cartoon example of a measured IBD energy spectrum obtained from the convolution of the reactor $\bar{\nu}_e$ flux and the IBD cross section in true neutrino energy.

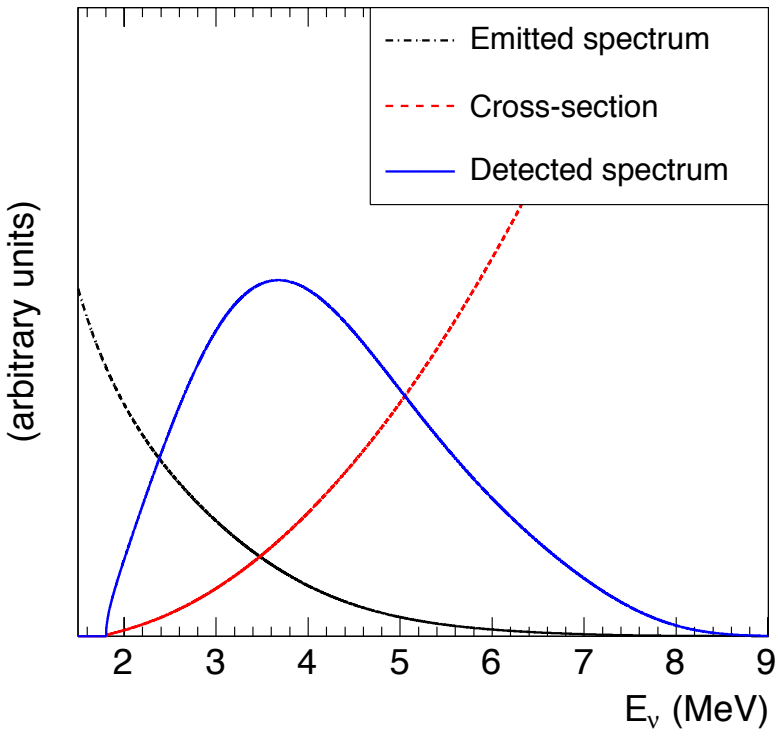

Figure 3.2: Cartoon of the measured IBD energy spectrum obtained from the convolution of the reactor $\bar{\nu}_e$ flux and the IBD cross section in true neutrino energy [56].

3.1.3 Organic Liquid Scintillator Detector

The Double Chooz detector is an organic liquid scintillator detector. Organic liquid scintillators are aromatic hydrocarbons typically composed of benzene-ring structures. In such molecules, valence electrons are not confined to a particular atom, but occupy delocalalized, molecular orbitals. Ionizing radiation excites the higher energy levels of the molecule, which then quickly de-excite to the first excited energy level by radiationless processes (internal degredation). Scintillation light is emitted due to transitions from this first excited electronic state to the ground state. Very often, however, the decay is not directly to the ground state but instead proceeds through an excited vibrational state of the ground state. Therefore, the photon is emitted at a lower energy and has a low probability to re-excite the scintillator [57].

Generally, secondary wavelength-shifting aromatic compounds ("fluors") are dissolved in the primary scintillator solvent. These fluors are chosen to absorb the light from the primary scintillator and re-emit it at longer wavelengths for which the scintillator is more transparent and for which photo-detection is more efficient. In fact, however, in scintillator solutions the energy absorbed by the solvent can be transferred to the solutes and then emitted directly at longer wavelengths. Typical decay times for scintillation light emission in organic liquid scintillator are $3 - 4$ ns.

The Double Chooz neutrino target is an organic liquid scintillator dissolved in n-dodecane ($C_{12}H_{26}$) and doped with Gadolinium (Gd). The Hydrogen-rich scintillator provides free proton targets for the IBD reaction. Prompt scintillation light is produced as the positron loses energy and then annihilates into two 511 keV γ rays. The neutron is identified by a delayed capture on Gd which occurs after a characteristic time scale of ~ 30 μs. The thermal neutron capture on Gd has a very large cross section and releases ~ 8 MeV of energy in γ rays which then produce additional scintillation light[1]. This is easily separated from the natural γ-ray background coming from the U and Th chains, which do not extend beyond ~ 3 MeV. Fig. 3.3 gives a cartoon illustration of an IBD delayed coincidence.

[1] γ rays produce scintillation light indirectly via the photoelectric effect, Compton scattering, or e^-e^+ pair production.

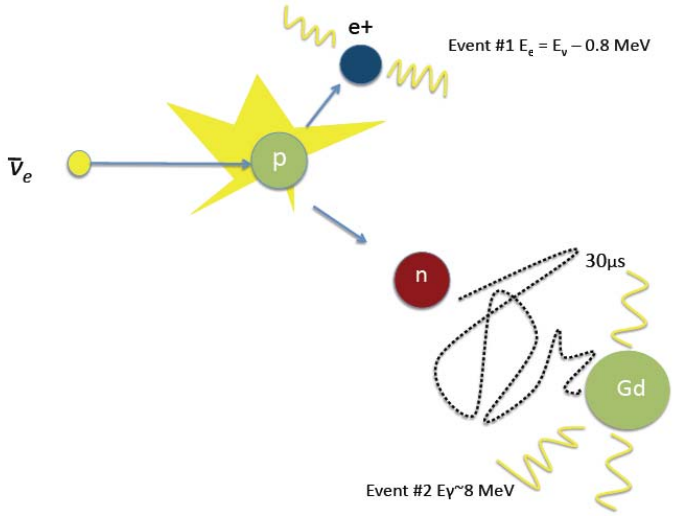

Figure 3.3: Cartoon of the IBD ($\bar{\nu}_e + p \rightarrow e^+ + n$) delayed coincidence signal in the DC far detector.

3.2 The Double Chooz Detector

The Double Chooz detector uses a multi-zone design. The far detector is illustrated in Fig. 3.4. The central detector region consists of four concentric cylindrical liquid volumes surrounded by a passive steel shielding. An outer muon veto sits above the steel shielding on top of the detector and a calibration glove box connects to the central volumes through a long neck called the "chimney". In what follows, we describe each of the detector components in detail.

3.2.1 $\bar{\nu}_e$ Target

The inner-most volume is called the "target" and defines the IBD interaction volume. It consists of 10.3 m^3 of a newly-developed liquid scintillator doped with Gd as a Gd-β-diketonate compound ($Gd(thd)_3$) [58] enclosed in an 8 mm thick acrylic vessel transparent to UV and visible light. The target vessel has an approximately cylindrical shape with a radius of 1.150 m and a height of 2.458 m.

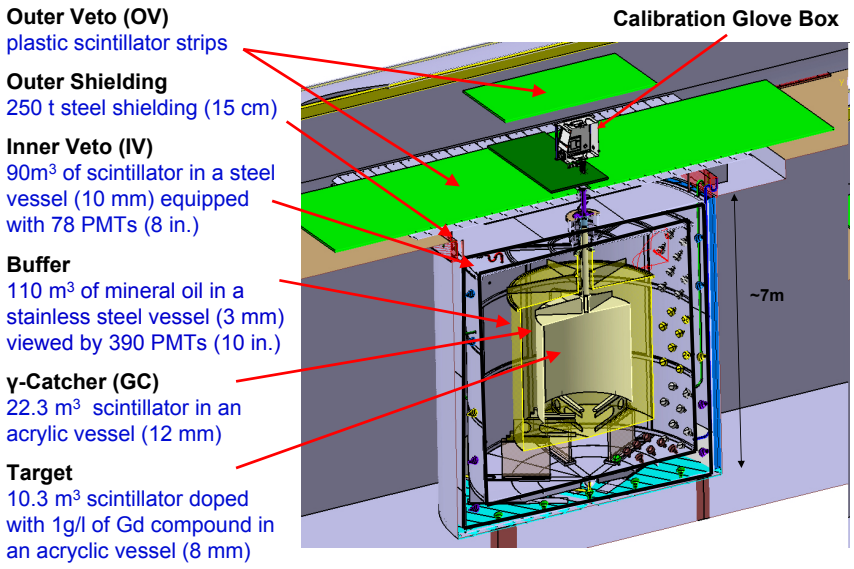

Figure 3.4: A cutout illustrating the major mechanical components of the DC far detector. Details of each structure are given in the text.

The scintillator uses ortho-Phenylxylylethane (PXE) as the primary aromatic, mixed with $> 99.5\%$ pure n-dodecane. PXE emits light in the UV, so two wavelength-shifting components, PPO and bis-MSB, are added to shift the emission spectrum to progressively longer wavelengths. In addition, oxolane (THF) is used to dissolve the $Gd(thd)_3$ before it is added to the scintillator. Table 3.2 summarizes the composition of the target liquid as well as the Hydrogen fraction by weight for each component.

The density of the target liquid was measured to be 0.8035 ± 0.0010 kg/l at 15°C [58]. The number of free proton targets can be deduced based on knowledge of the density, scintillator composition, and target volume. However, in Sec. 3.3 we describe a more precise measurement of the number of free protons in the target based on a weight measurement.

3.2.2 γ-catcher

The target is surrounded by 55 cm layer of Gd-free liquid scintillator called the "γ-catcher". The γ-catcher is comprised of 22.3 m^3 of liquid and is contained in a second, 12 mm

Component	Concentration	H [wt.%]
Dodecane	80% (vol.)	15.39
PXE	20% (vol.)	8.63
PPO	7 g/l	5.0
bis-MSB	20 mg/l	7.1
$Gd(thd)_3$	1 g/l Gd	8.5
THF	0.5% (wt.)	11.2

Table 3.2: Summary of the components making up the target liquid scintillator [58].

transparent acrylic vessel. The γ-catcher vessel has an approximately cylindrical shape with a radius of 1.708 m and a height of 3.572 m.

The γ-catcher is designed to ensure that the energy of the γ rays produced in the target volume is fully absorbed in the scintillating volumes. This improves the uniformity of the detector response and enhances the efficiency for detecting neutron captures on Gd at the edge of the target volume.

The γ-catcher scintillator composition was chosen to match the density (critical for mechanical stability) and light yield (important for good energy reconstruction) of the target. The γ-catcher is not doped with Gd. Therefore, the concentrations of PXE and PPO were lowered to match the target light yield. In order to match the density of the target, Shell Ondina 909—a white mineral oil (ρ = 0.811 kg/l at 23°C) with good transparency and a higher density than dodecane (ρ = 0.747 kg/l at 23°C)—was added as a solvent to the γ-catcher scintillator to compensate for the reduction in PXE (ρ = 0.984 kg/l at 23°C) [59]. In contrast to n-dodecane, the chemical composition of Shell Ondina 909 is not precisely known. Therefore, the Hydrogen fraction of the γ-catcher scintillator must be measured directly and was found to be 14.6 ± 0.2 % by weight [58]. Table 3.3 summarizes the composition of the γ-catcher liquids.

Component	Concentration
Mineral Oil	66% (vol.)
Dodecane	30% (vol.)
PXE	4% (vol.)
PPO	2 g/l
bis-MSB	20 mg/l

Table 3.3: Summary of the components making up the γ-catcher liquid scintillator [58].

3.2.3 Buffer

Surrounding the γ-catcher is a $\sim$ 1 m thick layer of non-scintillating oil called the "buffer". The buffer oil is a mixture consisting of 46% n-alkanes and 54% mineral oil by volume chosen to have density of 0.804 kg/l at 15°C. In total, the buffer is comprised of $\sim$ 110 m^3 of liquid and is contained in a 3 mm thick cylindrical steel vessel, on which 390 10-inch photomultiplier tubes (PMTs) are mounted. The PMTs have reflective μ metal shields and are angled towards the center of the detector to maximize scintillation light collection from the target. The buffer is designed to shield the scintillating volumes from γ radioactivity which may be present in detector materials such as the PMT glass and steel walls. The target, γ-catcher, and buffer volumes are collectively referred to as the inner detector (ID).

3.2.4 Inner Veto

Surrounding the buffer is the inner veto (IV), which consists of a $\sim$ 50 cm layer of liquid scintillator optically isolated from ID. Linear Alkyl Benzene (LAB) is used as the primary aromatic in the IV scintillator and is mixed with n-alkanes. Similar to the target and γ-catcher scintillators, PPO and bis-MSB are added as wavelength-shifting components. Table 3.4 summarizes the compositions of the IV liquids.

In total, the IV is comprised of $\sim$ 90 m^3 of liquid and is contained in a 10 mm thick cylindrical steel vessel instrumented with 78 fully-encapsulated, 8-inch PMTs. The IV is designed to detect cosmic ray muons entering or passing near the ID. To enhance the light collection in the IV, the outer wall of the buffer vessel is covered with a thin polymer film

reflector and the inner wall of the IV vessel is painted white.

Component	Concentration
LAB	50.0% (vol.)
n-alkanes	50.0% (vol.)
PPO	2 g/l
bis-MSB	20 mg/l

Table 3.4: Summary of the components making up the IV liquid scintillator [59].

3.2.5 Steel Shielding

A 15 cm layer of steel surrounds the buffer and is designed as a passive shield against ambient γ radiation in the far detector lab and in the rock surrounding the detector.

3.2.6 Outer Veto

A second, outer veto (OV) consisting of 1.6 m $\times$ 3.625 m modules of plastic scintillator strips with wavelength-shifting fibers sits on top of the detector. Each module consists of 64 strips arranged in two layers and is read out by custom-built electronics connected to a multi-anode PMT. Horizontal planes of modules are oriented in orthogonal directions to give position information for muons crossing the OV. The OV is designed to tag "near miss" muons which traverse the rock just outside the IV and can produce fast neutron backgrounds in the detector (see Ch. 7). It also serves as a redundant muon veto to the IV, which lacks complete 4π coverage of the ID due to dead regions from support material.

3.2.7 Glove Box

The glove box sits on legs above the IV. It connects to the target volume via the chimney, which has a diameter of 15 cm. The glove box is used to introduce calibration sources into the target in a clean and controlled environment.

3.2.8 Calibration Systems

Several calibration systems are used to characterize the response of the detector.

The ID light injection (IDLI) system and the IV light injection (IVLI) system are used to measure the gains of the ID and IV PMTs, respectively. Each consists of a central control box which distributes light from a variable-intensity LED to the ID or IV via optical fibers. By calculating the distance between the optical fibers and each PMT, the IDLI can also be used to measure the time offsets of the ID PMTs (see Sec. 3.4.1.2).

The Z-axis system allows radioactive sources to be deployed in the target along the central axis of the detector from the glove box. It consists of a source rod attached to a weight which is lowered into the detector by unwinding a spool of wire. The wire spool is controlled by a micro-step motor allowing fine control over the position of the source. The Z-axis system is used to calibrate the energy response of the detector in the target (see Ch. 5).

The guide tube (GT) wire driver system is used to introduce sources into the γ-catcher region of the detector. It consists of a closed-loop, stainless steel tube attached to the outside of the target acrylic vessel (see Fig. 3.5). Sources are attached to a wire and then fed into the tube using a computer-controlled driver motor. The GT is used to calibrate the energy response of the γ-catcher as well as understand systematic uncertainties associated with neutron physics.

3.3 Target Proton Measurement

The number of H atoms in the neutrino target can be deduced from knowledge of the chemical composition of the scintillator and a precision weight measurement of the neutrino target liquid.

Uncertainty in the purity of the liquid scintillator components is the major source of systematic error in the target H measurement. The n-dodecane used in the neutrino target, for example, consists of 99.5% n-paraffin, of which only 99.6% is n-dodecane. Calculations of the H fraction were made based on the known chemical composition of the scintillator components, taking into account the uncertainties in the purity of each component. The

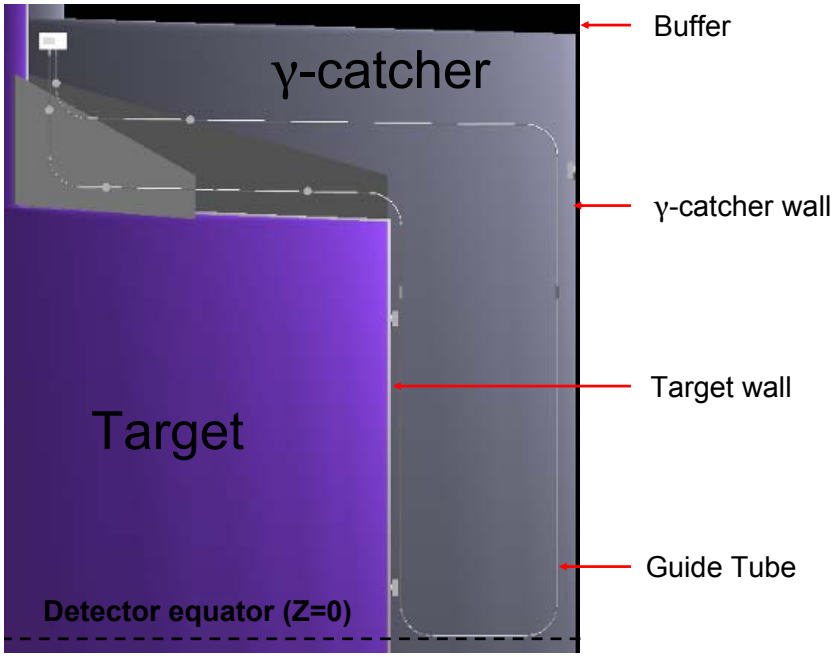

Figure 3.5: An image of the guide tube attached to the target wall from the detector MC simulation. The Z-axis of the detector runs along the left-hand side of the picture.

target was thus determined to have an H fraction of $13.60 \pm 0.04\%$ by weight [58]. A cross check of this result was preformed using a chemical analysis of the target scintillator and found to give consistent results.

To measure the weight of the target liquid, a weighing tank (WT) was installed in the far detector hall on 3 force gauges whose summed output was continually measured by a dedicated PC. The WT was filled with the neutrino target liquid and then measured. Next, the target liquid was transferred directly to the detector filling operating system (DFOS) and pumped into the target vessel. Temperatures in the neutrino target as well as in the WT were precisely monitored. After the filling of the neutrino target was complete, a second measurement of the WT was performed. To first order, the difference of these two measurements gives the weight of the neutrino target liquid. Corrections were applied to account for all known systematic effects and the total mass of the neutrino liquid target was determined to be 8288 ± 3 kg at 13.4 °C [60]. A cross-check of this result was performed using measurements of the target liquid density and the dimensions of the target vessel. These were found to be consistent with the more precise weighing tank measurement.

The number of H atoms in the neutrino target, N_H, can be expressed in terms of f, the fraction of H in the target scintillator by weight, and M_T, the mass of the neutrino target liquid as

$$N_H = f \times M_T / m_H, \tag{3.6}$$

where m_H is the mass of H. Based on the measurements of f and M_T given above, N_H is determined to be $(6.738 \pm 0.020) \times 10^{29}$, contributing an overall 0.3% normalization uncertainty to the predicted $\bar{\nu}_e$ flux at the far detector.

3.4 PMTs, Electronics, and Trigger system

Individual ID PMT pulses are processed by custom front-end electronics (FEE) and split in 2 different paths. In one path, PMT signals are sent to an 8-bit, flash-ADC (FADC), which digitizes the PMT waveform data at a rate of 500 MHz. The DAQ continually writes this data to one of 1024 separate circular buffers. In the second path, summed PMT signals are sent to the trigger system. If a trigger condition is satisfied, the trigger system sends a signal to the FADCs to start writing PMT waveform data to a new circular buffer, and the DAQ reads out a 256 ns window of the circular buffer containing the digitized waveform information for the event. The trigger system also generates a $\sim$ 1 Hz fixed rate trigger, which is used to monitor PMT pedestals.

3.4.1 PMT Response and Readout

During installation the gain of each PMT was measured and the high voltage (HV) for each PMT was adjusted so that each PMT had a nominal gain of 10^7. During commissioning the PMT gain was then lowered to 5/6 of the nominal value in order to mitigate the effects of unexpected PMT-induced background events (see Sec. 6.3).

Digitized PMT waveform data consist of 128 time samples of the PMT pulse measured in digitized units of current (DUI). The total PMT charge is measured in digitized units of charge (DUQ) and obtained by integrating the PMT pulse over the 2 ns time samples.

Digitized PMT pulses are integrated using a pulse reconstruction package called RecoPulse. RecoPulse uses a 112 ns sliding window to determine the maximum charge integral

of the PMT waveform. The pedestal is determined from the first 16 ns of the 256 ns readout window. However, if the RMS of this pedestal differs by more than 0.5 DUI from the RMS of pedestal computed using the full 256 ns window of the last fixed rate trigger, then the fixed rate trigger pedestal is used instead. In addition two thresholds are also applied in RecoPulse to distinguish real pulses from noise. First a minimum reconstructed charge Q_{min} is given by

$$Q_{min} = 5\sigma_{ped}\sqrt{W} \tag{3.7}$$

where σ_{ped} is the standard deviation of the pedestal and W is the number of time samples integrated for the for charge measurement. Second, reconstructed pulses are required to have an amplitude of > 1 DUI.

3.4.1.1 Gain Calibration

The time variation of the gain of the ID PMTs is calibrated using fits to the first and second photoelectron peaks of the PMT reconstructed charge spectra. In terms of the reconstructed charge x, fit function is given by

$$F(x) = \sum_{n=1}^{2} N \frac{e^{-\mu}\mu^n}{n!} \frac{1}{\sqrt{2\pi n\sigma_1^2}} e^{-\frac{(x-na)^2}{2n\sigma_1^2}} \tag{3.8}$$

where μ is the average number of PEs, a is the mean of the single PE peak, σ_1 is the width of the single PE peak, and N is an overall normalization.

The mean gain for all 390 PMTs is averaged over a period of 5 days and then used to convert the average ID PMT charge response into a calibrated number of photoelectrons (PEs). The reconstructed energy is then determined by scaling the calibrated PEs such that the mean of the reconstructed neutron capture peak on H corresponds to 2.22 MeV for ^{252}Cf source data at the center of the detector (see Sec. 5.3.2). As a check, Fig. 3.6 shows the stability of the neutron capture peak on Gd for neutrino candidates (see Fig. 6.15) after the gain calibration has been applied.

3.4.1.2 PMT Time Offset Calibration

IDLI data is taken every $4-8$ hours to monitor the stability of the ID PMT time offsets. ID PMTs are divided into 8 groups which are illuminated by 8 different LEDs. For each PMT

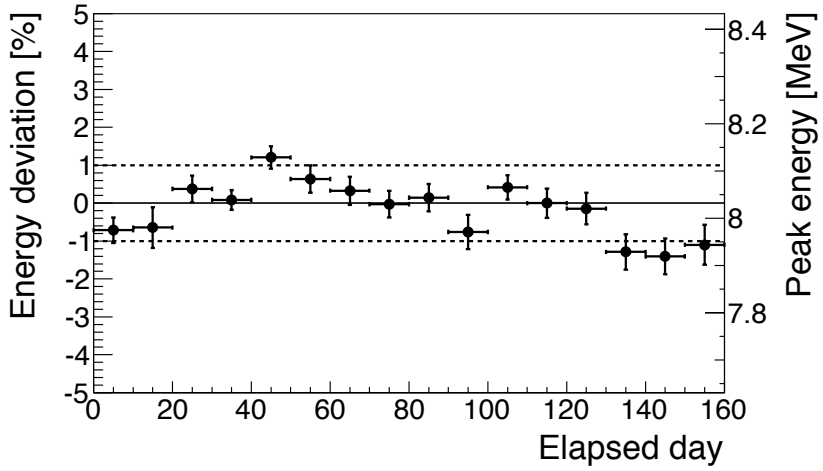

Figure 3.6: Mean of the neutron capture peak on Gd for IBD candidates given in Ch. 6 as function of calendar day. The mean energy of the peak is stable within 1% during the data-taking period.

the time difference ΔT is determined between the external IDLI trigger signal and the time when the PMT pulse reaches its maximum. For each group of PMTs ΔT is determined as a function of the distance between the PMT and the LED optical fiber and then fit to a linear function. Fig. 3.7 shows an example of the linear fit performed for each of the 8 PMT groups. The slopes of these 8 linear fits are averaged to give m_{avg}. The PMT time offsets are then determined as the residual difference between the measured ΔT and a second linear fit performed for each group of PMTs, in which the slope is fixed to m_{avg}.

3.4.2 The Trigger System

The trigger system consists of three independent trigger boards: two for the ID and one for the IV. Different trigger conditions are used for the ID trigger boards and the IV trigger boards. However, all three boards are connected to a single trigger master board which initiates a readout of all ID and IV PMTs whenever a trigger condition in any of the 3 trigger boards is satisfied.

Each ID trigger board is connected to 195 ID PMTs evenly distributed throughout the detector. The FEE sums the PMT pulses in 12 groups of 16 PMTs and one group of three

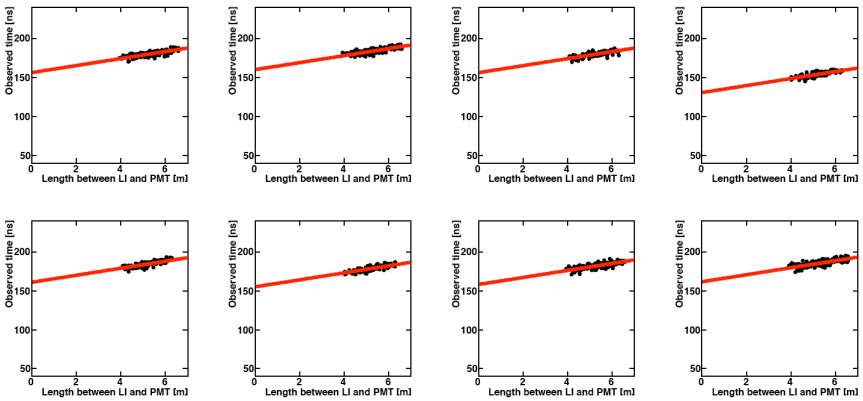

Figure 3.7: Plots of observed PMT hit times relative to the external IDLI trigger signal versus the distance between the PMT and the LED optical fiber. Linear fits are performed for each of the 8 groups of PMTs and then used to extract the individual PMT time offsets as described in the text [61].

PMTs for each ID trigger board. The total summed PMT signal as well as the summed PMT signal for each group is discriminated against different programmable thresholds. The neutrino threshold for the total summed PMT signal is set at a $\sim$ 350 keV equivalent energy and the threshold for the PMT group sum is set at a $\sim$ 250 keV equivalent energy threshold (scaled to the number of PMTs). In order to satisfy the neutrino trigger condition, ≥ 2 PMT groups must be above threshold and the total summed PMT signal must be above the neutrino threshold. Another threshold for the total summed PMT signal is set at a $\sim$ 200 keV equivalent energy threshold and pre-scaled such that only 1/1000 of the triggers above this threshold are read out.

The IV trigger board is connected to all 78 IV PMTs arranged in 5 groups of 3–6 PMTs. A threshold scan was performed *in situ* of the summed PMT signal discriminator and a suitable threshold was chosen above the γ-ray background at $\sim$ 4 MeV. The IV trigger condition is satisfied when both the summed PMT signal and at least one PMT group sum is above this threshold (scaled to the number of PMTs).

3.4.2.1 Trigger Efficiency

The trigger efficiency for the detector was determined by selecting a sample of events which passed the pre-scaled, low-energy threshold and counting how many of these events also passed the neutrino threshold. Fig. 3.8 shows the trigger efficiency as a function of reconstructed visible energy obtained using this method. The trigger efficiency is 50% at 350 keV and increases to $100.0\% + 0.0\% - 0.4\%$ at 700 keV, which is used for the IBD prompt energy analysis threshold (see Ch. 6). Just above 1 MeV, there is a slight dip in the trigger efficiency caused by one event which triggered the pre-scaled threshold but did not trigger the neutrino threshold. This dip is included in the quoted trigger efficiency uncertainty.

3.4.2.2 Electronics and Trigger Dead-time

The trigger system has a $64 - 128$ ns dead time after each trigger. A conservative estimate of the inefficiency due to any trigger dead-time is given by $R \times T$, where R is the the 120 Hz trigger rate and T the dead time is the known $64 - 128$ ns trigger dead-time. The resulting inefficiency is found to be 0.15×10^{-4}. In fact the 256 ns FADC readout window allows most

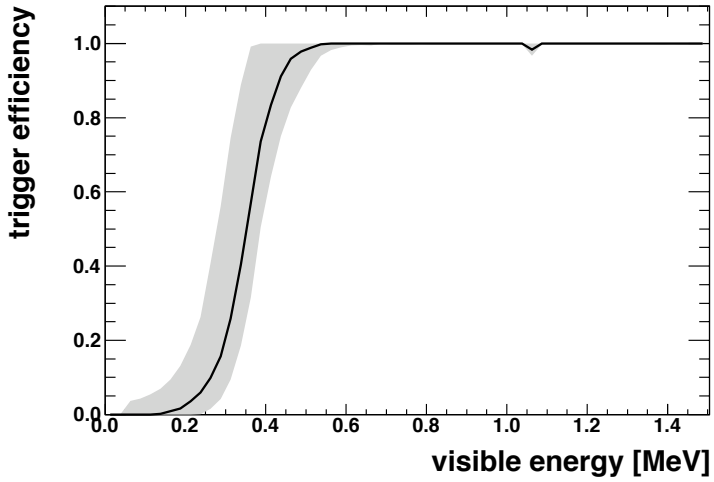

Figure 3.8: Trigger efficiency as a function of visible energy. The gray band represents the systematic uncertainty.

of the triggers in this $64 - 128$ ns window to be recovered and so the actually inefficiency is much smaller than this and can be neglected.

As a cross check, dedicated tests were performed with the IDLI during commissioning to measure any trigger dead-time for for light levels similar to those of IBD candidate events. No trigger dead time was observed.

Chapter 4

Reactor $\bar{\nu}_e$ Flux

Nuclear reactors are very pure, isotropic sources of $\bar{\nu}_e$. Antineutrinos are produced at a rate of $\sim 2 \times 10^{20}$ $\bar{\nu}_e$ $\mathrm{GW}_{\mathrm{th}}^{-1}$ s^{-1} from the β decays of fission fragments of 4 main fuel isotopes ^{235}U, ^{238}U, ^{239}Pu, and ^{241}Pu in the reactor core.

To see how this comes about, consider a typical fission reaction in the reactor core, in which a neutron induces a fission of $^{235}_{92}$U producing two unequal fission fragments and two neutrons

$$^{235}\mathrm{U} \ + \ n \rightarrow \ ^{A_1}\mathrm{X}_1 \ + \ ^{A_2}\mathrm{X}_2 \ + \ 2n, \tag{4.1}$$

where $A_1 + A_2 = 234$. Stable isotopes of heavy nuclei have a larger neutron content than stable isotopes of light nuclei. On average, ~ 6 β decays of the fission products of ^{235}U are needed to convert excess neutrons into protons and reach stable lighter elements [62]. For example, on average the lighter fission fragment has $A_1 \simeq 94$ and the heavier fission fragment has $A_2 \simeq 140$. The corresponding stable nuclei are $^{94}_{40}$Zr and $^{140}_{58}$Ce, which contain 6 more protons than the original ^{235}U nucleus and therefore reached after a sequence of 6 β decays.

Roughly 200 MeV is released per fission for each of the 4 main fuel isotopes [63]. This accounts for the rough estimate of the rate of $\bar{\nu}_e$ emitted from the reactor core given above. A precise prediction of the $\bar{\nu}_e$ spectrum from a nuclear reactor requires knowledge of the fission rates of the 4 main isotopes which contribute to the $\bar{\nu}_e$ flux as well as knowledge of the $\bar{\nu}_e$ energy spectrum per fission for each isotope.

4.1 Reactor Simulations and Fission Rates

An accurate determination of the time-dependent fission rates for each reactor core of each of the 4 main fuel isotopes, ^{235}U, ^{238}U, ^{239}Pu, and ^{241}Pu is required in order to make a precise prediction for the $\bar{\nu}_e$ flux. It is not possible to directly measure these fission rates while the reactor is operating. Instead, the fission rates as a function of time must be predicted from simulations of the reactor core.

Two different and complementary simulation codes are used for this purpose. The first code performs a Monte Carlo simulation of the entire reactor core using the MCNP Utility for Reactor Evolution (MURE) [64]. MCNP is a Monte Carlo N-particle code which is used to simulate neutron transport in a generalized geometry [65]. MURE makes successive calls to MCNP and computes the fuel depletion and fission rates during each simulated time interval. The second code is a deterministic, lattice-based simulation package called DRAGON [66] that solves neutron transport at the assembly level. DRAGON was modified to output the fission rates derived from the fuel evolution. Since DRAGON only simulates a 2-D cross section of an assembly, these total fission rates are approximated by scaling the cross-sectional fission rates by the height of the assembly. Both simulations depend on evaluated nuclear databases for thermal neutron capture cross sections. The JEFF3.1 [67] database is used by default, though other nuclear databases were substituted for this to quantify the uncertainty in the fission rates due to the choice of nuclear database.

In addition, each simulation relies on information regarding the properties of the reactor core in order to obtain accurate results. The French power company EDF operating the Chooz nuclear power plant provided detailed, assembly-level information including the geometry, materials used, fuel composition, uranium enrichment, location of control rods, etc. In addition, EDF also provided detailed information about the reactor core including the the geometry, water (moderator) temperature, density, and boron concentration, the locations of once- and twice- burned fuel assemblies, etc. Perhaps most importantly, EDF provided a detailed accounting of its thermal power measurement and associated uncertainties [68]. These are calibrated at the 0.4% level once per week. Relative variations of the weekly power measurements are determined from the temperature of the primary water loop cooling the reactor core. Fig. 4.1 shows the thermal power measured by EDF as a

function of calendar day for the duration of the $\bar{\nu}_e$ disappearance search data-taking period.

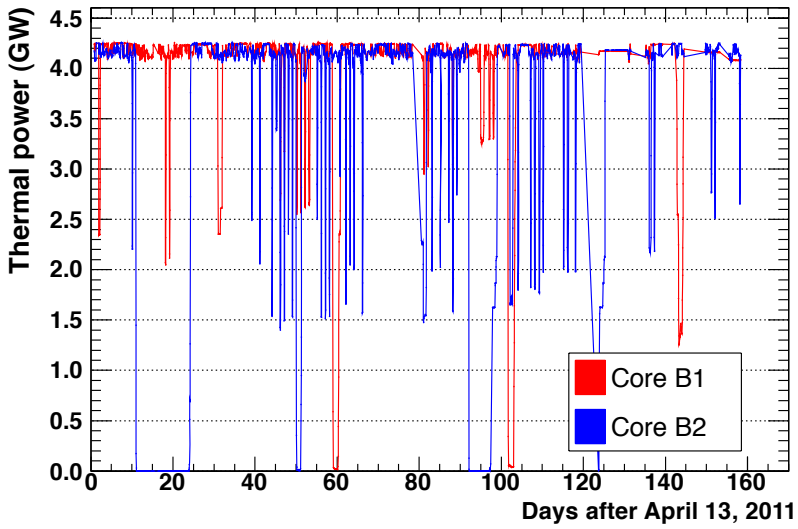

Figure 4.1: Mean thermal power of Chooz B1 and Chooz B2 for each data run in the $\bar{\nu}_e$ disappearance search data-taking period as a function of calendar day.

Both codes were tested against a reactor benchmark, in which the fuel inventory of two fuel rods in two different assemblies of a PWR similar to the Chooz reactors was measured from destructive assays [69]. This validated both reactor simulations and provided insight into the sensitivity of the fission rates on different reactor inputs. Because MURE simulates the full reactor core evolution, it is chosen as the default simulation code to compute the fission rates as a function of time. DRAGON, however, is used for quick, assembly-level cross checks, and differences between the fission rates computed by MURE and DRAGON at the assembly level; these are included as an overall systematic uncertainty on the fission rates. Fig. 4.2 shows the fission rates computed by MURE for Chooz B1 as a function of days since the start of the current reactor cycle spanning the $\bar{\nu}_e$ disappearance search data-taking period.

Systematic uncertainties in the fission rates due to uncertainties in the water (moderator) density, the initial fuel burn-up, the use of control rods in the reactor core, the fuel temperature, and several other sub-dominant inputs to the reactor core simulations were evaluated. First, a linear fit was performed to the dependence of the fission rates on the

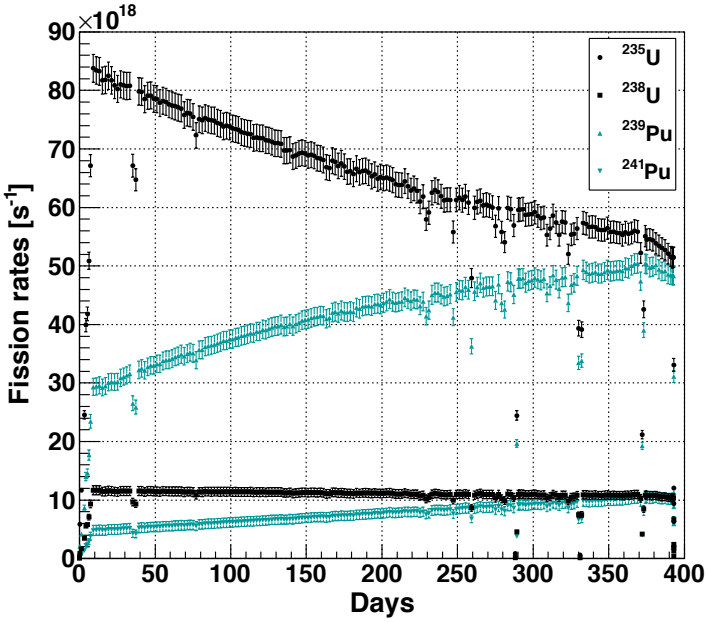

Figure 4.2: Fission rates for each of the 4 main fuel isotopes of the Chooz B1 reactor as a function of days since the start of the current reactor cycle spanning the $\bar{\nu}_e$ disappearance search data-taking period.

variation of each systematic parameter at the assembly level. Next, several different assemblies were simulated, each representing very different neutron environments found in the reactor core. The uncertainty of each systematic parameter was found to be very similar in each simulation for a given value of the ^{239}Pu/^{235}U ratio. Therefore, the assembly-level uncertainty on the fission rates as a function of ^{239}Pu/^{235}U is used to approximate the fission rate uncertainties for the entire reactor core. Fig. 4.3 shows main contributions to the fission rate uncertainty for the 4 main fuel isotopes as a function of days since the start of the current reactor cycle spanning the $\bar{\nu}_e$ disappearance search data-taking period.

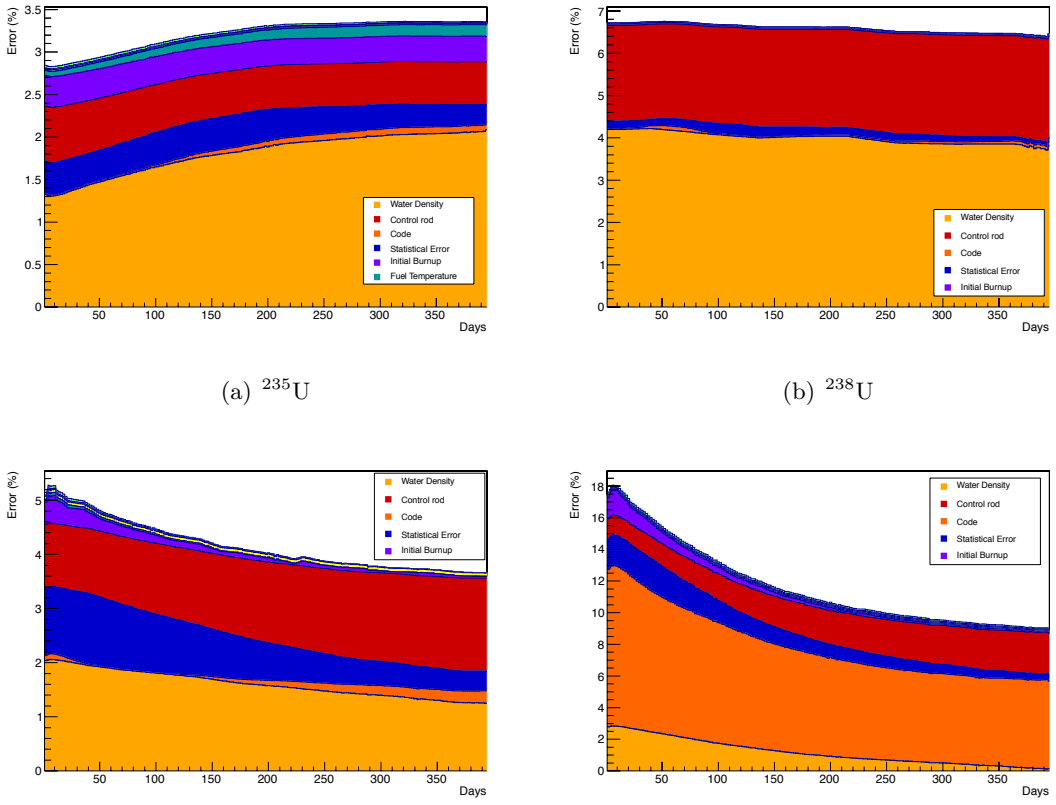

(a) ^{235}U

(b) ^{238}U

(c) ^{239}Pu

(d) ^{241}Pu

Figure 4.3: The fission rate error budget for each of the 4 main fuel isotopes in the reactor core as a function of days since the start of the reactor cycle in which $\bar{\nu}_e$ disappearance search data-taking occurred.

It is important to quantify the correlated uncertainties for the 4 fission rates. To de-

termine the correlation between the fission rates of ^{235}U and ^{238}U, for example, the fission rate of ^{235}U is plotted against the fission rate of ^{238}U for the entire reactor fuel cycle being considered. For each point, the error bars are computed as a function of the ^{239}Pu/^{235}U ratio. The correlation coefficient for ^{235}U and ^{238}U is then derived from a linear fit. In this way, the 4×4 correlation matrix, m^{α}_{kl}, is derived for all 4 fuel isotopes and given in Table 4.1.

Isotope	^{235}U	^{238}U	^{241}Pu	^{241}Pu
^{235}U	1	0.33	-0.93	-0.91
^{238}U	0.33	1	-0.36	-0.37
^{239}Pu	-0.93	-0.36	1	0.91
^{241}Pu	-0.91	-0.37	0.91	1

Table 4.1: The fission rate correlation matrix m^{α}_{kl} for the 4 main fuel isotopes ^{235}U, ^{238}U, ^{239}Pu, and ^{241}Pu. Details given in the text.

4.1.1 Blinding

Since the $\bar{\nu}_e$ disappearance measurement depends on comparing the predicted events from the reactor flux to the observed data events in the detector, one could naturally separate these two analyses to remove any possible biases in the final analysis. A blinding scheme was used to quarantine knowledge of the expected $\bar{\nu}_e$ energy spectrum to a few select members of the collaboration while the IBD selection cuts and the other inputs to the final $\bar{\nu}_e$ disappearance analysis where finalized. In particular, the reactor thermal power and fission rate estimates were withheld until the $\bar{\nu}_e$ disappearance analysis was finalized. This mitigated the possibility of inadvertently introducing bias into the result.

4.2 Antineutrino Spectrum

We would like to compute the $\bar{\nu}_e$ energy spectrum per fission for isotope k produced in the reactor. At the level of a single β-decay branch, this can be inferred from the associated

β-decay energy spectrum. However, techniques have also been developed to infer the total $\bar{\nu}_e$ energy spectrum per fission directly from the total β-decay energy spectrum per fission.

The β-decay energy spectrum per fission for isotope k emitted from a nuclear reactor is given by

$$\tilde{S}_k(E) = \sum_f Y_f(t) \sum_i b_f^i P_f^i(Z_f, E_{0f}^i, E) \tag{4.2}$$

where the $Y_f(t)$ is the β-decay rate at time t for the fission product f and $P_f^i(Z_f, E_{0f}^i, E)$ is the β-decay spectrum for β branch i of fission product f with branching ratio b_f^i and endpoint energy E_{0f}^i. For a given fission product f, the branching ratios b_f^i are normalized to 1. The β spectrum $P_f^i(Z_f, E_{0f}^i, E)$ is given by

$$P_f^i(Z_f, E_{0f}^i, E) = k_f^i p E (E - E_{0f}^i)^2 F(E, Z_f) C_f^i(E) \delta_f^i(Z_f, E), \tag{4.3}$$

where k_f^i is an arbitrary scale factor used to normalize $P_f^i(Z_f, E_{0f}^i, E)$, $F(E, Z)$ is the Fermi function describing the deceleration of the electron in the Coulomb field of the nucleus, $C_f^i(E)$ is a shape correction for the forbiddeness of the nuclear matrix element of the β decay, and $\delta_f^i(Z_f, E)$ describes sub-leading corrections to the Fermi theory, including finite-size, screening, weak magnetism, and radiative QED corrections [70].

Neglecting the recoil of the nucleus, the expression for the $\bar{\nu}_e$ energy spectrum for branch i of fission product f can be obtained from Eq. 4.3 with a modified radiative QED correction by setting $E = E_{0f}^i - E_\nu$. Thus, if all the variables in Eq. 4.2 and Eq. 4.3 are known, the $\bar{\nu}_e$ energy spectrum per fission can be computed in a straightforward fashion. However, knowledge of all the β branches for each fission fragment f of the 4 main fuel isotopes is incomplete and so other techniques must be employed.

Two different approaches are generally taken to compute the $\bar{\nu}_e$ energy spectrum per fission $S_k(E)$ from the β-decay energy spectrum per fission $\tilde{S}_k(E)$. The first "virtual branch" approach relies on precision measurements of the total β-decay energy spectra obtained for ^{235}U, ^{239}Pu, and ^{241}Pu in the 1980's at the Institute Laue Langevin (ILL) high flux reactor in Grenoble, France [71–73]. β-decay energy spectra were obtained by exposing thin layers of uranium and plutonium oxide to a thermal neutron flux for irradiation times of $12 - 36$ h and measuring the outgoing electron energy with a magnetic β spectrometer in steps of

$50 - 100$ keV[1]. The β-decay energy spectra thus obtained are fit to a sum of "virtual" β-decay branches and then converted to $\bar{\nu}_e$ spectra as outlined above. Specifically, the N measured β spectrum data points are considered n at a time, starting from the n highest energy bins. These n data points are fit to a β spectrum $P(\bar{Z}(E), E_0, E)$, with a form given by Eq. 4.3, in which the normalization k and the endpoint E_0 are allowed to float. The average nuclear charge as a function of endpoint energy $\bar{Z}(E_0)$ is determined from a fit to the Z distribution of fission fragments of a given fuel isotope using the ENSDF nuclear database [74].

In the second so-called *ab initio* approach of Mueller et. al. [56] the $\bar{\nu}_e$ energy spectrum is obtained directly from $P_f^i(Z_f, E_{0f}^i, E)$ at the branch level by using all known sources of β-decay data. The principle source of information on the branching ratios, endpoints, nuclear spin-parity, etc. comes from the ENSDF nuclear database. In some cases, where this data was shown to contain bias or was incomplete, it was supplemented with other β-decay measurements or data-driven models. $Y_f(t)$, the β-decay rate at time t for the fission product f, was estimated by simulating the burn-up in the reactor core using the MURE reactor simulation package described in Sec. 4.1. The total $\bar{\nu}_e$ energy spectrum for isotope k can then be obtained from Eq. 4.2 as a function of irradiation time. This method was found to be able to account for $\sim 90\%$ of the measured ^{235}U β spectrum. Using a hybrid approach, the remaining $\sim 10\%$ can be fit using virtual β branches as described above.

The *ab initio* approach has two main advantages. First, corrections to the ILL-based $\bar{\nu}_e$ energy spectra can be inferred for long-lived isotopes which continue to accumulate in the reactor core beyond the $12 - 36$ h of irradiation time. Second, the $\bar{\nu}_e$ energy spectrum can be determined for ^{238}U for which no suitable β-decay measurement exists. A recent work by Huber [70] employing the virtual branch approach includes a more complete theoretical description of the β-decay spectrum. Furthermore, smaller β-decay spectra residuals are demonstrated with respect to the ILL data than the *ab initio* or hybrid approaches. Therefore, the ^{235}U, ^{239}Pu, and ^{241}Pu spectra and associated uncertainties are taken from Huber [70], corrected for burn-up according to Mueller et. al. [56] taken at 100 d of irradi-

[1]The data were originally published in 250 keV bins, but the author made finer bins available to be used in a recent work [70] on the reactor $\bar{\nu}_e$ spectrum

ation time to simulate realistic reactor conditions. The ^{238}U spectrum and its uncertainty, including the effect of missing nuclear data, are taken from the *ab initio* approach of Mueller et. al. at 450 d of irradiation time.

The spectra referenced above are only given between $2-8$ MeV. However, polynomial fits were also provided for each of these reference spectra. These polynomial fits were used to compute the mean value of the $\bar{\nu}_e$ cross section per fission outside the range given in the references. An uncertainty of 20% was assigned to each of the bins in the extrapolated region, fully correlated amongst themselves. Fig. 4.4 shows the final reference spectra used for each of the 4 main fuel isotopes as well as the associated uncertainty bands. ^{238}U has the largest uncertainty because it is predicted entirely *ab initio*—no β suitable decay spectra for ^{238}U currently exist.

4.3 Predicted IBD Interactions in the Detector

In general, the rate and spectrum of $\bar{\nu}_e$ produced by a nuclear reactor R are determined by the time-dependent fission rates f_k^R, where k is an index that runs over the 4 main fuel isotopes in the reactor core, ^{235}U, ^{238}U, ^{239}Pu, and ^{241}Pu. As these cannot be measured directly *in situ*, they must be simulated based on knowledge of the reactor core. Alternatively, if the average energy released per fission $\langle E_f \rangle_k$, is known for each of the k isotopes, then the f_k^R may be expressed in terms of the fractional fission rates α_k^R and the thermal power of the reactor core P_{th}^R as

$$f_k^R = \frac{P_{th}^R}{\sum_k \alpha_k^R \langle E_f \rangle_k} \alpha_k^R, \tag{4.4}$$

where $\alpha_k^R = f_k^R / \sum_m f_m^R$. The advantage of this reformulation is that the thermal power of the reactor core can be measured directly and provided as input to the reactor core simulations, which are then used only to predict the α_k^R as a function of time.

The rate of $\bar{\nu}_e$ IBD interactions due to reactor R located a distance L_R away from a detector with N_p target protons can be expressed as

$$\frac{dN^R}{dt} = \frac{N_p}{4\pi L_R^2} \frac{P_{th}^R}{\langle E_f \rangle_R} \langle \sigma_f \rangle_R , \tag{4.5}$$

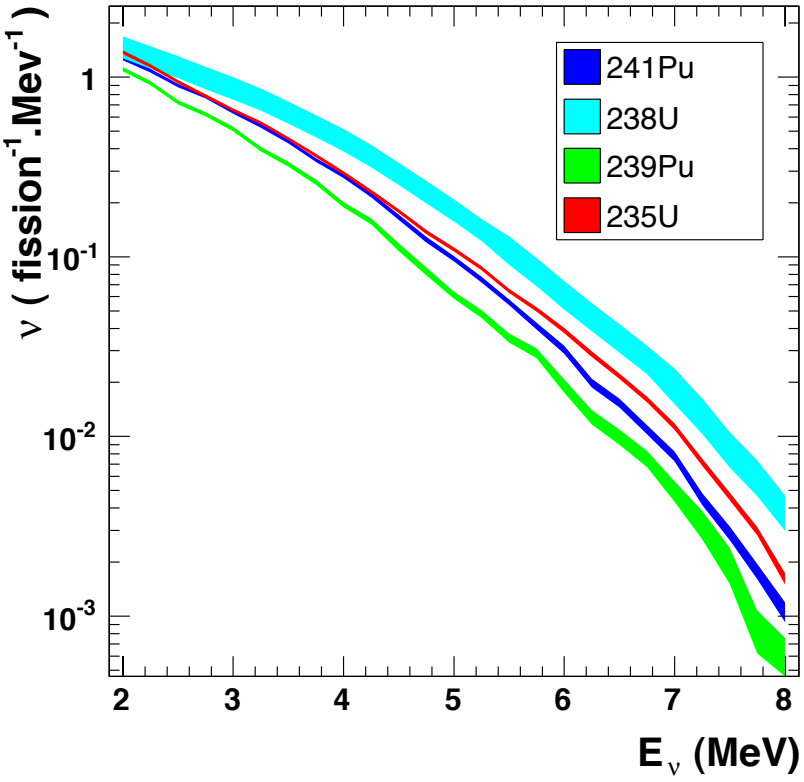

Figure 4.4: $\bar{\nu}_e$ energy spectrum per fission for each of the 4 main fuel isotopes which contribute to the $\bar{\nu}_e$ flux. The spectra for ^{235}U, ^{239}Pu, and ^{241}Pu are taken from Huber [70], corrected for finite irradiation time according to Mueller et. al. [56] The ^{238}U spectrum is taken from Mueller et. al.

where $\langle\sigma_f\rangle_R$ is the flux-weighted IBD cross-section per fission. In terms of $S_k(E)$, the $\bar{\nu}_e$ energy spectrum per fission for isotope k, the flux-weighted IBD cross-section per fission can be written as

$$\langle\sigma_f\rangle_R = \sum_k \alpha_k^R \langle\sigma_f\rangle_k \tag{4.6}$$

$$= \sum_k \alpha_k^R \int S_k(E)\sigma_{IBD}(E)dE, \tag{4.7}$$

where $\sigma_{IBD}(E)$ is the IBD cross section and $S_k(E)$ was discussed previously.

4.3.1 Normalizing to BUGEY4

The principal limitation of a single-detector $\bar{\nu}_e$ disappearance analysis is the uncertainty on the predicted $\bar{\nu}_e$ spectrum. The uncertainty in the spectra given in Sec. 4.2 is $\sim 2-3\%$. One approach to mitigate the impact of the uncertainty on the $\bar{\nu}_e$ reference spectra is to tie the normalization of $\langle\sigma_f\rangle_R$ to measurements obtained by very short-baseline reactor neutrino experiments. For these very short-baseline experiments, oscillation effects are small and the observed events are directly related to the antineutrino flux.

The most precise measurement of $\langle\sigma_f\rangle$ comes from the BUGEY4 experiment [41], which measured $\langle\sigma_f\rangle^{Bugey}$ to an accuracy of 1.377% at a distance of 15 m from a 2.8 $\mathrm{GW_{th}}$ PWR at the BUGEY nuclear power plant. We tie $\langle\sigma_f\rangle_R$ to the value measured by BUGEY4, and only use the $\bar{\nu}_e$ energy spectra predicted in Sec. 4.2 to correct for differences in the α_k^R between DC and BUGEY4. Namely, we use

$$\langle\sigma_f\rangle_R = \langle\sigma_f\rangle^{Bugey} + \sum_k \left(\alpha_k^R - \alpha_k^{Bugey}\right)\langle\sigma_f\rangle_k . \tag{4.8}$$

where the α_k^{Bugey} are average values given by the BUGEY4 experiment.

4.3.2 IBD Energy Spectrum

Eq. 4.5 gives the predicted rate of IBD interactions in the detector from $\bar{\nu}_e$'s produced by reactor R. Using the $\bar{\nu}_e$ energy spectrum per fission given in Sec. 4.2, the predicted rate of IBD interactions can be binned in true neutrino energy. The rate of IBD interactions for

neutrinos with energies between E_i and $E_i + \Delta E_i$ is given by

$$\frac{dN_i^R}{dt} = \frac{N_p}{4\pi L_R^2} \frac{P_{th}^R}{\langle E_f \rangle_R} \frac{\langle \sigma_f \rangle_R}{\sum_k \alpha_k^R \langle \sigma_f \rangle_k} \sum_k \alpha_k^R \langle \sigma_f \rangle_k^i \,, \tag{4.9}$$

where

$$\langle \sigma_f \rangle_k^i = \int_{E_i}^{E_i + \Delta E_i} S_k(E) \sigma_{IBD}(E) dE. \tag{4.10}$$

The final prediction for the IBD energy spectrum for a given $\bar{\nu}_e$ disappearance search data run at time t in terms of $\bar{\nu}_e$ energy is calculated by summing Eq. 4.9 over both Chooz B1 and Chooz B2 reactor cores and then integrating over the detector live time for that run

$$N_{i,t} = \sum_R \int_{t'} \frac{dN_i^R}{dt} dt'. \tag{4.11}$$

4.3.3 Generating MC Events

The $\bar{\nu}_e$ disappearance search data is taken over the course of many runs. MC events for the predicted IBD interactions in the detector are generated on a run-by-run basis. For each run, the thermal power information provided by EDF in 15-minute to 12-hour time intervals is retrieved. The fission rates obtained from the reactor simulations, which are performed over longer $12 - 48$ hour time intervals, are then rescaled according to the ratio of the measured thermal power to the simulated thermal power

$$f_k = \frac{P_{th}^{meas}}{P_{th}^{sim}} f_k^{sim} \tag{4.12}$$

For each EDF thermal power time interval the total calculated number of IBD events N_{calc}^R for each reactor is computed according to Eq. 4.5 by assuming the fission rates and the thermal power are constant and then multiplying by the detector run time in that interval. The actual number of IBD events observed from each reactor N_{obs}^R observed in a given run is obtained by drawing a random number of events from a Poisson distribution with a mean of N_{calc}^R.

In order to generate MC IBD events in the detector from each reactor, a series of random draws are performed to determine the MC IBD event time, energy, and propagation distance and then repeated until N_{obs}^R MC IBD events have been created. To do this the fission rates for each isotope are weighted by the corresponding flux-averaged IBD cross section per

fission $\langle\sigma_f\rangle$ and then binned in time. An isotope and a time are randomly selected according to the relative populations in each of these bins. Then for the chosen isotope, a $\bar{\nu}_e$ energy is randomly selected from the flux-averaged IBD cross section binned in 250 keV bins from 1.625–11.125 MeV. Finally, a creation vertex is randomly selected inside the reactor core and an interaction vertex is randomly chosen in the considered detector volume according to relative proton density.

Based on the $\bar{\nu}_e$ momentum and energy, the IBD final state positron and neutron momenta and energies can be simulated. The center-of-mass (CM) energies of the positron and neutron are computed in terms of the incoming $\bar{\nu}_e$ energy and the directions of the positron and neutron momenta in the CM frame are determined by randomly sampling an isotropic distribution. These quantities are then transformed back to the lab frame to produce MC IBD positron and neutron events that can be fed into the detector simulation described in Ch. 5.

4.4 Reactor Covariance Matrix

The predicted $\bar{\nu}_e$ spectrum given by Eq. 4.9 depends on the following 8 experimental quantities: N_p, L_R, P^R_{th}, σ_{Bugey}, $\langle E_f\rangle_k$, α^R_k, and $\langle\sigma_f\rangle^{i\,2}_k$. The uncertainties in each of these quantities contributes to the uncertainty in the predicted $\bar{\nu}_e$ spectrum. We would like to propagate the uncertainties of these 8 experimental quantities, which we will label $p^r,\ r = 1\ldots 8$, to a covariance matrix M^{tot}_{ij} given in terms of true neutrino energy bins E^i_ν. Each of the p^r is uncorrelated and so the covariance matrix M^{tot}_{ij} can be expressed as the sum of covariance matrices representing the contribution of each experimental quantity individually

$$M^{tot}_{ij} = M^L_{ij} + M^{P_{th}}_{ij} + M^{\sigma_{Bugey}}_{ij} + M^{\langle E_f\rangle}_{ij} + M^{\alpha_k}_{ij} + M^{\langle\sigma_f\rangle}_{ij}, \tag{4.13}$$

where we have omitted the uncertainty due to N_p, which just contributes an overall normalization uncertainty and will be included with the other normalization uncertainties in the final oscillation fit (see Sec. 6.6.6). Each covariance matrix in the sum given by Eq. 4.13 is

[2]The average values α^{Bugey}_k reported by the Bugey experiment have no associated error and are therefore treated as constant parameters.

computed from the variation of N_ν^i, the expected number of events in neutrino energy bin i, due to a variation in each experimental quantity p^r.

A given p^r may be binned by fission isotope, neutrino energy, or reactor. Let m run over all such bins, so that p_m^r describes the mth bin of parameter p^r. Then the total covariance matrix in neutrino energy can be expressed as

$$M_{ij}^r = \left\langle \delta N_\nu^i \delta N_\nu^j \right\rangle \tag{4.14}$$

$$= \sum_{lm} \frac{dN_\nu^i}{dp_l^r} \frac{dN_\nu^j}{dp_m^r} \left\langle \delta p_l^r \delta p_m^r \right\rangle \tag{4.15}$$

where $\langle \delta p_l^r \delta p_m^r \rangle$ is the covariance matrix associated with parameter p^r. The covariance matrices associated with each of the experimental parameters is given below.

Reactor baseline L:

$$M_{ij}^L = \sum_{t,R} \left(N_{i,t}^R \frac{2\sigma_{L_R}}{L_R} \right) \sum_{t,R} \left(N_{j,t}^R \frac{2\sigma_{L_R}}{L_R} \right), \tag{4.16}$$

where $L_1 = 1114.6$ m, $L_2 = 998.1$ m, and $\sigma_{L_R} = 20$ cm as described in Ch. 3.

Thermal Power P_{th}:

$$M_{ij}^{P_{th}} = \sum_{t,R} \left(N_{i,t}^R \frac{\sigma_{P_{th}^{t,R}}}{P_{th}^{t,R}} \right) \sum_{t,R} \left(N_{j,t}^R \frac{\sigma_{P_{th}^{t,R}}}{P_{th}^{t,R}} \right), \tag{4.17}$$

where $\sigma_{P_{th}^{t,R}}$ is 0.46% based on the EDF measurement [68].

Measured cross section per fission from Bugey σ_{Bugey}:

$$M_{ij}^{\sigma_{Bugey}} = \sum_{t,R} \left(N_{i,t}^R \frac{\sigma_{\sigma_{Bugey}}}{\langle \sigma_f \rangle_{t,R}} \right) \sum_{t,R} \left(N_{j,t}^R \frac{\sigma_{\sigma_{Bugey}}}{\langle \sigma_f \rangle_{t,R}} \right), \tag{4.18}$$

where the uncertainty in the cross section per fission comes from published `BUGEY4` data given as $(5.752 \pm 0.081) \times 10^{-43}$ cm^2/fission [41].

Mean energy released per fission $\langle E_f \rangle$:

$$M_{ij}^{\langle E_f \rangle} = \sum_k^{iso} \left(\sum_{t,R} \left(N_{i,t}^R \frac{\alpha_{k,t}^R}{\langle E_f \rangle_{t,R}} \sigma_{\langle E_f \rangle_k} \right) \sum_{t,R} \left(N_{j,t}^R \frac{\alpha_{k,t}^R}{\langle E_f \rangle_{t,R}} \sigma_{\langle E_f \rangle_k} \right) \right), \tag{4.19}$$

where k runs over the 4 main fuel isotopes and the mean energy released per fission and their uncertainties are taken from [63] and reproduced in Table 4.2.

Isotope	$\langle E_f \rangle\,[MeV]$	$\sigma_{\langle E_f \rangle}[MeV]$
^{235}U	201.92	0.46
^{238}U	205.52	0.96
^{239}Pu	209.99	0.60
^{241}Pu	213.60	0.65

Table 4.2: Summary of the average energy released per fission for each of the four main isotopes contributing to the reactor $\bar{\nu}_e$ flux.

Fractional fission rate α_k:

$$\begin{aligned} M_{ij}^{\alpha_k} &= \sum_{k,l}^{iso} \left(\sum_{t,R} N_{i,t}^R \left(\frac{\langle \sigma_f \rangle_k}{\langle \sigma_f \rangle_R} - \frac{\langle E_f \rangle_k}{\langle E_f \rangle_R} - \frac{\langle \sigma_f \rangle_k}{\sum_m \alpha_m^R \langle \sigma_f \rangle_m} + \frac{\langle \sigma_f \rangle_k^i}{\sum_m \alpha_m^R \langle \sigma_f \rangle_m^i} \right) \right. \\ &\times \left. \sum_{t,R} N_{j,t}^R \left(\frac{\langle \sigma_f \rangle_l}{\langle \sigma_f \rangle_R} - \frac{\langle E_f \rangle_l}{\langle E_f \rangle_R} - \frac{\langle \sigma_f \rangle_l}{\sum_m \alpha_m^R \langle \sigma_f \rangle_m} + \frac{\langle \sigma_f \rangle_l^j}{\sum_m \alpha_m^R \langle \sigma_f \rangle_m^j} \right) \right) \\ &\times \langle \delta\alpha_k \delta\alpha_l \rangle \end{aligned}$$

where k and l run over the 4 main fuel isotopes. The covariance matrix $\langle \delta\alpha_k \delta\alpha_l \rangle$ in the expression for $M_{ij}^{\alpha_k}$ is built up from the fission rate correlation matrix m_{kl}^{α} given in Table 4.1. First, the total fission rates and total fission rate uncertainties for each isotope are weighted by the appropriate baseline:

$$\bar{f}_k = 2 \sum_R \frac{f_k^R / L_R^2}{1/L_1^2 + 1/L_2^2} \tag{4.20}$$

$$\bar{\sigma}_{f_k} = 2 \sum_R \frac{\sigma_{f_k^R} / L_R^2}{1/L_1^2 + 1/L_2^2}, \tag{4.21}$$

Then the baseline-weighted uncertainty on the total fission rate fraction for the kth isotope $\bar{\alpha}_k$ is determined from $\sigma_{\bar{\alpha}_k} = \bar{\alpha}_k \bar{\sigma}_{f_k} / \bar{f}_k$, where $\bar{\alpha}_k = \bar{f}_k / \sum_m \bar{f}_m$. Finally, the covariance matrix $\langle \delta\alpha_k \delta\alpha_l \rangle$ is expressed in terms of the correlation matrix m_{kl}^{α} as

$$\langle \delta\alpha_k \delta\alpha_l \rangle = m_{kl}^{\alpha} \sigma_{\bar{\alpha}_k} \sigma_{\bar{\alpha}_l} \tag{4.22}$$

Flux-weighted IBD cross section per fission $\langle\sigma_f\rangle$:

$$\begin{aligned} M_{ij}^{\langle\sigma_f\rangle} &= \sum_{k,l}^{iso}\sum_{i',j'}\left(\sum_{t,R}\left(N_{i,t}^{R}\left(\frac{\alpha_k^R-\alpha_k^{Bugey}}{\langle\sigma_f\rangle_R}+\frac{\alpha_k^R\delta_{ii'}}{\sum_m \alpha_m^R\langle\sigma_f\rangle_m^{i'}}-\frac{\alpha_k^R}{\sum_m \alpha_m^R\langle\sigma_f\rangle_m}\right)\right)\right. \\ &\times \left.\sum_{t,R}\left(N_{j,t}^{R}\left(\frac{\alpha_l^R-\alpha_l^{Bugey}}{\langle\sigma_f\rangle_R}+\frac{\alpha_l^R\delta_{jj'}}{\sum_m \alpha_m^R\langle\sigma_f\rangle_m^{j'}}-\frac{\alpha_l^R}{\sum_m \alpha_m^R\langle\sigma_f\rangle_m}\right)\right)\right) \\ &\times \left\langle\delta\langle\sigma_f\rangle_k^{i'}\,\delta\langle\sigma_f\rangle_l^{j'}\right\rangle \end{aligned}$$

where k and l run over the 4 main fuel isotopes and i' and j' run over $\bar{\nu}_e$ energy bins. The covariance matrix $\left\langle\delta\langle\sigma_f\rangle_k^{i'}\,\delta\langle\sigma_f\rangle_l^{j'}\right\rangle$ in the expression for $M_{ij}^{\langle\sigma_f\rangle}$ is derived from the IBD cross section covariance matrix $M_{i'j'}^{\sigma_{IBD}}$ and the reference spectra covariance matrix $M_{i'j'}^{S_k}$ described in Sec. 4.2. In terms of these two covariance matrices, we have

$$\left\langle\delta\langle\sigma_f\rangle_k^{i'}\,\delta\langle\sigma_f\rangle_l^{j'}\right\rangle = \tilde{\sigma}_{IBD}^{i'}\tilde{\sigma}_{IBD}^{j'}M_{i'j'}^{S_k}+S_k^{i'}S_k^{j'}M_{i'j'}^{\sigma_{IBD}}. \tag{4.23}$$

where $\tilde{\sigma}_{IBD}^{j'}$ is the IBD cross section described in Sec. 3.1.2 integrated over the $\bar{\nu}_e$ energy bin $E^{j'}$. The covariance matrix $M_{i'j'}^{\sigma_{IBD}}$ is constructed as a sum of two terms. First, an overall normalization uncertainty of 0.17% is assigned to σ_{IBD} due to uncertainty on the neutron lifetime, measured to be 881.5 ± 1.5 s [16], which sets the overall normalization of σ_{IBD}. Second, a correlated shape uncertainty is included to account for differences between corrections which have been calculated for the IBD cross section given by Vogel [55]. The fractional difference $\delta\sigma_{IBD}/\sigma_{IBD}$ between the corrected σ_{IBD} due to Fayans [75] and the corrected σ_{IBD} due to Kurylov, Vogel, and Ramsey-Musolf [76] is well-approximated by the linear fit $f(E) = 0.0023\ \text{MeV}^{-1}\times(E-4.2\ \text{MeV})$. Therefore, in terms of these two pieces, we have

$$M_{ij}^{\sigma_{IBD}} = \left(\frac{\delta\sigma_{IBD}^i}{\sigma_{IBD}^i}\frac{\delta\sigma_{IBD}^j}{\sigma_{IBD}^j}+0.0017^2\right)\sigma_{IBD}^i\sigma_{IBD}^j \tag{4.24}$$

4.5 Summary

Table 4.3 summarizes the normalization uncertainties due to each of the inputs to the predicted $\bar{\nu}_e$ energy spectrum in the detector[3]. The largest contribution to the total 1.7%

[3]The uncertainty due to number of target protons is included as a overall normalization uncertainty as described in 6.6.6.

uncertainty comes from the 1.4% uncertainty in the BUGEY4 normalization. However, by normalizing to the BUGEY4 cross section per fission, the large $\sim$ 2–3% normalization uncertainties of the IBD reference spectra are effectively suppressed, and this gives a smaller uncertainty in the total reactor covariance matrix.

Covariance Matrix	**Description**	**Uncertainty**
M_{ij}^{L}	Reactor–Detector Baseline	0.038%
$M_{ij}^{P_{th}}$	Reactor Power	0.460%
$M_{ij}^{\sigma_{Bugey}}$	BUGEY4 Normalization	1.420%
$M_{ij}^{\langle E_f \rangle}$	Energy per Fission	0.157%
$M_{ij}^{\alpha_k}$	Fuel composition	0.872%
$M_{ij}^{\langle \sigma_f \rangle}$	Reference Spectra+IBD cross section	0.170%
M_{ij}^{tot}		**1.745%**

Table 4.3: Summary of total normalization uncertainty contributed by each component of the reactor covariance matrix. All uncertainties are treated as correlated between the two reactors.

In the single detector $\bar{\nu}_e$ disappearance search, the reactor covariance matrix is the largest source of systematic uncertainty in the overall normalization. In a two-detector $\bar{\nu}_e$ disappearance measurement, on the other hand, all of the reactor-related uncertainties[4] would be correlated between the near and far detectors. Therefore, the reactor-related uncertainties would largely cancel in a two-detector measurement and make a negligible contribution to the total systematic error.

[4] A possible exception is the reactor–detector baseline.

Chapter 5

Monte Carlo Simulation and Energy Calibration

We describe in detail the Monte Carlo (MC) software used to simulate particle interactions in the detector. We discuss some of the limitations of this code with respect to neutron transport and compute a correction to the number of IBD events predicted by the MC and its associated uncertainty.

Additionally, we describe how the energy scale of the detector is calibrated using γ sources of known energies as well as neutron sources, which initiate the release of γ radiation of known energies after capturing on H or Gd in the target or γ-catcher scintillator. Differences in the reconstructed full absorption and neutron-capture peaks between calibration source data and MC simulations also motivate the development of an energy- and position-dependent MC energy scale correction function. The covariance matrix describing the uncertainty on this correction function is then derived in detail.

5.1 MC Simulation

The DC Monte Carlo simulation (`DCGLG4sim`) is based on the `Geant4`[1] toolkit [77], an application widely used in particle and nuclear physics to simulate the passage of particles through matter. Broadly speaking, `DCGLG4sim` constructs the simulated DC detector and its

[1] Version 9.2.p02

immediate surroundings, defines the list of particle interactions to be modeled by `Geant4`, and includes custom models of scintillation light emission and PMT optical surfaces.

The DC detector simulation includes a detailed description of detector geometry and materials. Measured or calculated values of the molecular composition and densities of the liquids and acrylic vessels are used to calculate interaction cross sections and energy loss.

Particles are tracked by `Geant4` step-by-step as they propagate through the detector medium. At each step, the energy loss of a particle is simulated according to a process chosen from the list of defined interactions. If any secondary particles are created, then `Geant4` begins to track these particles as well. The process continues until all particles have been absorbed, deposited all their energy to the detector, or left the tracking volumes.

The IBD delayed coincidence signal consists of a prompt positron followed by a delayed neutron capture on Gd. Therefore, properly modeling electromagnetic and neutron interactions at low energies ($E < 10$ MeV) is essential for reproducing the observed data.

5.1.1 Electromagnetic Interactions

Three interactions are defined which describe the energy loss of γ's in detector material: the photoelectric effect, Compton scattering, and e^+e^- pair production. Parameterized models are used to compute cross-sections and generate final state particles which can then be tracked by `Geant4`.

The electromagnetic interactions defined for both e^- and e^+ are ionization due to inelastic collisions with atomic nuclei, elastic Coulomb scattering off of nuclei, and bremsstrahlung radiation. In addition, e^+ annihilation with atomic electrons is simulated both in flight and at rest.

Above a certain minimum secondary particle kinetic energy, T_{cut}, $e^\pm$ ionization energy loss is simulated via the explicit production of δ rays from Moeller (e^-e^-) or Bhabha (e^+e^-) scattering which `Geant4` then begins to track. Below T_{cut}, ionization is simulated as a continuous energy loss of the incident $e^\pm$ according to the Berger-Selzter formula /citeBerger. Fluctuations around this mean energy loss are then drawn from an energy straggling function.

T_{cut} is defined as the energy for which the $e^\pm$ stopping range is < 10 μm. The stopping

range is computed as

$$R(T) = \int_0^T \frac{1}{dE/dx} dE, \tag{5.1}$$

where T is the kinetic energy of the $e^{\pm}$ and dE/dx is the energy loss per unit length due to ionization and bremsstrahlung. For our target scintillator, $T_{cut} = 10.5$ (10.3) keV for electrons (positrons).

Similarly, above some minimum photon energy k_{cut}, $e^{\pm}$ radiation energy loss is simulated via the explicit production of bremsstrahlung γ rays. Below k_{cut}, bremsstrahlung is simulated as a continuous energy loss of the incident $e^{\pm}$. Here, k_{cut} is defined as the energy for which $L_{int} = 2$ μm, where L_{int} is defined as the γ interaction length for the photoelectric effect, Compton scattering, or e^+e^- pair production. For our target scintillator k_{cut} is below the default `Geant4` value. Therefore, this default `Geant4` value of $k_{cut} = 990$ eV is used instead. Again, fluctuations around the mean energy loss are drawn from an energy straggling function.

5.1.2 Neutron Interactions

Neutron transport in `Geant4` is described by a high precision, data-driven model, which simulates the interactions of neutrons from 20 MeV all the way down to thermal energies. The model includes elastic scattering, inelastic scattering, radiative capture, and fission. Cross sections, angular distributions, and final state information are taken from the `Geant4` evaluated neutron data library (G4NDL) derived primarily from linear interpolations of processed ENDF/B-VI evaluated nuclear data from the National Nuclear Data Center [78].

One major shortcoming of our `Geant4` neutron transport model is that it does not include the effects of molecular bonds on neutron elastic scattering. Molecular binding energies are typically of order 1 $\sim$ eV, and so we expect these effects to become important for neutron energies ~ 1 eV. This is well above the energy (~ 25 meV) at which neutrons become thermal. In Sec. 5.2, we study the effects of molecular bonds such as CH_2 on neutron transport near the target/γ-catcher boundary using a separate MC package commonly used for neutron transport by reactor physicists called `TRIPOLI-4`.

5.1.3 Optical Model

Optical photons in the detector are produced either by Čerenkov radiation or scintillation light emission. Typically, the measured scintillation light yield per unit length produced by a particle passing through scintillator is proportional to its ionization energy loss. However, for highly ionizing particles quenching can occur, in which there is an increase in scintillation inefficiency and the linear scaling breaks down. This effect is described semi-empirically by Birk's Law [79]

$$dL/dx(E) = \frac{L_0 dE/dx}{1 + k_B dE/dx}, \tag{5.2}$$

where L_0 is the scintillation light yield in the limit $dE/dx \to 0$ and k_B is an empirical parameter that must be determined from the data for each particle. Values of k_B for electrons and α'a were determined from lab measurements using the target and γ-catcher scintillator. The scintillation light yields for the target and γ-catcher were also determined from lab measurements. However, the absolute scale of these measurements is difficult to determine and so the scintillation light yield was tuned to calibration data *in situ*.

`DCGLG4sim` includes a detailed model of scintillation light emission based on a suite of lab measurements:

- Wavelength-dependent attenuation lengths
- Scintillation light yield
- Scintillation light resolution
- Scintillation light spectra
- Scintillation light waveforms
- Re-emission probability

Optical photons are generated according to the quenched energy deposition in the scintillating volumes given by Eq. 5.2 or via Čerenkov radiation. They are then tracked and propagated by `Geant4`. Both the effects of absorption and re-emission at longer wavelengths are included in the optical model. Polarization-dependent reflection and refraction are simulated at the boundaries between dielectric materials. At metal surfaces such as the buffer

wall or PMT μ-metal shields, optical photons can be absorbed or reflected according to specular and diffusive reflectivity parameters. Optical photons incident on the PMT optical surface are handled by a dedicated PMT model, for which a position-dependent collection efficiency is also simulated [80]. If the optical photon is absorbed by the photocathode a photoelectron is generated with some probability. For each event, the PE hit times and PMT channel numbers are aggregated and passed to the detector readout simulation.

5.1.4 Detector readout simulation

The detector readout simulation converts the MC information generated by `Geant4` into a format identical to the raw detector data. For each event, the raw data format consists of trigger information and a waveform for each PMT representing the digitized current response recorded by the flash ADC. The PMT response as well as the flash ADC digitization are simulated according to data from lab measurements. PMT-to-PMT gain variations are also included in order to realistically simulate the detector data.

5.2 Spill-In/Spill-Out

In an IBD interaction in the target, a neutron may wander up to 100 cm from the interaction point before capturing on Gd (see Fig. 6.16). This affects the IBD selection efficiency in two ways. First, there is an IBD selection inefficiency associated with neutrons from IBD interactions in the target which wander into the γ-catcher and capture on H. This is called "spill-out". Second, the opposite effect, in which a neutron from an IBD interaction in the γ-catcher wanders into the target and captures on Gd, can increase the IBD selection efficiency. This is called "spill-in". Based on MC simulations using `DCGLG4sim`, the spill-in flux was found to be 4.426%, whereas the spill-out flux was found to be only 2.329%. Therefore, there is a net spill-in flux of selected IBD events of $2.096\% \pm 0.6\%$ (stat) with respect to the number of selected IBD events which were generated in the target.

5.2.1 Neutron Transport using TRIPOLI-4

The limitations of the neutron transport code used in DCGLG4sim and described in Sec. 5.1.2 can have an impact on properly simulating these spill-in and spill-out effects in the detector. To measure the effect, two TRIPOLI-4 [81] simulations were performed [82] with a simplified DC geometry: one taking into account the CH_2 molecular bonds in the target and γ-catcher scintillator and one modeling the hydrogen in the target and γ-catcher scintillator as free gas.

Above energies of ~ 1 eV, there is little difference between the neutron thermalization process between the two simulations. However, when neutrons reach energies of ~ 1 eV the thermalization time in the simulation modeling the CH_2 molecular bonds begins to increase relative to the simulation using the free gas hypothesis. This can be understood simply from the fact that some of the proton recoil momentum is absorbed by the CH_2 molecule. Therefore less energy is lost by the neutron on each scatter and the scattered neutron momentum is less forward-peaked. The end result is that the neutron capture time increases, but the neutron capture distance decreases.

Because the γ-catcher does not contain Gd, the neutron capture distance decreases much more in the γ-catcher than in the target. The result is that the spill-in flux for the simulation modeling the CH_2 molecular bonds is $\sim 21.6\%$ less than the spill-in flux for the simulation using the free gas hypothesis. However, 66.2% of the spill-in neutrons for the simulation modeling the CH_2 molecular bonds capture within 100 μs, whereas only 61.4% of the spill-in neutrons for the simulation using the free gas hypothesis capture within 100 μs. The IBD delayed coincidence selection requires $\Delta T < 100$ μs (see Sec. 6.4). Therefore, we correct the spill-in flux ratio for the different ΔT selection efficiencies, and find that including the CH_2 molecular bonds in the simulation decreases the spill-in flux for events with $\Delta T < 100$ μs by only $\sim 15.4\%$. Table 5.1 gives a summary of the spill-in and spill-out as a fraction of the total number of events generated in the target volume.

5.2.2 MC Molecular Bond Correction

The spill-in and spill-out differences observed between modeling the H in our scintillator as a free gas versus explicitly modeling the CH_2 molecular bonds were used to correct the spill-in

Model	Spill-in ($\Delta T < 100$ μs)	Spill-out
CH_2	+6.54% (+4.33%)	−2.34%
Free Gas	+8.34% (+5.12%)	−2.30%
Ratio	0.784 (0.846)	1.017

Table 5.1: Summary of the spill-in and spill-out fractions measured with `TRIPOLI-4` simulations of neutron transport using the hypothesis of neutrons scattering off a free gas of protons versus modeling the CH_2 molecular bonds.

and spill-out predictions obtained using `DCGLG4sim`. The corrected spill-in flux is 3.742%, whereas the corrected spill-out flux is 2.36%, resulting in a net spill-in flux of 1.37% [83]. The difference between the net spill-in obtained with and without the `TRIPOLI-4` correction is taken as the 2σ systematic uncertainty on the corrected value of the spill-in. Therefore, the spill-in is found to be $1.37\% \pm 0.06\%$ (stat) $\pm 0.37\%$ (sys).

Because our default `DCGLG4sim` IBD MC overestimates the net spill-in flux, we correct for this by reducing the predicted number of IBD MC events by $\frac{101.37\%}{102.10\%} = 0.9929$. This correction is included with other normalization corrections as described in Sec. 6.6.6.

5.3 Energy Scale Calibration

An extensive calibration campaign was performed using both the Z-axis and guide tube source deployment systems [84, 85]. Table 5.2 lists the different γ and neutron sources that were deployed in the detector, the dominant types of radiation emitted for each, and the total γ energy of the corresponding full absorption and neutron-capture peaks. Each source was deployed at multiple positions along the Z-axis of the target and as well as off-axis positions in the γ-catcher. The energy scale can be calculated by comparing the total number of reconstructed photoelectrons to the total energy deposited.

5.3.1 MC Generators

Stand-alone MC generators were written to simulate the decay of each calibration source. The decay products are then input into the detector simulation described in sec. 5.1 and

Source	Measured Radiation	$\sum E_\gamma$ [MeV]
^{137}Cs	γ	0.66
^{68}Ge	β^+, γ	1.02
^{60}Co	γ	2.51
^{252}Cf	n, γ	2.22 (^{1}H), 7.94 (^{157}Gd)

Table 5.2: Summary of the types of the sources deployed in the detector using the Z-axis and guide tube calibration systems and the characteristics of their emitted radiation.

compared to the calibration source data.

The MC generators all assume that decay products are emitted isotropically, with the exception of the ^{60}Co generator, in which the angular correlations of the of the 1.173 MeV and 1.333 MeV γ's are properly taken into account [86]. The decay of ^{137}Cs is simulated by a single 0.66 MeV γ. For ^{68}Ge, the branching ratios for β^+ and γ emission are simulated. The ^{252}Cf generator models neutron energies with a Watt spectrum [87] and uses tabulated neutron multiplicities [88]. The prompt fission γ's are modeled according to data-driven fits taken from the literature [89].

5.3.2 Peak Fitting

In order to convert the total number of PE's seen by all PMTs in an event to an equivalent energy, the mean number of PE's of the full absorption peak (in the case of the γ sources) or the neutron capture peak (in the case of ^{252}Cf) must be determined.

Impurities in the ID PMT glass or acrylic vessels emit γ radiation that is a background for γ source calibration data and must be subtracted. Therefore, the total PE spectrum obtained for data-taking runs in which no source is deployed is subtracted from the total PE spectrum obtained from calibration source data, after normalizing to the same run time.

As an example of this but using the total charge spectrum instead of the total PE spectrum, Fig. 5.1 shows the charge spectrum obtained for a ^{68}Ge source deployment in the γ-catcher [85] superimposed with the charge spectrum obtained from a run in which no source is deployed. After subtracting the background the spectrum is fit to the sum of 2

gaussians. The full absorption peak charge and its uncertainty are taken as the mean and fit uncertainty of the corresponding gaussian.

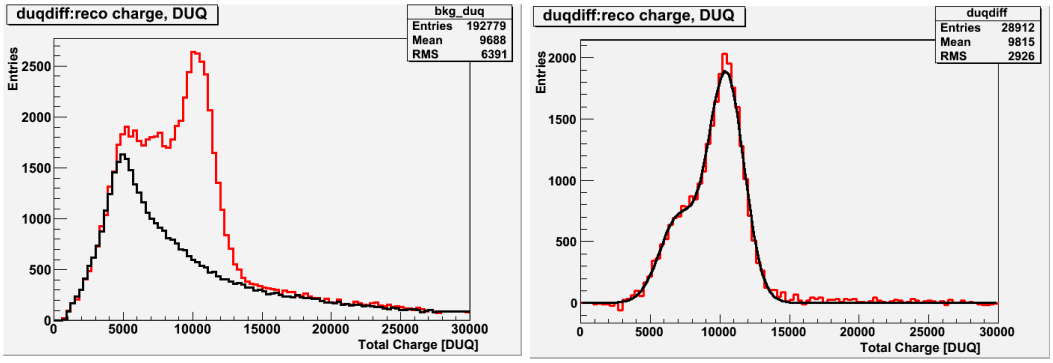

(a) Raw ^{68}Ge source data with accidental background

(b) Background-subtracted ^{68}Ge source data

Figure 5.1: The panel on the left shows the histogram of the raw charge spectrum for ^{68}Ge source calibration data taken in the γ catcher above the target lid in red. The black histogram is the accidental background evaluated from a physics run normalized to the same run time. The right panel shows the background-subtracted ^{68}Ge source calibration data in red and the best fit to a sum of 2 gaussians in black. The full absorption peak and its uncertainty are taken from the mean and fit uncertainty of the corresponding gaussian [85].

The ^{252}Cf total PE spectra for neutron captures on H and Gd are obtained by searching for the delayed coincidence of a prompt fission γ and a delayed neutron capture using selections similar to those described in Sec. 6.6.5. The energy scale for data and MC was determined to be 214 PE/MeV from ^{252}Cf source calibration data at the detector center using the full absorption peak of the 2.22 MeV γ emitted from neutron capture on H. This calibration point was chosen to set the overall energy scale because its energy most closely matches the peak of the expected IBD signal given in Ch. 4.

5.4 Energy Scale Correction Functions

The total number of PE's measured in an event is not expected to be perfectly linear in the total energy deposited. First of all, the use of the total number of PE's as an estimator

of the total light yield in an event neglects detector effects such as PMT solid angle and light attenuation. Second, the total light yield of an event is not strictly proportional to the total energy deposited, due to quenching effects and Čerenkov light emission.

Furthermore, the non-linearity of the energy scale may be different in the data than in the MC if physical parameters such as the buffer wall reflectivity, Birk's constant, the target and γ-catcher light yields, etc. have been not been precisely tuned to data. However, what is actually relevant for the $\bar{\nu}_e$ disappearance analysis is the ratio of the data to the MC. Therefore, we circumvent the issue of tuning the underlying physical parameters of the MC simulation by developing an empirical energy scale correction function to apply directly to the reconstructed MC events of the form:

$$E_{MC}^{corr} = \frac{PE_{MC} \times corr1(PE) \times corr2(Z)}{214\ PE/MeV} \tag{5.3}$$

This energy- and position-dependent correction function will remove any remaining discrepancies between energy scales of the data and MC.

5.4.1 Energy-dependent Fits

Fig. 5.2 shows the ratio of the full absorption and neutron-capture peaks for the source calibration data with respect to the MC at the center of the detector. The data/MC ratio at the ^{137}Cs full absorption peak is ~ 0.97, and it grows grows as a function of energy so that at the Gd capture peak the data/MC ratio is ~ 1.06.

The nonlinearity is fit to the energy-dependent correction function

$$corr1(PE) = p_0 \times \log(PE - p_1) + p_2, \tag{5.4}$$

where PE is the number of photoelectrons, log is the natural logarithm, and p_0, p_1 ,and p_2 are fit parameters. The best fit parameters are $(p_0,\ p_1,\ p_2) = (0.0287,\ 56.1478,\ 0.8423)$ and their covariance matrix is given by

$$M^{corr1} = \begin{pmatrix} 2.562 \cdot 10^{-6} & -0.01536 & -1.678 \cdot 10^{-5} \\ -0.01536 & 1.015 \cdot 10^{2} & 0.1019 \\ -1.678 \cdot 10^{-5} & 0.1019 & 1.102 \cdot 10^{-4} \end{pmatrix}. \tag{5.5}$$

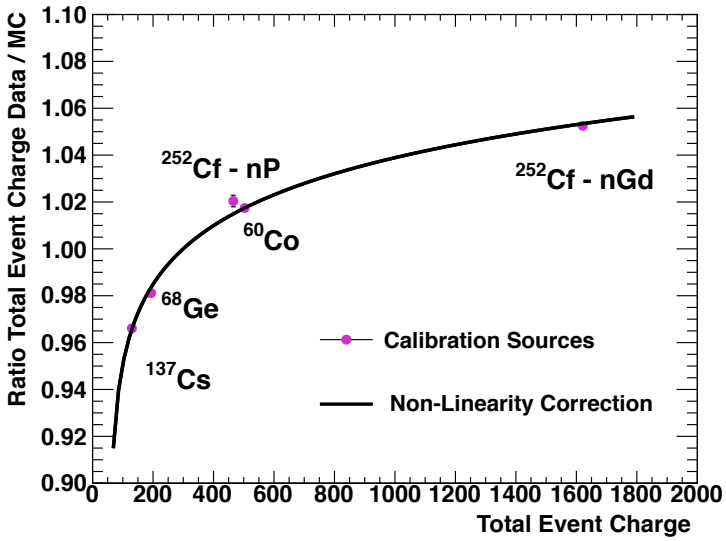

Figure 5.2: Ratio of the total charge of the full absorption and neutron-capture peaks extracted from ^{137}Cs, ^{68}Ge, ^{60}Co, and ^{252}Cf source calibration data with respect to the MC. The solid line is the best fit function, $corr1$, described in the text.

The χ^2/ndf of the fit is 7.68/2, which could indicate that the systematic uncertainties on the full absorption and neutron-capture peaks were underestimated and should be scaled by $\sqrt{3.84} \sim 2.0$. Fig. 5.3 shows the agreement between data and MC which has been corrected using the best fit $corr1$ at the center of the target and in the γ-catcher at $Z = 0$.

5.4.2 Position-dependent Fits

Calibration source scans along the Z-axis indicated a residual Z-dependent discrepancy in the ratio of the full absorption and neutron-capture peaks between data and MC even after applying $corr1$. Fig. 5.4 shows the ratio of the full absorption peaks for ^{137}Cs and ^{60}Co as a function of Z position.

We extend our correction function away from the center of the detector by using a 2nd order polynomial to model the Z-dependence:

$$corr2(Z) = p_3 + p_4 Z + p_5 Z^2, \tag{5.6}$$

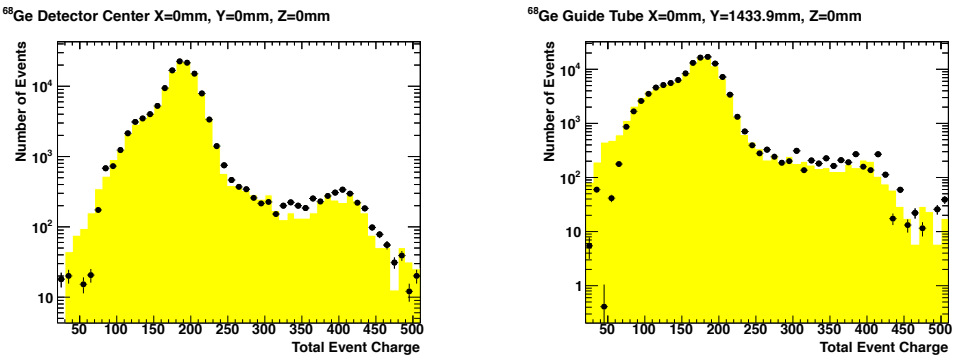

(a) ^{68}Ge source data and MC at $Z = 0$, along the Z-axis of the detector

(b) ^{68}Ge source data and MC at $Z = 0$, mid-way into the γ-catcher

Figure 5.3: The panel on the left shows the charge spectrum for ^{68}Ge source calibration data at the center of the detector superimposed with the corresponding MC spectrum which has been corrected using the best fit *corr*1. The panel on the right shows the charge spectrum for ^{68}Ge source calibration data at $Z = 0$ and mid-way into the γ-catcher superimposed with the corresponding MC spectrum which has been corrected with the best fit *corr*1.

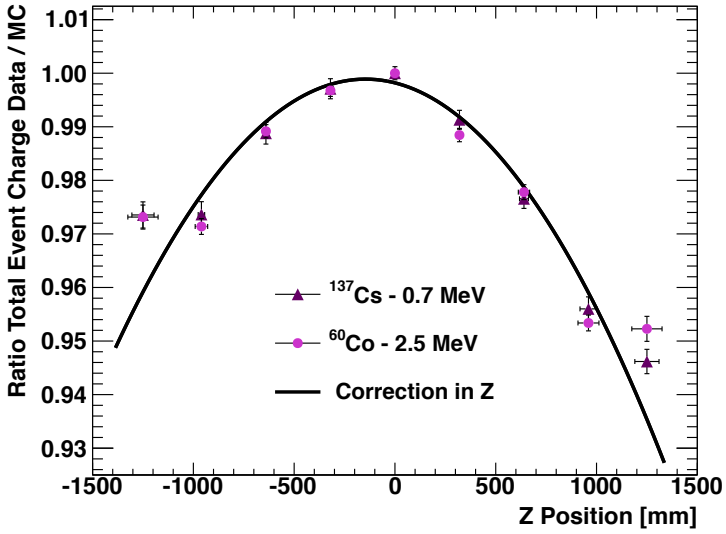

Figure 5.4: Ratio of the total charge of the full absorption peaks extracted from ^{137}Cs and ^{60}Co source calibration data with respect to the MC corrected according to Eq. 5.4 as a function of Z-position. The solid line is the best 2nd-order polynomial fit to the ^{137}Cs data points described in the text.

where Z is the MC vertical position given in mm and p_3, p_4, and p_5 are fit parameters. The best fit to ^{137}Cs is shown in Fig. 5.4. The best fit parameters are $(p_3,\ p_4,\ p_5) = (0.9982,\ 9.5148 \times 10^{-6},\ 3.2598 \times 10^{-8})$ and their covariance matrix is given by

$$M^{corr2} = \begin{pmatrix} 8.397 \cdot 10^{-7} & -2.646 \cdot 10^{-11} & -1.29 \cdot 10^{-12} \\ -2.646 \cdot 10^{-11} & 1.863 \cdot 10^{-12} & 4.174 \cdot 10^{-16} \\ -1.29 \cdot 10^{-12} & 4.174 \cdot 10^{-16} & 4.846 \cdot 10^{-18} \end{pmatrix}. \tag{5.7}$$

The χ^2/ndf of the fit are 20.23/6 and 29.2/6 for ^{137}Cs and ^{60}Co, respectively. Again, this may indicate that the systematic uncertainties on the these full absorption and neutron-capture peaks were underestimated and should be scaled by $\sqrt{4.9} \sim 2.2$.

5.4.3 Cross-check with Spallation Neutrons

The validity of the energy scale correction function given in Eq. 5.3 can be checked throughout the target volume using the H and Gd neutron-capture peaks from muon-induced spallation neutrons.

Fig. 5.5 shows the ratio of the H neutron-capture peak in the spallation neutron data with respect to the energy-scale-corrected MC in various bins of Z and ρ^2. Except for extreme Z-positions in the GC, the data/MC difference is within $7 - 8\%$.

Fig. 5.6 shows the ratio of the Gd neutron capture peak in the spallation neutron data with respect to the energy-scale-corrected MC in various bins of Z and ρ^2. Except for extreme ρ positions near the target/GC boundary, the data/MC difference is within 2.5%.

5.5 Energy Response Covariance Matrix

Uncertainty on the energy scale described above can have an effect on the $\bar{\nu}_e$ disappearance analysis. This uncertainty can be represented by a covariance matrix, M^{reco}, which describes the uncertainty in the predicted number of IBD events in a given reconstructed positron energy bin as well as the correlations between bins.

M^{reco} is generated using the **MULTISIM** method from the correction function fit parameter covariance matrices given in Eq. 5.5 and Eq. 5.7. The fit parameters of $corr1$

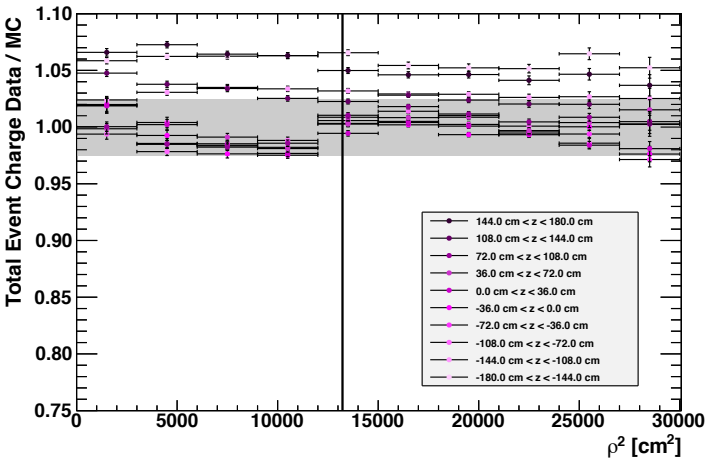

Figure 5.5: Ratio of the H capture peak extracted from the data with respect to the MC tuned using Eq. 5.4 – 5.6 for muon-induced spallation neutrons as a function of reconstructed Z and ρ^2 position. The maximum data/MC discrepancy of $\sim 7\%$ occurs at in the γ-catcher volume at extreme Z-positions.

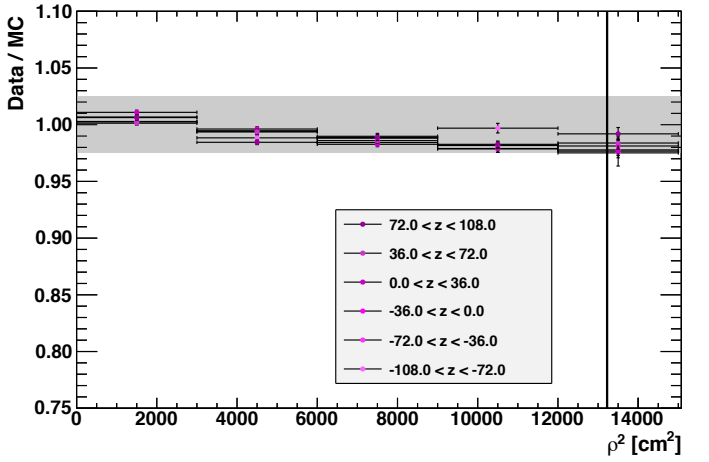

Figure 5.6: Ratio of the Gd capture peak extracted from the data with respect to the MC tuned using Eq. 5.4 – 5.6 for muon-induced spallation neutrons as a function of reconstructed Z and ρ^2 position. The maximum data/MC discrepancy is $\sim 2.5\%$ and occurs at the edge of the target.

and *corr*2 are treated as uncorrelated and therefore the total uncertainty on the energy scale correction function can be described in terms of a 6×6 covariance matrix

$$M^{corr} = \begin{pmatrix} M^{corr1} & \\ & M^{corr2} \end{pmatrix}. \tag{5.8}$$

5.5.1 MULTISIM Method

The **MULTISIM**[2] method can be used to propagate the uncertainties encoded in the covariance matrices of the *corr*1 and *corr*2 fit parameters to a covariance matrix, M^{reco}, which describes the uncertainties in the IBD signal plus background MC prediction in terms of reconstructed energy.

The method consists of performing multiple simulations (**MULTISIMS**) of the energy reconstruction of the IBD signal plus background MC prediction, each with a different set of parameters for *corr*1 and *corr*2. The parameters for each simulation are drawn from the multi-variate gaussian distribution

$$f(\vec{p}) \sim \exp\left[-\sum_{ij}(p_i - p_i^{best})(M^{corr})^{-1}_{ij}(p_j - p_j^{best})\right], \tag{5.9}$$

where p_i^{best} is the best fit value for parameter p_i given above and M_{ij}^{corr} is the fit parameter covariance matrix given in Eq. 5.8. Each simulation predicts a number of IBD signal and background events, N_a, reconstructed in prompt energy bin a, which is in general different from the predicted number of IBD signal and background events, N_a^{best}, obtained using the p_i^{best} for the energy scale correction function. The covariance matrix M^{reco} is calculated from the shifts in the number of IBD signal plus background MC events reconstructed in each prompt energy bin a with respect to the N_a^{best}, averaged over all simulations, i.e.

$$M_{ab}^{reco} = \frac{1}{K-1}\sum_{k}^{K}(N_a^k - N_a^{best})(N_b^k - N_b^{best}). \tag{5.10}$$

5.5.2 Modifying M^{corr1} and M^{corr2}

There are two issues with using the fit parameter covariance matrix M^{corr} of Eq. 5.8 to determine the energy response covariance matrix M^{reco}.

[2]The name for this MC-based error propagation technique is taken from the MiniBooNE experiment.

The first issue is that M^{corr} contains large correlations between the fit parameters. These large correlations are an artifact of our simple implementation of the energy scale correction function, which depends only on energy and Z but not ρ, and of the very small uncertainties assigned to the calibration data. If we attempt to account for our underestimated calibration data uncertainties by scaling M^{corr} by an expansion factor, the large covariances between the fit parameters will also be increased. The end result is that these large correlations produce **MULTISIMS** with unphysical energy scale correction functions[3] that bias the energy scale which gets into the final covariance matrix. As an approximate method to bypass this issue, we remove the fit parameter correlations from M^{corr1} and M^{corr2} and keep only the diagonal terms. By removing these correlations from M^{corr}, we are also effectively increasing the energy scale uncertainty.

The second issue, however, is that even after diagonalizing M^{corr}, the energy scale uncertainty it describes is not consistent with the residual discrepancy between data and MC observed with spallation neutrons and shown in Fig. 5.5 and Fig. 5.6. We address this issue by first multiplying M^{corr1} and M^{corr2} by 4 and 4.9, respectively so that the reduced χ^2 of the fits to calibration data are ~ 1. Next, we observe that for $|Z| < 108$ cm, the discrepancies between data and MC are $< 2.5\%$ for both neutron capture on H and on Gd. The largest discrepancies between data and MC of $\sim 7\%$ occur only at the extreme Z-positions in the γ catcher for neutron capture on H. Therefore, we expand the uncertainties associated only with $corr2$ by scaling M^{corr2} by a factor of 40 in order to cover the observed discrepancies between data and MC.

To verify that the energy scale uncertainty given by our choice of M^{corr} above is adequate to cover the residual discrepancy between data and MC observed in spallation neutron data, we simulate fluctuations in the energy scale correction function at 2.2 and 8 MeV for two positions along the Z-axis. For each of these four configurations, we make $50,000$ random draws for the set of 6 fit parameters, $p_i,\ i = 0 \ldots 5$, according to the multivariate gaussian distribution

$$f(\vec{p}) \sim \exp\left[-\sum_{ij}(p_i - p_i^{best})(M^{corr})^{-1}_{ij}(p_j - p_j^{best})\right], \tag{5.11}$$

[3]For example, an energy scale correction function may be inverted so that it increases at lower energies.

where p_i^{best} is the best fit for parameter i and M_{ij}^{corr} is the fit parameter covariance matrix modified as described above. Specifically, expression for fit parameter covariance matrix is given by

$$M^{corr} = \begin{pmatrix} 1.03 \cdot 10^{-5} & & & & & & \\ & 4.06 \cdot 10^{2} & & & & & \\ & & 4.41 \cdot 10^{-4} & & & & \\ & & & 1.65 \cdot 10^{-4} & & & \\ & & & & 3.65 \cdot 10^{-10} & & \\ & & & & & 9.5 \cdot 10^{-16} & \end{pmatrix} \quad (5.12)$$

Fig. 5.7 illustrates the results of these random draws. At the center of the detector, the energy scale uncertainty is 3.1% and 3.3% for $E = 2.2$ MeV and $E = 8$ MeV, respectively. At $Z = 135$ cm, the energy scale uncertainties are instead found to be 7.3% and 7.4%, respectively. Therefore, the M^{corr} given in Eq. 5.12 adequately covers the residual discrepancies between and MC throughout the target and γ-catcher as measured by spallation neutrons (see Fig. 5.5 and Fig. 5.6).

5.5.3 Results

The energy response covariance matrix, M^{reco}, was constructed with the same binning used in the final χ^2 oscillation fit described in Sec. 8.1. A total of 590 **MULTISIMS** were performed. Fig. 5.8 shows the MC signal plus background prompt energy spectra for the first 8 **MULTISIMS**, as well as for energy spectrum obtained by averaging over all 590 **MULTISIMS**.

Each **MULTISIM** simulates a different energy scale correction function for the MC. Therefore, each **MULTISIM** has a different IBD selection efficiency since the IBD selection depends on energy cuts (see Sec. 6.4). Fig. 5.9 shows the distribution of the number of IBD candidate events selected in the MC for the 590 **MULTISIMS**. The fractional spread of this distribution is $\sim 1.3\%$ and gives an indication of the uncertainty on the total number of IBD signal plus background events predicted in the MC due to energy reconstruction uncertainties.

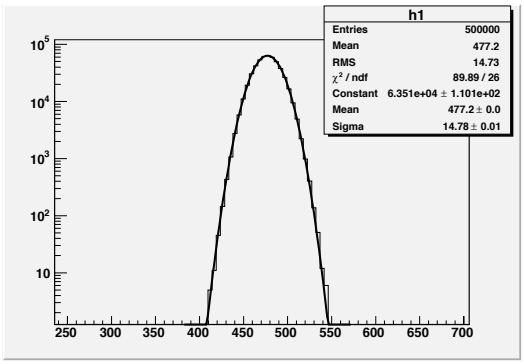

(a) E=2.2 MeV, Z=0 cm: 3.1% uncertainty

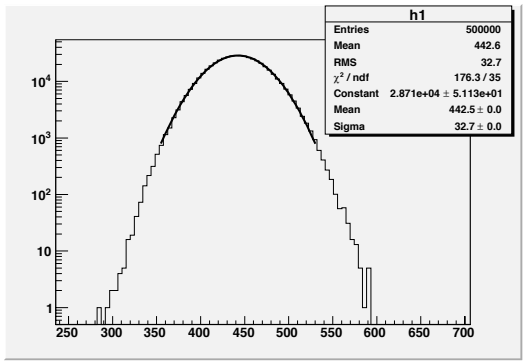

(b) E=2.2 MeV, Z=135 cm: 7.3% uncertainty

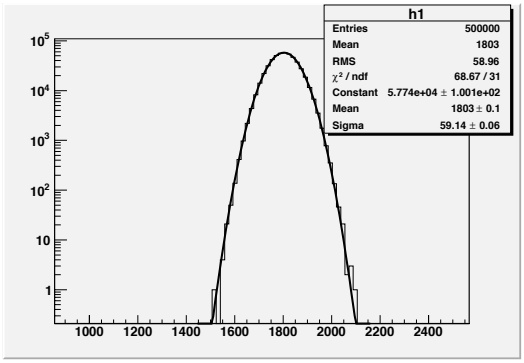

(c) E=8 MeV, Z=0 cm: 3.3% uncertainty

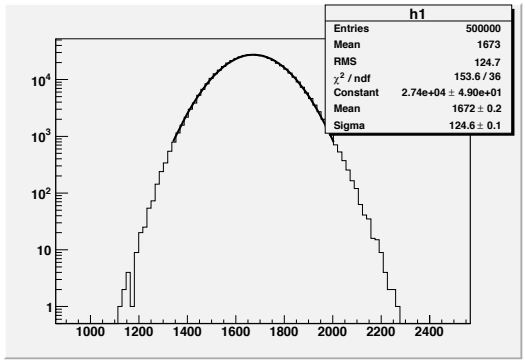

(d) E=8 MeV, Z=135 cm: 7.4% uncertainty

Figure 5.7: Energy scale uncertainties at 2.2 MeV and 8 MeV at the target center as well as along the Z-axis for $Z = 135$ cm.

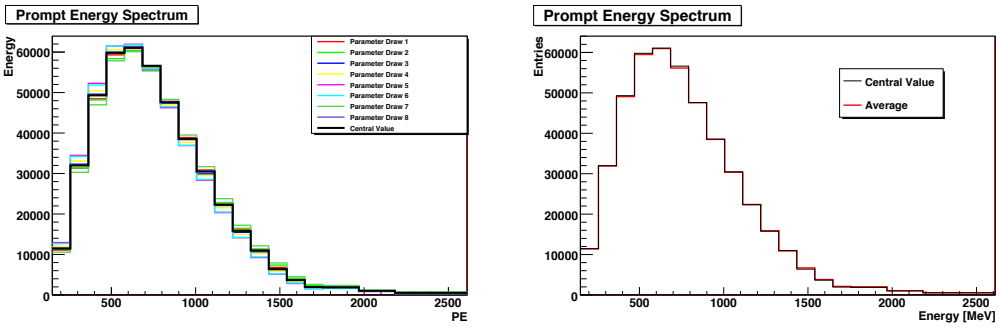

(a) MC IBD signal plus background prompt energy spectra for the first 8 **MULTISIMS**

(b) Average MC IBD signal plus background prompt energy spectrum

Figure 5.8: The panel on the left shows the MC IBD signal plus background prompt energy spectra for the first 8 **MULTISIMS** superimposed with the prompt energy spectrum of the MC central value IBD signal plus background prompt energy spectrum obtained using the best fit parameters for the energy scale correction functions described in the text. The panel on the right shows the MC IBD signal plus background prompt energy spectrum averaged over all **MULTISIMS** superimposed with the prompt energy spectrum of the MC central value IBD signal plus background prompt energy spectrum.

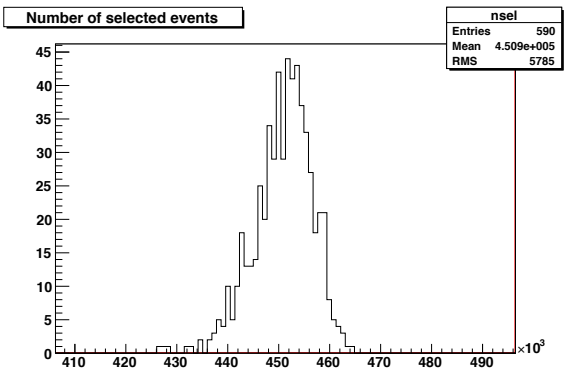

Figure 5.9: Distribution of the number of IBD candidate events selected in the MC for the 590 **MULTISIMS**.

For technical reasons, the background MC used in these **MULTISIMS** to generate the energy scale covariance matrix consisted only of ^{9}Li. However, since ^{9}Li is the largest background, the MC signal plus ^{9}Li background prompt energy spectrum is a good approximation of the total MC signal plus background prompt energy spectrum, which includes all sources of backgrounds (see Sec. 7.2). However, rather than rely on this approximation directly, we derive the fractional energy response covariance matrix from the full energy response covariance matrix using the MC signal plus ^{9}Li background energy spectrum. The fractional covariance matrix is then passed to the final oscillation fit machinery where the full covariance matrix is reconstituted using the total MC signal plus background prompt energy spectrum before being included in the χ^2 (see Ch. 8). The full and fractional covariance matrices obtained using the **MULTISIM** method are given in Fig. 5.10.

Fig. 5.11 gives the determinant and the normalization uncertainty[4] of M^{reco} as a function of the number of **MULTISIMS** showing the convergence of the covariance matrix generated using the **MULTISIM** method. The normalization uncertainty asymptotes to 1.3%, consistent with the fractional spread of Fig. 5.9.

[4]Sec. 8.2 describes how to compute the normalization uncertainty of a covariance matrix

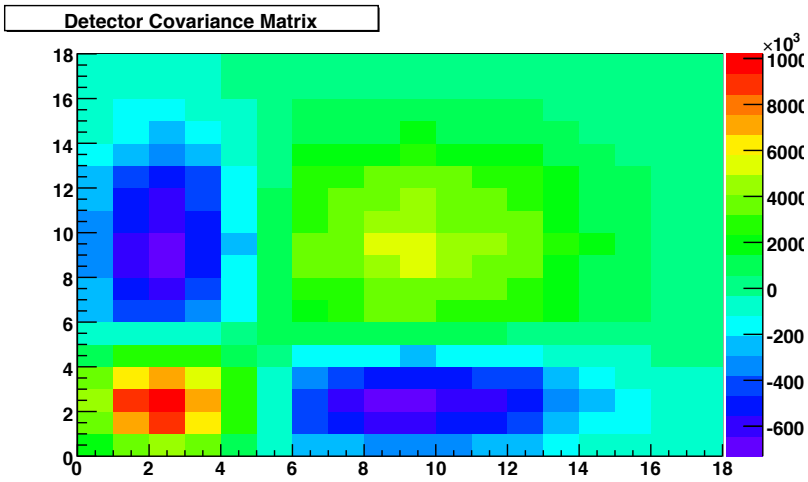

(a) Full covariance matrix M^{reco}

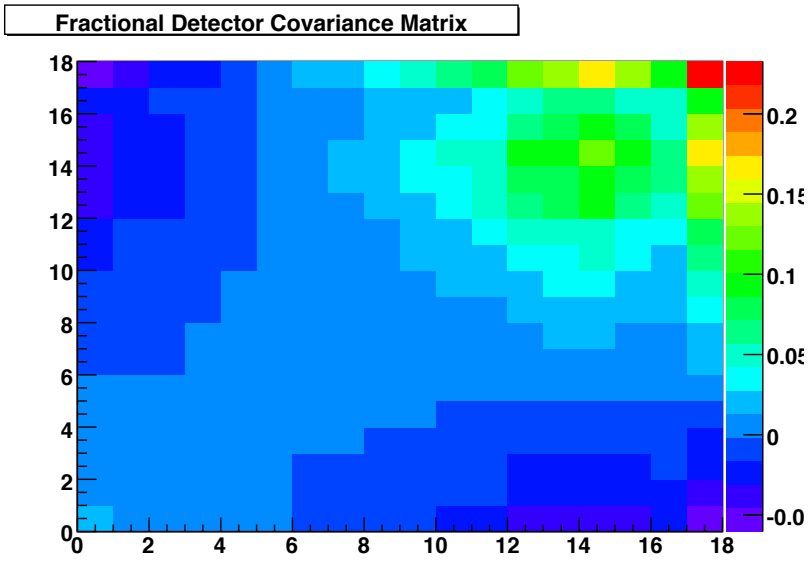

(b) Fractional covariance matrix M^{reco}

Figure 5.10: The panel on the left is a $2D$ histogram of the full energy response covariance matrix, M^{reco}. The panel on the right is a $2D$ histogram of the fractional energy response covariance matrix. The X and Y axes label the prompt energy bins.

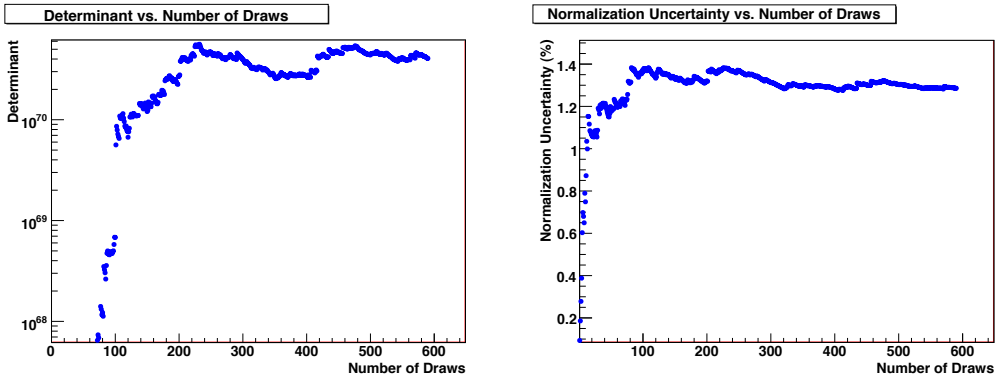

(a) Determinant (b) Normalization uncertainty

Figure 5.11: Determinant and normalization uncertainty of the detector energy response covariance matrix as a function of number of **MULTISIMS**.

Chapter 6

Signal Extraction and Efficiency Estimation

Data used for the $\bar{\nu}_e$ disappearance analysis were collected over a span of 159 days from April 13, 2011–September 18, 2011. A set of runs were identified in which detector operation was stable totaling 101.52 days of run time.

The IBD signal extraction is preformed in 3 steps. First, a muon veto is applied and all triggers vetoed by the muon veto are removed from the data stream. Next, a data quality cut is applied to remove triggers associated with spurious light emissions from the PMT base. Finally, delayed coincidences of a prompt event with $0.7 \leq E \leq 12.2$ MeV followed by a delayed event with $6 \leq E \leq 12$ MeV are extracted from the remaining triggers.

For each selection cut, the relative efficiency for selecting IBD events in the data and MC must be determined. Furthermore, the systematic uncertainty in the relative efficiency must also be calculated and included in the final $\bar{\nu}_e$ disappearance analysis described in Ch. 8.

6.1 Run selection and detector stabilitiy

Data-taking during the run period is separated into IBD search, "physics" runs and all other types. Other types of runs include source calibration runs as well as light injection calibration runs used to monitor the gains of both the inner detector and inner veto PMTs.

Fig. 6.1 shows a histogram of the daily data-taking efficiency, defined as the fraction of the day spent collecting data of that run type, for the first 206 days of running. The average data-taking efficiency during this period for all types of runs was 86.2%. The major sources of inefficiency were the DAQ initialization time between runs and the recovery time after DAQ crashes. The average data-taking efficiency for IBD search physics runs in this same period was 77.5%.

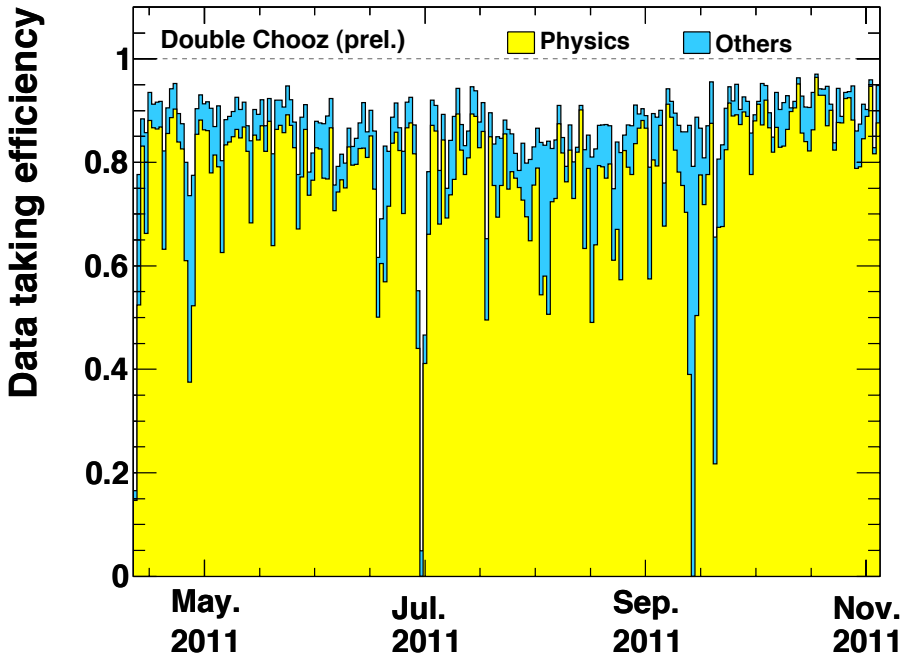

Figure 6.1: Daily data taking efficiency vs. calendar day. The blue histogram is the fraction of time spent taking data. The yellow histogram is the fraction of time spent taking neutrino search data.

Run quality metrics were developed to identify periods of detector instability which might affect the IBD search physics data. A set of 81 runs associated with a particular PMT (PMT 263) injecting large amounts of noise in the data was identified. These runs were excluded by a cut described in Sec. 6.3. Another set of 3 runs associated with increased HV instability was also identified and excluded from the analysis. Finally, any aborted runs lasting less than 5 minutes were also excluded.

The remaining set of 2,594 IBD search physics runs are called the "analyzed" runs as

they were used for the $\bar{\nu}_e$ disappearance analysis. Fig. 6.2 shows the data-taking efficiency histogram including the analyzed runs with the integrated data-taking time superimposed. The integrated data-taking time is the total run time for a given run type. The total run time for the set of analyzed runs is 101.5234 days.

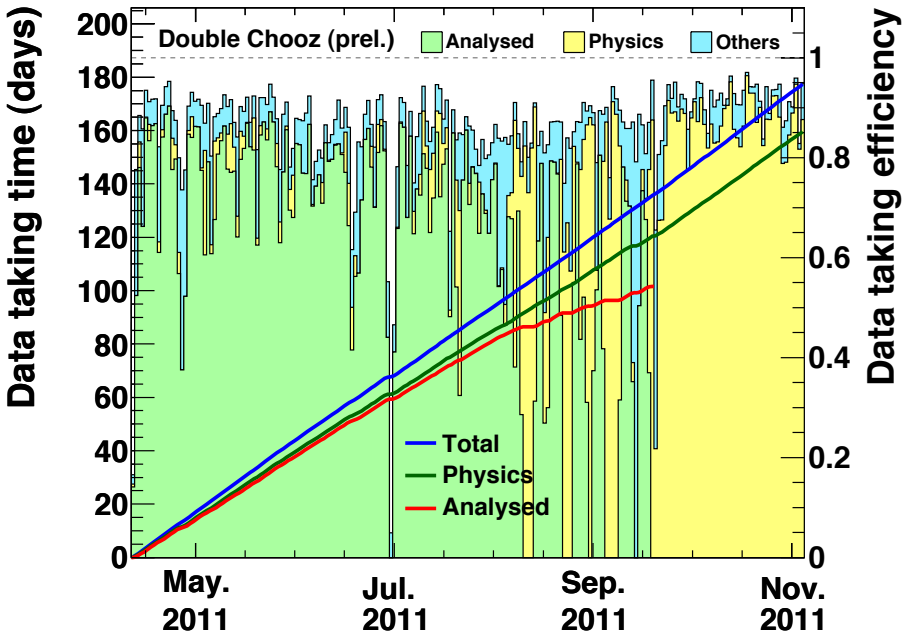

Figure 6.2: Curve representing integrated data taking (left vertical scale) vs. calendar day superimposed on histogram of daily data taking efficiency (right vertical scale) vs. calendar day. The blue, yellow, and green histograms are the daily run time, daily neutrino search run time, and daily analyzed neutrino search run time, respectively. Each has been normalized to 24 hours. The blue, green, and red curves are the integral of the blue, yellow, and green histograms, respectively.

6.2 Muon Veto

Cosmic ray muons can induce delayed coincidence signals in the detector which mimic inverse beta-decay. For example muon-induced spallation products can initiate particle showers in the detector, which produce multiple neutrons. Double neutron captures, in

which the first neutron captures on either H or Gd and the second neutron captures on Gd, can mimic the delayed coincidence signal of the IBD interaction. This section describes the muon veto used in the $\bar{\nu}_e$ disappearance analysis.

6.2.1 Inner Veto Muon Tagging

The IV efficiency for tagging muons can be determined by looking at events which trigger both the ID and are reconstructed in the OV. Fig 6.3 shows the IV charge distributions for this class of events. The IV muon-tagging efficiency for a given threshold, Q_{IV}^{thresh}, is determined by the fraction of these events with with $Q_{IV} > Q_{IV}^{thresh}$. A threshold of $10,000$ DUQ is used in the $\bar{\nu}_e$ disappearance analysis to tag muons in the IV. Fig. 6.3 shows that the inner veto muon-tagging efficiency for $Q_{IV}^{thresh} > 10,000$ DUQ is greater than 99.99%.

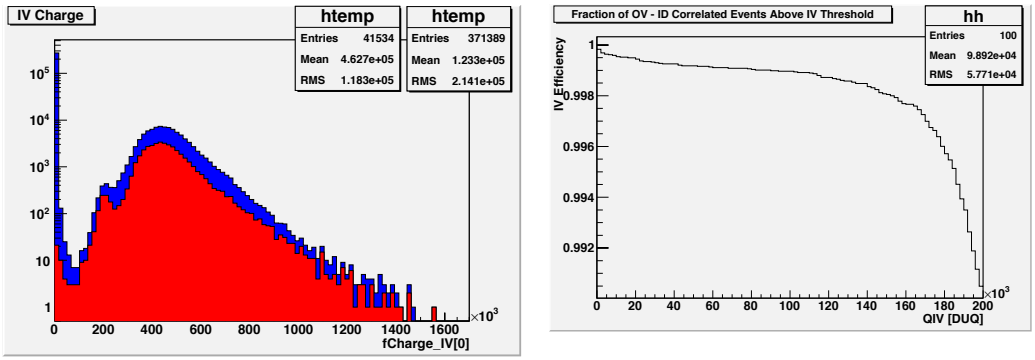

(a) IV Charge Spectrum

(b) IV Efficiency Curve

Figure 6.3: The plot on the left shows the IV charge spectrum for all events which trigger the the ID in blue and for events which trigger the ID and are reconstructed in the OV in red. The plot on the right is the IV efficiency for muons obtained by integrating the red histogram above Q_{IV}^{thres} and normalizing to the total integral.

6.2.2 Inner Detector Muon Tagging

Though most muons which enter the detector pass through the IV, there is also a class of down-going muons which enter the ID through the chimney region and do not pass though

the IV or OV. Most of these "chimney" muons deposit a large amount of energy in the ID. However, some traverse only a small amount of scintillator before stopping, and these cannot be distinguished from the prompt positron signal of IBD interactions. To partially eliminate these chimney muons, an ID muon veto with a threshold of 30 MeV is chosen as a compromise between maximizing the efficiency for rejecting these muons and allowing for an extended prompt energy window to study backgrounds (see Ch. 7).

6.2.3 Muon Veto Time Window

Fig. 6.4 shows the number of IBD candidates selected in the data as a function of the muon veto window ΔT_μ [90]. For large muon veto windows, the number of neutrino candidates decreases linearly with the window size as expected, since IBD events should not be correlated with muons. A linear fit is performed in the range $2 - 10$ ms and then extrapolated to smaller values of ΔT_μ. Fig. 6.4 also shows the fractional deviation in the number of IBD candidates with respect to this linear fit as a function of ΔT_μ. Below 800 μs, a fractional excess is seen in the number of neutrino candidates versus muon veto window size indicating the presence of correlated backgrounds. A conservative muon veto time window of 1 ms was chosen for the IBD selection to remove these muon-correlated background events.

6.2.4 Summary

Events that deposit $> 10,000$ DUQ in the IV or deposit > 30 MeV in the ID initiate a 1ms muon veto window for the IBD selection. Besides reducing the muon-induced backgrounds, this veto also caused dead-time for the real signal events. A total of 406101475 muon events were identified in the analysis period, resulting in a dead time of 4.70 days or 4.63%. Fig. 6.5 plots the daily dead time fraction and Fig. 6.6 the daily live time as a function of calendar day. The total live time for this analysis is 96.8 days.

6.3 Light Noise Rejection

During commissioning, electrical discharges in the bases of the inner detector PMTs were shown to produce light in the detector leading to spurious pulses from the PMTs [91].

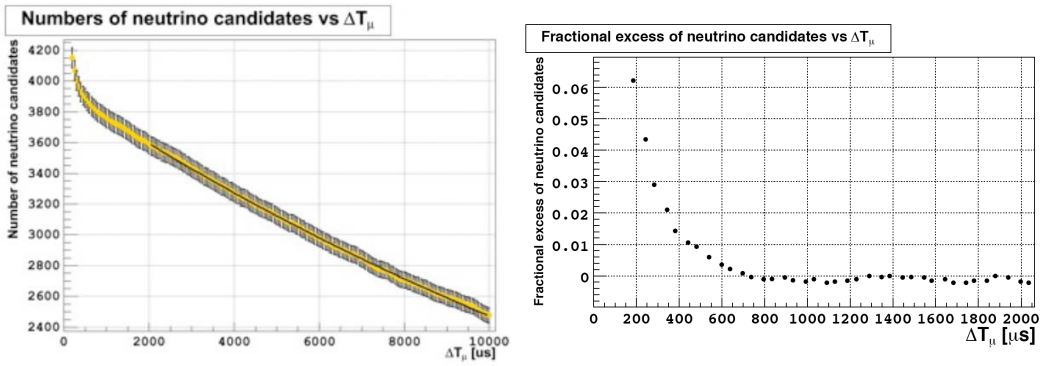

(a) Neutrino candidates vs. muon veto window (ΔT_μ)

(b) Fractional excess in neutrino candidates vs. muon veto window (ΔT_μ)

Figure 6.4: Number of neutrino candidates vs. muon veto window. For large values of the muon veto window, the number of neutrino candidates decreases linearly with the window size as expected for uncorrelated events. Below 800 μs, a fractional excess is seen in the number of neutrino candidates versus muon veto window size relative to a linear fit extrapolation from $2-10$ ms indicating the presence of correlated backgrounds [90].

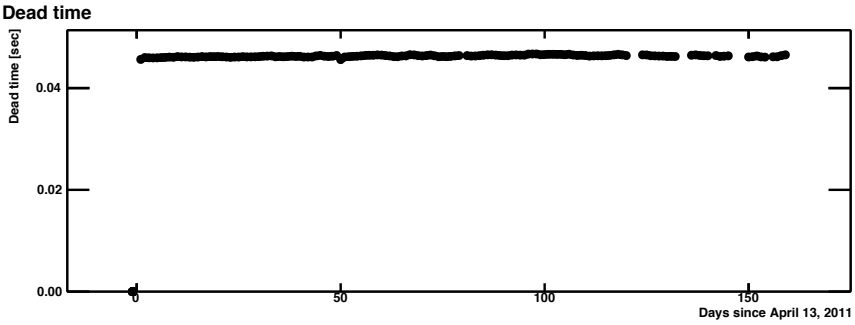

Figure 6.5: The dead time fraction as a function of calendar day computed as $R_\mu \Delta T_\mu$, where $R_\mu = 46$ Hz is the muon veto rate and $\Delta T_\mu = 1$ ms is the muon veto window.

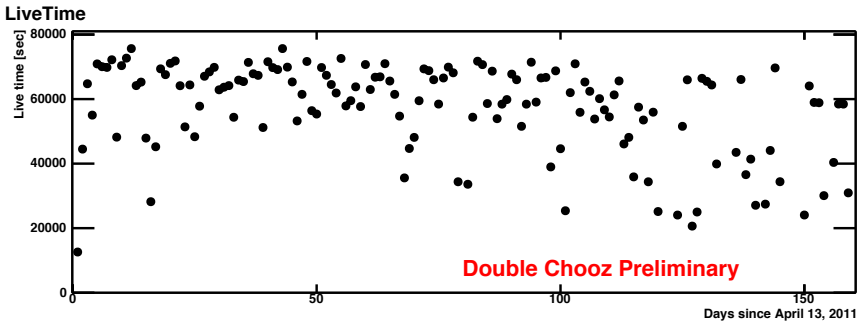

Figure 6.6: The live time as a function of calendar day computed as the run time less the muon veto dead time.

These types of non-signal pulses are referred to as "light noise". Light noise events with reconstructed energies in the delayed $6-12$ MeV energy window can constitute a significant background to the IBD selection if they are not handled properly. Several steps were taken to identify and mitigate the impact of the light noise background:

- Cuts were developed to identify light noise on an event-by-event basis based on lab measurements and MC studies
- PMTs which produced the most light noise were turned off prior to data taking
- Light noise events were rejected on an event-by-event basis
- Entire runs were excluded from the analysis which had an anomalously high rate of light noise associated with PMT 263

6.3.1 Identifying Light Noise Discriminants

MC studies indicated that the light noise produced in the base of a given PMT reflects off the buffer vessel surface as well as the mu-metal shielding surrounding the PMT, and that a majority of the light is seen by the PMT which produces it. Furthermore, lab measurements also established that the time scale associated with light noise events were generally longer than the time scale associated with PMT pulses from real particle detection.

Therefore, in contrast to physics events occurring in the target or gamma catcher regions of the detector, a light noise event is characterized by a single PMT collecting most of

the light and by PMT pulses with longer durations. Based on these characteristics, 2 discriminants were developed to identify light noise on an event-by-event basis: Q_{max}/Q_{tot} and T_{start}^{RMS}. The first variable is the maximum charge seen by any PMT divided by sum of all the PMT charges. The PMT which sees the most charge in an event is called the "max PMT". The second variable is the root-mean-square of the arrival times of the first photons seen by each PMT. Light noise events will typically have $Q_{max}/Q_{tot} \geq 0.1$ or $T_{start}^{RMS} \geq 40$ ns.

6.3.2 Turning off Noisy PMTs

During commissioning PMTs which produced the most light noise were identified from the distribution of max PMTs for events with $Q_{max}/Q_{tot} > 0.1$ and with reconstructed energies in the delayed $6-12$ MeV energy window. The 14 noisiest PMTs were identified and switched off prior to the start of data-taking. These PMTs were evenly distribution throughout the detector and so did not introduce any anisotropy in the detector response.

6.3.3 Event-by-event rejection

Events with $Q_{max}/Q_{tot} > 0.09$ or $T_{start}^{RMS} > 40$ ns were identified as light noise candidates and removed from the data stream. For IBD delayed coincidences, a more aggressive light noise cut can be placed on the delayed event than on the prompt event since events which deposit more energy in the ID tend to have smaller values of Q_{max}/Q_{tot}. Therefore, for the IBD selection, delayed neutron capture on Gadolinium events are further restricted to have $Q_{max}/Q_{tot} \leq 0.06$ though triggers which fail this condition are not removed from the data stream.

Fig. 6.7 shows a scatter plot of Q_{max}/Q_{tot} versus T_{start}^{RMS} for all gamma and neutron source calibration data taken in the target depositing between $0.5-12$ MeV. Fig. 6.8 shows the physics rejection factor as a function of Q_{max}/Q_{tot} and Fig. 6.9 shows the physics rejection factor as a function of T_{start}^{RMS}. Taken together, these cuts introduce a physics rejection factor of $< 0.8\%$ based on the calibration data. MC simulations indicate that the rejection factor is even lower than this ($< 0.1\%$) for IBD events and so can be neglected.

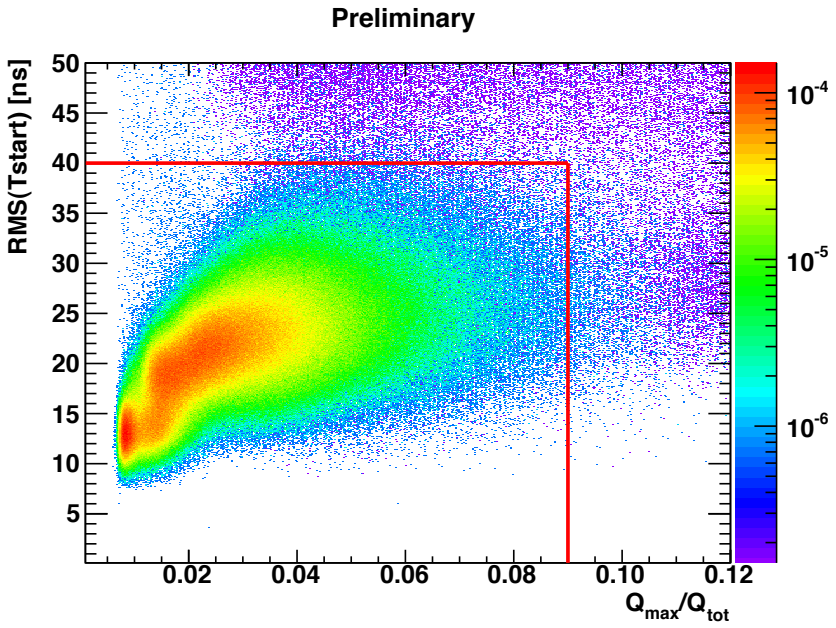

Figure 6.7: T_{start}^{RMS} vs. Q_{max}/Q_{tot} for gamma and neutron source calibration data deployed along the central axis of the target. The red lines indicate the light noise cuts used for the prompt event in the IBD selection.

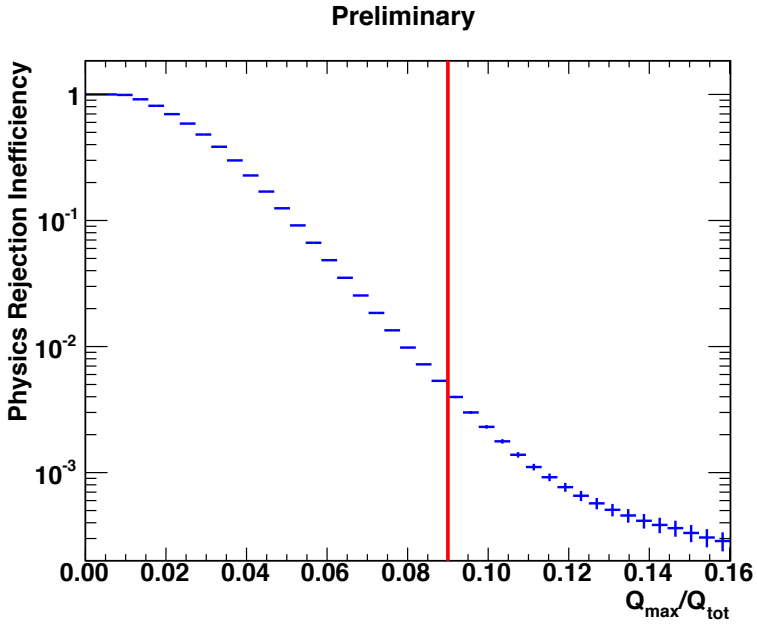

Figure 6.8: Fraction of source calibration events in 6.7 which are rejected by the given Q_{max}/Q_{tot} light noise cut. The red line indicates the light noise cut used for the prompt event in the IBD selection.

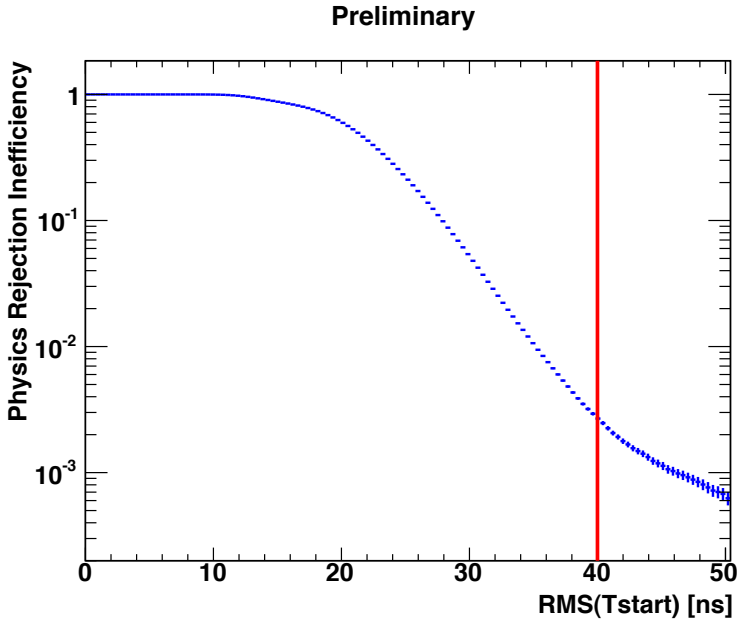

Figure 6.9: Fraction of source calibration events in 6.7 which are rejected by the given T_{start}^{RMS} light noise cut. The red line indicates the light noise cut used for the prompt event in the IBD selection.

6.3.4 PMT 263 Light Noise Fluctuations

Midway through the run period PMT 263 began to produce a large amount of light noise in the detector, some of which was not rejected by the light noise cut given above and contributing to the event rate in the IBD search delayed $6 - 12$ MeV energy window. Fig. 6.10 is a scatter plot of the rate of events in the delayed energy window for which PMT 263 was the max PMT versus the rate of all events in the delayed energy window for physics runs from April 13, 2011 – September 18, 2011 [92]. There is a clear correlation present for runs with > 0.007 Hz of events in the delayed energy window for which PMT 263 was the max PMT. These runs therefore suffer from a large contamination of light noise events due to PMT 263 and are excluded from the analysis.

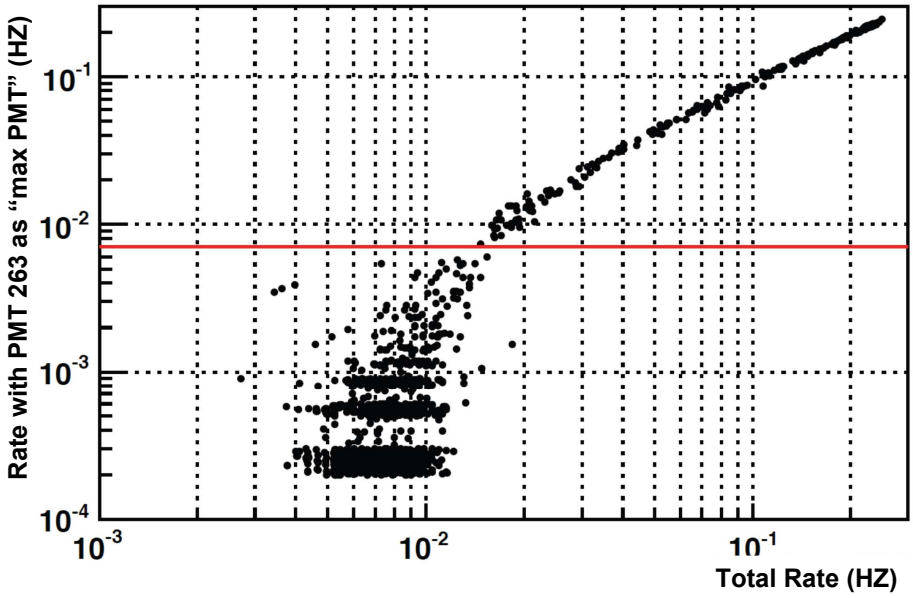

Figure 6.10: Rate of events in the IBD search delayed energy window in which PMT 263 was the max PMT vs. total event rate in the delayed energy window. Above 0.02 Hz there is a clear correlation between the rate associated with PMT 263 and total rate. Runs are excluded if the rate of events for which PMT 263 was the max PMT in the delayed energy window was greater than 0.007 Hz.

6.4 IBD Delayed Coincidence Selection

The inverse beta-decay delayed coincidence signal is defined by a prompt positron event, depositing between $0.7 - 12.2$ MeV of visible energy in the detector and a delayed neutron capture on Gadolinium depositing between $6 - 12$ MeV of visible energy in the detector in a time window of $2 - 100$ μs. The delayed coincidence signal is required to be isolated from other triggers in the sense that there can be no additional triggers with $E \geq 0.5$ MeV within 100 μs before or 400 μs after the prompt event.

The number of IBD candidate signal plus background events selected in the data is $4,121$, corresponding to an average IBD candidate rate of 42.6 d^{-1}. The number of IBD events selected in the no-oscillation, signal-only MC for the same live time and run period is 4010. Figure 6.11 gives an overlay of the IBD candidates rate of the data and MC as a function of calendar day.

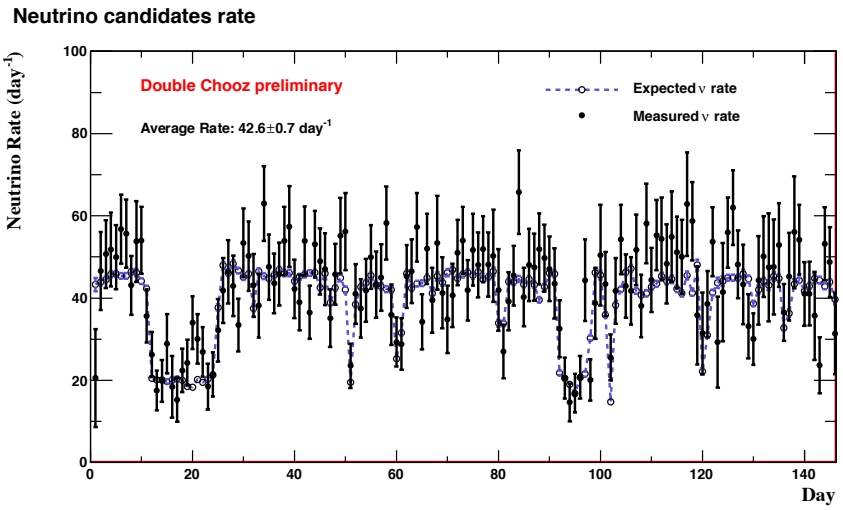

Figure 6.11: The black data points are the measured daily IBD candidate signal plus background rates versus calendar day. The blue dashed curve is the expected IBD rate versus calendar day for the no-oscillation, signal-only MC for the same live time and run period.

6.4.1 Prompt energy cuts

The lower limit of the prompt energy window, $E \geq 0.7$ MeV, was chosen to be $> 99.9\%$ efficient for selecting neutrinos (see Sec. 6.6.4). The upper limit of the prompt energy window, $E \leq 12.2$ MeV, was chosen to be well above the ~ 9 MeV endpoint of the IBD spectrum (see Ch. 4). This introduces fast neutrons, stopping muons, and cosmogenic ^{9}Li background events with prompt energies between $9-12.2$ MeV into the IBD candidate sample. However, given some knowledge of the energy distribution of each of these backgrounds, these high energy events can be used to constrain the backgrounds at lower energies, where a clean measurement of the backgrounds is not possible. Precise knowledge of these backgrounds at low energies is important because this is where spectral distortions in the IBD signal due $\sin^2(2\theta_{13})$ are expected to occur.

6.4.2 Delayed energy cuts

The presence of a gamma catcher in the Double Chooz design ensures that the energy from neutron capture events on Gadolinium is fully absorbed most of the time. However, the delayed event neutron capture on Gadolinium visible energy distribution for IBD candidates has a tail that extends down to energies of 5 MeV and below. The lower limit of the delayed energy window was chosen to be a relatively flat part of the energy spectrum with relatively good agreement between data and MC (see Sec. 6.6.5). The upper limit of the delayed energy window was conservatively chosen to be 12 MeV. This is well above the full absorption peak of neutron capture on Gadolinium and has negligible inefficiency for selecting IBD candidates.

6.4.3 ΔT cut

The ΔT distributions for IBD candidate events and accidental coincidences of uncorrelated events satisfying the prompt and delayed event energy cuts show that delayed coincidences with a $\Delta T > 100$ μs are dominated by accidental coincidences. The lower limit of the delayed coincidence time window was chosen to eliminate instrumental backgrounds, such as light noise. IBD candidate events with $\Delta T > 2$ μs were shown to have reconstructed

positions uniformly distributed throughout the target, while those with $\Delta T \leq 2$ μs were not.

6.4.4 Isolation cut

In order to suppress correlated backgrounds coming from chimney muons, an isolation cut is also imposed: IBD candidates with an additional trigger with visible energy ≥ 0.5 MeV in the 100 μs preceding a prompt event or the 400 μs following the prompt event are discarded. This isolation cut removes events in the neutron capture peaks of both H and Gd at $\sim$ 2.2 MeV and $\sim$ 8 MeV, respectively. This indicates that the isolation cut is effective in rejecting double neutron capture events (see Sec. 6.2).

6.4.5 Summary of IBD selection cuts

The following is a summary of the IBD selection cuts listed above:

- 1 ms Muon Veto: $Q_{IV} > 10,000$ DUQ or $E > 30$ MeV
- Prompt Event $0.7 \leq E \leq 12.2$ MeV, $Q_{max}/Q_{tot} \leq 0.09$, and $T_{start}^{RMS} \leq 40$ ns
- Delayed Event $6 \leq E \leq 12$ MeV, $Q_{max}/Q_{tot} \leq 0.06$, and $T_{start}^{RMS} \leq 40$ ns
- Coincidence: 2 μs $< \Delta T <$ 100 μs
- Isolation Cut: described in 6.4.4.

6.5 IBD data and MC comparisons

In the following, IBD candidate events extracted from the data are compared to a no-oscillation, signal-only MC generated for the same live time and run period (see Ch. 4). Some discrepancies are apparent indicating the presence of backgrounds in the IBD candidate sample. These background contributions must first be estimated in order to perform a $\bar{\nu}_e$ disappearance search. The background estimation is discussed in Ch. 7.

6.5.1 Reconstructed energy and time correlation

Fig. 6.12 shows the agreement between data and MC for the time correlation between the prompt and delayed events and is consistent with delayed neutron capture on Gd. Fig. 6.13 shows the correlation between the prompt and delayed event reconstructed energies in the data and is consistent with IBD interactions in the detector producing prompt positrons followed by delayed neutron captures on Gd. Fig. 6.14 and Fig. 6.15 show these prompt and delayed event reconstructed energies overlayed with the MC. Both distributions indicate the presence of backgrounds in the data, which are discussed in Ch. 7. The delayed energy Gadolinium neutron capture peak is $\sim 1\%$ higher in the MC than in the data, but this discrepancy is within the uncertainties included in the detector response covariance matrix described in Ch. 5.

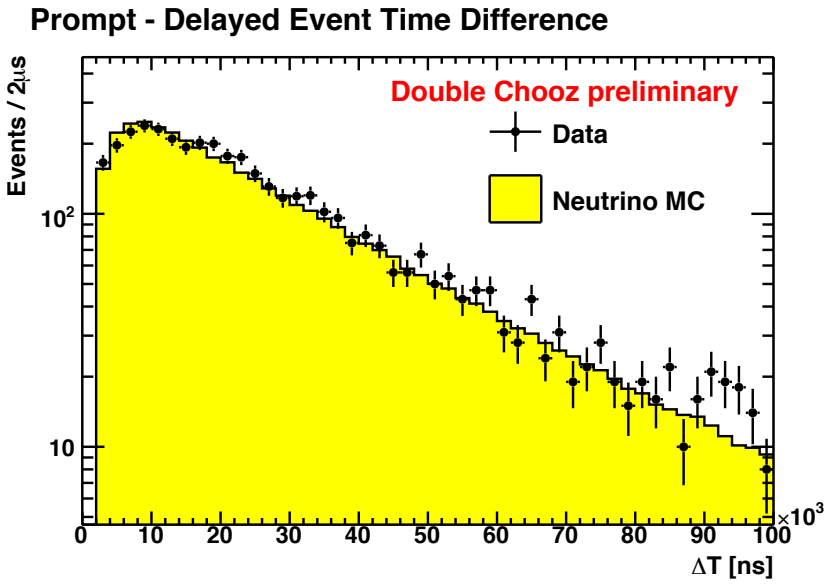

Figure 6.12: Histogram of the time difference between prompt and delayed events. The black points are the IBD candidates extracted from the data including signal and background. The yellow histogram is the no-oscillation, signal-only MC expectation.

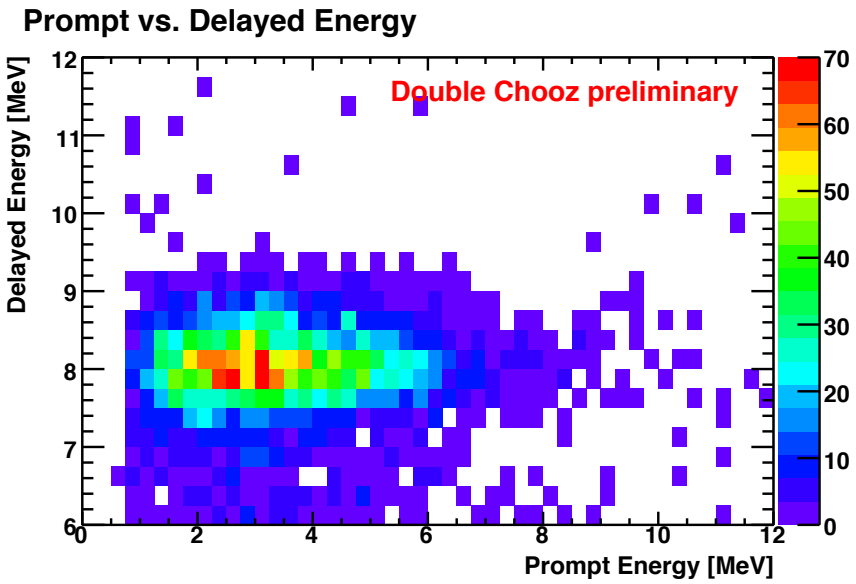

Figure 6.13: 2 D histogram of the prompt event reconstructed energy vs. delayed event reconstructed energy for IBD candidates extracted from the data.

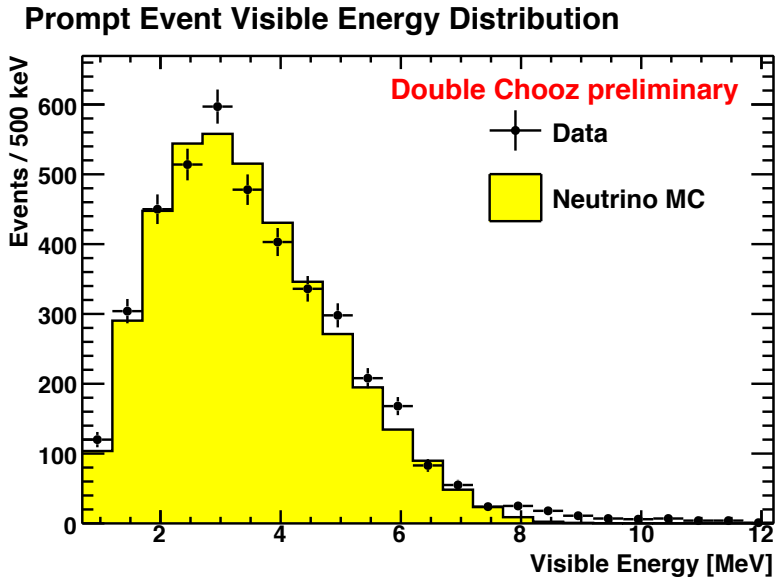

Figure 6.14: Histogram of the prompt event reconstructed energy distribution. The black points are the IBD candidates extracted from the data including signal and background. The yellow histogram is the no-oscillation, signal-only MC expectation.

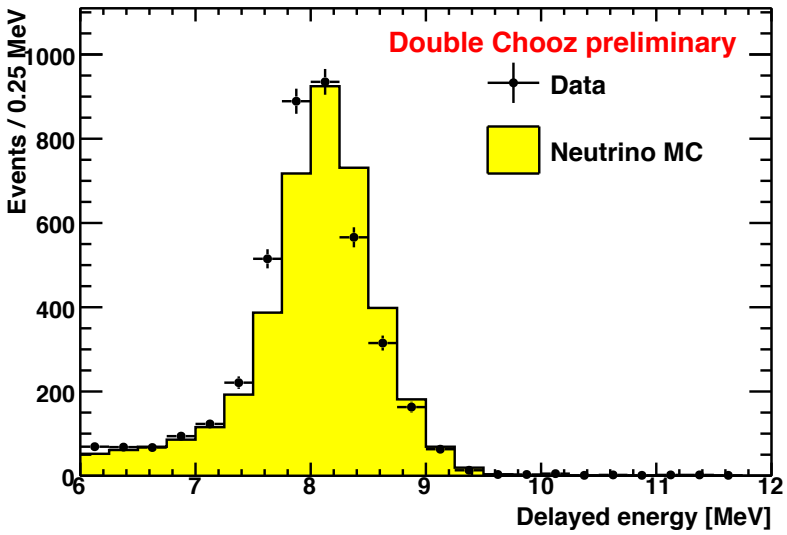

Figure 6.15: Histogram of the delayed event reconstructed energy distribution. The black points are the IBD candidates extracted from the data including signal and background. The yellow histogram is the no-oscillation, signal-only MC expectation.

6.5.2 Reconstructed Position

Fig. 6.16 shows the spatial correlation of the prompt and delayed events for the IBD candidates selected in the data overlayed with the MC. The data and MC show good agreement in the ΔT distribution. The Δr $\equiv \sqrt{(\Delta x)^2 + (\Delta y)^2 + (\Delta z)^2}$ variable is not used in an analysis cut, but the spatial correlation of the prompt and delayed signals serves as a nice cross-check. Finally, the reconstructed positions of the prompt and delayed events are given in Fig. 6.17–6.24. The vertices are distributed uniformly through target region of detector and are consistent with neutron capture on Gd in the target region only. With respect to the MC, there is a slight excess of events around $\rho^2 < 500$ cm^2 and $Z > 50$ cm. These are correlated background events and are described in Ch. 7.

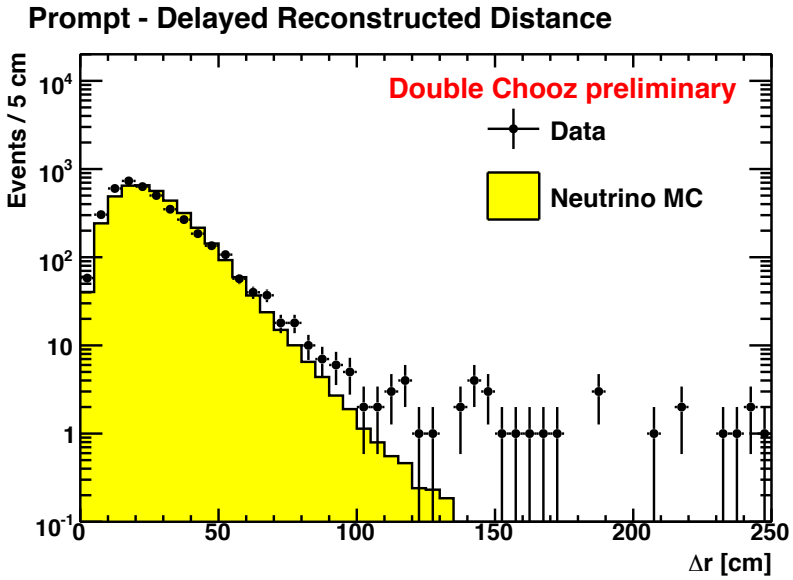

Figure 6.16: Histogram of the reconstructed distance between prompt and delayed events. The black points are the IBD candidates extracted from the data including signal and background. The yellow histogram is the no-oscillation, signal-only MC expectation.

6.6 Relative Data/MC efficiency

Ultimately, the $\bar{\nu}_e$ disappearance analysis depends on comparing measured IBD events extracted from the data to a MC prediction. Therefore, differences in the signal extraction efficiency between data and MC must be measured and corrected. In what follows, we consider the relative IBD selection efficiency between data and MC for each of the selection cuts given in Sec. 6.4.5.

6.6.1 Muon Veto Efficiency

As described in Sec. 6.2.4, the $T_\mu^{veto} = 1$ ms muon veto introduces an IBD selection inefficiency of $R_\mu T_\mu^{veto} = 4.63\%$, where R_μ is the muon rate. However, this inefficiency must be corrected to account for muons whose veto windows overlap and for the time correlation between the IBD delayed coincidence pair [93].

For example, if two muons are separated by $\Delta T_{\mu\mu} < 1$ ms, then the total veto time for these overlapping muons is actually $\Delta T_{\mu\mu} + 1$ ms. Therefore, a correction of -0.2% is

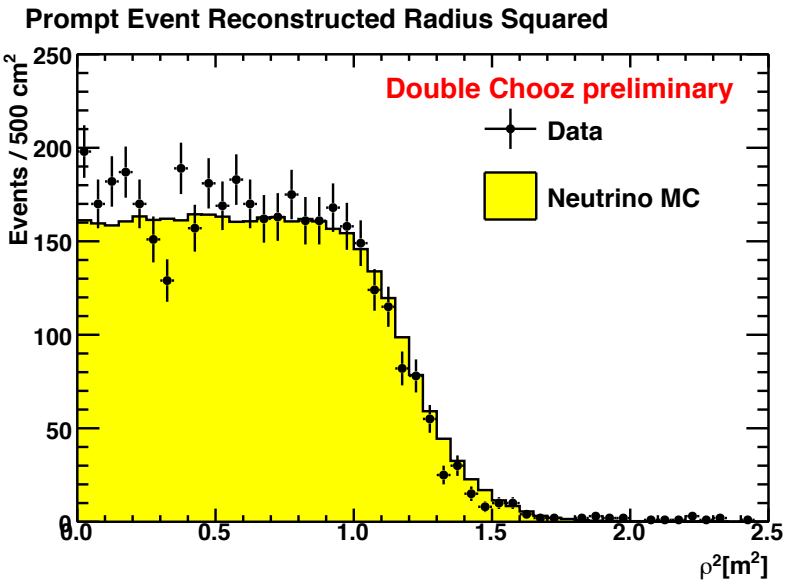

Figure 6.17: Histogram of the prompt event reconstructed ρ^2 position. The black points are the IBD candidates extracted from the data including signal and background. The yellow histogram is the no-oscillation, signal-only MC expectation.

applied to the above inefficiency to account for this overlapping muon effect based on the measured $\Delta T_{\mu\mu}$ distribution for the run period.

In addition the effective muon veto time window is actually larger than 1 ms for delayed coincidence pairs, because both the prompt and delayed events must fall outside the veto window. Thus, this effects leads to a further correction of +0.1% for IBD events with an approximately exponential ΔT distribution with a time constant of ~ 26 μs.

In summary, the muon veto introduces an IBD selection inefficiency of 4.53% in the data. A correction factor of 0.9647 must be applied to the MC, in which no muons are simulated. Because the resolution of the trigger clock is 16 ns << 1 ms, the uncertainty on the muon veto correction factor is negligible.

6.6.2 Light Noise Cut Efficiency

Light noise cuts were chosen to have negligible inefficiency for selecting IBD events. Fig. 6.25 and 6.26 show the Q_{max}/Q_{tot} and T_{start}^{RMS} distributions for the prompt event of IBD can-

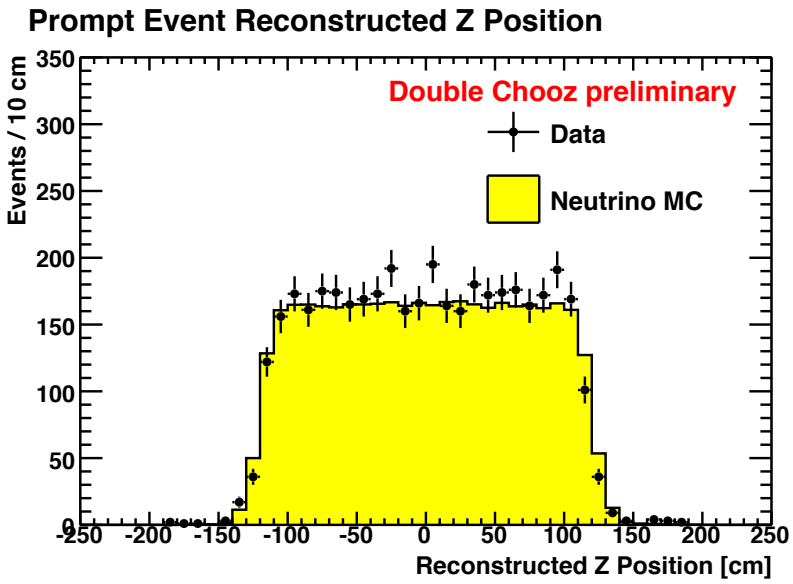

Figure 6.18: Histogram of the prompt event reconstructed Z position. The black points are the IBD candidates extracted from the data including signal and background. The yellow histogram is the neutrino-only MC expectation.

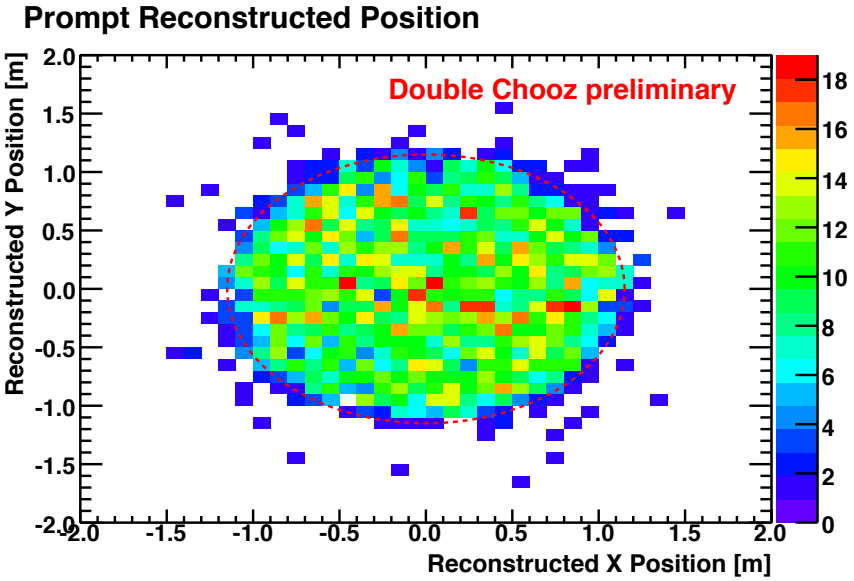

Figure 6.19: 2 D histogram of the prompt event X versus Y reconstructed position for IBD candidates extracted from the data. The red dashed line indicates the target volume.

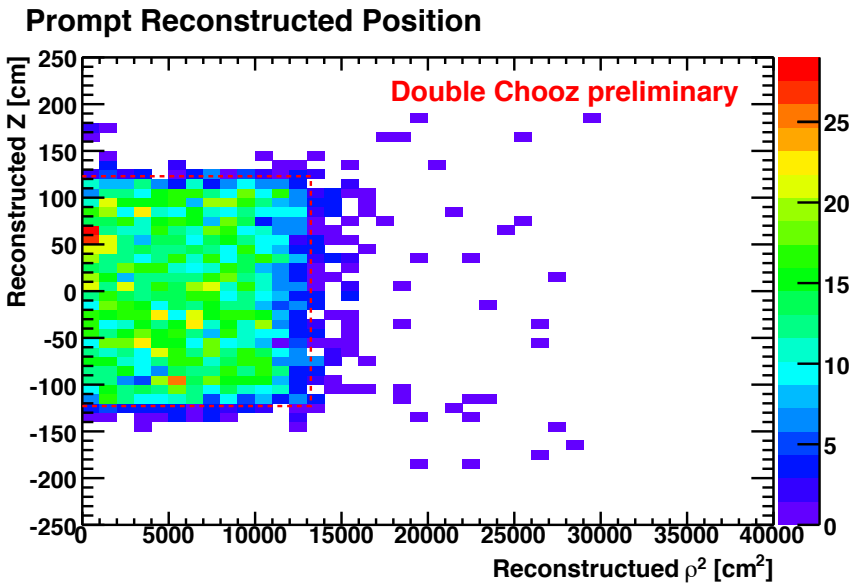

Figure 6.20: 2 D histogram of the prompt event Z versus ρ^2 reconstructed position for IBD candidates extracted from the data. The red dashed line indicates the target volume.

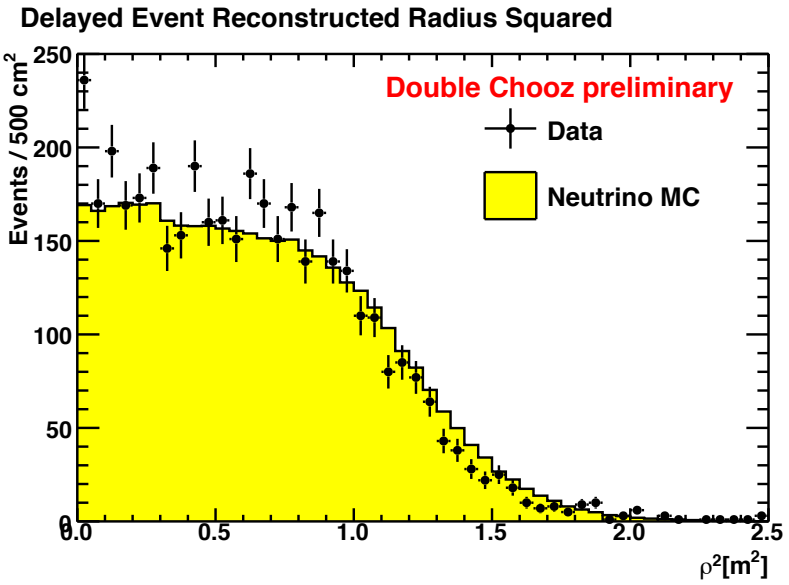

Figure 6.21: Histogram of the delayed event reconstructed ρ^2 position. The black points are the IBD candidates extracted from the data including signal and background. The yellow histogram is the no-oscillation, signal-only MC expectation.

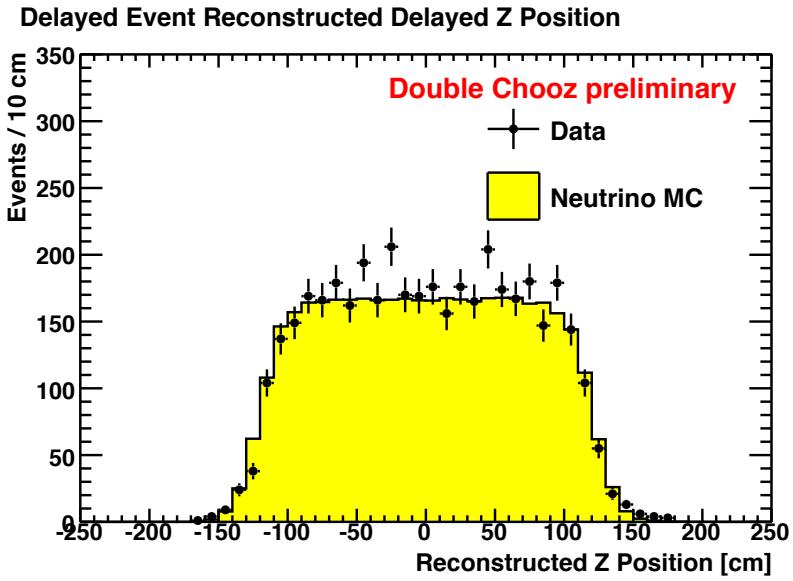

Figure 6.22: Histogram of the delayed event reconstructed Z position. The black points are the IBD candidates extracted from the data including signal and background. The yellow histogram is the no-oscillation, signal-only MC expectation.

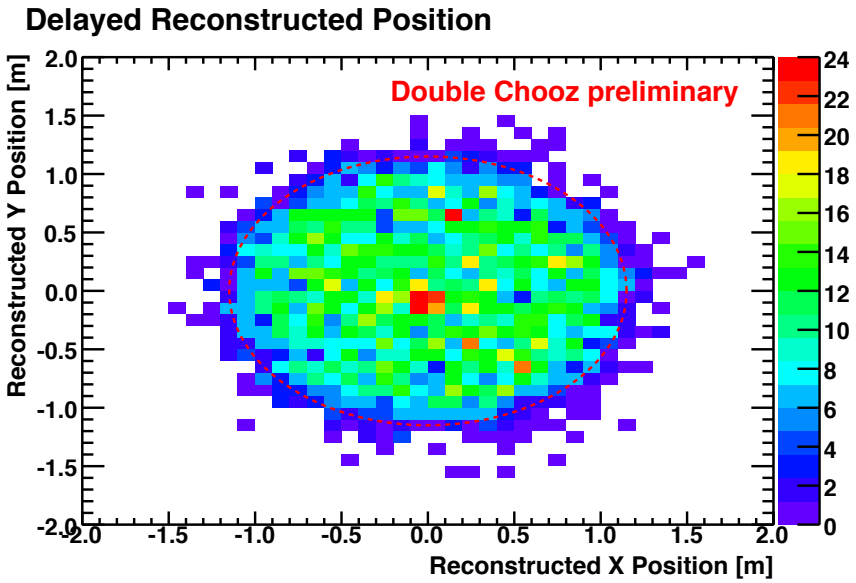

Figure 6.23: 2 D histogram of the delayed event X versus Y reconstructed position for IBD candidates extracted from the data. The red dashed line indicates the target volume.

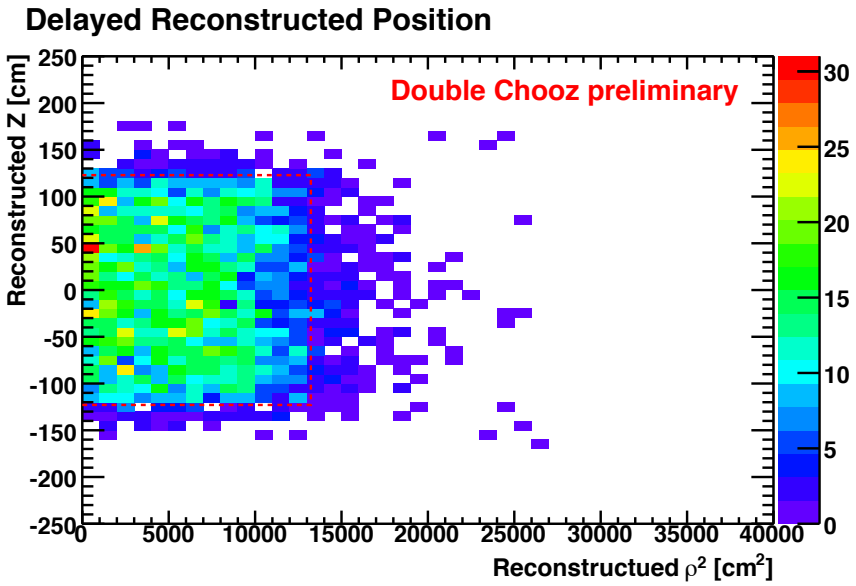

Figure 6.24: 2 D histogram of the delayed event Z versus ρ^2 reconstructed position for IBD candidates extracted from the data. The red dashed line indicates the target volume.

didates (signal and background) in data and MC, while Fig. 6.27 and 6.28 show the same distributions for the delayed event. There is a slight shift of the data with respect to the MC in both distributions, but in all cases the light noise cut is well separated from the distribution of IBD candidate events and induces negligible inefficiency.

6.6.3 Isolation Cut Efficiency

The isolation cut introduces an IBD selection inefficiency due to the random coincidence of a trigger with $E \geq 0.5$ MeV within 100 μs before or 400 μs after the prompt event of an IBD delayed coincidence pair. This inefficiency can be accurately determined from the data by measuring the rate of triggers which satisfy the isolation cut energy threshold and multiplying by the 500 μs isolation window. The isolation cut IBD selection efficiency for the data is found to be 99.5% with negligible uncertainty (see, for example Sec. 6.6.1). Therefore, the IBD signal MC must be corrected to account for this inefficiency since it contains no backgrounds.

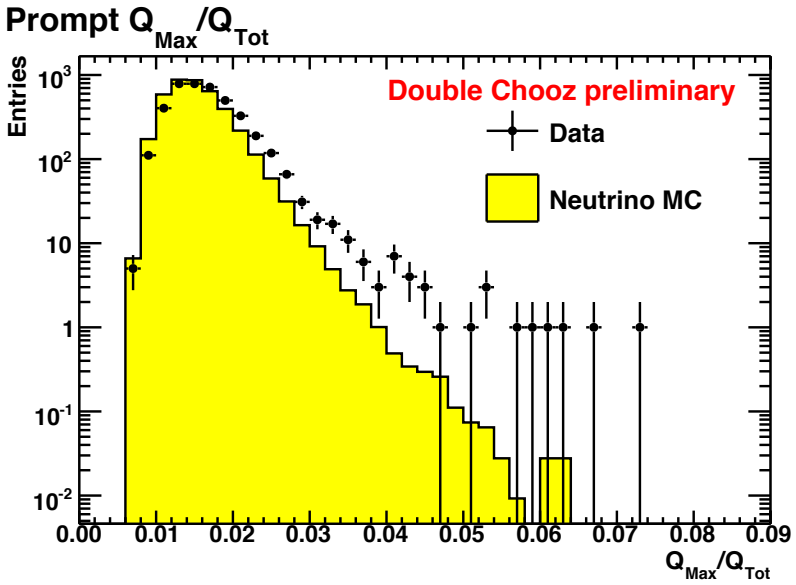

Figure 6.25: Histogram of the prompt event Q_{max}/Q_{tot} distribution. The black points are the IBD candidates extracted from the data including signal and background. The yellow histogram is the neutrino-only MC.

6.6.4 Prompt Energy Cut Efficiency

The minimum visible energy for the prompt event of an IBD delayed coincidence is 1.022 MeV coming from the 2 positron annihilation γ's and well above the 0.7 MeV low-energy prompt selection cut. As described in sec. 5.3, the ^{68}Ge calibration source also produces 2 positron annihilation γ's totaling 1.022 MeV which is used to tune the detector MC. Fig. 5.3 illustrates the very good agreement the ^{68}Ge source data and the tuned MC. Based on this good agreement, the IBD signal MC is used to determine the inefficiency of the prompt low-energy cut. The inefficiency is found to be $< 0.1\%$ and therefore negligible.

6.6.5 Delayed Event Cut Efficiencies

The largest uncertainties introduced by the IBD selection cuts come from the delayed event cut efficiencies described below. These were measured by comparing ^{252}Cf source calibration data with the tuned MC detector simulation described in Ch. 5.

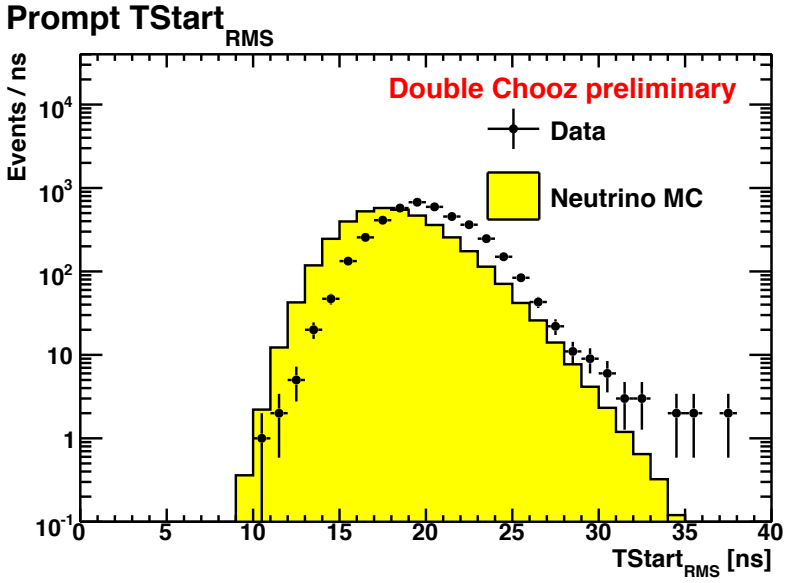

Figure 6.26: Histogram of the prompt event T_{start}^{RMS} distribution. The black points are the IBD candidates extracted from the data including signal and background. The yellow histogram is the neutrino-only MC.

6.6.5.1 ΔT Cut Efficiency

We compute the ΔT cut efficiency for the IBD selection using ^{252}Cf source calibration data. ^{252}Cf neutron events are selected by looking for the delayed coincidence of a prompt event ($7 < E < 30$ MeV) and a subsequent neutron capture on Gd ($4 < E < 25$ MeV). We define the ΔT cut efficiency as the ratio of the number of ^{252}Cf neutron events with $2 < \Delta T < 100$ μs to the number of ^{252}Cf neutron events with $2 < \Delta T < 200$ μs. Fig. 6.29 shows the ΔT cut efficiency as a function of the Z position of the source for data and MC. The relative difference between data and MC is shown in Fig. 6.30. Integrating over Z position, we find an uncertainty of 0.5% in the relative ΔT cut efficiency for data and MC [94].

6.6.5.2 Gd Capture Fraction

IBD candidate events are identified by a delayed coincidence of a prompt positron signal and a delayed neutron capture on Gd. However, some fraction of neutrons in the target will

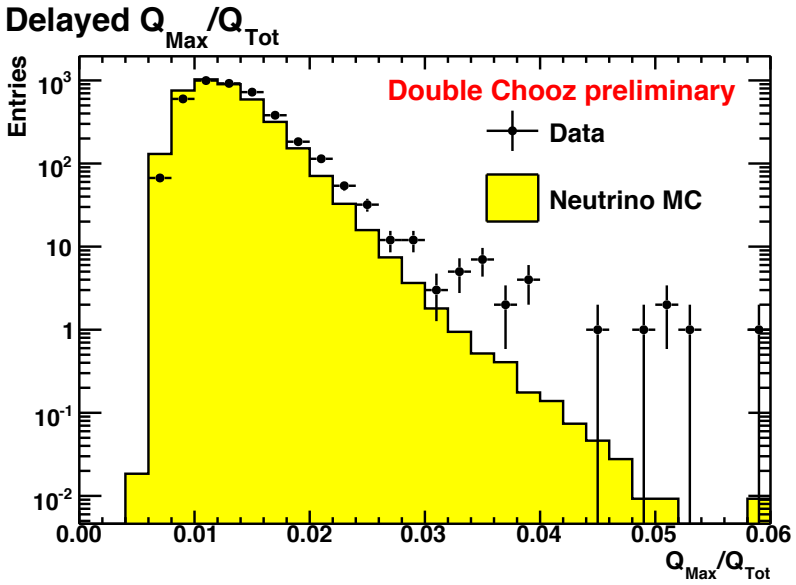

Figure 6.27: Histogram of the delayed event Q_{max}/Q_{tot} distribution. The black points are the IBD candidates extracted from the data including signal and background. The yellow histogram is the neutrino-only MC.

capture on H instead of Gd. The delayed energy cut is completely inefficiency at selecting IBD events in which the neutron captures on H. Therefore, delayed event cut efficiency depends directly on the fraction of neutrons which capture on Gd.

^{252}Cf calibration source data for 7 Z-axis positions near the center of the detector were used to compute the Gd capture fraction. Delayed coincidences were defined as a prompt event with $0.7 < E < 30$ MeV followed by a delayed event with $0.7 < E < 25$ MeV within 1 ms. The delayed event energy spectrum for data at all 7 positions is shown in Fig. 6.31. The H, Gd, Gd+H, and Gd+Gd peaks are fit to gaussians and the Gd capture fraction is obtained from their relative strengths. Fig. 6.32 shows the same spectrum for the MC, which looks similar to the data except that the exponential background is no longer present under the H peak. The measured Gd capture fractions thus obtained are [94]:

- $\frac{Gd}{(H+Gd)} : 0.880 \pm 0.005$ (^{252}Cf MC)
- $\frac{Gd}{(H+Gd)} : 0.860 \pm 0.005$ (^{252}Cf Data)

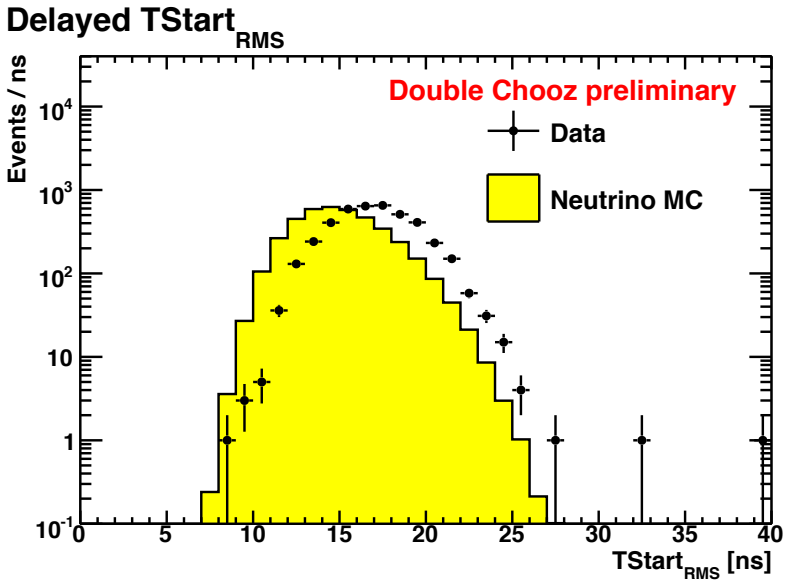

Figure 6.28: Histogram of the delayed event T_{start}^{RMS} distribution. The black points are the IBD candidates extracted from the data including signal and background. The yellow histogram is the neutrino-only MC.

Therefore, the MC is corrected by a factor of 0.98 ($1 \pm 0.58\%$).

6.6.5.3 Delayed Energy Cut Efficiency

In the IBD delayed energy spectrum, a low-energy tail is visible in addition to the full absorption peak of neutron capture on Gd. Events in the low-energy tail occur when a Gd capture γ escapes the scintillating volumes before depositing its full energy. These events result in a delayed energy cut inefficiency for IBD events which produce neutrons that capture on Gd. This inefficiency can be measured as a function of Z position using ^{252}Cf source calibration data.

^{252}Cf neutron events are selected by looking for the delayed coincidence of a prompt event ($7 < E < 30$ MeV) and a subsequent neutron capture on Gd ($4 < E < 12$ MeV). The delayed energy cut efficiency is defined as the ratio of the number of neutron capture events with $6 < E < 12$ MeV to the number of neutron capture events with $4 < E < 12$ MeV. Fig. 6.33 shows the delayed energy cut efficiency as a function of Z-axis position for data

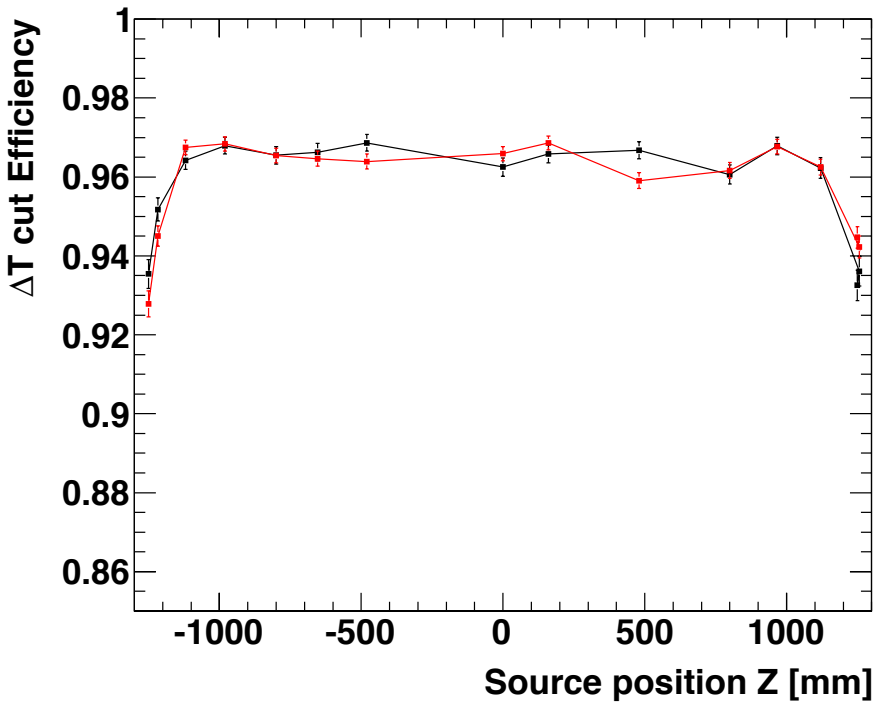

Figure 6.29: Plot of the ΔT cut efficiency for ^{252}Cf source calibration data and MC as a function of Z position [94].

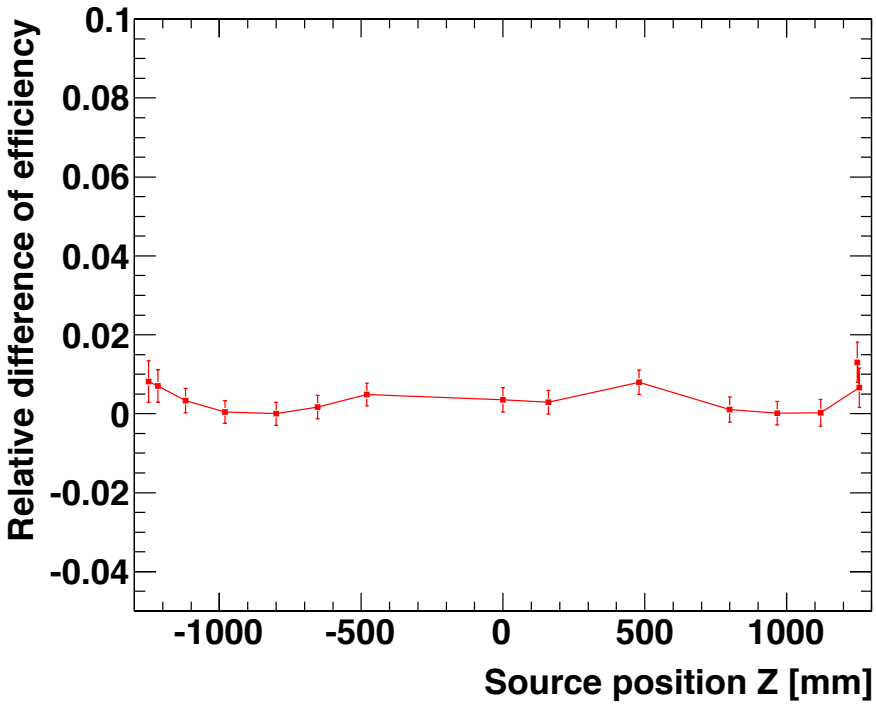

Figure 6.30: Plot of relative difference in the ΔT cut efficiency for ^{252}Cf source calibration data and MC as a function of Z position [94].

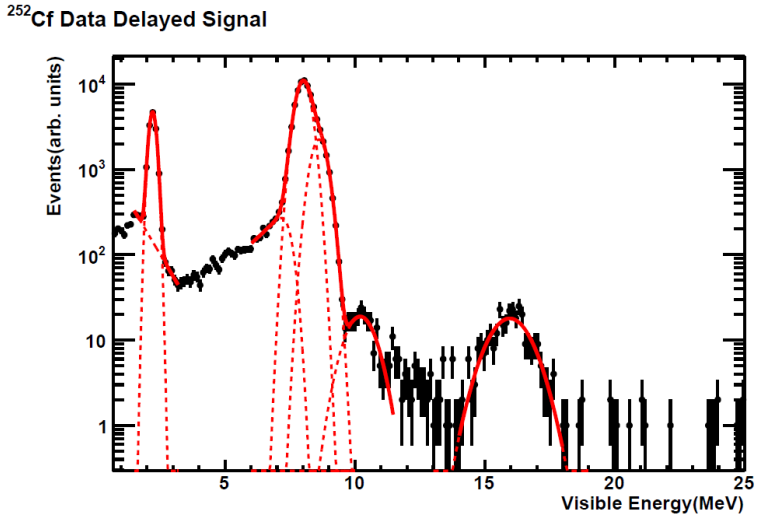

Figure 6.31: Plot of the delayed energy spectrum for neutron candidates from ^{252}Cf source data and the combined fit to the H, Gd, Gd+H, and Gd+Gd peaks as described in the text [94].

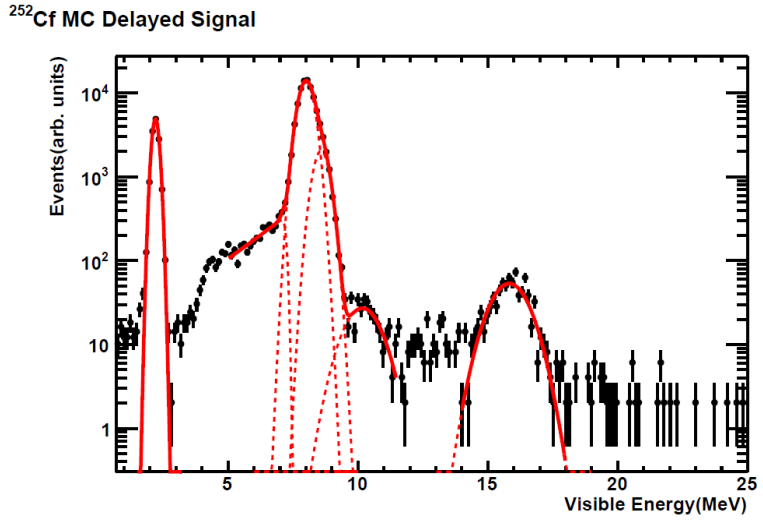

Figure 6.32: Plot of the delayed energy spectrum for neutron candidates from the ^{252}Cf MC and the combined fit to the H, Gd, Gd+H, and Gd+Gd peaks as described in the text [94].

and MC. A weighted average of the measured difference between data and MC as a function of the distance to target volume boundary was performed over the target volume. From this the uncertainty in the delayed energy cut was determined to be 0.6% [94].

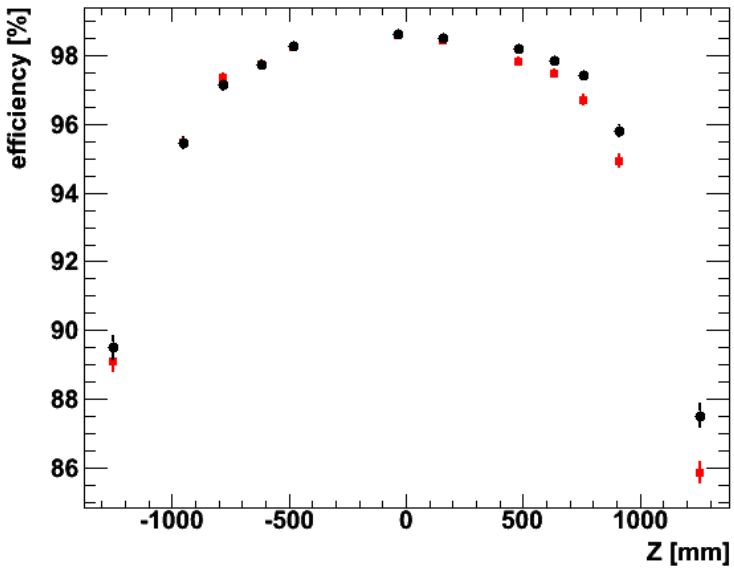

Figure 6.33: Plot of the the delayed energy cut efficiency for ^{252}Cf calibration source data and MC as a function of Z position [94].

6.6.6 Summary of IBD selection efficiencies

A summary of the IBD selection efficiencies is given in Tab. 6.1. In addition, the normalization uncertainties associated with the target proton measurement described in Sec. 3.3, the trigger threshold described in Sec. 3.4.2.1, and the spill-in/spill-out correction described in Sec. 5.2 are also included in the table to give a overall MC correction factor and normalization uncertainty.

Uncertainty	Central Value	Uncertainty
Muon Veto Cut	0.9547	Negligible
Mult. and Isolation	0.995	Negligible
ΔT cut	1.0	0.5%
Gd/H Ratio	0.98	0.58%
Delayed Energy Cut	1.0	0.6%
N_p Measurement	1.0	0.3%
Trigger Threshold	1.0	0.4%
Spill-in/out	0.9929	0.37%
Total	**0.9243**	**1.1%**

Table 6.1: Sources of uncertainty, their correction factor to be applied to the MC and the associated systematic uncertainty.

Chapter 7

Background Estimation

We consider 4 types of backgrounds in the IBD event selection: accidentals, cosmogenic ^{9}Li and ^{8}He, fast neutrons, and stopping muons. The expected rates of each background are determined from the data. Additionally, it is possible to extract the expected prompt energy spectra for the accidental, fast neutron, and stopping muon backgrounds from the data itself. For the ^{9}Li background, however, this is not possible given our limited statistics, and so a Monte Carlo simulation is used to estimate the prompt energy spectrum in this case.

An unambiguous measurement of the total background rate was made from ~ 22 hours of data-taking statistics that occurred during a period in which both Chooz reactors were off. The measured number and properties of the IBD candidate events found in an extended prompt energy range from $12 - 30$ MeV provide a key validation of our background rate estimates.

7.1 Accidental Background

Uncorrelated singles events can sometimes produce a delayed coincidence that mimics the IBD signal. For example, low-energy gamma radiation from impurities in detector materials such as the acrylic vessels or the PMT glass can produce signals in the γ-catcher satisfying the IBD search prompt event selection cuts. Likewise, muon-induced spallation neutrons produced in the rock surrounding the detector can propagate to the target region and be

captured on Gadolinium. If these two independent events occur within $2 - 100$ μs of one another, they are indistinguishable from an IBD event. These accidental backgrounds can be very accurately measured from the data itself.

7.1.1 Off-time Window Method

The accidental background rate and spectrum is measured directly from the data using the off-time window method. In this method, delayed coincidences are formed using the same cuts as the IBD search except that a different time window is used. For example, a time window of $1,002 - 1,100$ μs between the prompt and delayed events might be used to form delayed coincidence pairs. This time window is the same size as the original window, but it is shifted by $T_{shift} = 1$ ms and will not count any real IBD events.

7.1.2 Applying The Isolation Cut

There is a subtle issue involved in applying the IBD search isolation cut to the off-time window method. The IBD search isolation cut eliminates delayed coincidence pairs for which an extra (third) trigger satisfying $E_{ID} \geq 0.5$ MeV and $Q_{IV} \leq 10,000$ DUQ occurs within 100 μs before the prompt event or within 400 μs after the prompt event (see Ch. 6). In the off-time window method, the prompt event and the delayed event are separated by $T_{shift} \geq 1$ ms. In this case, two separate isolation windows must be applied—one to the event satisfying the IBD search prompt event selection and one to the event satisfying the IBD search delayed event selection. Fig. 7.1 gives an illustration of the method.

A correction must be applied to account for the fact that one isolation window is used in the IBD search whereas twos separate isolation windows are used for the off-time window accidental background measurement. In the first case the probability that a delayed coincidence pair is rejected due to an uncorrelated trigger satisfying $E_{ID} \geq 0.5$ MeV and $Q_{IV} \leq 10,000$ DUQ occurring within 100 μs before the prompt event or within 400 μs after the prompt event is $1 - \exp\left[-RT_{iso}\right] = 0.5\%$, where $T_{iso} = 500$ μs and R is the rate of triggers satisfying $E_{ID} \geq 0.5$ MeV and $Q_{IV} \leq 10,000$ DUQ. In the second case the probability that an off-time window delayed coincidence pair is rejected is $1 - \exp\left[-2RT_{iso}\right] = 1\%$. Therefore, the accidental background measurement obtained using the off-time window method

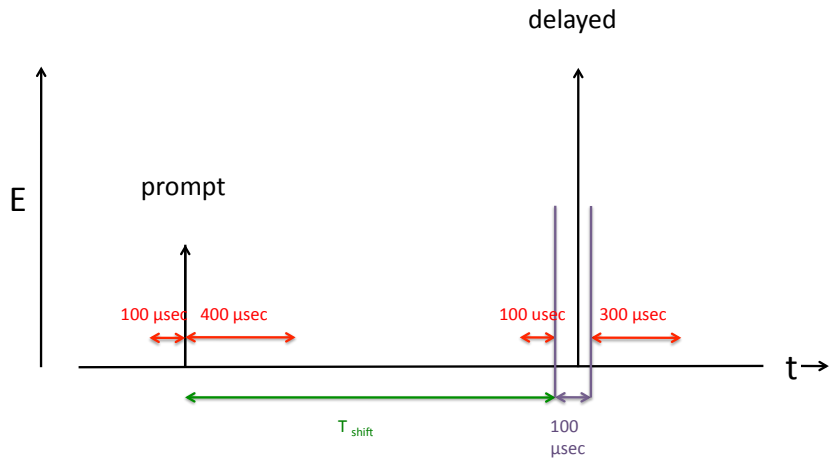

Figure 7.1: Cartoon of the off-time window method.

must be multiplied by $\frac{\exp[-RT_{iso}]}{\exp[-2RT_{iso}]} = 100.5\%$ to correct for this effect.

7.1.3 Combining Off-time Windows

The statistical uncertainty for the accidental background measurement can be reduced by combining many off-time windows since the choice of T_{shift} is somewhat arbitrary. As long as T_{shift} is much larger than the time scale associated with correlated delayed coincidence pairs, any T_{shift} may be used. Every choice of $T_{shift} \geq 1$ ms will give a valid accidental background measurement. Therefore, the statistical error on the accidental background measurement can be reduced by averaging the results obtained by choosing many different values of T_{shift}, each representing distinct, non-overlapping off-time windows.

The background due to accidental coincidences was evaluated using 198 off-time windows (from $1.002 - 1.1$ ms, $1.502 - 1.6$ ms, $2.002 - 2.1$ ms, etc) for which the isolation cut (as defined in Ch. 6) was applied to both the prompt and delayed event. A total of $6,339$ accidental coincidences were found. This corresponds to an accidental background rate of 0.33 d^{-1}. Fig. 7.2 shows the prompt event energy spectrum for these candidates scaled down by a factor of 198.

7.1.4 Systematic Uncertainty

The number of accidental coincidences should not depend on the the time between the prompt and delayed event. However, long-lived β-emitters produced in muon spallation processes such as ^{12}B may contaminate our accidental background sample. This can happen if an unvetoed muon produces ^{12}B in the ID without depositing a significant amount of energy in the target or γ-catcher and fakes a prompt IBD event. The lifetime ($\tau = 29.14 \pm 0.03$ ms) and endpoint energy ($Q = 13.4$ MeV) of ^{12}B [95] are such that the β-decay electron may be emitted in one of the 198 off-time windows $1 - 100$ ms after the prompt event and satisfy the IBD delayed event selection criteria. If this is the case, the distribution of these radioactive decays in time will be peaked towards smaller values of T_{shift}.

We assign a systematic error on the accidental background rate to account for a possible contamination of radioactive isotopes such as ^{12}B in our sample of off-time window coincidences. We group our sample of off-time window coincidences in 11 bins, each consisting of

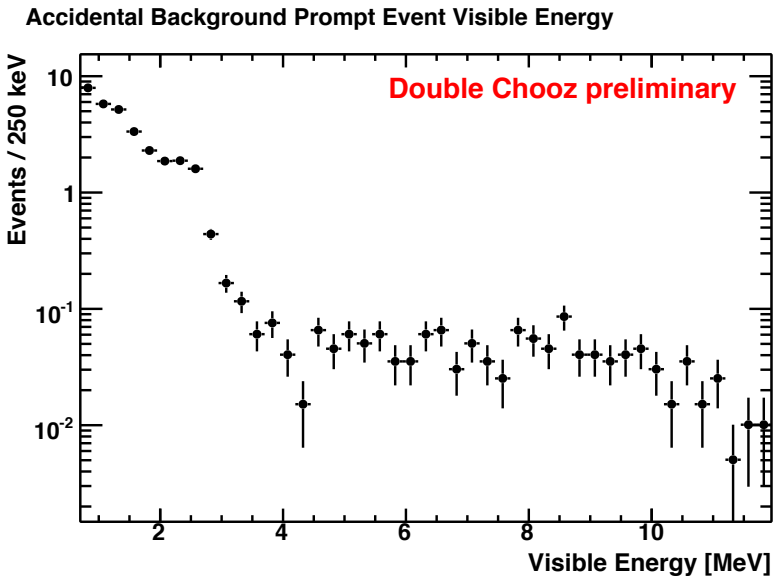

Figure 7.2: Prompt energy spectrum for the accidental background obtained from the off-time window method as described in the text.

18 adjacent off-time windows, and plot them as a function of the time between the prompt and the delayed event. The horizontal line fit shown in Fig. 7.3 gives an estimate for the accidental background if there is no contamination from correlated events in the off-time window sample. The difference between the rate given by this fit and the rate given by the linear fit shown in Fig. 7.4 gives an estimate of the systematic uncertainty in the accidental background rate due to contamination from correlated backgrounds. Based on the 1σ upper limit on the rate obtained by the linear fit, a conservative error of 8.5% is used, corresponding to an accidental background rate of 0.33 ± 0.03 d^{-1}.

7.1.5 Energy Spectrum

Due to a possible contamination of radioactive isotopes such as ^{12}B in our off-time window sample, we use the singles spectrum between $0.7 - 12$ MeV to model the prompt energy spectrum of the accidental background instead of the prompt energy spectrum obtained from the off-time window method. The singles spectrum is obtained by looking for single events which satisfy the prompt event selection criteria after applying the same muon veto,

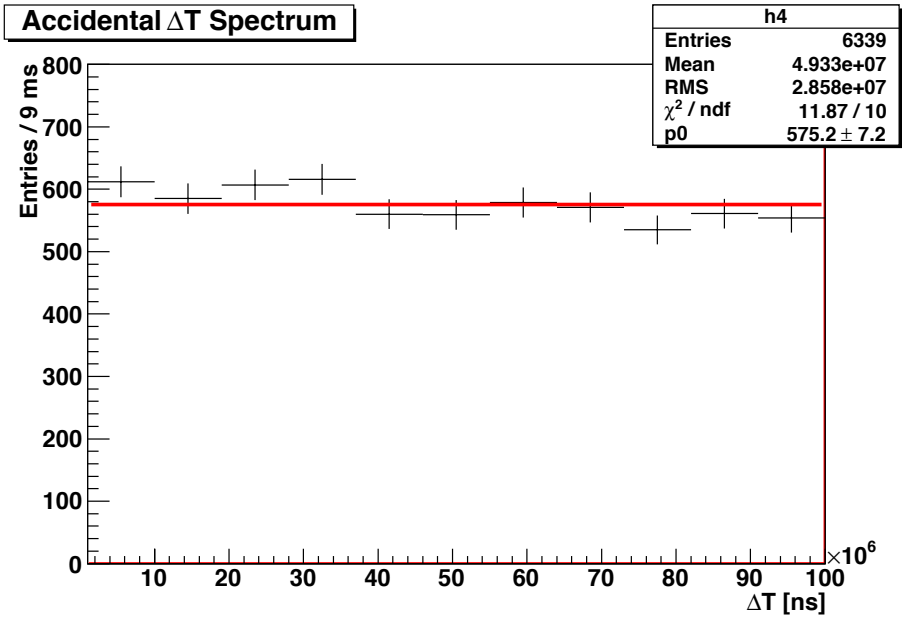

Figure 7.3: ΔT distribution for accidental background events found using the off-time window method. The best fit flat distribution is given by the red line.

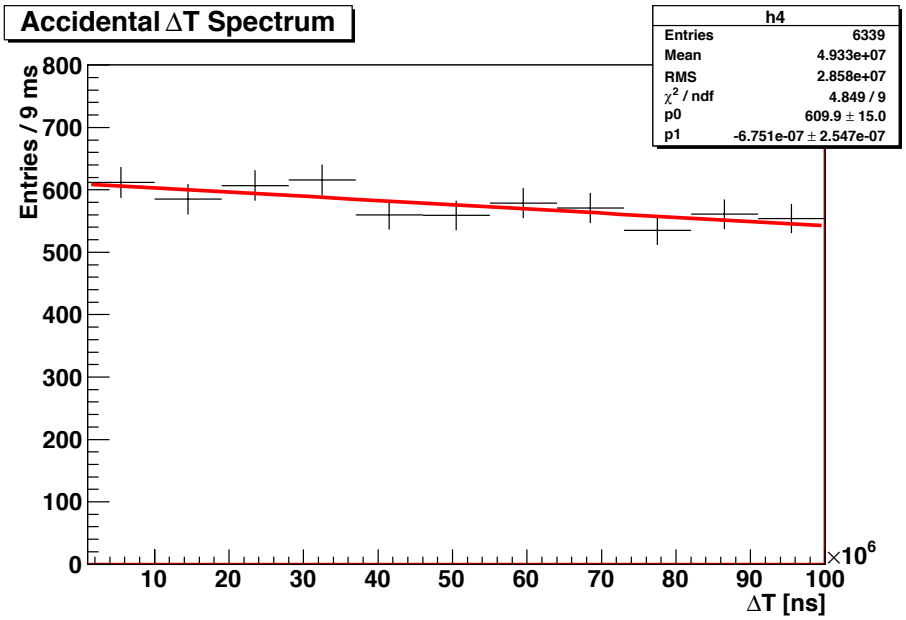

Figure 7.4: ΔT distribution for accidental background events found using the off-time window method. The best fit linear distribution is given by the red line.

light noise rejection cuts, and isolation cuts that are applied to the prompt event in the off-time window method given above. The correlated background contamination in this sample of events is negligible. Fig. 7.5 shows the good agreement between the singles spectrum and the prompt energy spectrum measured using the off-time window method.

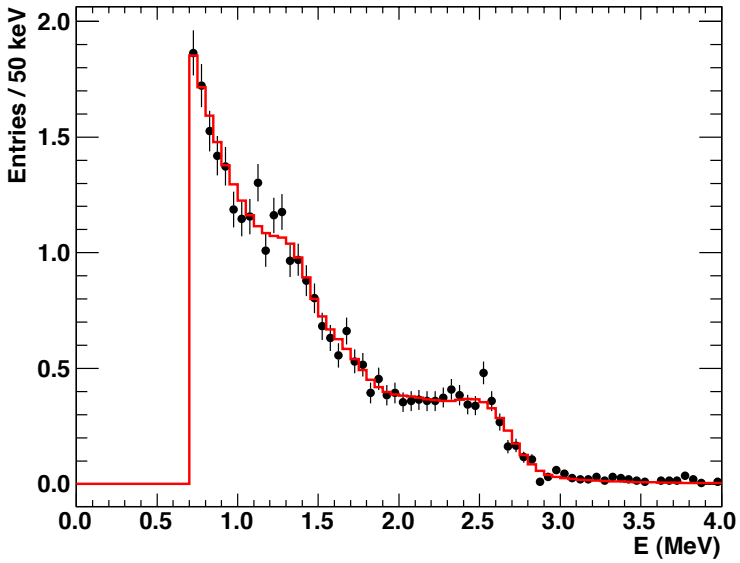

Figure 7.5: Prompt energy spectrum for accidental background events. The red histogram is the spectrum obtained from singles events. The black points are the prompt energy spectrum obtained from the off-time window method. The shoulders at $\sim$ 1.4 MeV and $\sim$ 2.6 MeV are due to the decay of ^{40}K and ^{208}Tl, respectively.

7.2 Lithium-9 Background

High energy cosmic ray muons produced in the atmosphere can propagate through the mountain above the DC far detector hall and interact in the detector or its surroundings. The inelastic scattering of high energy muons off of atomic nuclei can cause nuclear breakup and initiate showers of secondary particles and excited nuclei. This is called muon spallation.

Muon spallation processes can produce long-lived, radioactive isotopes in our detector which mimic our IBD signal. In particular, ^{9}Li (Q= 13.6 MeV) and ^{8}He (Q= 10.7 MeV)

are β-n emitters with lifetimes of 257 ms and 172 ms, respectively. ^{9}Li β-decays to neutron-unstable excited states of ^{9}Be with a branching ratio of $(50.8 \pm 0.9)\%$, and ^{8}He β-decays to neutron-unstable excited states of ^{8}Li with a branching ratio of $(16 \pm 1)\%$. Due to their long lifetimes, they are difficult to veto. Therefore, our strategy is to measure and subtract these backgrounds[1].

7.2.1 Rate estimation

Limits on the ^{9}Li background contamination in the IBD candidate sample are obtained from fits to the ΔT_μ distribution of muons preceding IBD candidate events, where ΔT_μ is the time difference between the muon and the prompt event of the IBD delayed coincidence pair. The ΔT_μ distribution for IBD signal events is a flat distribution, since IBD signal events are uncorrelated to preceding muons. The ΔT_μ distribution for ^{9}Li background events, on the other hand, consists of an exponential term plus a constant term. The exponential term describes the time-correlation between the β-n cascade of the ^{9}Li and the cosmic muon which produced it. The constant term describes the ΔT_μ distribution for uncorrelated muons preceding the ^{9}Li background event.

To obtain an upper limit on $N_{^9\mathrm{Li}}$, the number of ^{9}Li background events in our IBD candidate sample, we fit the ΔT_μ distribution for muons[2] preceding IBD candidate events with an exponential term fixed at the ^{9}Li lifetime ($\tau = 257$ ms) plus a constant term:

$$f(\Delta T_\mu) = \frac{N_{^9\mathrm{Li}}}{\tau} e^{-\Delta T_\mu/\tau} + C. \tag{7.1}$$

Fig. 7.6 shows the ΔT_μ distribution with the best fit to the data. The 1 σ upper limit on $N_{^9\mathrm{Li}}$ is obtained from $\Delta\chi^2$ curve also given in Fig. 7.6 and corresponds to an upper limit on the ^{9}Li background rate of 3.5 d^{-1}.

[1]Recent measurements [34] indicate that ^{9}Li is produced about ~ 3 times more often than ^{8}He. Since the β-n branching ratio for 9Li is also ~ 3 times greater than for ^{8}He [96], we neglect ^{8}He in the IBD event selection, which should contribute a background rate that is less than $\sim 20\%$ of the uncertainty on the 9Li background rate.

[2]Here muons are defined by $Q^{IV} > 40,000$ DUQ or $E > 70$ MeV

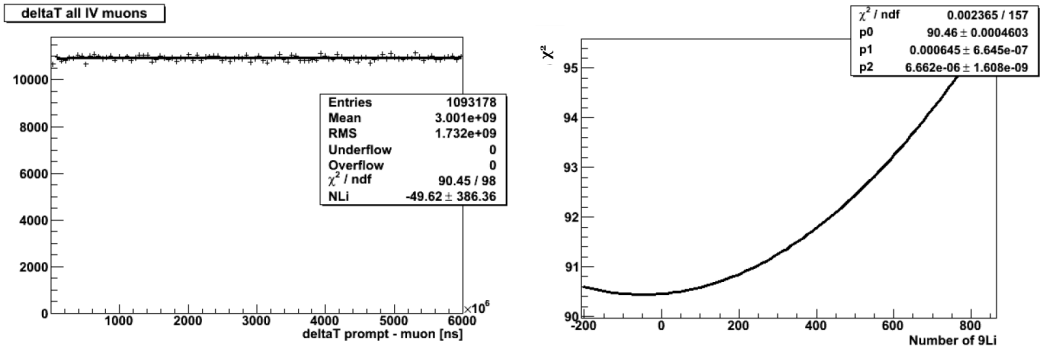

(a) ΔT_μ distribution

(b) χ^2 curve

Figure 7.6: The left panel shows the ΔT_μ distribution for muons preceding IBD candidates fit by Eq. 7.1. The right panel shows the corresponding χ^2 curve from which the upper limit on $N_{^9\mathrm{Li}}$ is extracted. The best fit value of $N_{^9\mathrm{Li}}$ is negative [97].

High energy, showering muons are more likely to produce ^{9}Li than low energy, minimum-ionizing muons. Therefore, the lower limit on $N_{^9\mathrm{Li}}$ can be obtained by fitting the ΔT_μ distribution as above, but restricted to only those muons which deposit more than 600 MeV in the inner detector and are more likely to be showering muons. Fig. 7.7 shows the restricted ΔT_μ distribution fit with the same function given in Eq. 7.1. The exponential corresponding to time-correlations for ^{9}Li background events is clearly visible in this restricted ΔT_μ distribution. The 1σ lower limit on $N_{^9\mathrm{Li}}$, the number of ^{9}Li events in the IBD candidate sample, obtained from the fit is 116 events. This corresponds to a lower limit on the ^{9}Li background rate of 1.2 d^{-1}.

From the upper and lower limits obtained from the fits to theΔT_μ distribution, the ^{9}Li background rate is estimated to be 2.3 ± 1.2 d^{-1}.

7.2.2 Shape estimation

It was not possible to extract a high-statistics, prompt energy spectrum for the ^{9}Li background from the fits described above. Therefore, the shape of the ^{9}Li background was estimated using Monte Carlo. A Monte Carlo generator was written for simulating ^{9}Li β-n decay according to recent nuclear data [96]. First, a β^- branch to an excited state of ^{9}Be

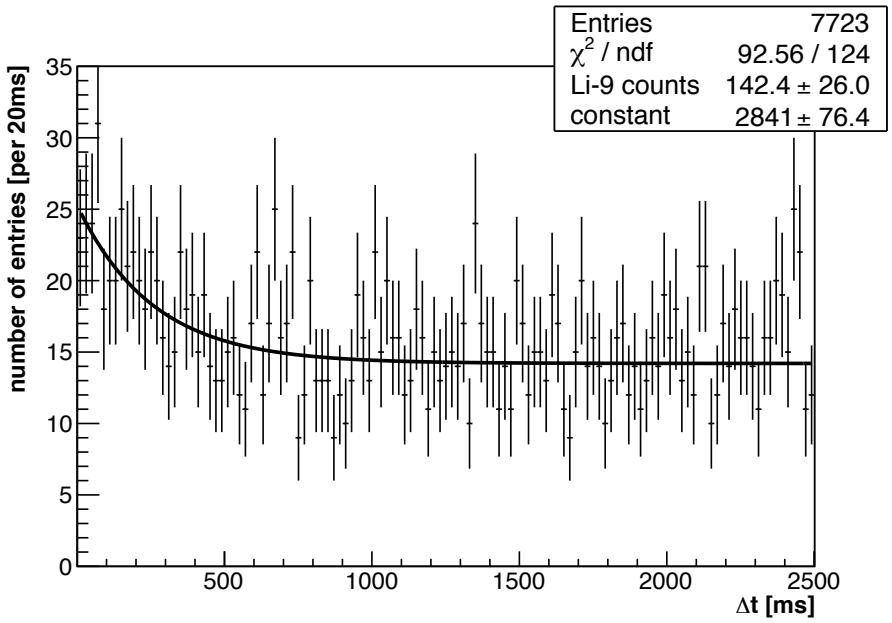

Figure 7.7: ΔT_μ distribution for muons with $E_{ID} > 600$ MeV preceding IBD candidates fit by Eq. 7.1. From this fit a 1σ lower limit on $N_{^9\mathrm{Li}}$ is obtained.

is randomly selected according to its measured branching ratio. Then, a β^- is injected in the detector Monte Carlo simulation with an energy which is randomly selected from the analytically computed β^- decay spectrum. Finally, the break-up of the excited ^{9}Be to $\alpha + \alpha + n$ proceeds either through ^{8}Be or through ^{5}He.

Fig. 7.8 shows the energy level diagram for ^{9}Be along with the decay branches of ^{9}Li. If the excited ^{9}Be breaks up via ^{5}He then most of the energy in the decay is transmitted to α's. If, however, the ^{9}Be breaks up via ^{8}Be, then most of the energy in the decay is transmitted to the neutron. Because α's are highly ionizing, quenching effects are larger for α's than for neutrons. Therefore, the amount of scintillation light produced depends strongly on the ^{9}Be break up channel. Based on a survey of existing data [98–100], we find that decays through ^{5}He are preferred though there are large uncertainties in the branching ratios [101].

The spectrum shown in Fig. 7.9 that is used for the ^{9}Li MC background prediction is generated [101] by simulating the break up of the 2.43 MeV and 2.78 MeV states of ^{9}Be

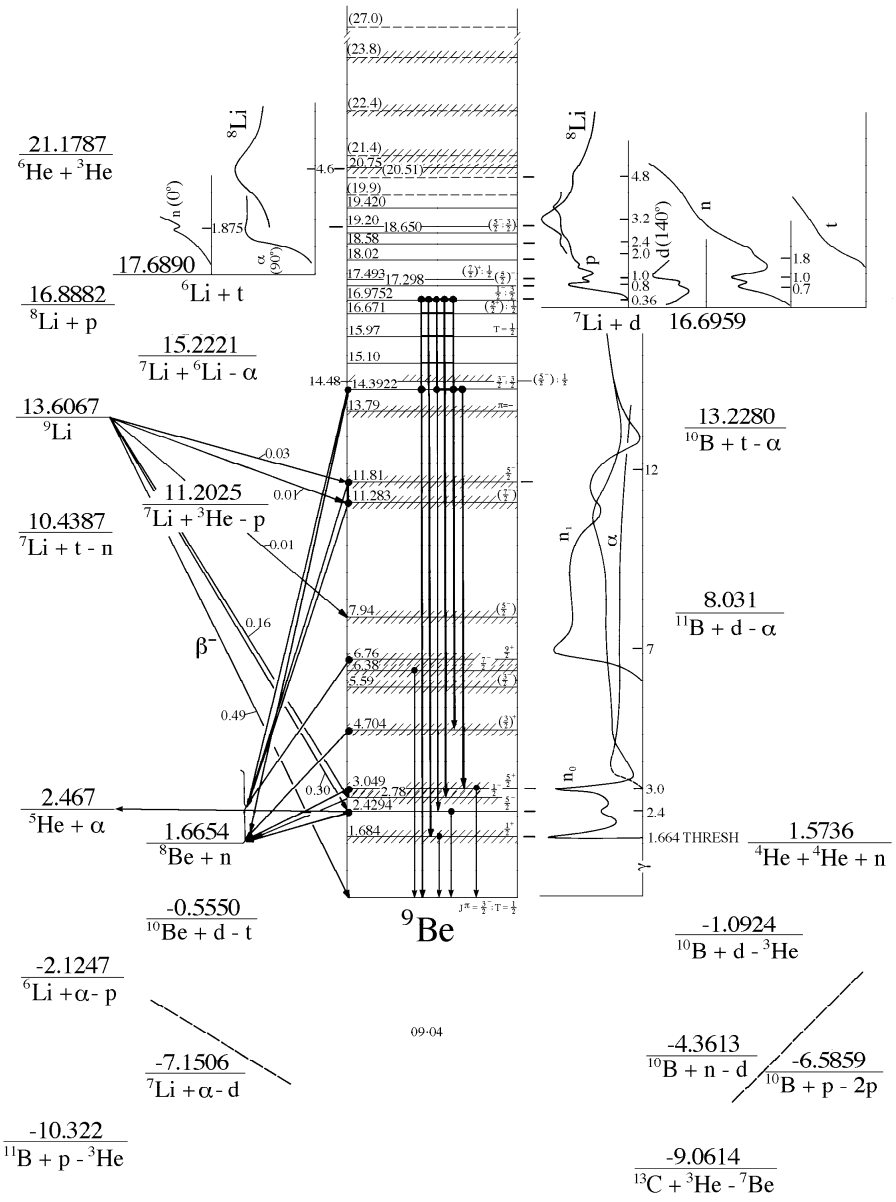

Figure 7.8: The energy level diagram for ^{9}Be showing the ^{9}Li β-decay branches and the nuclear breakup channels for excited states of ^{9}Be through ^{8}Be and ^{5}He [96].

going through the ^{8}Be ground state and the 7.94 MeV, 11.28 MeV, and 11.81 MeV states of ^{9}Be going through the ^{5}He(1/2) state. The shape uncertainty shown in Fig. 7.10 comes from instead simulating the break up of the 7.94 MeV, 11.28 MeV, and 11.81 MeV states of ^{9}Be also through the ^{8}Be ground state. This creates the maximum possible neutron energy and therefore the largest change in the spectrum.

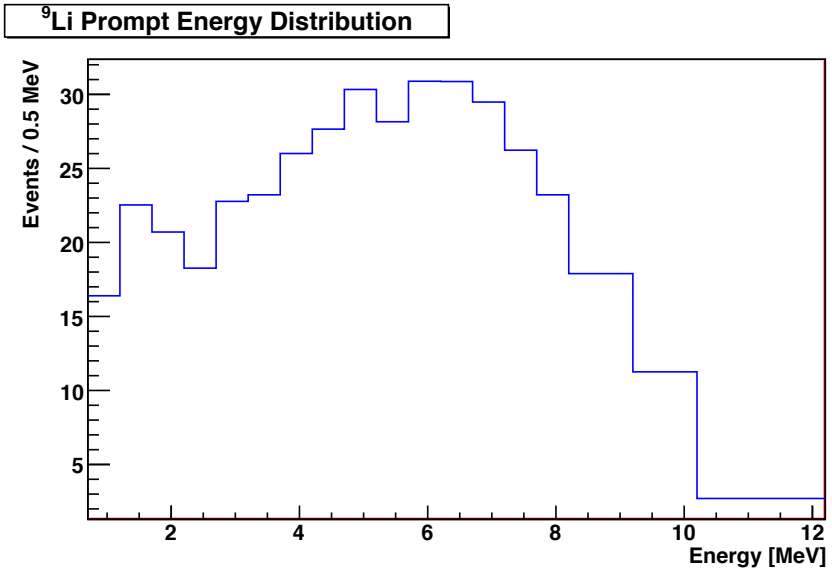

Figure 7.9: The prompt energy spectrum for ^{9}Li candidates used for the MC central value prediction.

7.3 Fast Neutron and Stopping Muon Background

Near-miss cosmic muons interacting in the rock and steel shielding surrounding the detector can produce fast neutrons which penetrate the inner detector. If these fast neutrons scatter off a proton and subsequently capture on Gd in the target region, then they can fake an IBD event if the recoiling proton has a reconstructed energy between $0.7 - 12$ MeV.

Furthermore, the inner veto does not give full 4π coverage of the inner detector around the chimney region. Therefore, a vertical muon entering the detector through the chimney may not be vetoed. If the muon does not penetrate too far into the ID before stopping, it may have a reconstructed visible energy between $0.7 - 12$ MeV. If the muon then decays

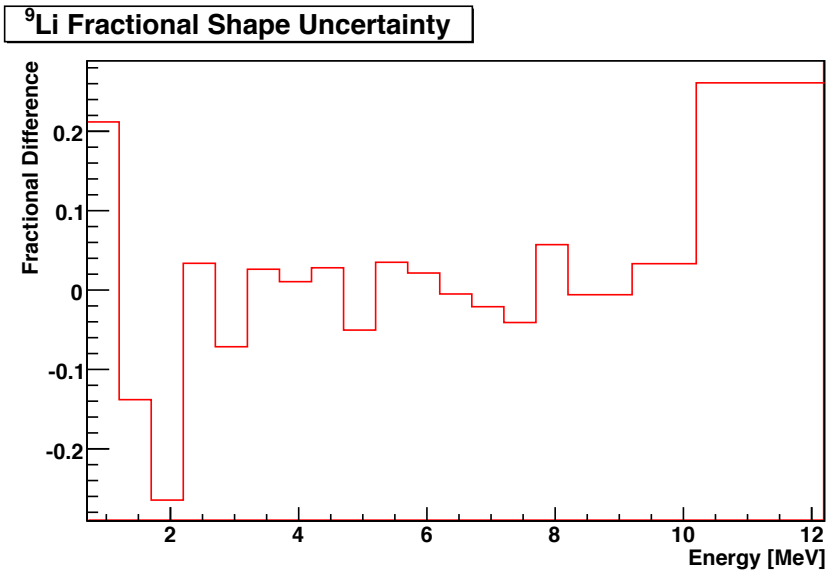

Figure 7.10: The bin-by-bin fractional differences between the ^{9}Li MC central value prediction and an alternate ^{9}Li MC prediction. These fractional differences represent the uncertainty in the ^{9}Li shape and are used to construct a ^{9}Li shape covariance matrix as described in Sec. 8.2.5.

after > 2 μs and emits an electron with an energy in the range $6 - 12$ MeV, then the delayed coincidence of the muon and its Michel electron will fake an IBD event. Because of the geometric restrictions of the stopping muon background, most of these events are reconstructed towards the top of the γ-catcher and target along the central axis of the detector.

7.3.1 Fast Neutron MC and IV tagging

In order to understand the properties of the fast neutron background, a detailed MC simulation of muons propagating through the overburden of the Double Chooz far detector and creating fast neutrons was performed [102, 103]. The flux of fast neutrons penetrating the detector but which were not produced by muons traversing the inner veto was studied.

A key observation regarding this fast neutron background is that some fast neutrons entering the detector first scatter in the inner veto before creating a delayed coincidence in the inner detector. The MC simulation showed that the difference in inner veto and inner detector PMT hit times for fast neutrons which scatter in both sub-detectors is typically < 256 ns[3] [104]. Since both the inner veto and the inner detector are read out when either sub-detector is triggered (see Ch. 3), this opens the possibility to tag the prompt event of delayed coincidences initiated by fast neutrons by the amount of charge deposited or the number of hit PMTs in the inner veto.

The MC simulation also showed no correlation between the inner detector energy spectrum and the charge deposited (or the number of hit PMTs) in the inner veto. Therefore, tagging fast neutrons by the charge deposited in the inner veto does not bias the shape of the prompt energy spectrum in the inner detector. Two analyses were developed to measure the fast neutron and stopping muon backgrounds based on this inner veto tagging concept.

7.3.2 IVHit Analysis

The first analysis [105] looks at IBD candidates in an extended prompt energy range of $0.7 - 30$ MeV. Fig. 7.11 shows the prompt energy spectrum for these extended IBD candidates. The spectrum above 12 MeV is relatively flat and consists of 164 events. Since this prompt

[3] A 100 MeV neutron, for example, travels with a velocity greater than 40% the speed of light.

energy range is above the expected neutrino signal for correlated IBD events as well as the accidental and ^{9}Li backgrounds, it is expected that these events consist primarily of fast neutrons or stopping muons.

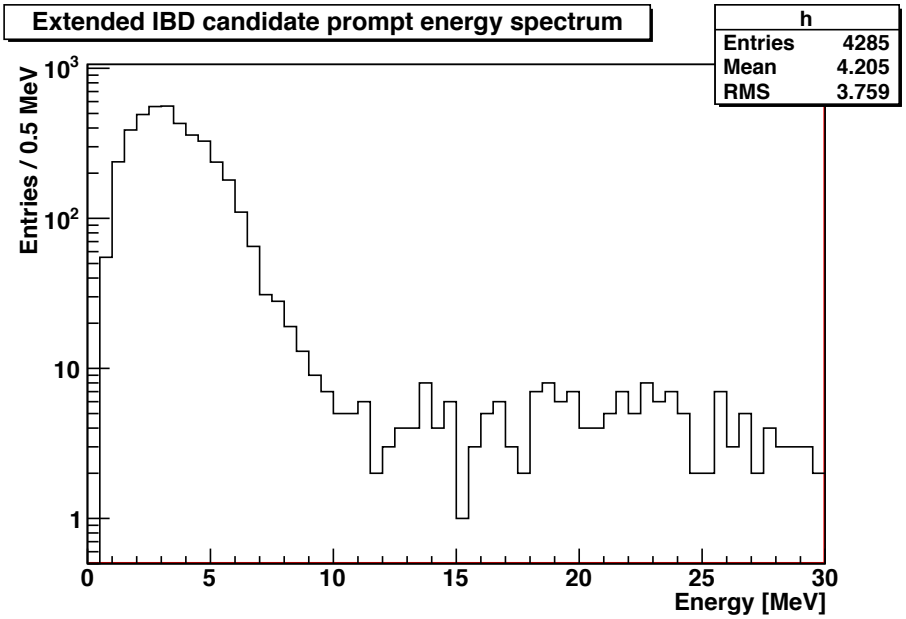

Figure 7.11: The prompt energy spectrum for IBD candidates with an extended prompt energy range up to 30 MeV.

A rough separation is made of the stopping muons and the fast neutrons based on the $\tau_\mu = 2.2$ μs muon lifetime and the geometrical restrictions for muons, which enter through the chimney and stop before producing a significant amount of scintillation light. Stopping muons are defined as events with $\Delta T < 6.6$ μs, $Z > 50$ cm, and $\rho < 40$ cm.

Based on this definition, 59 events are classified as stopping muons in the energy range between $12 - 30$ MeV.

The **IVHit** sample is defined as the set of extended IBD candidates given above whose prompt event has more than one hit PMT in the inner veto. This cut is designed to remove two unwanted classes of events from the fast neutron and stopping muon background sample:

- Neutrino interactions in random coincidence with inner veto activity
- Accidental backgrounds in which the prompt event interacts in both the inner veto

and inner detector

The prompt energy spectrum from $12-30$ MeV for the **IVHit** sample consists of 44 events and is also relatively flat. The ratio $44/164 = 0.268$ can therefore be interpreted as the efficiency with which fast neutrons and stopping muons are tagged by > 1 hit inner veto PMT requirement.

The **IVHit** sample is fit to an exponential plus a constant term in the range $0.7-30$ MeV to model the expected flat spectrum in addition to a possible contamination from the two unwanted classes of events mentioned above at low energies. Fig. 7.12 shows the best fit to the data.

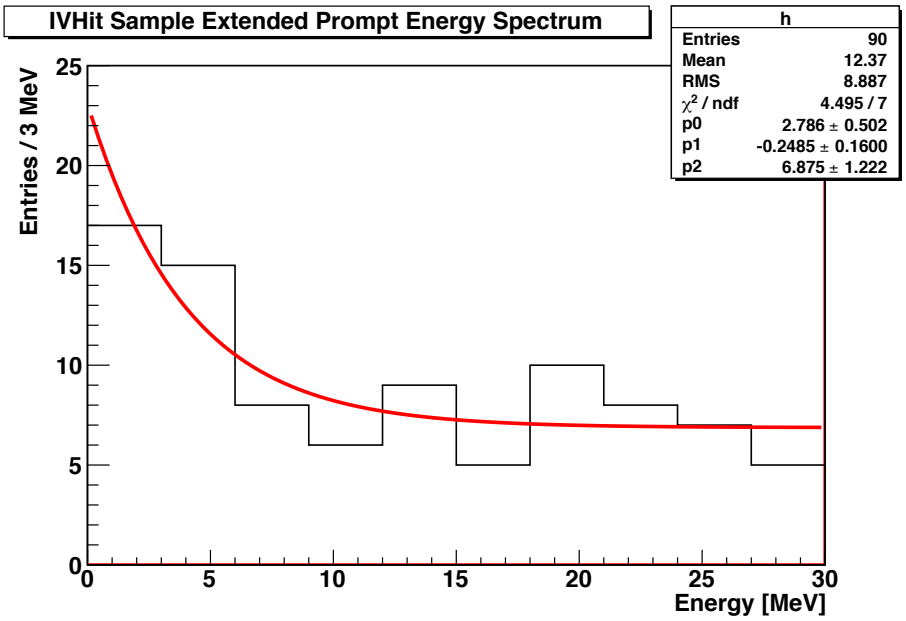

Figure 7.12: The prompt energy spectrum for IBD candidates with an extended prompt energy range up to 30 MeV whose prompt event has more than one hit inner veto PMT.

Integrating the constant term in the fit over the range $0.7-12$ MeV and scaling by the **IVHit** efficiency gives 98 expected fast neutron and stopping muon background events in the IBD candidate sample. We can estimate the relative contribution of the stopping muons based on the rough separation between fast neutrons and stopping muons given above. Scaling the 59 stopping muon events in the energy range $12-30$ MeV to the energy

range $0.7 - 12$ MeV gives 37 expected stopping muon events in the IBD candidate window, assuming a flat spectrum.

The determination of the number of stopping muon events in the IBD candidate window given above is very uncertain. As a conservative estimate for the combined fast neutron and stopping muon background rate, the central value is given as the fast neutron background rate plus one-half times the stopping muon background rate, with an uncertainty equal to 100% of the stopping muon background rate. Based on a live time of 96.8 days the combined background rate is therefore 0.82 ± 0.38 d^{-1}.

7.3.3 IVCharge Analysis

The second analysis [106] estimates the fast neutron background from a sample of events in which delayed coincidences are tagged by a charge deposition in the inner veto of $10^4 < Q^{IV} < 10^5$ DUQ ($\sim 5 < E^{IV} < 50$ MeV) for the prompt event. This **IVCharge** sample is obtained from a modified IBD selection in which the following criteria have been changed which respect to those given in Ch. 6:

- 1 ms muon veto after $Q^{IV} > 10^5$ DUQ (~ 50 MeV)
- $10 < \Delta T < 100$ μs (to reject stopping muons)
- $0.7 < E_{prompt} < 30$ MeV
- $10^4 < Q^{IV}_{prompt} < 10^5$ DUQ ($\sim 5 < E^{IV} < 50$ MeV)

Fig. 7.13 shows the resulting fast neutron prompt energy spectrum. The prompt spectrum is well-fit by a linear function.

Stopping muons, on the other hand, are selected based on a triangular fiducial volume cut and a ΔT cut based on the muon lifetime. The fiducial volume cut is determined by looking at a sample of IBD-like events with $\Delta T < 4$ μs in an extended $12 - 30$ MeV prompt energy range. Fig. 7.14 shows the fiducial cut, which is designed to select almost all of the events in this sample. As described in Sec. 7.3.2, only fast neutrons and stopping muons are expected to populate this energy range and the hard cut on ΔT preferentially selects stopping muons (which decay with a lifetime of $\tau_\mu = 2.2$ μs) relative to fast neutrons.

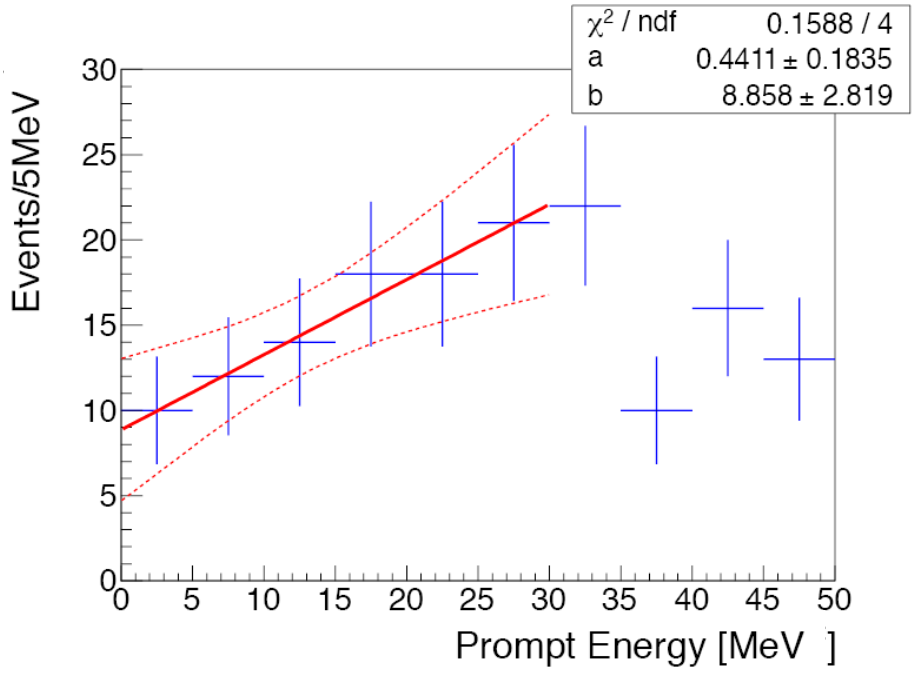

Figure 7.13: The prompt energy spectrum for fast neutrons with a linear fit below 30 MeV [106].

Therefore, stopping muons are defined as events with $0.5 < \Delta T < 5$ μs, $30 < Z < 179$ cm, and $Z > 1.23$ m$^{-1} \times (X^2 + Y^2) + 0.3$ m.

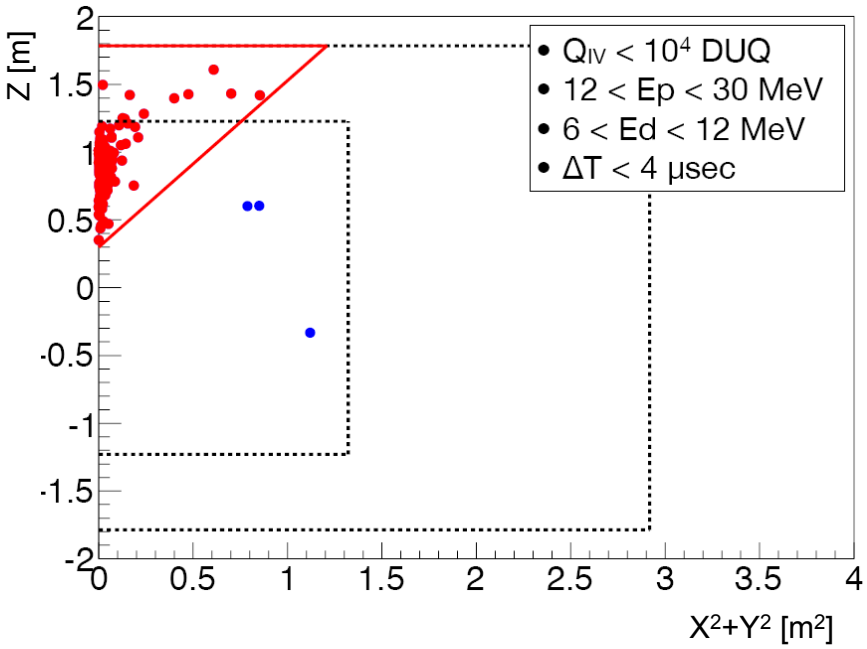

Figure 7.14: Vertex distribution for IBD candidates in the prompt energy range 12−30 MeV with $\Delta T < 4$ μs. The triangular fiducial volume is defined by $0.3 < Z < 1.79$ m, and $Z > 1.23$ m$^{-1} \times (X^2 + Y^2) + 0.3$ m [106].

The stopping muon prompt and delayed energy spectra are obtained after subtracting the (primarily neutrino) events in the off-time window with large $\Delta T > \tau_\mu$ from $5.5 < \Delta T < 10$ μs. Fig. 7.15 shows the stopping muon prompt energy spectrum fit to a Landau distribution and Fig. 7.16 shows the stopping muon delayed energy spectrum fit to a linear fit[4].

In order to determine the relative contributions of the stopping muon and fast neutron backgrounds for IBD candidate events with $0.7 < E_{prompt} < 12$ MeV, two fits are performed on IBD-like candidate events in the $12 < E_{prompt} < 30$ MeV prompt energy window. First,

[4]The fiducial volume cut distorts the expected Michel spectrum to give a negatively-sloped linear spectrum in the $6 - 12$ MeV range

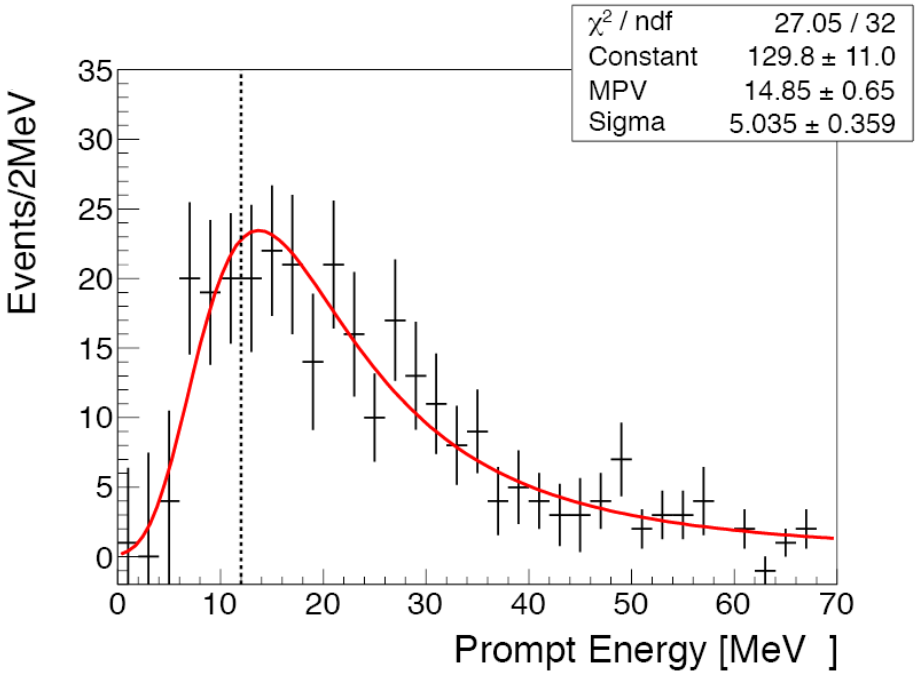

Figure 7.15: The prompt energy spectrum for stopping muons with a Landau fit from $0 - 70$ MeV [106]

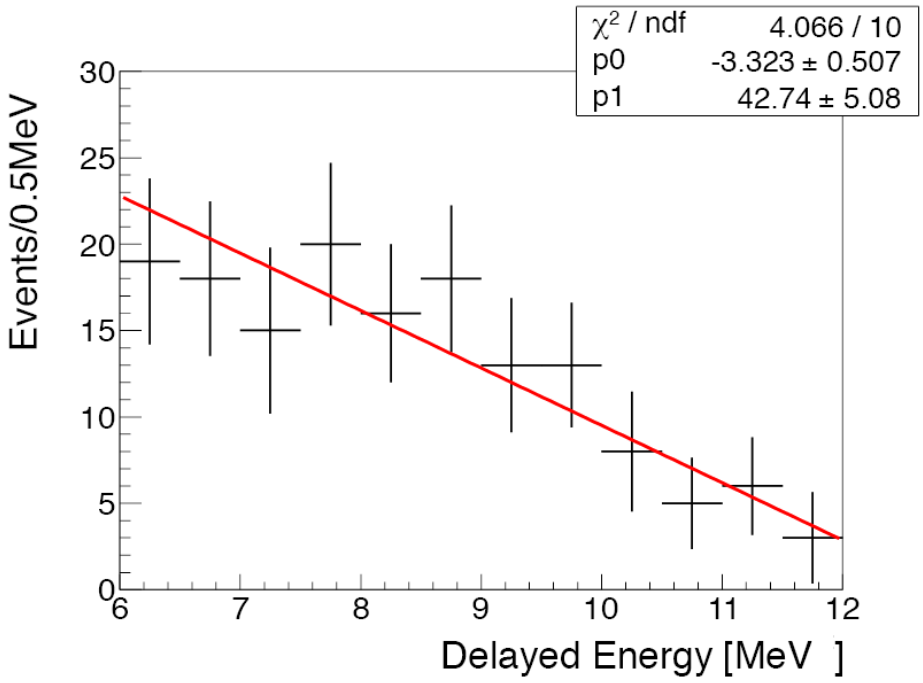

Figure 7.16: The delayed energy spectrum for Michel electron from stopping muons with a linear fit between $6-12$ MeV. Note that the fiducial volume cut distorts the expected Michel spectrum to give a negatively-sloped linear spectrum in the $6-12$ MeV range [106].

the ΔT distribution is fit to a sum of an exponential with a 2.2 μs time constant and a Landau distribution[5] whose parameters have been fixed to those which best fit the IBD ΔT distribution. Second, the reconstructed delayed energy spectrum is fit to the sum of linear term whose parameters have been fixed to those given by the fit shown in Fig. 7.16 and a Gd capture peak function whose parameters have been fixed to those given by fits to IBD delayed energy spectrum shown in Fig. 6.15. The two fits are shown in Fig. 7.17. Table 7.1 summarizes the ratios of stopping muons and fast neutrons obtained from the two fits.

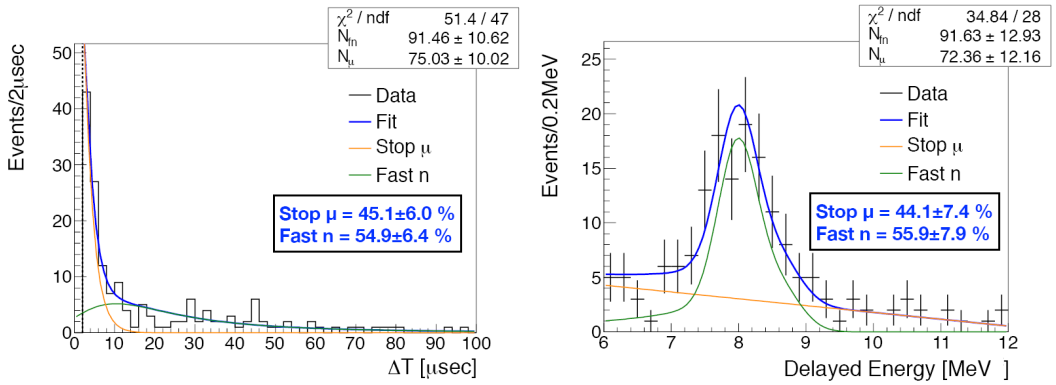

(a) ΔT Fit (b) Delayed Energy Fit

Figure 7.17: Combined fits to the ΔT and delayed energy distributions for the fast neutron and stopping muon backgrounds [106].

Method	Fast neutron fraction	Stopping muon fraction
Fit to ΔT spectrum	$54.9 \pm 6.4\%$	$45.1 \pm 6.0\%$
Fit to delayed energy spectrum	$55.9 \pm 7.9\%$	$44.1 \pm 7.4\%$

Table 7.1: Summary of the relative contribution of fast neutrons to stopping muons for various fits [106].

The two fits give consistent results. However, the relative contribution of fast neutrons to stopping muons obtained from the fit to the reconstructed delayed energy spectrum has larger uncertainties and fully covers the result obtained from the fit to the ΔT distribution.

[5]The choice of the Landau function here is purely phenomenological.

Therefore to be conservative, the relative contribution of the fast neutron and stopping muon background for IBD candidate events with $0.7 < E_{prompt} < 12$ MeV is determined from the fit to the reconstructed delayed energy spectrum.

The combined fast neutron and stopping muon spectrum prompt energy spectrum obtained by combining Fig. 7.13 and Fig. 7.15 according to the ratio obtained from the fit to the reconstructed delayed energy spectrum is given in Fig. 7.18. It is not flat, but increases linearly as a function of energy. Based on a linear fit, the total fast neutron and stopping muon background rate is found to be 0.75 ± 0.17 d^{-1}, which is consistent with the rate obtained in the **IVHit** analysis given in Sec. 7.3.2 above. As described in Sec. 8.2.5, the deviation of this spectrum from a flat distribution is included in the final fit as a shape covariance matrix.

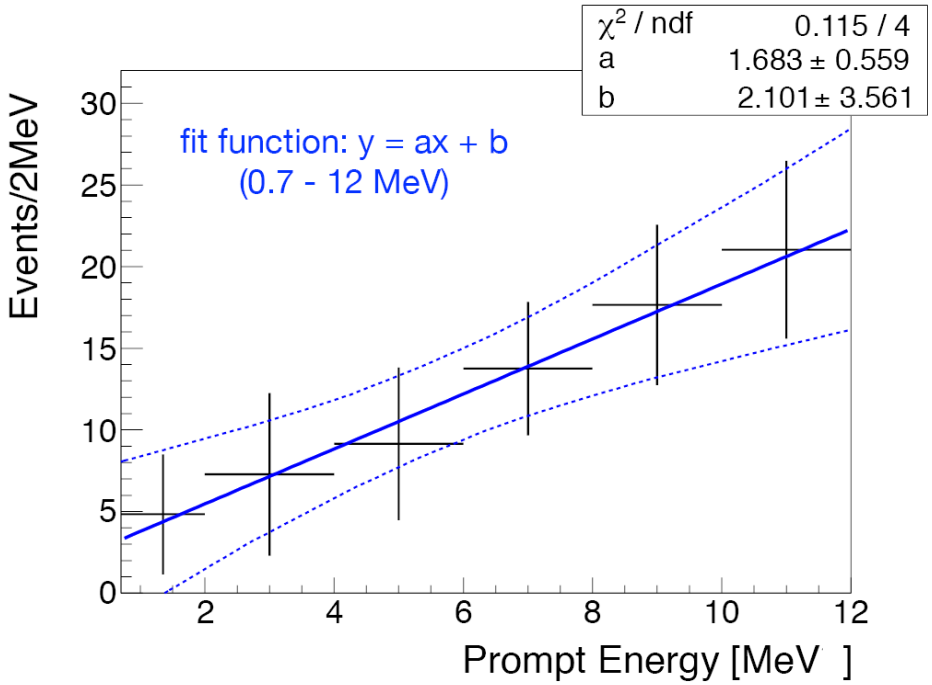

Figure 7.18: The prompt energy spectrum for the combined fast neutron and stopping muon background with a linear fit from $0 - 12$ MeV [106].

7.4 Summary

Table 7.2 summarizes the various background rate estimates described above.

Background	Rate (d^{-1})	Uncertainty (d^{-1})	Fractional Uncertainty
Accidental	0.33	0.03	9%
^{9}Li	2.3	1.2	52%
Fast-N/Stop μ	0.82	0.38	46%

Table 7.2: Summary of the background rate estimations. The systematic uncertainties of the ^{9}Li and fast neutron and stopping muon backgrounds are derived from multiple analyses.

7.5 Both Reactors Off

For a period of $\sim$ 24 hours on Oct. 22, 2011, both Chooz reactors were off. This allowed for a unique opportunity to verify the background rate estimates given above. During 22.3 hours of livetime, 2 IBD candidates were identified with prompt energy between $0.7 - 12$ MeV and 1 extended IBD candidate was identified with prompt energy between $12 - 30$ MeV. Table 7.3 summarizes the characteristics of each of these events.

Candidate	Prompt Energy (MeV)	ΔT (μs)	E_μ (MeV)	ΔT_μ (ms)
1	9.8	4.1	739	201
2	4.8	26	627	241
3	26.5	2.2	523	206

Table 7.3: Summary of the extended IBD candidate events found during 22.3 hours of data-taking with both Chooz reactors off.

The two IBD candidate events have prompt energies and prompt-delayed time differences consistent with ^{9}Li. The reconstructed positions of the 2 events are shown in Fig. 7.19 and Fig. 7.20. Both events occur within 257 ms of a high energy, showering muon and their reconstructed prompt and delayed positions lie near the reconstructed track of the showering muon.

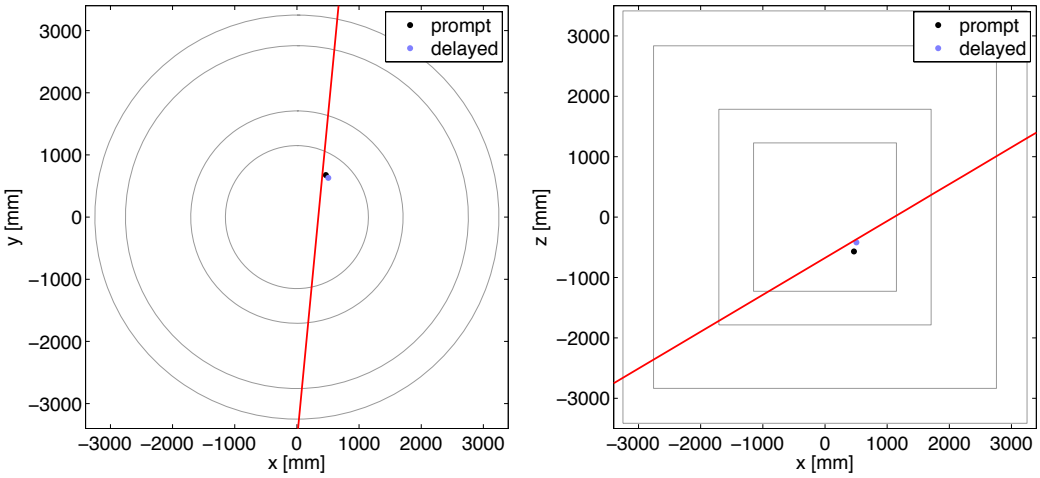

(a) XY Reconstructed Position (b) XZ Reconstructed Position

Figure 7.19: Reconstructed position for the prompt and delayed event along with the reconstructed muon track for the showering muon immediately preceding the first delayed coincidence pair found with both reactors off.

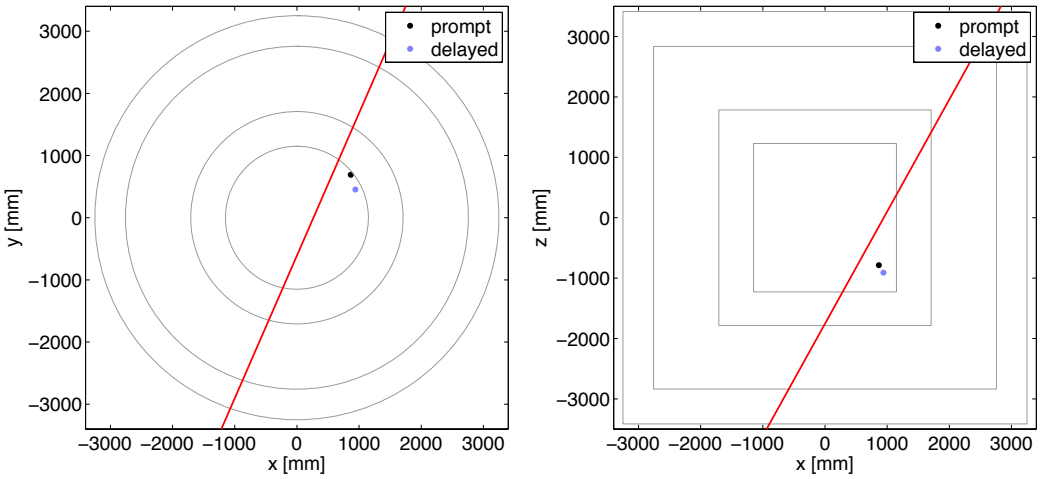

(a) XY Reconstructed Position (b) XZ Reconstructed Position

Figure 7.20: Reconstructed position for the prompt and delayed event along with the reconstructed muon track for the showering muon immediately preceding the second delayed coincidence pair found with both reactors off.

The one IBD candidate in the extended prompt energy window from $12-30$ MeV does not occur within 17 s of any high energy showering muon. The reconstructed track of the highest energy muon which occurs within 17 s of the extended IBD candidate is show in Fig. 7.21 along with the reconstructed positions of the prompt and delayed events. This muon has an energy of 523 MeV and reconstructs > 1 m away from the delayed coincidence pair. The fact that this event is reconstructed at the top of the target and γ-catcher along the Z-axis, has a prompt energy of 26.5 MeV, and a ΔT of 2.2 μs makes this a candidate stopping muon event.

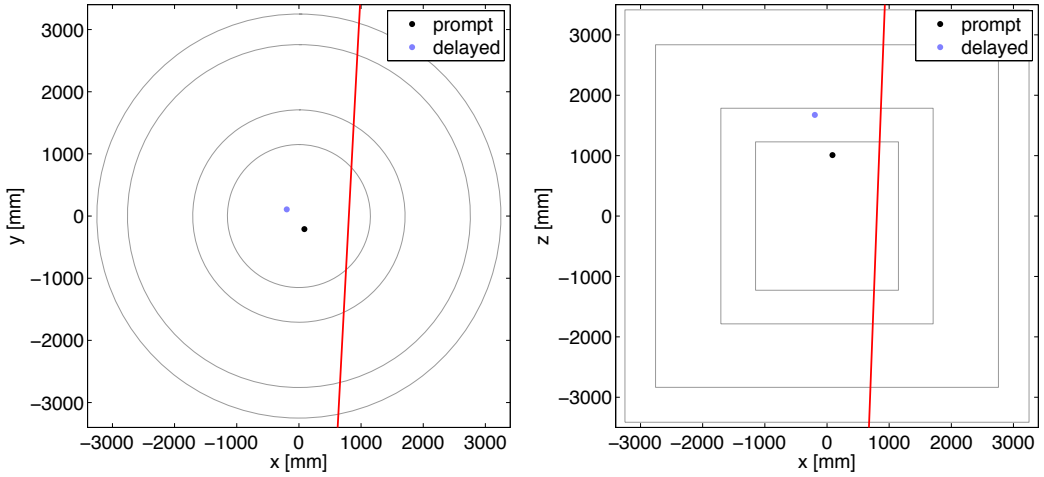

(a) XY Reconstructed Position (b) XZ Reconstructed Position

Figure 7.21: Reconstructed position for the prompt and delayed event along with the reconstructed muon track for the highest energy muon within 17 s of the third delayed coincidence pair found with both reactors off.

Our predicted background rates are consistent with the observation of these three extended IBD candidate events during 22.3 hours of data-taking with both Chooz reactors off. This is a robust and unambiguous confirmation of our background rate estimates.

Chapter 8

$\bar{\nu}_e$ Disappearance Analysis

Double Chooz looks for $\bar{\nu}_e \rightarrow \bar{\nu}_x$ oscillations where $x \neq e$ via $\bar{\nu}_e$ disappearance. The analysis consists of first calculating the expected $\bar{\nu}_e$ flux from the Chooz nuclear reactors as described in Ch. 4. Next, a Monte Carlo simulation tuned to calibration data (see Ch. 5) is used to generate a set of events which predicts the expected prompt energy spectrum due to IBD interactions in the detector in the absence of oscillations. These events will be re-weighted in the oscillation fit based on the parent neutrino energy E and propagation distance L according to the $\bar{\nu}_e$ survival probability given in Eq. 8.15. The predicted IBD signal events are combined with sets of events generated from the background models described in Ch. 7 to give a prediction for the total signal + background prompt energy spectrum. This predicted spectrum is then compared to the measured IBD candidate prompt energy spectrum which is extracted from the data according to Ch. 6. If oscillations are occurring, there will be a deficit in the number of observed IBD interactions with respect to the no-oscillation prediction, and the prompt energy spectrum will be distorted. By reweighting our IBD signal events according to Eq. 2.38 to fit the data, we can extract the value of $\sin^2(2\theta_{13})$.

8.1 χ^2 Oscillation Fit

We estimate the value of $\sin^2(2\theta_{13})$ under the neutrino oscillation hypothesis by performing a χ^2 fit of the predicted events to the measured data binned in reconstructed prompt energy.

The χ^2 fit is given by

$$\chi^2(\sin^2(2\theta_{13})) = \sum_{ij}(N_i^{data} - N_i(\sin^2(2\theta_{13}))M(\sin^2(2\theta_{13}))_{ij}^{-1}(N_j^{data} - N_j(\sin^2(2\theta_{13})), \quad (8.1)$$

where N_i^{data} is the measured number of IBD candidate events in prompt energy bin i, $N_i(\sin^2(2\theta_{13}))$ is the predicted number of IBD candidate events with oscillations in prompt energy bin i, and M is the covariance matrix describing the uncertainties in the predicted number of events. M contains both statistical uncertainties as well as the systematic uncertainties in the positron energy spectrum including bin-to-bin correlations.

The oscillation formula given in Eq. 2.38 depends not only on $\sin^2(2\theta_{13})$ but also on the value of Δm^2. Therefore, the predicted number of events N_i also depends on the value of Δm^2 and so in principle the χ^2 in Eq. 8.1 should be minimized with respect to both $\sin^2(2\theta_{13})$ and Δm^2. However, the value of Δm^2 is fairly well constrained by other experiments [16] and so for the $\bar{\nu}_e$ oscillation fits described in this thesis, $\Delta m^2 = 2.4 \times 10^{-3}$ eV^2 is treated as a fixed parameter with no uncertainty. We evaluate the impact of this approximation in Sec. 8.5.2 by performing χ^2 fits at different values of $\sin^2(2\theta_{13})$.

In general, both N_i and M depend on the value of $\sin^2(2\theta_{13})$ as oscillations affect both the predicted number of IBD events as well as the uncertainty in the prediction. However, when the predicted number of events in each reconstructed positron energy bin i is large, the statistical uncertainty in M can be estimated by the observed number of events N_i^{data}[1]. Furthermore, if the systematic variances and covariances are not very sensitive to the value of $\sin^2(2\theta_{13})$, then these can be approximated in M by their values for the no oscillation prediction $\sin^2(2\theta_{13}) = 0$. These two approximations remove the dependence of M on $\sin^2(2\theta_{13})$ in our χ^2 oscillation fits.

We perform two different types of χ^2 fits: a rate-only fit and an energy-dependent fit. The rate-only fit tests whether there is an overall deficit in the measured number of IBD candidates with respect to the no oscillation expectation. The energy-dependent fit tests not only whether there is an overall deficit in the measured number of IBD candidates but also if the measured prompt energy spectrum is distorted in a way consistent with neutrino oscillations.

[1]We investigate the impact of this approximation on the final result in Sec. 8.5.3.

The rate-only fit uses just one prompt energy bin which encompasses the entire energy range from $0.7 - 12.2$ MeV. The energy-dependent fit, on the other hand, divides the reconstructed prompt energy range from $0.7 - 12.2$ MeV into 18 variable-width bins: 15 bins from $0.7 - 8.2$ MeV with a width of 0.5 MeV, two bins from $8.2 - 10.2$ MeV with a width of 1 MeV, and one bin from $10.2 - 12.2$ MeV with a width of 2.0 MeV.

In each case the best fit, $\sin^2(2\theta_{13})_{best}$, is found by minimizing the χ^2 defined in Eq. 8.1 as a function of $\sin^2(2\theta_{13})$. The $\Delta\chi^2$ test statistic is then defined as the excursion of the χ^2 about its minimum as a function of $\sin^2(2\theta_{13})$:

$$\Delta\chi^2(\sin^2(2\theta_{13})) \equiv \chi^2(\sin^2(2\theta_{13})) - \chi^2_{min}(\sin^2(2\theta_{13})_{best}) \tag{8.2}$$

In the large sample limit, $\sin^2(2\theta_{13})_{best}$ is gaussian-distributed about the true value of $\sin^2(2\theta_{13})$ and $\Delta\chi^2(\sin^2(2\theta_{13}))$ follows a χ^2 distribution with one degree of freedom [16]. The 90% (68%) confidence interval for $\sin^2(2\theta_{13})$ is then determined by the range of values of $\sin^2(2\theta_{13})$ for which $\Delta\chi^2(\sin^2(2\theta_{13})) \leq 2.71$ (1.0). A more robust frequentist determination of the 90% confidence interval following the Feldman-Cousins (FC) unified approach is discussed in Sec. 8.6.

For the energy-dependent fit, the minimum value of χ^2 can also be used to evaluate the goodness-of-fit for the oscillation hypothesis. If the predicted number of events in each reconstructed positron energy bin i is sufficiently large, then minimum of Eq. 8.1 follows a χ^2 distribution with $N - 1$ degrees of freedom [16], where N is the number of bins, in this case 18.

8.2 Covariance Matrix Formalism

The covariance matrix formalism consists of using a covariance matrix, M_{ij}, in our χ^2 definition to encode our knowledge of the uncertainties in N_i, the predicted number of IBD signal plus background events in prompt energy bin i, as well as the correlations between bins.

There are 6 major sources of uncertainty that contribute to our definition of M_{ij}:

- M_{ij}^{stat}, the statistical uncertainty in the predicted number of IBD events

- M_{ij}^{reac}, the systematic uncertainty in the predicted reactor $\bar{\nu}_e$ flux and IBD cross section described in Ch. 4.

- M_{ij}^{reco}, the systematic uncertainty in the relative energy reconstruction differences between data and MC described in Sec. 5.5

- M_{ij}^{eff}, the systematic uncertainty in the relative efficiency for selecting IBD events in the data and the MC give in Table 6.1

- $M_{ij}^{b,rate}$, the rate uncertainty in the predicted number of events for the bth background described in Ch. 7

- $M_{ij}^{b,shape}$, the spectral uncertainty in the predicted number of events for the bth background also described in Ch. 7

These sources of uncertainty are all uncorrelated. Therefore, the full covariance matrix used in the χ^2 in Eq. 8.1 is just the sum of the covariance matrices describing each of these sources of uncertainty:

$$M_{ij} = M_{ij}^{stat} + M_{ij}^{reac} + M_{ij}^{reco} + M_{ij}^{eff} + M_{ij}^{b,rate} + M_{ij}^{b,shape} \tag{8.3}$$

In general, each of these covariance matrices M_{ij} can be further decomposed into a sum of 3 sub-matrices: a normalization matrix, a shape matrix, and a mixed shape/normalization matrix [107], i.e.

$$M_{ij} = M_{ij}^{norm} + M_{ij}^{shape} + M_{ij}^{mixed}, \tag{8.4}$$

where

$$M_{ij}^{norm} = \frac{N_i N_j}{N_T^2} \sum_{kl} M_{kl}, \tag{8.5}$$

$$M_{ij}^{shape} = M_{ij} - \frac{N_j}{N_T} \sum_{k=1}^{n} M_{ik} - \frac{N_i}{N_T} \sum_{k=1}^{n} M_{kj} + \frac{N_i N_j}{N_T^2} \sum_{kl} M_{kl}, \tag{8.6}$$

$$M_{ij}^{mixed} = \frac{N_j}{N_T} \sum_{k=1}^{n} M_{ik} + \frac{N_i}{N_T} \sum_{k=1}^{n} M_{kj} - 2\frac{N_i N_j}{N_T^2} \sum_{kl} M_{kl}, \tag{8.7}$$

and

$$N_T = \sum_i N_i. \tag{8.8}$$

The normalization matrix allows the predicted number of events N_i for each energy bin i to change by same overall factor $\sqrt{\sum_{kl} M_{kl}}/N_T$. This can describe pure normalization uncertainties such as M_{ij}^{eff} and $M_{ij}^{b,rate}$. The shape matrix allows the predicted number of events N_i to migrate between bins while the normalization is held constant. This can describe uncertainties which conserve the total number of events N_T, such as $M_{ij}^{b,shape}$. The mixed matrix describes uncertainties which change the overall normalization but affect each bin differently. In the cases where this is needed, such as with M_{ij}^{stat}, M_{ij}^{reac} and M_{ij}^{reco}, it is often simpler to work directly with the full covariance matrix instead.

In a rate-only χ^2 fit, the contribution of a given source of error to the overall uncertainty in the predicted number of IBD events is given by the norm of the corresponding covariance matrix M_{ij}, defined as $\sqrt{\sum_{ij} M_{ij}}/N_T$. Therefore, this number is useful for comparing the relative contributions of each source of uncertainty to the total uncertainty[2]. It should be stressed, however, that the same is not true for an energy-dependent χ^2 fit, in which the correlations encoded in the covariance matrix provide additional constraints on the fit.

8.2.1 Statistical Uncertainties

Statistical uncertainties are included as a diagonal covariance matrix with the elements along the diagonal corresponding to the measured number of events in prompt energy bin i:

$$M_{ij}^{stat} = N_i^{data}\delta_{ij}, \tag{8.9}$$

where δ_{ij} is the Kronecker delta. This matrix corresponds to assigning an uncorrelated uncertainty of $\sqrt{N_i^{data}}$ to the predicted number of events in each energy bin, N_i. By construction, the norm of this matrix is equal to $1/\sqrt{\sum N_i^{data}} = 1.56\%$.

8.2.2 Reactor Covariance Matrix

Sec. 4.4 details the construction of the covariance matrix M_{ij}^{tot}=$\langle\delta\alpha_i\delta\alpha_j\rangle$, which describes the uncertainty in the predicted number of IBD events α_i interacting in the detector as a

[2]For the purposes of comparison, we normalize the relative contribution of each source of uncertainty to the total number of measured events, i.e. we take $N_T = 4121$.

function of true neutrino energy E_ν^i. As described in Sec. 4.3.3, the α_i are associated with a set of MC IBD events. Each MC IBD event represents not only the parent neutrino but also the final state positron and neutron generated in the IBD interaction. A re-weighting scheme in true neutrino energy E_ν^i is used to convert the covariance matrix M_{ij}^{tot} given in Eq. 4.13 from true neutrino energy E_ν^i to reconstructed positron energy in terms of which the final χ^2 fits are performed.

The re-weighting scheme requires that the set of MC IBD events generated according to Sec. 4.3.3 first be passed to the detector simulation, then be reconstructed, and finally be selected according to the IBD delayed coincidence criteria (see Sec. 6.4.5) in a way analogous to the data. After this has been done, the MC IBD events can be binned either in terms of true neutrino energy E_ν^i or in terms of reconstructed positron energy $E_{e^+}^j$.

Let β_j represent the MC IBD events binned in reconstructed positron energy $E_{e^+}^j$. We wish to construct the covariance matrix $\langle \delta\beta_i \delta\beta_j \rangle$, which describes the reactor-induced uncertainties on the IBD MC events in reconstructed positron energy in terms of the uncertainty on the IBD MC events in true neutrino energy. To do this, we simulate a fluctuation in the energy spectrum represented by the α_i by creating a new spectrum α_i' drawn from the multi-variate Gaussian distribution

$$\exp\left[-\sum_{ij}(\alpha_i' - \alpha_i)(M^{tot})_{ij}^{-1}(\alpha_j' - \alpha_j)\right]. \tag{8.10}$$

In this way we constrain our new spectrum α_i' to be drawn from spectra that are consistent with the central value MC prediction α_i and its associated uncertainty, represented by M_{ij}^{tot}. Next, we re-weight each IBD MC event with true neutrino energy in bin i by the ratio α_i'/α_i. Finally, the IBD MC events are re-binned with these new weights in reconstructed positron energy to produce a fluctuated reconstructed positron spectrum β_j'.

A large number, K, of fluctuated spectra are simulated and the reactor covariance matrix is then given in terms of reconstructed positron energy by

$$M_{ij}^{reac} = \frac{1}{K-1}\sum_{K}(\beta_i' - \beta_i)(\beta_j' - \beta_j). \tag{8.11}$$

In fact, instead of constructing weights from the ratio α_i'/α_i, a spline is fit to each set of α_i' and to the central value MC prediction α_i. The weights for each IBD MC event are

constructed from the ratio of these splines evaluated at the true neutrino energy of the event [108].

A total of 180,000 fluctuated spectra were simulated to produce M_{ij}^{reac}. The norm of the resulting reactor covariance matrix contributes a normalization uncertainty of 1.70% of the measured number of IBD candidate events.

8.2.3 Efficiency Covariance Matrix

As described in Sec. 6.6, we assess corrections to account for differences in the relative efficiency for selecting IBD events in the data and Monte Carlo as well as their associated uncertainties. The relative efficiency uncertainty between data and Monte Carlo enters into the fit as an overall normalization uncertainty. Therefore, we combine the relative efficiency uncertainty with all other sources of normalization uncertainty given in Table 6.1. This total normalization uncertainty is then described by a normalization covariance matrix

$$M_{ij}^{eff} = 0.011^2 N_i N_j \tag{8.12}$$

where N_i is the predicted number of signal IBD candidate events in energy bin i in the case of no oscillations. By construction, we see that the norm of this matrix contributes a normalization uncertainty of 1.1% of the predicted number of signal IBD candidate events[3].

8.2.4 Energy Response Covariance Matrix

The energy response covariance matrix is described in Sec. 5.5. Uncertainties in the parameters that model the differences in the energy scales between data and MC induce uncertainties in the shape of the predicted reconstructed positron energy as events migrate between energy bins. However, they can also induce normalization uncertainties by changing the number of selected IBD candidates events in a correlated way.

As described in Sec. 5.5.3, the fractional energy response covariance matrix shown in Fig. 5.10 is converted back to a full covariance matrix using the expected MC IBD signal plus background prompt energy spectrum. The norm of the resulting energy response covariance

[3]The norm of M_{ij}^{eff} contributes a normalization uncertainty of 1.07% of the measured number of IBD candidate events.

matrix differs slightly from the value quoted in Sec. 5.5.3 and contributes a normalization uncertainty which is 1.66% of the measured number of IBD candidate events.

8.2.5 Background Covariance Matrix

Ch. 7 describes the evaluation of the rate and shape uncertainties for the various backgrounds considered. The rate uncertainties are included as a normalization error via a covariance matrix

$$M_{ij}^{b,rate} = \sigma_{b,rate}^2 N_i^b N_j^b, \tag{8.13}$$

where $\sigma_{b,rate}$ is the relative rate uncertainty for the bth background and N_i^b is predicted number of events for the bth background in prompt energy bin i. The norm of this matrix equals $\sigma_{b,rate}\frac{N_T^b}{N_T}$, where $N_T^b = \sum N_i^b$.

The background shape uncertainties are handled differently for each of the backgrounds. The shape of the accidental background spectrum is measured very accurately from the data as described in Sec. 7.1. Therefore, no systematic uncertainty is assigned to the shape of the accidental background spectrum. The shape of the fast neutron and stopping muon background, on the other hand, is rather uncertain. As described in Sec. 7.3, the primary analysis for the shape of the fast neutron and stopping muon background predicts a flat spectrum, while a second, independent analysis predicts a linear spectrum increasing as a function of energy. In order to cover both analyses, the fast neutron and stopping muon background was modeled as a flat spectrum, with a fully correlated shape uncertainty determined from the bin-by-bin differences, δN_i^b, between the flat model and the alternative linear hypothesis, in which both were normalized to the predicted rate of 0.82 d^{-1}. Thus, the fast neutron and stopping muon background shape uncertainty was included as a covariance matrix of the form

$$M_{ij}^{b,shape} = \delta N_i^b \delta N_j^b \tag{8.14}$$

Similar to the fast neutron background, the shape uncertainty for the ^{9}Li background was treated as fully correlated and taken as the difference between a central value prediction and an alternative hypothesis as described in Sec. 7.2. Fig. 7.10 gives the bin-by-bin differences, δN_i^b, between the central value prediction and the alternative hypothesis that are used to construct the shape covariance matrix for the ^{9}Li background as in Eq. 8.14.

8.2.6 Summary

Table 8.1 summarizes the contribution of each covariance matrix to the total normalization uncertainty as a fraction of the measured number of IBD candidate events. The total rate-only uncertainty is 4.2%.

Covariance matrix	Variance
Statistical	1.56%
Reactor	1.70%
Energy Reconstruction	1.66%
Efficiency	1.07%
Accidental	0.07%
^{9}Li	2.82%
Fast-N/Stopping μ	0.89%
Total	**4.24%**

Table 8.1: Summary of the variance of each covariance matrix contributing to the total covariance matrix given in Eq. 8.1.

8.3 Fit Procedure

The ingredients for the χ^2 fit are:

- Predicted signal IBD MC events with oscillations
- Predicted background MC events
- Measured signal + background IBD candidate events from data
- Total covariance matrix

The generation of MC IBD signal events is described in Sec. 4.3.3. A factor of 100 more MC IBD events are generated than are predicted for the 101.52 days of detector run time corresponding to the data. This reduces the uncertainty associated with statistical fluctuations in the MC so that they become negligible compared to the statistical fluctuations

in the data. The MC IBD signal events are then re-weighted by a factor of 1/100 so that they correspond to the expected number of IBD signal events in the data. The MC IBD signal events are then re-weighted by an additional factor of 0.9243 to correct for data/MC differences summarized in Table 6.1. Finally, oscillations are simulated by re-weighting the MC IBD events generated with no oscillations by the survival probability in Eq. 8.15 for a given value of $\sin^2(2\theta_{13})$ based on the parent neutrino energy E and propagation distance L.

The estimates for the expected number of background events are described in Ch. 7. For each of the backgrounds, a set of MC background events is generated according to the measured background rate by randomly sampling from the corresponding prompt energy spectrum. The accidental and fast neutron/stopped muon backgrounds use the reconstructed prompt energy spectra measured directly from the data to generate MC background events. For the ^{9}Li background, however, the MC prompt energy spectrum shown in Fig. 7.9 is used to generate MC events since no ^{9}Li energy spectrum could be extracted from the data as described in Sec. 7.2.2.

Similar to the MC IBD events, a factor of 100 more MC background events are generated than are predicted for the 101.52 days of detector run time corresponding to the data, and these are then re-weighted by a factor of 1/100. However, in contrast to the IBD MC events, the MC background events just consist of random pulls from reconstructed energy spectra. Therefore, they should not be re-weighted by IBD selection efficiency corrections, which are already taken into account by the background estimation itself. Therefore, the MC background events are only re-weighted by an additional factor of 0.9547 to correct for the muon veto dead time, whose effect is not included in the MC background simulation.

Finally, the measured signal plus background IBD events from the data are extracted according to the procedure described in Ch. 6 and the construction of the total covariance matrix is described in Sec. 8.2 above. Table 8.2 summarizes the total number of signal + background IBD candidate events extracted from the data, the total number of predicted signal events from each reactor assuming no oscillations, as well as the total number of events predicted for each background.

Event class	Number of events
Data	4121
Reactor 1 IBD	1941
Reactor 2 IBD	2069
9Li	223
Fast-N/Stopping μ	79
Accidental	32
Total	4344

Table 8.2: Summary of the total number of events extracted from the data as well as the number of predicted events for each signal and background event type.

A custom-built tool kit called **CUFITS** [109] was used to perform sensitivity studies as well as the final χ^2 fit based on the above inputs. **CUFITS** is built with the **ROOT** [110] analysis framework and ultimately relies on a translation of **MINUIT** [111] to C++ for the χ^2 minimization. Specifically, the **MIGRAD** routine is used to minimize χ^2 as a function of $\sin^2(2\theta_{13})$. At each step in the minimization procedure for $\sin^2(2\theta_{13})$, **CUFITS** reweights each signal MC event with parent neutrino energy E and propagation distance L by the survival probability

$$P(\bar{\nu}_e \to \bar{\nu}_e) = 1 - \sin^2(2\theta_{13}) \sin^2(1.267 \Delta m^2 L/E), \tag{8.15}$$

where Δm^2 is measured in eV^2, L is measured in meters, and E is measured in MeV. The the value of χ^2 is then re-computed for the reweigthed events.

8.4 Fit Results

The rate-only fit consists of fitting the χ^2 function given in Eq. 8.1 using just one reconstructed positron energy bin. Fig. 8.1 gives the χ^2 curve as a function of $\sin^2(2\theta_{13})$. The best fit value is determined from the minimum of the χ^2 curve and the 1σ confidence interval is determined by the value of $\sin^2(2\theta_{13})$ for which $\Delta\chi^2(\sin^2(2\theta_{13})) = 1$. From the rate-only fit, we determine $\sin^2(2\theta_{13}) = 0.104 \pm 0.081$ (68% C.L.).

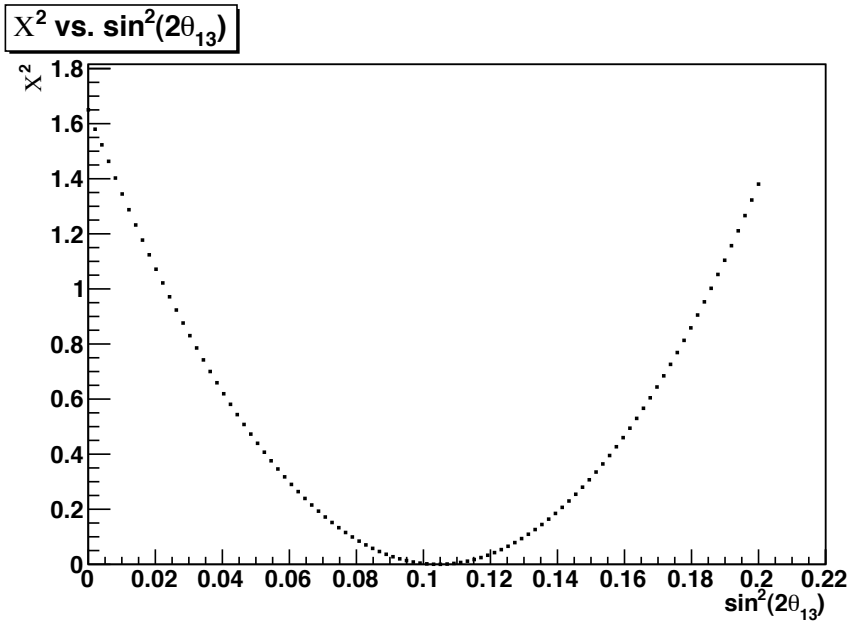

Figure 8.1: $\Delta\chi^2$ curve for rate-only fit. The best fit value is $\sin^2(2\theta_{13}) = 0.104 \pm 0.081$.

The energy-dependent fit consists of fitting the χ^2 function given in Eq. 8.1 using the 18 reconstructed positron energy bins described in Sec. 8.1. Fig. 8.2 shows the reconstructed prompt energy spectrum for the data and the Monte Carlo prediction for the case of no oscillations and for the best fit value of $\sin^2(2\theta_{13})$. The black points are the data shown with statistical errors only. The blue histogram histogram is the no-oscillation Monte Carlo prediction and the red histogram is the best-fit oscillated spectrum. The residual plot is also shown in the lower panel of Fig. 8.2. From this plot, it appears that the high point at $\sim$ 3 MeV is a statistical fluctuation, reducing the quality of our fit and pulling the fit to smaller values of $\sin^2(2\theta_{13})$.

Fig. 8.3 gives the resulting χ^2 curve as a function $\sin^2(2\theta_{13})$. We find $\chi^2/ndf = 23.7/17$ at the minimum corresponding to a goodness-of-fit of 12.8%. The best fit value corresponds to $\sin^2(2\theta_{13}) = 0.086 \pm 0.051$ (68% C.L.). From $\Delta\chi^2 = 2.92$ at $\sin^2(2\theta_{13}) = 0$, we exclude the no oscillation hypothesis at 91.25% C.L.

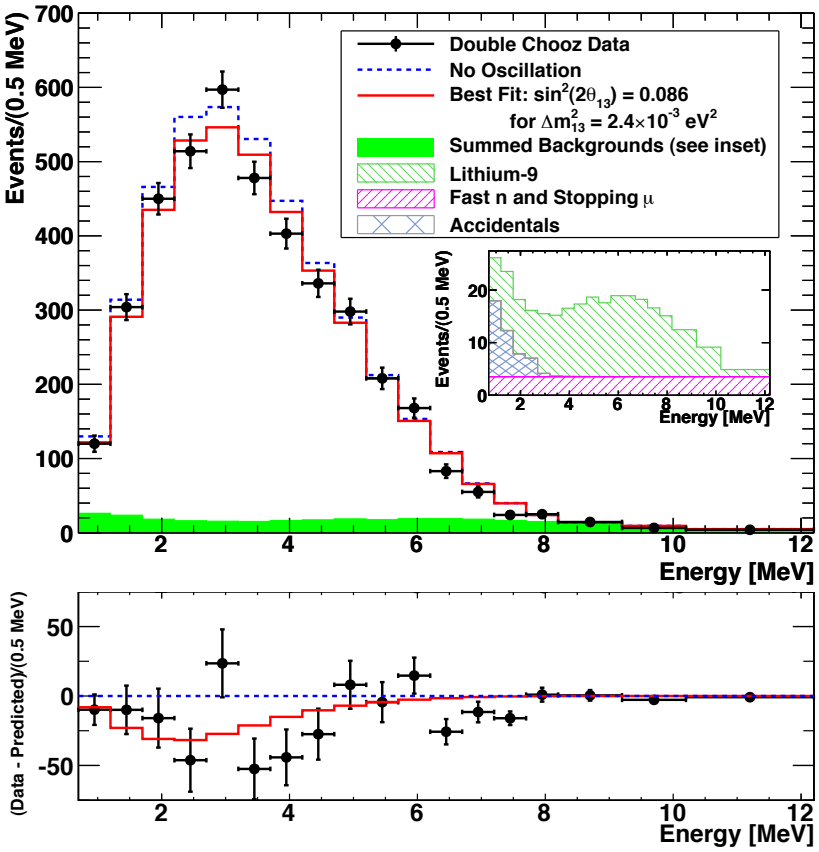

Figure 8.2: Prompt energy spectrum for IBD candidate events. The black points are the data shown with statistical errors only. The blue histogram is the no oscillation Monte Carlo prediction and the red stacked histogram is the best-fit oscillated prediction with the *a priori* estimates for the backgrounds given in the inset plot. The best fit value of $\sin^2(2\theta_{13}) = 0.086 \pm 0.051$.

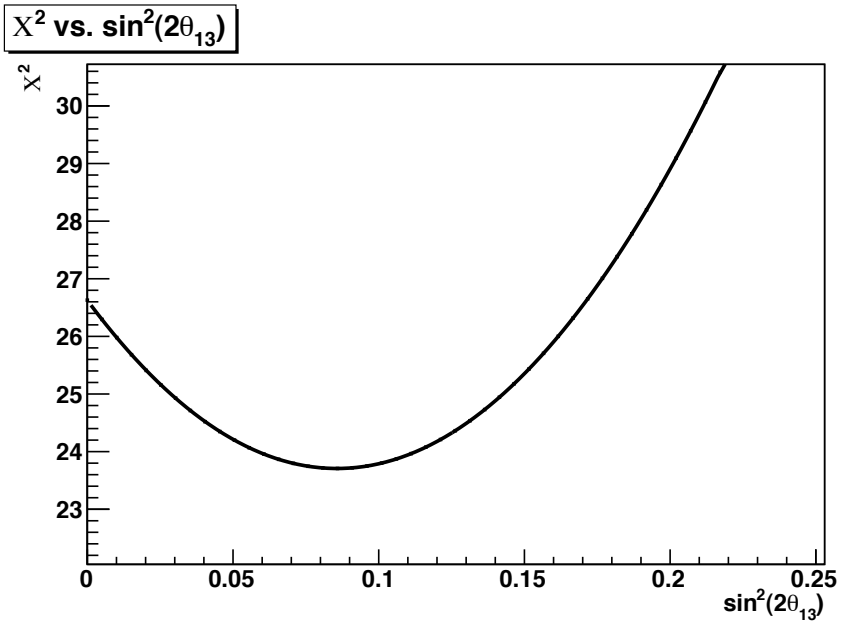

Figure 8.3: χ^2 curve for the energy-dependent fit. The best fit value corresponds to $\sin^2(2\theta_{13}) = 0.086 \pm 0.051$.

In summary we measure the following values for $\sin^2(2\theta_{13})$ from our χ^2 fits:

$$\textbf{Rate-only Fit} : \sin^2(2\theta_{13}) = 0.104 \pm 0.081 \text{ (68\% C.L.)} \tag{8.16}$$

$$\textbf{Energy-dependent Fit} : \sin^2(2\theta_{13}) = 0.086 \pm 0.051 \text{ (68\% C.L.)} \tag{8.17}$$

8.5 Pull Term Fits

A mathematically equivalent method of minimizing the χ^2 given in Eq. 8.1 as a function $\sin^2(2\theta_{13})$ is to minimize a related pulls-based χ^2 in terms of $\sin^2(2\theta_{13})$ and one or many systematic parameters or "pulls" [112]. The advantage of the pulls-based approach is that one learns the value of the pulls at the χ^2 minimum giving an indication of how the data constrains the systematic parameters and how each systematic parameter contributes to the overall χ^2.

We constructed a pulls-based χ^2 in terms of the three systematic parameters as

$$\begin{aligned}\chi^2(\sin^2(2\theta_{13}), K_n, K_{^9Li}, \varepsilon) = &\sum_{ij}(N_i^{data} - N_i(\sin^2(2\theta_{13}), K_n, K_{^9Li}, \varepsilon)) \times M_{ij}^{-1} \\ &\times (N_j^{data} - N_j(\sin^2(2\theta_{13}), K_n, K_{^9Li}, \varepsilon)) \\ &+ \left(\frac{K_n - 1}{\sigma_{K_n}}\right)^2 + \left(\frac{K_{^9Li} - 1}{\sigma_{K_{^9Li}}}\right)^2 + \left(\frac{\varepsilon - 1}{\sigma_\varepsilon}\right)^2, \end{aligned} \tag{8.18}$$

where K_n is a parameter which multiplies the fast neutron/stopped muon background rate, $K_{^9Li}$ is a parameter which multiplies the ^9Li background rate, and ε is parameter which multiplies the energy scale described in Sec. 5.3. The *a priori* uncertainties assumed for σ_{K_n}, $\sigma_{K_{^9Li}}$, and σ_ε are 46%, 52%, and 5%, respectively.

The pulls-based χ^2 given in Eq. 8.18 is minimized with respect to $\sin^2(2\theta_{13})$, K_n, $K_{^9Li}$, and ε. The result is shown in Fig. 8.4. The fit has a $\chi^2/ndf = 23.66/17$ which gives a goodness-of-fit of 12.89%. The best fit value corresponds to $\sin^2(2\theta_{13}) = 0.085 \pm 0.051$ (68% C.L.). The fit constrains the fast neutron/stopped muon background rate to be 0.78 $(1 \pm 38\%)$ d^{-1}, the ^{9}Li background rate to be 1.87 $(1 \pm 26\%)$ d^{-1}, and the energy scale to be 0.998 ± 0.005.

The pulls-based approach gives a nice confirmation of the best fit value of $\sin^2(2\theta_{13})$ obtained in our previous results. In addition, the pulls-based fit demonstrates that the ^{9}Li rate is constrained to 81.5% of its *a priori* value and with an uncertainty that is decreased by over half. Furthermore, the energy scale uncertainty is reduced from 5% to 0.5% with a the central value that is very close to the input value.

8.5.1 Systematic vs. Statistical Uncertainty

The 1σ uncertainties for the rate-only and energy-dependent fits can be divided into a statistical uncertainty and a systematic uncertainty by means of a sensitivity study. We determine the contribution of the systematic uncertainty by fitting a high-statistics sample of MC IBD signal + background events to the MC IBD signal + background prediction for the case of no oscillations using Eq. 8.1. By construction then, $\sin^2(2\theta_{13})_{best} = 0$ and $\chi^2_{min} = 0$. In this case the one-sided 68% confidence interval is determined by the systematic uncertainty due to the covariance matrix σ_{sys}. We can then extract the statistical

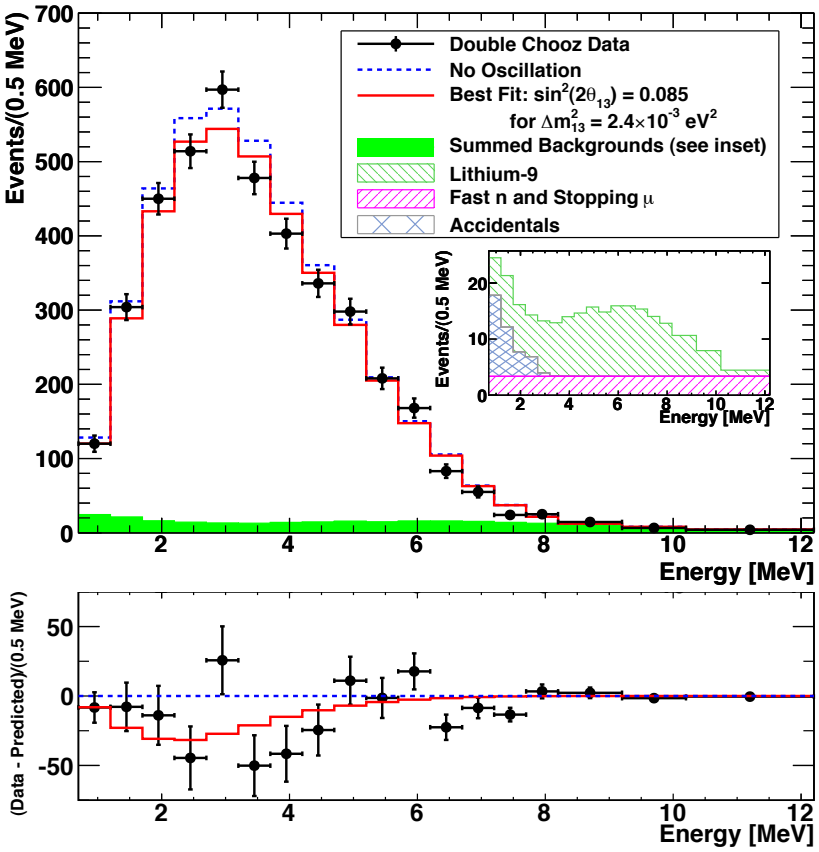

Figure 8.4: Prompt energy spectrum for IBD candidate events. The black points are the data shown with statistical errors only. The blue histogram is the no oscillation Monte Carlo prediction and the red stacked histogram is the best-fit oscillated prediction with the *a posteriori* pulled estimates for the backgrounds given in the inset plot. The best fit value of $\sin^2(2\theta_{13}) = 0.085 \pm 0.051$.

uncertainty in the measurements of $\sin^2(2\theta_{13})$ given in Eq. 8.16 via

$$\sigma_{tot}^2 = \sigma_{sys}^2 + \sigma_{stat}^2. \tag{8.19}$$

The sensitivity study is performed using a mock data sample with the observed numbers of events N_i^{data} in the χ^2 function in Eq. 8.1 taken as the no-oscillation Monte Carlo prediction but with 100 times the expected data statistics. Similarly, the Monte Carlo prediction for each value of $\sin^2(2\theta_{13})$ is also made with 100 times the expected data statistics. Finally, the statistical part of the covariance matrix is adjusted for 100 times the expected data statistics. The 1σ systematic uncertainty on $\sin^2(2\theta_{13})$ is then determined as the value of $\sin^2(2\theta_{13})$ for which $\Delta\chi^2(\sin^2(2\theta_{13})) = 1$.

The 1σ systematic uncertainties on $\sin^2(2\theta_{13})$ from the sensitivity studies using 100 times the expected data statistics for the rate-only and energy-dependent fits are 0.076 and 0.030, respectively. Based on Eq. 8.16 and Eq. 8.19, the statistical uncertainties on $\sin^2(2\theta_{13})$ for the rate-only and energy-dependent fits are then 0.030 and 0.041, respectively.

Therefore, the fit results Eq. 8.16 may be expressed in terms of the individual statistical and systematic contributions to the total uncertainty as

$$\textbf{Rate-only Fit} : \sin^2(2\theta_{13}) = 0.104 \pm 0.030 \text{ (stat.)} \pm 0.076 \text{ (syst.)} \text{ (68\% C.L.)}$$
$$\textbf{Energy-dependent Fit} : \sin^2(2\theta_{13}) = 0.086 \pm 0.041 \text{ (stat.)} \pm 0.030 \text{ (syst.)} \text{ (68\% C.L.)}$$

8.5.2 Dependence of Fit Results on Δm^2

We performed a check on the impact of keeping Δm^2 fixed in our the oscillation fits by performing our energy-dependent χ^2 fit for different values of Δm^2. We choose values of Δm^2 derived [113] from the latest MINOS measurement [44] assuming a normal and inverted hierarchy, respectively. Table 8.3 summarizes the results of our fits at three different values of Δm^2. A smaller Δm^2 pushes our best fit value of $\sin^2(2\theta_{13})$ slightly higher and increases the uncertainty by a similar amount. However, we see that for values of Δm^2 in the range allowed by MINOS, the variation in $\sin^2(2\theta_{13})$ is less than $\sim 10\%$ of the quoted uncertainty.

Δm^2 [eV^2]	$\sin^2(2\theta_{13})$
2.4×10^{-3}	0.086 ± 0.051
2.35×10^{-3}	0.088 ± 0.052
2.29×10^{-3}	0.091 ± 0.053

Table 8.3: Summary of the energy-dependent fit results for three different values of Δm^2

8.5.3 Observed Vs. Expected Events for Statistical Uncertainty

We consider three different approaches to estimating the statistical uncertainty on the MC IBD prediction:

$$\sigma^2_{stat} = N_{data} \qquad \text{Neyman's method}$$

$$\sigma^2_{stat} = N_{MC} \qquad \text{Pearson's method}$$

$$\sigma^2_{stat} = \frac{1}{2}(N_{data} + N_{MC}) \qquad \text{James's method}$$

In the fits described in Sec. 8.4, we have used Neyman's method to estimate the statistical uncertainty. We check the impact of using Person's or James's method on our final results by computing the statistical uncertainty using the value of N_{MC} at the best fit oscillation prediction and fixing the backgrounds at their *a posteriori* rates given by the energy-dependent fits performed using the pulls approach.

Using Pearson's method we find a best fit value of $\sin^2(2\theta_{13}) = 0.080 \pm 0.051$ (68% C.L.) and a goodness-of-fit of 19.4% for $\chi^2/ndf = 23.70/17$. Using James's method, we find a best fit value of $\sin^2(2\theta_{13}) = 0.083 \pm 0.051$ (68% C.L.) and a goodness-of-fit of 16.25% for $\chi^2/ndf = 22.61/17$.

We find that Pearson's method gives a lower best fit value of $\sin^2(2\theta_{13})$ than does Neyman's method, whereas James's method gives a best fit value of $\sin^2(2\theta_{13})$ which lies between the two. In either case, the systematic shift is less than $\sim 10\%$ of the quoted uncertainty.

8.6 Frequentist Studies

The confidence interval construction in the previous section assumes that the best fit value of $\sin^2(2\theta_{13})$ is gaussian-distributed about the true value of $\sin^2(2\theta_{13})$ and that $\Delta\chi^2(\sin^2(2\theta_{13}))$ follows a χ^2 distribution with 1 degree of freedom. Furthermore, this method does not the restrict confidence interval construction to physical values of $\sin^2(2\theta_{13})$. If a one-sided confidence interval is used in place of the corresponding two-sided confidence interval whenever the two-sided interval includes unphysical values of $\sin^2(2\theta_{13})$, then the resulting interval will undercover the true value of $\sin^2(2\theta_{13})$ at the quoted significance.

The FC unified approach to confidence interval construction [114] addresses the above issues. They suggest constructing the frequentist confidence interval using a test statistic based on the likelihood ratio

$$\lambda = \frac{L(\mathbf{x};\mathbf{\Theta})}{L(\mathbf{x};\hat{\mathbf{\Theta}})}, \tag{8.20}$$

where $\mathbf{x}$ represents the measured data, $\mathbf{\Theta}$ the parameters in the theory to be estimated from the data, and $\hat{\mathbf{\Theta}}$ the value of $\mathbf{\Theta}$ in the physically-allowed region which maximizes $L(\mathbf{x},\mathbf{\Theta})$. According to the FC prescription, points in parameter space with larger values of λ are added to acceptance intervals before points with smaller values of λ. In the gaussian limit, ordering by the largest values of λ is equivalent to ordering by the smallest values of the test statistic

$$-2\lambda = \Delta\chi^2 = \sum_i \frac{(N_i - N_i^{pred})^2}{\sigma_i^2} \tag{8.21}$$

In this analysis, we construct confidence intervals using the $\Delta\chi^2(\sin^2(2\theta_{13}))$ test statistic defined in eq. 8.2, where the minimum value of $\chi^2(\sin^2(2\theta_{13}))$ is searched for only in the physically-allowed region.

8.6.1 FC 90% Confidence Interval

The 90% confidence interval is constructed according to the FC procedure as follows. First, a set of physically-allowed values of $\sin^2(2\theta_{13})$ are chosen in the region of interest. Then, for each of these values of $\sin^2(2\theta_{13})$ we compute the value of $\Delta\chi^2_{data}(\sin^2(2\theta_{13}))$ for the data. In addition, for each of these values of $\sin^2(2\theta_{13})$, a set of $\sim 10,000$ fake experiments are simulated. For each fake experiment, the simulated number of events N_i^{fake} in each prompt

energy bin i is drawn from the multivariate gaussian distribution

$$\exp\left[-\sum_{ij}(N_i^{fake} - N_i(\sin^2(2\theta_{13}))M_{ij}^{-1}(N_j^{fake} - N_j(\sin^2(2\theta_{13}))\right] \tag{8.22}$$

using a Cholesky decomposition. For each of these $10,000$ experiments, **MINUIT** is used to find the best fit, $\sin^2(2\theta_{13})_{best}$ which minimizes $\chi^2(\sin^2(2\theta_{13}))$. The value of $\Delta\chi^2(\sin^2(2\theta_{13}))$ is then computed with respect to this minimum at the generated value of $\sin^2(2\theta_{13})$. Next, the critical value $\Delta\chi_c^2(\sin^2(2\theta_{13}))$ is determined from the distribution of the $\Delta\chi^2(\sin^2(2\theta_{13}))$ values obtained from each fake experiment, such that only 10% of fake experiments have $\Delta\chi^2(\sin^2(2\theta_{13})) > \Delta\chi_c^2(\sin^2(2\theta_{13}))$ for a 90% C.L. limit.

For each generated value of $\sin^2(2\theta_{13})$, the acceptance interval is defined as the set of best fit values, $\sin^2(2\theta_{13})_{best}$, for which $\Delta\chi^2(\sin^2(2\theta_{13})) < \Delta\chi_c^2(\sin^2(2\theta_{13}))$. Fig. 8.5 shows the $\Delta\chi^2(\sin^2(2\theta_{13}))$ distribution for various values of $\sin^2(2\theta_{13})$. The colored portion of the each histogram represents the 10% of fake experiments with $\Delta\chi^2(\sin^2(2\theta_{13})) > \Delta\chi_c^2(\sin^2(2\theta_{13}))$ for that value of $\sin^2(2\theta_{13})$. The union of all such acceptance intervals defines the 90% FC confidence belt. The FC 90% confidence interval is then determined from where the vertical line $\sin^2(2\theta_{13})_{best} = 0.086$ intercepts the 90% confidence belt, as shown in Fig. 8.6. From this we determine the 90% confidence interval

$$\sin^2(2\theta_{13}) \in [0.17, 0.16] \text{ (90\% C.L.)} \tag{8.23}$$

8.6.2 No oscillation probability

In Sec. 8.4 the value of $\Delta\chi^2(0) = 2.92$ was used to determine at what significance the $\sin^2(2\theta_{13}) = 0$ hypothesis could be excluded, again assuming that the best fit value of $\sin^2(2\theta_{13})$ is gaussian-distributed about the true value of $\sin^2(2\theta_{13})$ and that $\Delta\chi^2(\sin^2(2\theta_{13}))$ follows a χ^2 distribution with 1 degree of freedom. Following a procedure similar to the one outlined above, the significance with which the $\sin^2(2\theta_{13}) = 0$ hypothesis can be excluded can be evaluated within a frequentist FC framework.

Fig. 8.7 shows the $\Delta\chi^2(\sin^2(2\theta_{13}))$ distribution for fake experiments generated with $\sin^2(2\theta_{13}) = 0$. The colored portion of the histogram corresponds to the fraction of fake experiments with $\Delta\chi^2(0) > \Delta\chi_{data}^2(0)$. Of the 9950 fake experiments performed, we reject

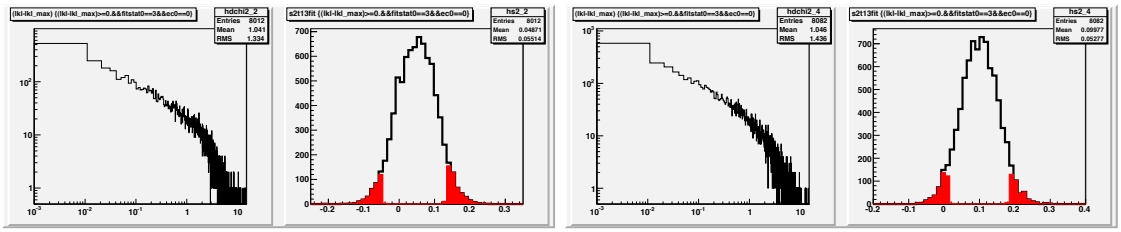

(a) $\sin^2(2\theta_{13})_{true} = 0.05$ (b) $\sin^2(2\theta_{13})_{true} = 0.10$

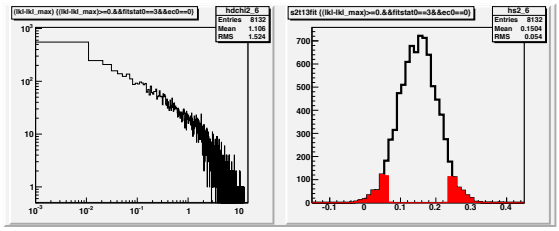

(c) $\sin^2(2\theta_{13})_{true} = 0.15$

Figure 8.5: Examples of distribution of test statistic and best fit oscillation amplitude values for ensembles with different values of $\sin^2(2\theta_{13})_{true}$. Red highlights best fit values corresponding to the 10% of simulated experiments with the worst test statistic values. The distribution of the best values is centered on the true value, indicating that the fit is unbiased.

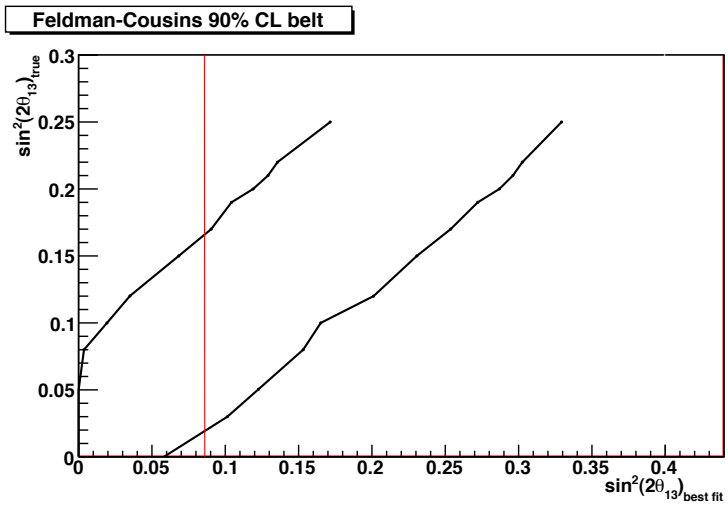

Figure 8.6: 90% C.L. frequentist belt

1805 of the fake experiments due to **MINUIT** reporting a status indicating there was a problem calculating the error matrix for the fit. We reject 47 additional fake experiments that have unphysical (negative) $\Delta\chi^2$ values. Of the remaining 8098 experiments, we find that only 434 had a $\Delta\chi^2(0)$ larger than the data. Therefore, we conclude that

Probability of no oscillations: 5.4%[4].

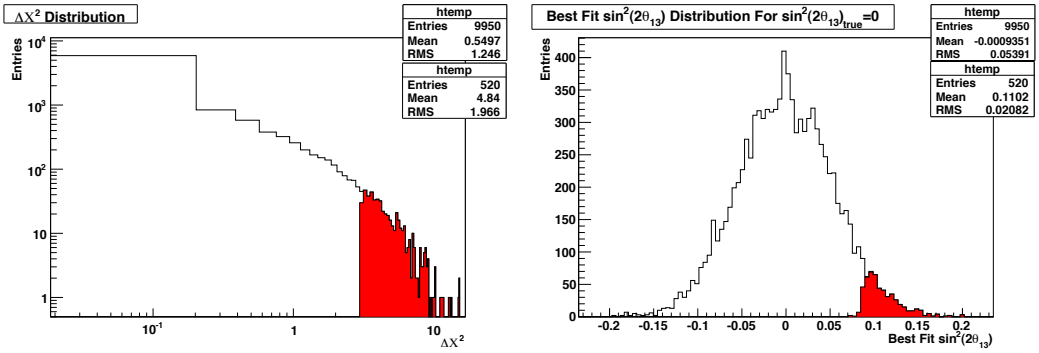

(a) test statistic (b) best fit values

Figure 8.7: Distribution of test statistic and best fit oscillation amplitude values obtained with simulated experiments containing no oscillation. Red highlights the toy experiments corresponding to test statistic values larger than 2.92

[4]After the publication (see Ch. 9), we discovered that calling **HESSE** after the minimization alleviated the problem with **MINUIT** reporting a problematic fit status. Re-running the analysis with this fix gave a probability of the no oscillations of 5.3%, indicating that no bias had been induced by neglecting the problematic experiments

Chapter 9

Conclusions

Based on an energy-dependent χ^2 fit to an oscillation hypothesis for $\sim$ 100 days of data, we measure

$$\sin^2(2\theta_{13}) = 0.086 \pm 0.041 \text{ (stat.)} \pm 0.030 \text{ (syst.)}$$

with a $\chi^2/ndf = 23.7/17$ giving a goodness-of-fit of 12.8%. Based on a frequentist study, we exclude $\sin^2(2\theta_{13}) = 0$ at 94.6% C.L.

A combined analysis of the recent T2K results [45] and DC data is shown in Fig. 9.1. The plots on the left correspond to the normal mass hierarchy and are produced using a fixed $\Delta m^2 = 2.35 \times 10^{-3}$ eV^2. The plots on the right correspond to the inverted mass hierarchy and are produced using a fixed $\Delta m^2 = 2.29 \times 10^{-3}$ eV^2.

Table 9.1 gives the 1, 2, and 3σ confidence intervals for $\sin^2(2\theta_{13})$ from the combined fits of T2K and DC data for the normal and inverted mass hierarchies. In both cases $\sin^2(2\theta_{13}) = 0$ is excluded at $> 3\sigma$.

$\sin^2 2\theta_{13}$	best fit	1σ	2σ	3σ
normal ordering:	0.092	$0.051 - 0.140$	$0.021 - 0.186$	$0.002 - 0.233$
inverted ordering:	0.092	$0.056 - 0.146$	$0.024 - 0.198$	$0.002 - 0.246$

Table 9.1: Tabulated confidence intervals for $\sin^2(2\theta_{13})$ from the combined fits of T2K and DC data.

The first Double Chooz $\bar{\nu}_e$ disappearance search results presented in this thesis were

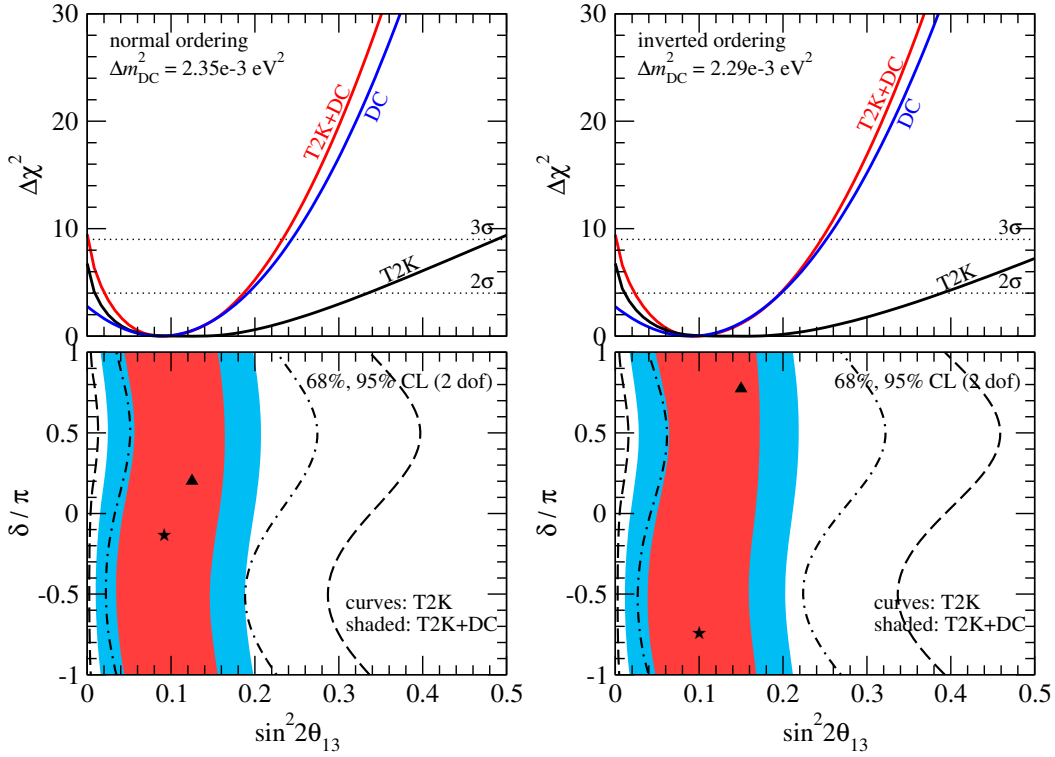

(a) Normal Hierarchy (b) Inverted Hierarchy

Figure 9.1: The lower panels show the 68% and 95% C.L. $\Delta\chi^2$ contours for two degrees of freedom in the $(\sin^2 2\theta_{13}, \delta)$ parameter space, where δ is the Dirac CP violating phase. The colored region represents the contours for the combination of T2K and DC data and the dashed black curves represent the contours for T2K data alone. The star corresponds to the best fit point for the combined T2K and DC analysis, and the triangle corresponds to the best fit point for T2K data alone. The upper panels show the $2D$ $\Delta\chi^2$ contours marginalized over the CP violating phase δ.

recently published [115] (see App. A). In addition, first results from the Daya Bay [48] and RENO [49] experiments were subsequently released. Table 9.2 consolidates the various measurements of $\sin^2(2\theta_{13})$ which have been made in the last year.

Experiment	Best fit $\sin^2(2\theta_{13})$	Reference
Double Chooz	0.086 ± 0.051	[115]
T2K	$0.11\ ^{+0.10}_{-0.05}$	[45]
MINOS	$0.041\ ^{+0.041}_{-0.031}$	[44]
Daya Bay	0.092 ± 0.017	[48]
RENO	0.113 ± 0.023	[49]

Table 9.2: Summary of recent $\sin^2(2\theta_{13})$ measurements. The $\sin^2(2\theta_{13})$ 1σ confidence interval for long-baseline accelerator ν_e appearance experiments (T2K, MINOS) is taken for the normal hierarchy at $\delta = 0$ and $2\sin^2\theta_{23} = 1$.

The DC measurement of $\bar{\nu}_e$ disappearance corresponding to a relatively large value of $\sin^2(2\theta_{13})$ presented in this thesis has been subsequently corroborated by two similar reactor neutrino experiments. The uncertainties of these subsequent measurements are considerably smaller than the DC results because they both perform a multi-detector oscillation analysis (see Sec. 3.1.1). The DC near detector should start taking data in 2014 and will allow for a much more precise measurement of $\sin^2(2\theta_{13})$ similar to other reactor neutrino experiments.

In the short span of a year, θ_{13} has gone from being the last unknown mixing angle to being the harbinger of a new era of in the neutrino sector in which we move from discovery to precision measurements. The Double Chooz first results presented in this thesis gave crucial direction to the field of reactor $\bar{\nu}_e$ disappearance experiments, indicating that the value of $\sin^2(2\theta_{13})$ was just below current upper limits.

Bibliography

[1] E. Fermi. Versuch einer Theorie der β-Strahlen. I. *Zeitschrift fur Physik*, 88:161–177, 1934.

[2] C. L. Cowan et al. Detection of the free neutrino: a confirmation. *Science*, 124(3212):103–104, 1956.

[3] G. Danby et al. Observation of high-energy neutrino reactions and the existence of two kinds of neutrinos. *Phys. Rev. Lett.*, 9:36–44, Jul 1962.

[4] M. L. Perl et al. Evidence for anomalous lepton production in $e^+ - e^-$ annihilation. *Phys. Rev. Lett.*, 35:1489–1492, Dec 1975.

[5] K. Kodama et al. Observation of tau neutrino interactions. *Physics Letters B*, 504(3):218 – 224, 2001.

[6] B. Pontecorvo. Inverse beta processes and nonconservation of lepton charge. *Sov.Phys.JETP*, 7:172–173, 1958.

[7] Z. Maki et al. Remarks on the unified model of elementary particles. *Progress of Theoretical Physics*, 28(5):870–880, 1962.

[8] R. Davis et al. Search for neutrinos from the sun. *Phys. Rev. Lett.*, 20:1205–1209, May 1968.

[9] S. L. Glashow. Partial-symmetries of weak interactions. *Nuclear Physics*, 22(4):579 – 588, 1961.

[10] A. Salam and J.C. Ward. Electromagnetic and weak interactions. *Physics Letters*, 13(2):168 – 171, 1964.

[11] S. Weinberg. A model of leptons. *Phys. Rev. Lett.*, 19:1264–1266, Nov 1967.

[12] Ch. Kraus et al. Final results from phase II of the Mainz neutrino mass search in tritium beta decay. *Eur.Phys.J.*, C40:447–468, 2005.

[13] V.M Lobashev et al. Direct search for mass of neutrino and anomaly in the tritium beta-spectrum. *Physics Letters B*, 460(1-2):227 – 235, 1999.

[14] R. N. Mohapatra and G. Senjanović. Neutrino mass and spontaneous parity nonconservation. *Phys. Rev. Lett.*, 44:912–915, Apr 1980.

[15] H. Georgi et al. Hierarchy of interactions in unified gauge theories. *Phys. Rev. Lett.*, 33:451–454, Aug 1974.

[16] K. Nakamura et al. (Particle Data Group). The review of particle physics. *Journal of Physics G: Nuclear and Particle Physics*, 37(075021), 2010.

[17] M. Kobayashi and T. Maskawa. CP-Violation in the Renormalizable Theory of Weak Interaction. *Progress of Theoretical Physics*, 49:652–657, feb 1973.

[18] W-M Yao et al. Review of particle physics. *Journal of Physics G: Nuclear and Particle Physics*, 33(1):1, 2006.

[19] L. Wolfenstein. Neutrino oscillations in matter. *Phys. Rev. D*, 17:2369–2374, May 1978.

[20] H. Nunokawa et al. What fraction of boron-8 solar neutrinos arrive at the earth as a ν_2 mass eigenstate? *Phys. Rev. D*, 74:013006, Jul 2006.

[21] A. Aguilar et al. Evidence for neutrino oscillations from the observation of $\bar{\nu}_e$ appearance in a $\bar{\nu}_\mu$ beam. *Phys. Rev. D*, 64:112007, Nov 2001.

[22] Aguilar-Arevalo et al. Search for electron neutrino appearance at the $\delta m^2 \sim 1\text{eV}^2$ scale. *Phys. Rev. Lett.*, 98:231801, Jun 2007.

[23] Aguilar-Arevalo et al. Search for electron antineutrino appearance at the $\delta m^2 \sim 1\text{eV}^2$ scale. *Phys. Rev. Lett.*, 103:111801, Sep 2009.

[24] Y. Fukuda et al. Evidence for oscillation of atmospheric neutrinos. *Phys. Rev. Lett.*, 81:1562–1567, Aug 1998.

[25] M. H. Ahn et al. Measurement of neutrino oscillation by the K2K experiment. *Phys. Rev. D*, 74:072003, Oct 2006.

[26] P. Adamson et al. Measurement of the neutrino mass splitting and flavor mixing by minos. *Phys. Rev. Lett.*, 106:181801, May 2011.

[27] K. Abe et al. First muon-neutrino disappearance study with an off-axis beam. *Phys. Rev. D*, 85:031103, Feb 2012.

[28] J. N. Bahcall et al. New solar opacities, abundances, helioseismology, and neutrino fluxes. *The Astrophysical Journal Letters*, 621(1):L85, 2005.

[29] W. Hampel et al. GALLEX solar neutrino observations: Results for GALLEX IV. *Phys.Lett.*, B447:127–133, 1999.

[30] M. Altmann et al. GNO solar neutrino observations: Results for GNO I. *Phys.Lett.*, B490:16–26, 2000.

[31] J. N. Abdurashitov et al. Solar neutrino flux measurements by the Soviet-American gallium experiment (SAGE) for half the 22-year solar cycle. *Journal of Experimental And Theoretical Physics*, 95(2):181, 2002.

[32] Y. Fukuda et al. Solar neutrino data covering solar cycle 22. *Phys. Rev. Lett.*, 77:1683–1686, Aug 1996.

[33] B. Aharmim et al. Independent measurement of the total active ^{8}B solar neutrino flux using an array of ^{3}He proportional counters at the sudbury neutrino observatory. *Phys. Rev. Lett.*, 101:111301, Sep 2008.

[34] S. Abe et al. Precision measurement of neutrino oscillation parameters with KamLAND. *Phys. Rev. Lett.*, 100:221803, Jun 2008.

[35] Y. Declais et al. Search for neutrino oscillations at 15-meters, 40-meters, and 95-meters from a nuclear power reactor at Bugey. *Nucl.Phys.*, B434:503–534, 1995.

[36] G. Zacek et al. Neutrino-oscillation experiments at the gösgen nuclear power reactor. *Phys. Rev. D*, 34:2621–2636, Nov 1986.

[37] A.A. Kuvshinnikov et al. Measuring the $\bar{\nu}_e + p \to e^+ + n$ cross-section and beta decay axial constant in a new experiment at Rovno NPP reactor. (In Russian). *JETP Lett.*, 54:253–257, 1991.

[38] G.S. Vidyakin et al. Limitations on the characteristics of neutrino oscillations. *JETP Lett.*, 59:390–393, 1994.

[39] Z. D. Greenwood et al. Results of a two position reactor neutrino oscillation experiment. *Phys. Rev.*, D53:6054–6064, 1996.

[40] F. Boehm et al. Final results from the palo verde neutrino oscillation experiment. *Phys. Rev. D*, 64:112001, Nov 2001.

[41] Y. Declais et al. Study of reactor antineutrino interaction with proton at bugey nuclear power plant. *Physics Letters B*, 338(2-3):383 – 389, 1994.

[42] M. Apollonio et al. Search for neutrino oscillations on a long base-line at the CHOOZ nuclear power station. *Eur. Phys. J.*, C27:331–374, 2003.

[43] A. Cervera et al. Golden measurements at a neutrino factory. *Nucl.Phys.*, B579:17–55, 2000.

[44] P. Adamson et al. Improved search for muon-neutrino to electron-neutrino oscillations in minos. *Phys. Rev. Lett.*, 107:181802, Oct 2011.

[45] K. Abe et al. Indication of electron neutrino appearance from an accelerator-produced off-axis muon neutrino beam. *Phys. Rev. Lett.*, 107:041801, Jul 2011.

[46] D. S. Ayres et al. Proposal to build a 30 kiloton off-axis detector to study $\nu_\mu \to \nu_e$ oscillations in the numi beamline, 2005. http://nova-docdb.fnal.gov/cgi-bin/ShowDocument?docid=593.

[47] F. Ardellier et al. Double Chooz: A Search for the neutrino mixing angle θ_{13}, 2006. arXiv:0606025 [hep-ex].

[48] F. P. An et al. Observation of electron-antineutrino disappearance at Daya Bay, 2009. arXiv:1203.1669v2 [hep-ex].

[49] S-B Kim et al. Observation of reactor electron antineutrino disappearance in the RENO experiment, 2012. arXiv:1204.0626v2 [hep-ex].

[50] J.H. Christenson et al. Evidence for the 2π Decay of the K_2^0 Meson. *Phys.Rev.Lett.*, 13:138–140, 1964.

[51] V.A. Kuzmin et al. On anomalous electroweak baryon-number non-conservation in the early universe. *Physics Letters B*, 155:36 – 42, 1985.

[52] M. Fukugita and T. Yanagida. Baryogenesis Without Grand Unification. *Phys.Lett.*, B174:45, 1986.

[53] M. Apollonio et al. Initial results from the chooz long baseline reactor neutrino oscillation experiment. *Physics Letters B*, 420(3-4):397 – 404, 1998.

[54] D.H. Wilkinson. Analysis of neutron β-decay. *Nuclear Physics A*, 377(2-3):474 – 504, 1982.

[55] P. Vogel and J. F. Beacom. Angular distribution of neutron inverse beta decay, $\bar{\nu}_e + p \rightarrow e^+ + n$. *Phys. Rev. D*, 60:053003, Jul 1999.

[56] Th. A. Mueller et al. Improved predictions of reactor antineutrino spectra. *Phys. Rev. C*, 83:054615, May 2011.

[57] W. R. Leo. *Techniques for nuclear and particle physics experiments.* Springer-Verlag, New York, 2 edition, 1994.

[58] C. Aberle et al. Large scale Gd-beta-diketonate based organic liquid scintillator production for antineutrino detection, 2011. arXiv:1112.5941v1 [physics.ins-det].

[59] Christoph Aberle. *Optimization, simulation and analysis of the scintillation signals in the Double Chooz experiment*. PhD thesis, Ruprecht-Karls-Universität, Heidelberg, Germany, 2011.

[60] T. Lasserre. Target H preliminary results. *Double Chooz Internal Note: DC-doc-3281-v1*, 2011.

[61] Y. Abe and M. Ishitsuka. Mean gain and t0 calibration constants from IDLI for 3 months data. *Double Chooz Internal Note: DC-doc-3017-v1*, 2011.

[62] C. Bemporad et al. Reactor-based neutrino oscillation experiments. *Rev. Mod. Phys.*, 74:297–328, Mar 2002.

[63] V. Kopeikin et al. Reactor as a source of antineutrinos: Thermal fission energy. *Physics of Atomic Nuclei*, 67:1892–1899, 2004.

[64] O. Meplan. MURE. MCNP utility for reactor evolution. User Guide. Version 1.0. *Tech. Rep. LPSC 0912 and IPNO-09-01*, 2009.

[65] J. F. Briesmeister. MCNP - A general monte carlo N-particle transport code, Version 4C. *LA-13709-M*, 2009.

[66] R. Roy G. Marleau and A. Hebert. DRAGON: A collision probability transport code for cell and supercell calculations. *Report IGE-157*, Institut de génie nucléaire, École Polytechnique de Montréal, Montréal, Québec, 1994.

[67] A. Santamarina, D. Bernard, Y. Rugama, and OECD Nuclear Energy Agency. *The JEFF-3.1.1 Nuclear Data Library: JEFF Report 22, Validation Results from JEF-2.2 to JEFF-3.1.1.* Data bank. Nuclear Energy Agency, Organisation for Economic Cooperation and Development, 2009. see also $http://www.oecd-nea.org/dbforms/data/eva/evatapes/jeff\_31/index-JEFF3.1.1.html$.

[68] E. Tournu et al. Improving pressurized water reactor performance through instrumentation: Application case of reducing uncertainties on thermal power. *EPRI*, page 1001470, 2001.

[69] C.L. Jones et al. Reactor simulation for antineutrino experiments using DRAGON and MURE, 2012. arXiv:1109.5379v2 [nucl-ex].

[70] P. Huber. Determination of antineutrino spectra from nuclear reactors. *Phys. Rev. C*, 84:024617, Aug 2011.

[71] F. von Feilitzsch et al. Experimental beta-spectra from ^{239}Pu and ^{235}U thermal neutron fission products and their correlated antineutrino spectra. *Physics Letters B*, 118:162 – 166, 1982.

[72] K. Schreckenbach et al. Determination of the antineutrino spectrum from ^{235}U thermal neutron fission products up to 9.5 MeV. *Physics Letters B*, 160:325 – 330, 1985.

[73] A.A. Hahn et al. Antineutrino spectra from ^{241}Pu and ^{239}Pu thermal neutron fission products. *Physics Letters B*, 218(3):365 – 368, 1989.

[74] Evaluated nuclear structure data file. National Nuclear Data Center. http://www.nndc.bnl.gov/ensdf/.

[75] S. A. Fayans. Radiative corrections and recoil effects in the reaction $\bar{\nu}_e + p \rightarrow n + e^+$ at low energies. (In Russian). *Sov. J. Nucl. Phys.*, 42:590, 1985.

[76] A. Kurylov et al. Radiative corrections to low-energy neutrino reactions. *Phys. Rev. C*, 67:035502, Mar 2003.

[77] S. Agostinelli et al. GEANT4: A Simulation toolkit. *Nucl.Instrum.Meth.*, A506:250–303, 2003.

[78] V. McLane et al. ENDF/B-VI summary documentation. *BNL-NCS-17541, 4th Edition, Suppl. I*, 1996. http://www.nndc.bnl.gov/csewg/.

[79] J B Birks. Scintillations from organic crystals: Specific fluorescence and relative response to different radiations. *Proceedings of the Physical Society. Section A*, 64(10):874, 1951.

[80] Dario Motta and Stefan Schonert. Optical properties of Bialkali photocathodes. *Nucl.Instrum.Meth.*, A539:217–235, 2005.

[81] J. P. Both et al. User manual for version 4.3 of the `TRIPOLI-4` monte carlo method particle transport computer code. *CEA Report: CEA-R-6044, CEA/Saclay, France*, 2003.

[82] T. Mueller. Spill-in/out studies and other interesting stuff about neutron physics. *Double Chooz Internal Note: DC-doc-3031-v1*, 2011.

[83] J. Haser et al. Update on our spill-in/out values. *Double Chooz Internal Note: DC-doc-3445-v3*, 2011.

[84] Z. Djurcic et al. Calibration source data info. *Double Chooz Internal Note*, 2011.

[85] J. Busenitz et al. Summary information for the first step of the source deployment. *Double Chooz Internal Note: DC-doc-2946-v1*, 2011.

[86] J.T. Larsen et al. A seven-detector system for γ–γ angular correlations. *Nuclear Instruments and Methods*, 69(2):229 – 239, 1969.

[87] Yu. Musienko et al. Studies of neutron irradiation of avalanche photodiodes using Cf-252. *Nucl.Instrum.Meth.*, A447:437–458, 2000.

[88] N. Ensslin et al. Application guide to neutron multiplicity counting. *LA-13422-M*, 1998.

[89] T. Valentine. Evaluation of prompt fission gamma rays for use in simulating nuclear safeguard measurements. *ORNL/TM-1999/300*, 1999.

[90] A. Remoto. Muon identification: synthesis and EU++ proposal. *Double Chooz Internal Note: DC-doc-3230-v2*, 2011.

[91] F. Suekane. Report for the light noise. *Double Chooz Internal Note: DC-doc-2565-v1*, 2011.

[92] T. Kawasaki. Treatment of PMT 263 noisy run. *Double Chooz Internal Note: DC-doc-3132-v1*, 2011.

[93] G. Horton-Smith. Fine corrections to live time. *Double Chooz Internal Note: DC-doc-3288-v1*, 2011.

[94] P. Chang. Neutrino efficiency analysis results. *Double Chooz Internal Note: DC-doc-3364-v3*, 2012.

[95] F. Ajzenberg-Selove. Energy levels of light nuclei A = 11-12. *Nucl.Phys.*, A506:1–158, 1990.

[96] D.R. Tilley et al. Energy levels of light nuclei. *Nuclear Physics A*, 745:155 – 362, 2004.

[97] Emily Conover et al. Cosmogenics backgrounds: United synthesis. *Double Chooz Internal Note: DC-doc-3257-v2*, 2010.

[98] Y. Prezado et al. Large asymmetry in the strongest β-transition for A=9. *Physics Letters B*, 576:55 – 61, 2003.

[99] Y. Prezado et al. Low-lying resonance states in the ^{9}Be continuum. *Physics Letters B*, 618(1-4):43 – 50, 2005.

[100] T. A. D. Brown et al. Decay studies for states in ^{9}Be up to 11 MeV: Insights into the $n +^8$ Be and $\alpha +^5$ He cluster structure. *Phys. Rev. C*, 76:054605, Nov 2007.

[101] L. A. Winslow. Decay spectrum for ^{9}Li. *Double Chooz Internal Note: DC-doc-3482-v2*, 2011.

[102] Alfred Tang et al. Muon simulations for Super-Kamiokande, KamLAND, and CHOOZ. *Phys. Rev. D*, 74:053007, Sep 2006.

[103] A. Meregaglia et al. Fast neutrons: simulation and updated results. *Double Chooz Internal Note: DC-doc-1327-v1*, 2010.

[104] D. Shrestha. Fast neutron analysis MC and data. *Double Chooz Internal Note: DC-doc-3117-v2*, 2011.

[105] A. Cabrera. IV-Tagged correlated background estimation. *Double Chooz Internal Note: DC-doc-3471-v6*, 2011.

[106] K. Nakajima. A Technical Note of a Fast Neutron Analysis at 1st Publication Stage. *Double Chooz Internal Note: DC-doc-3631-v2*, 2012.

[107] M. H. Shaevitz. Separating components of error matrices. *BooNE Technical Note: TN-253*, 2008.

[108] S. J. Brice. An improved way to propagate π^+ production uncertainties. *MiniBooNE Technical Note: TN-257*, 2008.

[109] J. Busentiz et al. Final fits framework. *Double Chooz Internal Note: DC-doc-1755-v1*, 2010.

[110] R. Brun and Fons Rademakers. An object oriented data analysis framework. *Phys. Rev.*, A389:81–86, 1997. http://root.cern.ch/.

[111] F. James. Minuit: Function minimization and error analysis. reference manual. *CERN Program Library Long Writeup D506*, 1998. http://wwwasdoc.web.cern.ch/wwwasdoc/minuit/minmain.html.

[112] D. Stump et al. Uncertainties of predictions from parton distribution functions. i. the lagrange multiplier method. *Phys. Rev. D*, 65:014012, Dec 2001.

[113] Hiroshi Nunokawa et al. Another possible way to determine the neutrino mass hierarchy. *Phys. Rev.*, D72:013009, 2005.

[114] Gary J. Feldman and Robert D. Cousins. Unified approach to the classical statistical analysis of small signals. *Phys. Rev. D*, 57:3873–3889, Apr 1998.

[115] Y. Abe et al. Indication of reactor $\bar{\nu}_e$ disappearance in the double chooz experiment. *Phys. Rev. Lett.*, 108:131801, Mar 2012.

Appendix A

Double Chooz First Results Publication

The Double Chooz $\bar{\nu}_e$ disappearance search presented in this work was published in Physical Review Letters. In the following pages we reproduce the article accepted for publication.

PRL 108, 131801 (2012) PHYSICAL REVIEW LETTERS week ending 30 MARCH 2012

Indication of Reactor $\bar{\nu}_e$ Disappearance in the Double Chooz Experiment

Y. Abe,[28] C. Aberle,[21] T. Akiri,[4,15] J. C. dos Anjos,[5] F. Ardellier,[15] A. F. Barbosa,[5,*] A. Baxter,[26] M. Bergevin,[9] A. Bernstein,[16] T. J. C. Bezerra,[30] L. Bezrukhov,[14] E. Blucher,[6] M. Bongrand,[15,30] N. S. Bowden,[16] C. Buck,[21] J. Busenitz,[2] A. Cabrera,[4] E. Caden,[10] L. Camilleri,[8] R. Carr,[8] M. Cerrada,[7] P.-J. Chang,[17] P. Chimenti,[34] T. Classen,[9,16] A. P. Collin,[15] E. Conover,[6] J. M. Conrad,[20] S. Cormon,[25] J. I. Crespo-Anadón,[7] M. Cribier,[15,4] K. Crum,[6] A. Cucoanes,[25,15] M. V. D'Agostino,[3] E. Damon,[10] J. V. Dawson,[4,36] S. Dazeley,[16] M. Dierckxsens,[6] D. Dietrich,[33] Z. Djurcic,[3] M. Dracos,[24] V. Durand,[15,4] Y. Efremenko,[27] M. Elnimr,[25] Y. Endo,[29] A. Etenko,[19] E. Falk,[26] M. Fallot,[25] M. Fechner,[15] F. von Feilitzsch,[31] J. Felde,[9] S. M. Fernandes,[26] D. Franco,[4] A. J. Franke,[8] M. Franke,[31] H. Furuta,[30] R. Gama,[5] I. Gil-Botella,[7] L. Giot,[25] M. Göger-Neff,[31] L. F. G. Gonzalez,[35] M. C. Goodman,[3] J. TM. Goon,[2] D. Greiner,[33] B. Guillon,[25] N. Haag,[31] C. Hagner,[11] T. Hara,[18] F. X. Hartmann,[21] J. Hartnell,[26] T. Haruna,[29] J. Haser,[21] A. Hatzikoutelis,[27] T. Hayakawa,[22,15] M. Hofmann,[31] G. A. Horton-Smith,[17] M. Ishitsuka,[28] J. Jochum,[33] C. Jollet,[24] C. L. Jones,[20] F. Kaether,[21] L. Kalousis,[24] Y. Kamyshkov,[27] D. M. Kaplan,[13] T. Kawasaki,[22] G. Keefer,[16] E. Kemp,[35] H. de Kerret,[4,36] Y. Kibe,[28] T. Konno,[28] D. Kryn,[4] M. Kuze,[28] T. Lachenmaier,[33] C. E. Lane,[10] C. Langbrandtner,[21] T. Lasserre,[15,4] A. Letourneau,[15] D. Lhuillier,[15] H. P. Lima Jr,[5] M. Lindner,[21] Y. Liu,[2] J. M. López-Castanõ,[7] J. M. LoSecco,[23] B. K. Lubsandorzhiev,[14] S. Lucht,[1] D. McKee,[2,17] J. Maeda,[29] C. N. Maesano,[9] C. Mariani,[8] J. Maricic,[10] J. Martino,[25] T. Matsubara,[29] G. Mention,[15] A. Meregaglia,[24] T. Miletic,[10] R. Milincic,[10] A. Milzstajn,[15] H. Miyata,[22] D. Motta,[15,*] Th. A. Mueller,[15,30] Y. Nagasaka,[12] K. Nakajima,[22] P. Novella,[7] M. Obolensky,[4] L. Oberauer,[31] A. Onillon,[25] A. Osborn,[27] I. Ostrovskiy,[2] C. Palomares,[7] S. J. M. Peeters,[26] I. M. Pepe,[5] S. Perasso,[10] P. Perrin,[15] P. Pfahler,[31] A. Porta,[25] W. Potzel,[31] R. Queval,[15] J. Reichenbacher,[2] B. Reinhold,[21] A. Remoto,[25,4] D. Reyna,[3] M. Röhling,[33] S. Roth,[1] H. A. Rubin,[13] Y. Sakamoto,[32] R. Santorelli,[7] F. Sato,[29] S. Schönert,[31] S. Schoppmann,[1] U. Schwan,[21] T. Schwetz,[21] M. H. Shaevitz,[8] D. Shrestha,[17] J-L. Sida,[15] V. Sinev,[14,15] M. Skorokhvatov,[19] E. Smith,[10] J. Spitz,[20] A. Stahl,[1] I. Stancu,[2] M. Strait,[6] A. Stüken,[1] F. Suekane,[30] S. Sukhotin,[19] T. Sumiyoshi,[29] Y. Sun,[2] Z. Sun,[15] R. Svoboda,[9] H. Tabata,[30] N. Tamura,[22] K. Terao,[20] A. Tonazzo,[4] M. Toups,[8] H. H. Trinh Thi,[31] C. Veyssiere,[15] S. Wagner,[21] H. Watanabe,[21] B. White,[27] C. Wiebusch,[1] L. Winslow,[20] M. Worcester,[6] M. Wurm,[11] E. Yanovitch,[14] F. Yermia,[25] K. Zbiri,[25,10] and V. Zimmer[31]

(Double Chooz Collaboration)

[1]*III. Physikalisches Institut, RWTH Aachen University, 52056 Aachen, Germany*
[2]*Department of Physics and Astronomy, University of Alabama, Tuscaloosa, Alabama 35487, USA*
[3]*Argonne National Laboratory, Argonne, Illinois 60439, USA*
[4]*APC, AstroParticule et Cosmologie, Université Paris Diderot, CNRS/IN2P3, CEA/IRFU, Observatoire de Paris, Sorbonne Paris Cité, 75205 Paris Cedex 13, France*
[5]*Centro Brasileiro de Pesquisas Físicas, Rio de Janeiro, RJ, cep 22290-180, Brazil*
[6]*The Enrico Fermi Institute, The University of Chicago, Chicago, Illinois 60637, USA*
[7]*Centro de Investigaciones Energéticas, Medioambientales y Tecnológicas, CIEMAT, E-28040, Madrid, Spain*
[8]*Columbia University, New York, New York 10027, USA*
[9]*University of California, Davis, California 95616-8677, USA*
[10]*Physics Department, Drexel University, Philadelphia, Pennsylvania 19104, USA*
[11]*Institut für Experimentalphysik, Universität Hamburg, 22761 Hamburg, Germany*
[12]*Hiroshima Institute of Technology, Hiroshima, 731-5193, Japan*
[13]*Department of Physics, Illinois Institute of Technology, Chicago, Illinois 60616, USA*
[14]*Institute of Nuclear Research of the Russian Academy of Science, Moscow 117312, Russia*
[15]*Commissariat à l'Energie Atomique et aux Energies Alternatives, Centre de Saclay, IRFU, 91191 Gif-sur-Yvette, France*
[16]*Lawrence Livermore National Laboratory, Livermore, California 94550, USA*
[17]*Department of Physics, Kansas State University, Manhattan, Kansas 66506, USA*
[18]*Department of Physics, Kobe University, Kobe, 657-8501, Japan*
[19]*NRC Kurchatov Institute, 123182 Moscow, Russia*
[20]*Massachusetts Institute of Technology, Cambridge, Massachusetts 02139, USA*
[21]*Max-Planck-Institut für Kernphysik, 69029 Heidelberg, Germany*
[22]*Department of Physics, Niigata University, Niigata, 950-2181, Japan*
[23]*University of Notre Dame, Notre Dame, Indiana 46556-5670, USA*
[24]*IPHC, Université de Strasbourg, CNRS/IN2P3, F-67037 Strasbourg, France*

PRL 108, 131801 (2012) PHYSICAL REVIEW LETTERS week ending 30 MARCH 2012

[25]SUBATECH, CNRS/IN2P3, Université de Nantes, Ecole des Mines de Nantes, F-44307 Nantes, France
[26]Department of Physics and Astronomy, University of Sussex, Falmer, Brighton BN1 9QH, United Kingdom
[27]Department of Physics and Astronomy, University of Tennessee, Knoxville, Tennessee 37996, USA
[28]Department of Physics, Tokyo Institute of Technology, Tokyo, 152-8551, Japan
[29]Department of Physics, Tokyo Metropolitan University, Tokyo, 192-0397, Japan
[30]Research Center for Neutrino Science, Tohoku University, Sendai 980-8578, Japan
[31]Physik Department, Technische Universität München, 85747 Garching, Germany
[32]Tohoku Gakuin University, Sendai, 981-3193, Japan
[33]Kepler Center for Astro and Particle Physics, Universität Tübingen, 72076, Tübingen, Germany
[34]Universidade Federal do ABC, UFABC, Sao Paulo, Santo André, SP, Brazil
[35]Universidade Estadual de Campinas-UNICAMP, Campinas, SP, Brazil
[36]Laboratoire Neutrino de Champagne Ardenne, domaine d'Aviette, 08600 Rancennes, France
(Received 27 January 2012; published 28 March 2012)

The Double Chooz experiment presents an indication of reactor electron antineutrino disappearance consistent with neutrino oscillations. An observed-to-predicted ratio of events of $0.944 \pm 0.016(\text{stat}) \pm 0.040(\text{syst})$ was obtained in 101 days of running at the Chooz nuclear power plant in France, with two 4.25 GW_{th} reactors. The results were obtained from a single 10 m^3 fiducial volume detector located 1050 m from the two reactor cores. The reactor antineutrino flux prediction used the Bugey4 flux measurement after correction for differences in core composition. The deficit can be interpreted as an indication of a nonzero value of the still unmeasured neutrino mixing parameter $\sin^2 2\theta_{13}$. Analyzing both the rate of the prompt positrons and their energy spectrum, we find $\sin^2 2\theta_{13} = 0.086 \pm 0.041(\text{stat}) \pm 0.030(\text{syst})$, or, at 90% C.L., $0.017 < \sin^2 2\theta_{13} < 0.16$.

DOI: 10.1103/PhysRevLett.108.131801 PACS numbers: 14.60.Pq, 13.15.+g, 25.30.Pt, 95.55.Vj

We report first results of a search for a nonzero neutrino oscillation [1] mixing angle θ_{13} based on reactor antineutrino disappearance. This is the last of the three neutrino oscillation mixing angles [2,3] for which only upper limits [4,5] are available. θ_{13} sets the required sensitivity of long-baseline experiments attempting to measure CP violation in the neutrino sector or the mass hierarchy.

In reactor experiments [6,7] addressing the disappearance of $\bar{\nu}_e$, θ_{13} determines the survival probability of electron antineutrinos at the "atmospheric" squared-mass difference Δm^2_{atm}. This probability is given by

$$P_{\text{surv}} \approx 1 - \sin^2 2\theta_{13} \sin^2(1.267 \Delta m^2_{\text{atm}} L/E), \qquad (1)$$

where L is the distance from the reactor to the detector in meters and E the energy of the antineutrino in MeV. The full formula can be found in Ref. [1]. Equation (1) provides a direct way to measure θ_{13}, since the only additional input is the well measured value of $|\Delta m^2_{\text{atm}}| = (2.32^{+0.12}_{-0.08}) \times 10^{-3}$ eV^2 [8]. Other running reactor experiments [9,10] are using the same technique.

Electron antineutrinos of <9 MeV are produced by reactors and detected through inverse beta decay (IBD): $\bar{\nu}_e + p \rightarrow e^+ + n$. Detectors based on hydrocarbon liquid scintillators provide the free proton targets. The IBD signature is a coincidence of a prompt positron signal followed by a delayed neutron capture. The $\bar{\nu}_e$ energy $E_{\bar{\nu}_e}$ is reconstructible from E_{prompt}, the positron visible energy ($E_{\bar{\nu}_e} \cong E_{\text{prompt}} + 0.78$ MeV).

Recently, indications of nonzero θ_{13} have been reported by two accelerator appearance experiments: T2K [11] and MINOS [12]. Global fits (e.g., [13,14]) indicate central values in the range $0.05 < \sin^2 2\theta_{13} < 0.10$, accessible to the Double Chooz experiment [15,16].

We present here our first results with a detector located $\sim$1050 m from the two 4.25 GW_{th} thermal power reactors of the Chooz nuclear power plant and under a 300 MWE rock overburden. The analysis is based on 101 days of data including 16 days with one reactor off and 1 day with both reactors off.

The antineutrino flux of each reactor depends on its thermal power and, for the four main fissioning isotopes, ^{235}U, ^{239}Pu, ^{238}U, and ^{241}Pu, their fraction of the total fuel content, their energy released per fission, and their fission and capture cross sections. The fission rates and associated errors were evaluated by using two reactor simulation codes: MURE [17,18] and DRAGON [19]. This allowed assessing the sensitivity to important reactor parameters. These simulations were evaluated through benchmarks [20] and comparisons with Electricité de France (EDF) assembly simulations. The maximum discrepancies observed were included in the fission rate systematic error.

MURE was used to develop a 3D simulation of the reactor cores. EDF provided the information required to simulate the fission rates including initial burnups of assemblies. To determine the inventories of each assembly composing the core at the startup of the data-taking cycle, assembly simulations were performed and the inventories at the given burnup computed. The energies per fission computed by Kopeikin, Mikaelyan, and Sinev [21] and nuclear data evaluated from the JEFF3.1 database [22] were used. The evolutions of the core simulations with time were performed by using the thermal power and the boron

concentration from the EDF database, yielding the relative contributions to fissions of the main isotopes.

The associated antineutrino flux was computed by using the improved spectra from Ref. [23], converted from the Institut Laue-Langevin reference electron spectra [24–26], and the updated *ab initio* calculation of the ^{238}U spectrum [27]. The Institut Laue-Langevin spectra were measured after irradiating U or Pu for ~1 day. Contributions from β decays with lifetimes longer than 1 day were accounted for as prescribed in Ref. [27].

The Double Chooz detector system (Fig. 1) consists of a main detector, an outer veto, and calibration devices. The main detector comprises four concentric cylindrical tanks filled with liquid scintillators or mineral oil. The innermost 8 mm thick transparent (UV to visible) acrylic vessel houses the 10 m^3 ν-target liquid, a mixture of *n*-dodecane, ortho-phenylxylylethane, 2,5-diphenyloxazole, bis-(2-methylstyryl)benzene, and 1 g gadolinium/l as a beta-diketonate complex. The scintillator choice emphasizes radiopurity and long term stability [28]. The ν-target volume is surrounded by the γ catcher, a 55 cm thick Gd-free liquid scintillator layer in a second 12 mm thick acrylic vessel, used to detect γ rays escaping from the ν target. The light yield of the γ catcher was chosen to provide identical photoelectron (pe) yield across these two layers [29]. Next is the buffer, a 105 cm thick mineral oil layer. It shields from radioactivity of photomultipliers (PMTs) and of the rock and is an improvement over CHOOZ [4]. 390 10-inch PMTs [30–32] are installed on the stainless steel buffer tank inner wall to collect light from the inner volumes. These three volumes and the PMTs constitute the inner detector (ID).

Outside the ID, and optically separated from it, is a 50 cm thick ''inner veto'' liquid scintillator (IV). It is equipped with 78 8-inch PMTs and functions as a cosmic muon veto and as a shield to spallation neutrons produced outside the detector. The detector is surrounded by 15 cm of demagnetized steel to suppress external γ rays. The main detector is covered by an outer veto system.

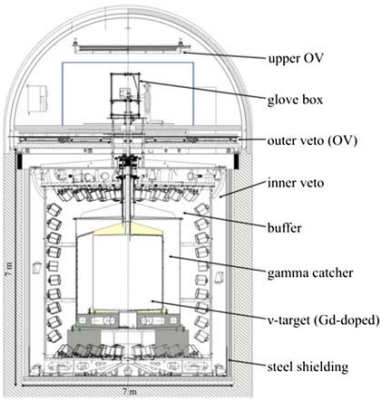

FIG. 1 (color online). A cross-sectional view of the Double Chooz detector system.

The readout is triggered by custom energy sum electronics [33–35]. The ID PMTs are separated into two groups of 195 PMTs uniformly distributed throughout the volume, and the PMT signals in each group are summed. The signals of the IV PMTs are also summed. If any sum is above a set energy threshold, the detector is read out with 500 MHz flash-ADC electronics [36,37] with customized firmware and a deadtime-free acquisition system. Upon each trigger, a 256 ns interval of the waveforms of both ID and IV signals is recorded. The low trigger rate (120 Hz) allowed the ID readout threshold to be set at 350 keV, well below the 1.02 MeV minimum energy of an IBD positron, greatly reducing the threshold systematics.

The experiment is calibrated by several methods. A multiwavelength LED-fiber light injection system produces fast light pulses illuminating the PMTs from fixed positions. Radio-isotopes ^{137}Cs, ^{68}Ge, ^{60}Co, and ^{252}Cf were deployed in the target along the vertical symmetry axis and, in the γ catcher, through a rigid loop traversing the interior and passing along boundaries with the target and the buffer. The detector was monitored by using spallation neutron captures on H and Gd, residual natural radioactivity, and daily light injection system runs. The stability of the peak energy of neutron captures on Gd in IBD candidates is shown in Fig. 2. The energy response was found to be stable within 1% over time.

The signature of IBD events is a delayed coincidence between a prompt positron energy deposition E_{prompt} and a delayed energy deposition E_{delay} due to the neutron capture on H or Gd within Δt_{e^+n}. The fiducial volume is constrained to the target vessel without position cuts by requiring a $\bar{\nu}_e$ event to have a capture on Gd, identified by its emission of ~8 MeV in γ rays. The analysis compares the number and energy distribution of detected events to a prediction based on the reactor data.

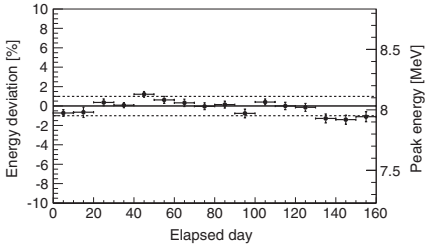

FIG. 2. The peak of the energy of neutron captures on Gd in IBD events (right scale) and its deviation from its average value (left scale) as a function of the elapsed (calendar) day.

Energy measurements are based on the total charge Q_{tot} collected by the PMTs and corrected for gain variations. The energy is reconstructed by scaling Q_{tot} so that the energy of the gamma emitted following neutron capture on H reconstructs to 2.22 MeV at the target center. This corresponds to ~200 pe/MeV. Our Monte Carlo (MC) calculation, based on GEANT4 [38], is used to model the detector response and calculate its acceptance. It uses parameters for quenching [39], absorption, reemission, refraction, etc., determined from laboratory measurements of the detector liquids. Comparisons between actual and simulated calibration data were used to develop a parametric function to correct the simulation and to assess the uncertainties in the energy reconstruction. The function is a product of two factors. One, dependent on energy, ranges from 0.97 to 1.05 for 0.7–10.0 MeV. The other, dependent on position, ranges from 0.94 to 1.00 over the target volume.

The following criteria are applied to select $\bar{\nu}_e$ candidates. Triggers within 1000 μs after a cosmic muon crossing the IV or ID (46 s^{-1}) are rejected to limit spallation neutron and cosmogenic backgrounds. This is followed by five selections: (1) a cut rejecting events caused by some sporadically glowing PMT bases, producing light illuminating a few PMTs and spread out in time: $Q_{\text{max}}/Q_{\text{tot}} < 0.09$ (0.06) for the prompt (delayed) energy and $\text{rms}(t_{\text{start}}) < 40$ ns, where Q_{max} is the maximum charge recorded by a single PMT and $\text{rms}(t_{\text{start}})$ is the standard deviation of the times of the first pulse on each PMT; (2) $0.7\,\text{MeV} < E_{\text{prompt}} < 12.2\,\text{MeV}$; (3) $6.0\,\text{MeV} < E_{\text{delay}} < 12.0$ MeV; (4) $2\ \mu\text{s} < \Delta t_{e^+n} < 100\ \mu$s, where the lower cut eliminates correlated noise and the upper cut is determined by the ~30 μs capture time on Gd; (5) a multiplicity cut to reject correlated backgrounds defined as no additional valid trigger from 100 μs preceding the prompt candidate to 400 μs after it. These selections yield 4121 candidates or 42.6 ± 0.7 events/day, uniformly distributed within the target, for an analysis live time of 96.8 days.

Contributions from residual background events have been estimated as follows. Uncorrelated coincidences result mainly from the association of a prompt energy deposition due to radioactivity (7.6 s^{-1}) and a later candidate neutron capture (≃ 20/hour). This background is measured by applying selections 1–5 but modifying 4 such that the 2–100 μs time window is shifted by 1000 μs relative to the prompt trigger. To improve the precision of this background measurement, 198 such windows, each shifted from the previous one by 500 μs, were used, leading to 0.33 ± 0.03 events/day.

Fast neutrons induced by muons traversing the rock can interact in the target producing a recoil proton and, later, be captured, simulating an IBD event. We estimate this rate to be 0.83 ± 0.38 events per day (including a contribution from stopping muons) by applying cuts 1–5 but modifying selection 2 such that $12.2\,\text{MeV} < E_{\text{prompt}} < 30$ MeV, and then extrapolating to the signal region, assuming a flat energy spectrum. We account for an uncertainty in this extrapolation, and for the contribution of stopping muons, by including a shape error ranging up to ±70% of the flat extrapolation at lower energies.

^{9}Li β-n emitters are produced preferentially by energetic muons. They were studied by searching for a triple delayed coincidence between a muon depositing >600 MeV in the detector and a $\bar{\nu}_e$-like pair of events, where the delay between the muon and prompt event is dictated by the 178 ms ^{9}Li half-life, which precludes vetoing on all muons. Fitting the resulting time distribution with a flat component and an exponential with the ^{9}Li lifetime results in an estimated rate of 2.3 ± 1.2 events/day. This rate is assigned the energy spectrum of the ^{9}Li decay branches. A shape uncertainty of up to 20% accounts for uncertainties in some decay branches. ^{8}He is not considered, since it is less abundantly produced [40]. The total background rate $3.46 \pm 1.26\ \text{d}^{-1}$ is summarized in Table I.

The overall background envelope is independently verified by analyzing 22.5 hours of both-reactors-off data (< 0.3 residual $\bar{\nu}_e$ events). Two $\bar{\nu}_e$ candidates, with prompt energies of 4.8 and 9.8 MeV, pass cuts 1–5. They were associated within 30 cm and 220 ms with the closest energetic muon and are thus likely to be associated with ^{9}Li.

Detector-related corrections and efficiencies as well as their uncertainties were evaluated by using the MC simulations. The energy response introduces a 1.7% systematic uncertainty determined from fits to calibration data. The number of free protons in the target scintillator, 6.747×10^{29} based on its weight measurement, has an uncertainty of 0.3%, originating from the knowledge of the scintillator hydrogen ratio. A simulation including molecular bond effects [41] indicates that the number of IBD events occurring in the gamma catcher with the neutron captured in the target (spill in) exceeds the number of events in the target with the neutron escaping to the gamma catcher (spill out) by $1.4\% \pm 0.4\%$, 0.8% lower than our standard MC prediction, which was therefore reduced accordingly. Above the 700 keV analysis threshold, the trigger efficiency is $100.0^{+0}_{-0.4}\%$, assessed with a low threshold prescaled trigger. Calibration data taken with the 252 Cf source were used to check the MC for biases in the neutron selection criteria and estimate their contributions to

TABLE I. The breakdown of the estimated background rate. Additional shape uncertainties are described in the text.

Background	Rate/day	Syst. uncertainty (% of signal)
Accidental	0.33 ± 0.03	<0.1
Fast neutron	0.83 ± 0.38	0.9
^{9}Li	2.3 ± 1.2	2.8

the systematic uncertainty. The fraction of neutron captures on Gd is found to be $(86.0 \pm 0.5)\%$ near the center of the target, 2.0% lower than the simulation prediction, which was reduced accordingly with a relative systematic uncertainty of 0.6%. The simulation reproduces the 96.5% efficiency of the Δt_{e^+n} cut with an uncertainty of 0.5% and the 94.5% fraction of neutron captures on Gd accepted by the 6.0 MeV cut with an uncertainty of 0.6%. The MC normalization was adjusted for the muon veto (-4.5%) and the multiplicity veto (-0.5%) dead times.

The covariance matrix of the emitted $\bar{\nu}_e$ spectra was computed as prescribed in Ref. [27]. MURE provided the fractions of fissions per isotope $^{235}\mathrm{U} = 48.8\%$, $^{239}\mathrm{Pu} = 35.9\%$, $^{241}\mathrm{Pu} = 6.7\%$, and $^{238}\mathrm{U} = 8.7\%$ and the fission rate covariance matrix. The resulting relative uncertainties on the above fission fractions are $\pm 3.3\%$, $\pm 4\%$, $\pm 11.0\%$, and $\pm 6.5\%$, respectively. The error associated with the thermal power is $\pm 0.46\%$ at full power [42,43], fully correlated between the two cores.

To avoid being affected by possible very short baseline $\bar{\nu}_e$ oscillations [4,44,45], we adopt the reactor $\bar{\nu}_e$ spectrum of Refs. [23,27] but fix the global normalization by using the Bugey4 rate measurement [46] with its associated 1.4% uncertainty. A relative correction of $(0.9 \pm 1.3)\%$ of the Bugey4 value accounts for the difference in core inventories. The IBD differential cross section is taken from Ref. [47], by using 881.5 ± 1.5 s [1] as the neutron lifetime. The systematic uncertainties are summarized in Table II. The expected no-oscillation number of $\bar{\nu}_e$ candidates is 4344 ± 165, including background.

The measured daily rate of IBD candidates as a function of the no-oscillation expected rate for different reactor power conditions is shown in Fig. 3. The extrapolation to zero reactor power of the fit to the data (including the both-reactors-off) yields 3.2 ± 1.3 events/day, in agreement with our background estimate and the both-reactors-off data.

Our measurement can be expressed as an observed IBD cross section per fission, σ_f^{DC}, which depends on the number of events observed, the number of target protons, the detector efficiency, the number of fissions occurring during our measurement, and the distance to the reactors, yielding $\sigma_f^{\mathrm{DC}} = (5.383 \pm 0.210)10^{-43}$ cm^2/fission. The Bugey4 measurement, corrected to match our fractions of isotopes quoted above, yields a cross section per fission of $(5.703 \pm 0.108)10^{-43}$ cm^2/fission. The ratio of these two measurements is independent of any possible very short baseline oscillations. [Without Bugey4 normalization, the prediction, for our running conditions and by using the reference spectra [23,27], is $(6.209 \pm 0.170)10^{-43}$ cm^2/fission.]

The ratio of observed to expected events is $R_{\mathrm{DC}} = 0.944 \pm 0.016(\mathrm{stat}) \pm 0.040(\mathrm{syst})$, corresponding to $\sin^2 2\theta_{13} = 0.104 \pm 0.030(\mathrm{stat}) \pm 0.076(\mathrm{syst})$ for $\Delta m^2_{13} = 2.4 \times 10^{-3}$ eV^2.

The analysis is improved by comparing the positron spectrum in 18 variably sized energy bins between 0.7 and 12.2 MeV to the expected number of $\bar{\nu}_e$ events, again by using $\Delta m^2_{13} = 2.4 \times 10^{-3}$ eV^2. The analysis, performed with a standard χ^2 estimator, uses covariance matrices to include uncertainties in the antineutrino signal, detector response, signal and background statistics, and background spectral shape. With few positrons expected above 8 MeV, the region 8–12.2 MeV reduces the uncertainties in the correlated backgrounds with some additional contribution to the statistical uncertainty.

The best fit results in $\sin^2 2\theta_{13} = 0.086 \pm 0.041(\mathrm{stat}) \pm 0.030(\mathrm{syst})$ with a χ^2/DOF of $23.7/17$, whereas the $\sin^2 2\theta_{13} = 0.0$ hypothesis results in a χ^2/DOF of $26.6/18$. Using a frequentist approach [48], we find an allowed region of $0.017 < \sin^2 2\theta_{13} < 0.16$ at 90% C.L. and exclude the no-oscillation hypothesis at the 94.6% C.L.

We determine our best estimate of the $\bar{\nu}_e$ and background rates with a pulls-based approach [49], the results

TABLE II. Contributions of the detector and reactor errors to the absolute normalization systematic uncertainty.

Detector		Reactor	
Energy response	1.7%	Bugey4 measurement	1.4%
E_{delay} containment	0.6%	Fuel composition	0.9%
Gd fraction	0.6%	Thermal power	0.5%
Δt_{e^+n}	0.5%	Reference spectra	0.5%
Spill in/out	0.4%	Energy per fission	0.2%
Trigger efficiency	0.4%	IBD cross section	0.2%
Target H	0.3%	Baseline	0.2%
Total	2.1%	Total	1.8%

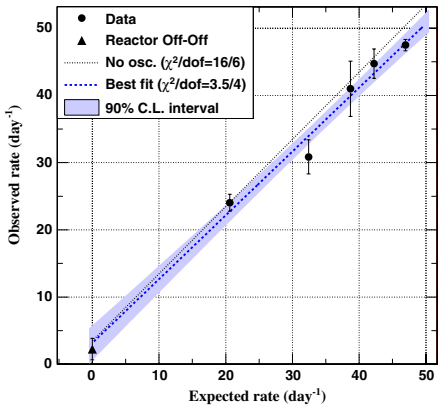

FIG. 3 (color online). Daily number of $\bar{\nu}_e$ candidates as a function of the expected number of $\bar{\nu}_e$. The dashed line is a fit to the data; the band is the 90% C.L. of this fit. The dotted line is the expectation in the no-oscillation scenario. The triangle indicates the measurement with both reactors off.

TABLE III. Summary of the effect of a pulls term approach on the fast neutron and ^{9}Li backgrounds and on the energy scale. Uncertainty values are in parentheses.

	Fast n. bkg (%)	^{9}Li (%)	EScale (value)
Rate only	100 (46)	100 (52)	0.997 (0.007)
Rate + shape	95.2 (38)	81.5 (25.5)	0.998 (0.005)

of which are shown in Table III. From the best fit we obtain a contribution from ^{9}Li reduced by ~19% and with an uncertainty decreased from 52% to 26%. The fast neutron value is decreased by 5% with almost unchanged uncertainty.

Figure 4 shows the measured positron spectrum superimposed on the expected spectra for the no-oscillation hypothesis and for the best fit (including fitted backgrounds).

Combining our result with the T2K [11] and MINOS [12] measurements leads to $0.003 < \sin^2 2\theta_{13} < 0.219$ at the 3σ level.

In summary, Double Chooz has searched for $\bar{\nu}_e$ disappearance by using a 10 m^3 detector located 1050 m from two reactors. A total of 4121 events were observed where 4344 ± 165 were expected for no oscillation, with a signal to background ratio of $\approx$ 11:1. In the context of neutrino oscillations, this deficit leads to $\sin^2 2\theta_{13} = 0.086 \pm 0.041(\text{stat}) \pm 0.030(\text{syst})$, based on an analysis using rate and energy spectrum information. The no-oscillation hypothesis is ruled out at the 94.6% C.L. Double Chooz continues to run, to reduce statistical and background systematic uncertainties. A near detector will soon lead to reduced reactor and detector systematic uncertainties and to an estimated 1σ precision on $\sin^2 2\theta_{13}$ of ~0.02.

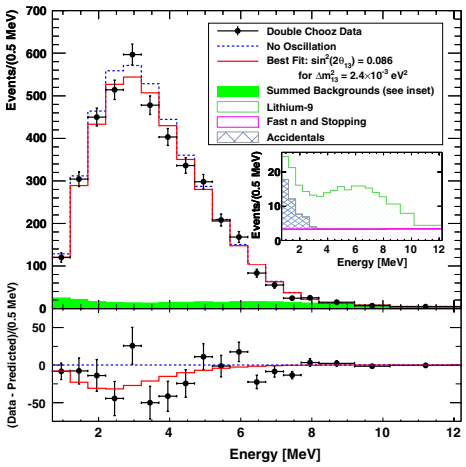

FIG. 4 (color online). Top: Expected prompt energy spectra, including backgrounds, for the no-oscillation case and for the best fit $\sin^2 2\theta_{13}$, superimposed on the measured spectrum. Inset: Stacked histogram of backgrounds. Bottom: Difference between data and the no-oscillation spectrum (data points) and difference between the best fit and no-oscillation expectations (curve).

We thank all the technical and administrative people who helped build the experiment and the CCIN2P3 computer center for their help and availability. We thank, for their participation, the French electricity company EDF, the European fund FEDER, the Région de Champagne Ardenne, the Département des Ardennes, and the Communauté des Communes Rives de Meuse. We acknowledge the support of CEA and CNRS/IN2P3 in France, MEXT and JSPS of Japan, the Department of Energy and the National Science Foundation of the United States, the Ministerio de Ciencia e Innovación (MICINN) of Spain, the Max Planck Gesellschaft and the Deutsche Forschungsgemeinschaft DFG (SBH WI 2152), the Transregional Collaborative Research Center TR27, the Excellence Cluster "Origin and Structure of the Universe" and the Maier-Leibnitz-Laboratorium Garching, the Russian Academy of Science, the Kurchatov Institute and RFBR (the Russian Foundation for Basic Research), the Brazilian Ministry of Science, Technology and Innovation (MCTI), the Financiadora de Estudos e Projetos (FINEP), the Conselho Nacional de Desenvolvimento Científico e Tecnológico (CNPq), the São Paulo Research Foundation (FAPESP), and the Brazilian Network for High Energy Physics (RENAFAE) in Brazil.

*Deceased.

[1] K. Nakamura *et al.* (Particle Data Group), J. Phys. G **37**, 075021 (2010).
[2] B. Pontecorvo, Sov. Phys. JETP **7**, 172 (1958).
[3] Z. Maki, M. Nakagawa, and S. Sakata, Prog. Theor. Phys. **28**, 870 (1962).
[4] M. Appolonio *et al.*, Phys. Lett. B **466**, 415 (1999).
[5] F. Boehm *et al.*, Phys. Rev. Lett. **84**, 3764 (2000).
[6] H. Minakata, H. Sugiyama, O. Yasuda, K. Inoue, and F. Suekane, Phys. Rev. D **68**, 033017 (2003).
[7] H. Minakata, H. Sugiyama, O. Yasuda, K. Inoue, and F. Suekane, Phys. Rev. D **70**, 059901 (2004).
[8] P. Adamson *et al.* (MINOS Collaboration), Phys. Rev. Lett. **106**, 181801 (2011).
[9] X. Guo *et al.* (Daya Bay Collaboration), arXiv:hep-ex/0701029.
[10] J. K. Ahn *et al.* (RENO Collaboration), arXiv:1003.1391.
[11] K. Abe *et al.* (T2K Collaboration), Phys. Rev. Lett. **107**, 041801 (2011).
[12] P. Adamson *et al.* (MINOS Collaboration), Phys. Rev. Lett. **107**, 181802 (2011).
[13] T. Schwetz, M. Tortola, and J. W. F. Valle, arXiv:1108.1376v1.

[14] G. L. Fogli, E. Lisi, A. Marrone, A. Palazzo, and A. M. Rotunno, Phys. Rev. D **84**, 053007 (2011).

[15] F. Ardellier *et al.* (Double Chooz Collaboration), arXiv: hep-ex/0606025v4.

[16] G. Mention, Ph.D. thesis, Université Claude Bernard - Lyon I, 2005, http://tel.archives-ouvertes.fr/tel-00010528/fr/.

[17] O. Meplan, Technical Reports No. LPSC 0912 and No. IPNO-09-01, 2009.

[18] MURE, Mcnp Utility for Reactor Evolution: Couples Monte-Carlo Transport with Fuel Burnup Calculations, 2009, http://www.nea.fr/tools/abstract/detail/nea-1845.

[19] R. R. G. Marleau and A. Hebert, Technical Report No. IGE-157, 1994.

[20] C. Jones, A. Bernstein, J. M. Conrad, Z. Djurcic, M. Fallot, L. Giot, G. Keefer, A. Onillon, and L. Winslow, arXiv:1109.5379v1.

[21] V. I. Kopeikin, L. A. Mikaelyan, and V. V. Sinev, Phys. At. Nucl. **67**, 1892 (2004) [Phys. At. Nucl. **67**, 1892 (2004)].

[22] Jeff and eff projects, http://www.oecd-nea.org/dbdata/jeff/.

[23] P. Huber, Phys. Rev. C **84**, 024617 (2011).

[24] W. G. K. Schreckenbach, G. Colvin, and F. von Feilitzsch, Phys. Lett. **160B**, 325 (1985).

[25] A. F. von Feilitzsch and K. Schreckenbach, Phys. Lett. **118B**, 162 (1982).

[26] A. A. Hahn, K. Schreckenbach, W. Gelletly, F. von Feilitzsch, G. Colvin, and B. Krusche, Phys. Lett. B **218**, 365 (1989).

[27] T. Mueller *et al.*, Phys. Rev. C **83**, 054615 (2011).

[28] C. Aberle, C. Buck, B. Gramlich, F. X. Hartmann, M. Lindner, S. Schönert, U. Schwan, S. Wagner, and H. Watanabe, arXiv:1112.5941.

[29] C. Aberle, C. Buck, F. X. Hartmann, and S. Schönert, Chem. Phys. Lett. **516**, 257 (2011).

[30] T. Matsubara *et al.*, Nucl. Instrum. Methods Phys. Res., Sect. A **661**, 16 (2011).

[31] C. Bauer *et al.*, JINST **6**, P06008 (2011).

[32] E. Calvo, M. Cerrada, C. Fernández-Bedoya, I. Gil-Botella, C. Palomares, I. Rodríguez, F. Toral, and A. Verdugo, Nucl. Instrum. Methods Phys. Res., Sect. A **621**, 222 (2010).

[33] C. Kuhnt, Master's thesis, RWTH Aachen, 2010, http://www.physik.rwth-aachen.de/fileadmin/user_upload/www_physik/Institute/Inst_3B/Forschung/DChooz/'publications/DC_thesis_CK.pdf.

[34] F. Beissel, A. Cucoanes, C. Kuhnt, S. Lucht, B. Reinhold, M. Rosenthal, S. Roth, A. Stahl, A. Stüken, and C. Wiebusch, "The Trigger and Timing System of the Double Chooz Experiment" (to be published).

[35] B. Reinhold, Ph.D. thesis, RWTH Aachen, 2009.

[36] A. Cabrera, Nucl. Instrum. Methods Phys. Res., Sect. A **617**, 473 (2010).

[37] T. Akiri, Ph.D. thesis, Université Paris-Diderot, 2010, http://tel.archives-ouvertes.fr/tel-00580175/fr/.

[38] S. Agostinelli *et al.*, Nucl. Instrum. Methods Phys. Res., Sect. A **506**, 250 (2003).

[39] C. Aberle, C. Buck, F. X. Hartmann, S. Schönert, and S. Wagner, JINST **6**, P11006 (2011).

[40] S. Abe *et al.* (KamLAND Collaboration), Phys. Rev. C **81**, 025807 (2010).

[41] J. P. Both, A. Mazzolo, O. Petit, Y. Peneliau, and B. Roesslinger, Technical Report No. CEA-REPORT: CEA-R-6044, DTI, CEA/Saclay, France, 2003.

[42] E. Tournu and S. Fortier, EPRI Report No. 2001.1001470, Palo Alto, CA, 2001.

[43] Standard Report No. AFNOR XP X 07-020, Palo Alto, CA, 1996.

[44] G. Mention, M. Fechner, Th. Lasserre, Th. A. Mueller, D. Lhuillier, M. Cribier, and A. Letourneau, Phys. Rev. D **83**, 073006 (2011).

[45] C. Giunti and M. Laveder, arXiv:1111.5211v2.

[46] Y. Declais *et al.*, Phys. Lett. B **338**, 383 (1994).

[47] P. Vogel and J. F. Beacom, Phys. Rev. D **60**, 053003 (1999).

[48] G. J. Feldman and R. D. Cousins, Phys. Rev. D **57**, 3873 (1998).

[49] D. Stump, J. Pumplin, R. Brock, D. Casey, J. Huston, J. Kalk, H. L. Lai, and W. K. Tung, Phys. Rev. D **65**, 014012 (2001), Appendix B.

Appendix B

OV Event Builder

As described in Sec. 3.2.6, the OV consists of many modules of plastic scintillator strips each read out by a separate custom-built PMT electronics board. The OV data acquisition software (OV DAQ) is designed such that the data acquisition of the OV modules is subdivided into K independent threads. Each thread establishes a USB connection to a hub, which manages a data stream for 8–10 OV modules that are daisy-chained together using Category-6 cables. The USB hub generates a token which is passed to the modules over a serial link. If a module has no data, the token is passed along the link. If a module has data, it transmits the data to the serial link along with the token. The data circulates back to the USB hub and is buffered before being read out by the OV DAQ and then written to disk.

An additional USB hub manages a separate daisy chain of trigger boards. Each trigger board is connected to all modules in a geometrically well-defined sector of the OV. In the far detector, one trigger board is connected to the upper plane of OV modules and the other two trigger boards are each connected to one half of the lower plane of OV modules. The main purpose of the trigger boards is to distribute the 62.5 MHz clock signal emitted by the DC trigger system to each of the OV PMT boards. However, they also provide data about the pattern of OV modules in a given sector that are triggered simultaneously.

In general, a muon traversing the OV will produce hits in multiple strips in multiple modules. In order to build muon events from the hit-level data, all strips hit in a given time window should be grouped together, regardless of the USB data stream in which they are

read out.

If the token-passing latencies are sufficiently short and the data rate is sufficiently low, then the data in a given USB data stream will be time-ordered. However, given our latencies and rates, a certain amount of time misordering of the data is expected. Therefore, in order to group hits in time, the USB data streams should first be time-sorted.

The OV Event Builder is a program run concurrently with the OV DAQ designed to build groups of time-correlated hits from a set of K unordered, independent USB data streams. It outputs a single, serialized data stream, from which muon positions and tracks can then be reconstructed. Fig. B.1 gives a block diagram of the data flow in the OV.

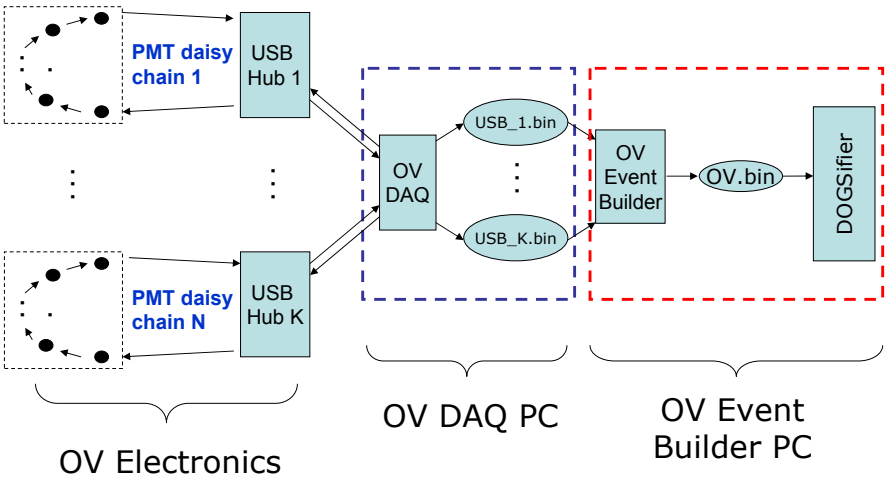

Figure B.1: Block diagram of the data flow in the OV.

B.1 Data Handling, Transfer and Processing

The OV DAQ handles each USB data stream as an entirely independent and separate thread. Each USB data stream writes raw binary data to disk in a separate file. The files are given a name that identifies the time at which the file was created as well as the USB

hub managing the data stream. After a user-programmable number of seconds (5 seconds as currently implemented), each thread automatically closes the file to which it is currently writing and starts writing to a new file. The OV DAQ indicates that it has successfully closed a raw data file by renaming it (the `.bin` file extension is removed).

The OV Event Builder runs on a different machine from the OV DAQ (currently `dcfovmon`) and remotely mounts the disks to which the OV DAQ writes raw data using the Network File System (NFS) protocol. The OV Event Builder looks for new files to process by sorting all OV DAQ raw data files without the `.bin` extension in a given run folder and selecting the oldest file corresponding to each of the K USB streams. The path to the raw OV DAQ data is specified by four parameters passed to the OV Event Builder as a command line option at run time: the OV DAQ host name (default: `dcfovdaq`), the data disk (default: 2), the data folder (default: `OVDAQ/DATA`), and the run number. The absolute path is then constructed as

`/${OVDAQHost}/data${Disk}/${DataFolder}/Run_${RunNumber}/binary.`

The file sorting and USB hub identification is done by parsing the file names of the OV DAQ raw data files which are of the form `XXXXXXXXXX_Y`, where `XXXXXXXXXX` designates the 10-digit unix time stamp corresponding to the creation time of the file and `Y` corresponds to a variable-length number indicating the USB hub, from which the data was read out.

The OV Event Builder then launches separate threads to process each of the oldest files found for each USB data stream. The threads read in, decode, and sort these files concurrently. After joining the various threads, the OV Event Builder then moves the raw data files for a given run from the OV DAQ raw data folder named 'binary' to a folder named 'decoded'. In addition it adds the extension `.done` to each of the files. Moving and renaming the files signals to the OV online monitor that the raw data files have been successfully closed by the OV Event Builder and can now be read in by monitoring software.

The OV Event Builder then merges the USB data streams in time-order and writes time-correlated OV events to a local disk. The path of the output data is specified by two parameters passed to the OV Event Builder as command line options at run time: the output data disk (default: 1) and the run number.

The absolute path is built as `/data${OutputDisk}/OVDAQ/DATA/Run_${RunNumber}` and the output file name has a specific format given by `DCRunFXXXXXXXXPYYYYOVDAQ.bin`, where F designates the detector (F: far, N: near), `XXXXXXXX` is an 8-digit run number, P designates the type of data (P: physics, D: debug, C: calibration), and `YYYY` is a 4-digit sub-run number used internally by the OV Event Builder. The OV Event Builder can be configured to write output data to a new file every M seconds (default: 5). The sub-run number is incremented each time a new output data file is opened.

B.1.1 Online Mode

In so-called "online mode", the OV Event Builder increments a semaphore each time it successfully closes an output data file. A separate process called the 'DOGSifier' is designed to merge the OV data with the data from the rest of the experiment. The DOGSifier runs on the same machine as the OV Event Builder and watches the semaphore that is incremented by the OV Event Builder. When the semaphore increases by one, the DOGSifier reads in the last data file output by the OV Event Builder and converts it into the final ROOT-based DC data format. The DOGSifier then decrements the semaphore. A similar strategy is used by the DOGSifier to read in data from the rest of the experiment and convert it into the final DC data format. In this way data from the OV can be merged with data from the rest of the experiment in close to real-time.

The path of the DOGSifier output data is `$DOGS_PATH/DATA`, where `$DOGS_PATH` is an envrionment variable which must be set. Currently, a symbolic link is used to redirect this path to `/data2/OVCommissioning/DATA`. The naming convention used for the DOGSifier output files is `DCRunXXXXXXX_RAW_v17_OV_YYYY.root`, where `XXXXXXX` specifies the run number and `YYYY` is a string specifying the type of DC data file ('base' or 'muon').

Both the OV Event Builder and the DOGSifier can also be run in "offline mode". In this case there is no communication between the OV Event Builder process and the DOGSifier, i.e. no semaphore is incremented or decremented. In the OV Event Builder this mode can be activated with a command line option and is used as a failover if there are any exceptions creating or incrementing the semaphore. After the OV Event Builder finishes processing all the OV DAQ raw data for a given run in offline mode, the DOGSifier can be run with

the total number of OV Event Builder output data files (i.e. the total number of sub-runs) passed as a command line argument. The DOGSifier will then look for and process the OV Event Builder output data files for that run.

Though the OV Event Builder and the DOGSifier are run in online mode by default, the DOGSifier is not currently configured to merge OV data with the data from rest of the experiment. Therefore, two separate instances of the DOGSifier are run: one to convert OV data into the final DC data format and one to convert the data from the rest of the experiment into the final DC data format. The two data streams are then merged offline using unix time stamps and 62.5 MHz clock counts by a dedicated process described in App. C.

B.2 OV DAQ Raw Data

The OV raw data consists of three types of packets, each containing a certain number of 24-bit words:

- PMT board data packets,
- Trigger board data packets, and
- Unix time stamp packets.

PMT board data packets contain the value of a 32-bit 62.5 MHz clock counter, the number of 24-bit words in the packet, the module number, the type of data in the packet, and channel-wise information about the charge generated by the multi-anode PMT. There are two types of channel-wise information that can be provided in a PMT board data packet. The first type only includes boolean information about whether or not each pixel of the multi-anode PMT is above a certain threshold. These are called “latch packets”, and they consist of a fixed number of words. The second type includes information about the amount of charge generated by each of the pixels of the multi-anode PMT that are above a certain threshold. The analog charge is converted to a digital scale using a 12-bit analog-to-digital converter (ADC). These “ADC packets” have a variable number of words, which depends on the number pixels N that are above threshold.

Trigger board data packets are similar in structure to PMT board latch data packets, except that they consist of two fewer words. PMT board latch packets require four words to encode whether each of the 64 PMT pixels was above threshold. A trigger board, however, is connected to a sector of the OV containing at most 24 PMT boards and only two words are required to encode whether each of these boards had a channel above threshold.

Finally, unix time stamp packets consist of two words, one for the high 16 bits of the unix time stamp and one for the low 16 bits of the unix time stamps. These packets are generated by the OV DAQ every second and injected into each of the USB data streams. Though they are only assumed to be accurate within ± 1 s, these packets provide an important reference for merging events.

The structure of the various types of data packets are given below along with a description of each word. Each 24-bit word is divided into 8 control bits defining the type of word and 16 data bits encoding the data contained in the word.

B.2.1 PMT board ADC packets

Control [23:16]	Data [15:0]	Description
11 000000	1111111111111111	Header word
11 000000	1, mod#[6:0], wdcnt[7:0]	Data type, module #, word count
11 000000	time[31:16]	High 16 bits of 62.5 MHz clock counter
11 000000	time[15:0]	Low 16 bits of 62.5 MHz clock counter
11 000000	0000, adc[11:0]	} ADC and channel # repeated N times
11 000000	0000000000, ch#[5:0]	
11 000000	parity[15:0]	Parity word

B.2.2 PMT board latch packets

Control [23:16]	Data [15:0]	Description
11 000000	1111111111111111	Header word
11 000000	0, mod#[6:0], wdcnt[7:0]	Data type, module #, word count
11 000000	time[31:16]	High 16 bits of 62.5 MHz clock counter
11 000000	time[15:0]	Low 16 bits of 62.5 MHz clock counter
11 000000	disc[15:0]	Discriminator output for channels 0–15
11 000000	disc[31:16]	Discriminator output for channels 16–31
11 000000	disc[47:32]	Discriminator output for channels 32–47
11 000000	disc[63:48]	Discriminator output for channels 48–63
11 000000	parity[15:0]	Parity word

B.2.3 Trigger board latch packets

Control [23:16]	Data [15:0]	Description
11 000000	1111111111111111	Header word
11 000000	0, mod#[6:0], wdcnt[7:0]	Data type, module #, word count
11 000000	time[31:16]	High 16 bits of 62.5 MHz clock counter
11 000000	time[15:0]	Low 16 bits of 62.5 MHz clock counter
11 000000	disc[15:0]	Discriminator output for modules 0–15
11 000000	00000000, disc[23:16]	Discriminator output for modules 16–23
11 000000	parity[15:0]	Parity word

B.2.4 Unix timestamp packets

Control [23:16]	Data [15:0]	Description
11 001000	timestamp_hi[31:16]	High 16 bits of unix time stamp
11 001001	timestamp_lo[15:0]	Low 16 bits of unix time stamp

B.3 OV Event Building Algorithm

The OV Event Builder algorithm consists of the following steps:

- Reading in and decoding OV raw data,

- Baseline-subtracting raw ADC data,
- Applying offline thresholds and topological cuts,
- Time-sorting individual USB streams,
- Merging data from different USB streams, and
- Building OV events.

B.3.1 Reading in OV raw data

The OV event builder reads in the raw OV DAQ binary data, which consists of both data packets passed from the OV electronics as well unix time stamps inserted into the data files by the OV DAQ readout program. As each data packet is read in by the OV Event Builder, it is decoded and assigned a global unix time corresponding to the unix time stamp most recently found in the data stream for that particular USB.

The raw data at the beginning of the first file of a run is handled as a special case since it may happen that no unix time stamp has been processed yet. In this case, the Event Builder looks for the first unix time stamp, and then associates all preceding data packets with a unix time stamp one second prior.

B.3.2 Baseline Subtraction

At the start of each OV data-taking run, a pedestal measurement is performed by forcing the read out of each PMT board 50 times. The OV Event Builder reads in and decodes these data packets and computes the baseline of each channel of each PMT board. The baselines are then stored in a dedicated OV pedestal MySQL table for each run. Subsequent ADC data packets read in by the OV Event Builder during the data-taking run are then baseline-subtracted according to the values in this table.

B.3.3 Offline Thresholds

Due to a larger than expected radioactive background in the DC far detector hall, the OV PMT board firmware was programmed to only read out modules with at least one "μ-

like double" above threshold. A μ-like double is defined as a pair of PMT pixels that are connected to strips, which are stacked on top of each other in the OV module two-layer design. Fig. B.2 shows a cartoon of an OV module with 10 strips and illustrates an example of a μ-like double.

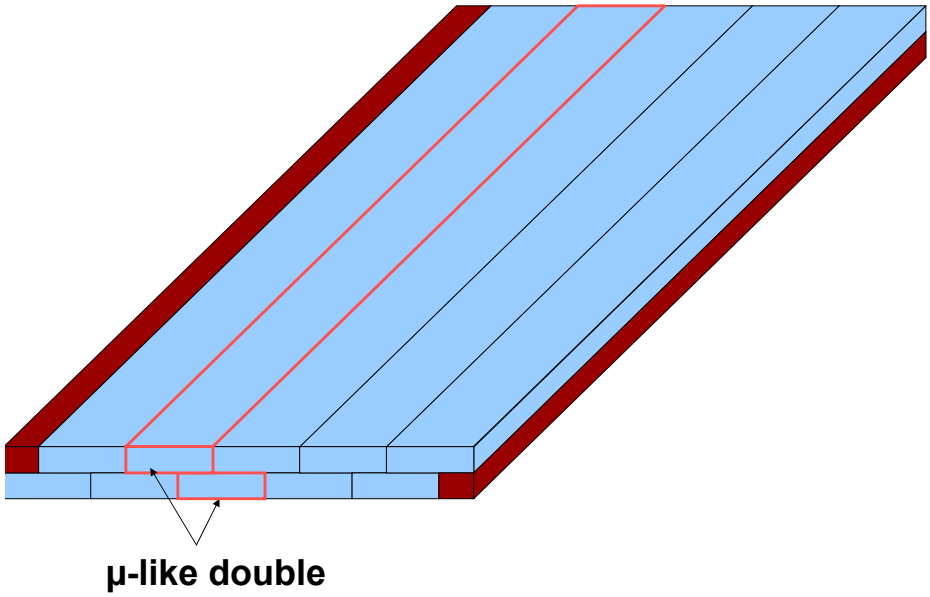

Figure B.2: Cartoon of an OV module with 10 strips illustrating an example of a μ-like double.

Two different types of offline thresholds can be applied in the OV Event Builder. First, similar to the threshold condition imposed in the OV PMT board firmware, the OV Event Builder can require that both of the hits in the μ-like double exceed a certain ADC threshold ("double-layer threshold") in order to keep the entire data packet. Alternatively, the OV Event Builder can be configured to require that only one of the two hits in the μ-like double exceed a certain ADC threshold ("single-layer threshold"). The default configuration is to apply a double-layer threshold of 73 ADC counts, corresponding to a threshold of $\sim$ 1.5 P.E.

B.3.4 Time Sorting

Fig. B.3 shows the time difference in terms of 62.5 MHz clock counts between subsequent data packets for a typical USB raw data stream. Most of the time differences are nonnegative, indicating that many of the OV DAQ raw data packets are already time-ordered. There is, however, a population of negative time differences, which indicates that the USB raw data stream is not completely time-sorted. Therefore, an insertion sort—which performs well on data which is nearly sorted—is used to time-order each of the USB data streams.

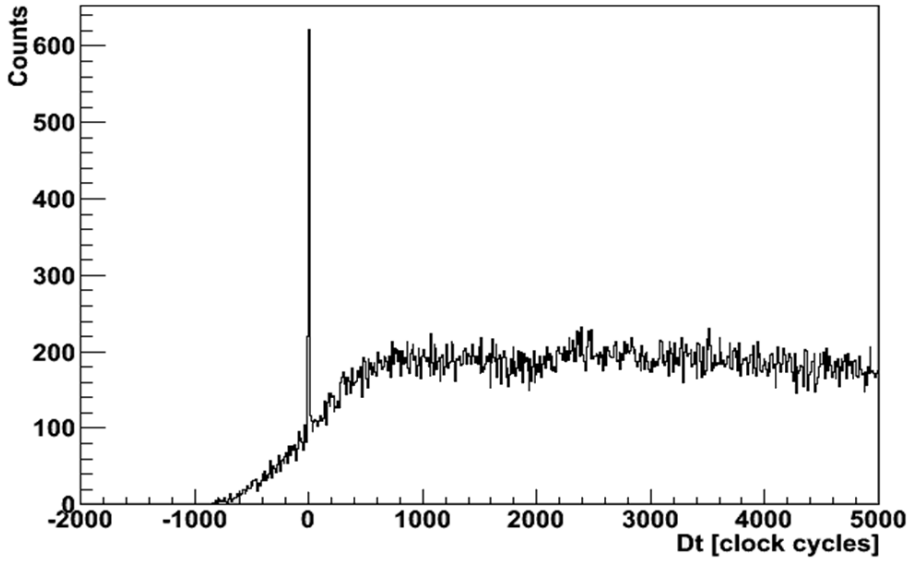

Figure B.3: ΔT between OV data packets in OV DAQ raw data. Entries with $\Delta T < 0$ correspond to misordered pairs of packets.

A subtlety arises in the time-ordering because the 32-bit OV PMT board clock counters are periodically reset by a hardware signal sent from the DC trigger system. The reset signal is synchronized to the master 62.5 MHz DC clock and comes once every 2^{29} clock cycles (every $\sim$ 8 s). As a result, an OV data packet generated just before the reset will have a clock counter value much larger than a data packet generated just after the reset. Therefore, if two data packets have been assigned unix time stamps within $\pm$1 s of each

other[1], they are ordered according to their clock counter values only if the clock counters differ by less than ~ 2 s. Otherwise, a clock counter reset is assumed to have occurred in the intervening time and the ordering is reversed. This scheme is valid so long as the clock counters are reset less frequently than once every ~ 4 s.

B.3.5 Merging USB Data Streams

OV events are constructed from time-ordered, internal buffers of data packets for each USB data stream. First, the OV data packet which occurs next in time is found from among the K USB data stream input buffers. Next, this "incoming" packet is compared to the last packet added to the OV Event Builder output buffer. If the incoming data packet does not occur more than three clock cycles[2] after the last data packet added to the output buffer, the incoming packet is added to the output buffer. Otherwise, the data packets already in the output buffer are serialized and written to disk as an OV event and a new output buffer is created for the incoming OV data packet. This process continues until the end of one of the K USB data stream input buffers is reached. The OV Event Builder then launches separate threads to read in, decode, and sort the next data file for each of the K USB data streams.

B.3.6 Building OV events

An OV event is comprised of two nested logical structures: OV data packets and OV hits. An OV hit consists of a pair of numbers representing the ADC value and the channel number of a single strip hit in a module. An OV data packet consists of a number of OV hits, along with the module number[3], data type, and 62.5 MHz clock counter value. An OV event,

[1]The unix time stamps are only considered accurate within ± 1 s, so they are only used to order two OV data packets if their unix time stamps differ by more than 1 s.

[2]The number of clock cycles is configurable. It was chosen to cover the largest expect time spread for hits resulting from a single muon crossing the OV.

[3]A unique numbering is used for the OV modules, which is obtained from the OV online configuration MySQL table. Far detector modules are numbered 100–199 and near detector modules are numbered 200–299.

then consists of a number of OV data packets, along with the unix time stamp associated with the event.

When writing an OV event to disk, first an OV event header is written specifying the unix time stamp and the number of OV data packets in the event. Then for each OV data packet, an OV data packet header is written to disk. This header specifies the module number, data type, 62.5 MHz clock counter value, and the number of OV hits in the OV data packet. Immediately following each OV data packet header, the individual OV hits for that data packet are then written to disk. In this way, the DOGSifier can in principle read OV events in real time as they are written to disk by the OV Event Builder without knowing in advance the size of each event (i.e. the number of hits).

B.4 Recovery and Reprocessing Modes

The OV Event Builder is able to process the same run more than once. In the event that the OV Event Builder does not completely finish processing a run cleanly, it can resume processing the run in a special "recovery mode". On the other hand, if the the run was fully processed but needs to be re-processed with a different offline threshold applied, the OV Event Builder can also be run in a special "reprocessing mode".

The OV Event Builder determines the appropriate running mode is automatically by first checking the OV Event Builder comment field in the OV run summary MySQL table. This field is updated with the last unix time stamp processed each time the OV Event Builder has successfully written and closed an output file. Therefore, if this field is empty the OV Event Builder is assumed to have never been executed for the given run and the processing proceeds normally. However, if this field is filled the OV Event Builder is instead run in either recovery mode or reprocessing mode. The OV Event Builder is run in reprocessing mode if the OV run stop time is also filled in the MySQL OV run summary table and if all the OV DAQ raw data files have been moved to the decoded folder. Otherwise, the OV Event Builder is run in recovery mode.

B.4.0.1 Reprocessing Mode

In reprocessing mode, the goal is to just re-run the OV Event Builder, but with different threshold parameters. Therefore, the OV raw data files are first moved back to the OV raw data binary folder from the decoded folder and the `.done` extensions are removed. Then the OV raw data is processed in the same way as it is normally processed, except the output is written to a new path.

The OV Event Builder checks that the threshold type and the threshold value provided as command line options[4] differ from the values found in the OV run summary table[5]. An entry is made in the OV Event Builder MySQL table indicating the new path of the OV Event Builder output for the reprocessed data as well as the offline threshold parameters used to reprocess the data. The OV Event Builder output for the reprocessed data is written to a path given by

`/data${OutputDisk}/OVDAQ/REP/Run_${RunNumber}/$RepString/Run_${RunNumber},`

where `$RepString` is constructed from the threshold type `X` and threshold value `YYYY` as `TXADCYYYYP100P200`. In the above, no threshold corresponds to `X`=0, a single-layer threshold corresponds to `X`=1, and a double-layer threshold corresponds to `X`=2.

B.4.0.2 Recovery Mode

In recovery mode, we try to reproduce the identical state of the OV Event Builder at the moment when it had previously stopped processing the run. To do this, we first move the last three OV raw data files for each USB data stream from the decoded folder to the binary folder and remove the `.done` extensions. This ensures that in recovery mode the internal buffers of OV Event Builder will be the same as they were immediately prior to when the original processing stopped.

The OV Event Builder then uses the OV Event Builder comment and the sub-run number in the OV run summary MySQL table to determine when it should resume writing

[4]The default is to apply a double-layer threshold of 73 ADC counts.

[5]If a run has been successfully processed with a certain offline threshold, it cannot be re-run with that same threshold.

data to disk. These fields are updated with the last unix time stamp read in and the last sub-run number assigned each time the OV Event Builder has successfully written to and closed an output file. The OV Event Builder writes data to `/dev/null` until the unix time stamp it reads in is greater than the unix time stamp found in the MySQL OV run summary table. At this point, the sub-run number is assigned to the value retrieved from MySQL and normal processing is resumed.

This strategy assumes that the OV Event Builder processing originally stopped after successfully writing to and closing an output data file. If the processing instead stopped in the middle of writing to an OV Event Builder output file, then this partially filled output file should first be manually removed before running in recovery mode.

B.5 Configuration and Options

The OV Event Builder is written in C++ but has a few dependencies on ROOT. In particular, ROOT TThread classes are used to handle the reading and sorting of the separate USB data streams. Therefore, ROOT must be properly installed in order to run the OV Event Builder. The OV Event Builder has been tested with ROOT 5.22 compiled on Scientific Linux 5 with gcc 4.4.0.

The OV Event Builder also uses functions to manipulate semaphores, which are defined in the `sem_tools.hh` header file in the DOGSifier directory. Therefore, the OV Event Builder also has a dependence on the DC online software via the `libDCDOGSifier.so` shared library against which it must be linked. Therefore, the DC online software repository must be properly downloaded and installed on the OV Event Builder computer. Furthermore, the DOGSifier must be compiled in a special mode to disable merging OV data with data from the rest of the experiment. To compile the DOGSifier in this special mode, `make offline` must be invoked in the DOGSifier directory and then `make` must be invoked in the DOGSifier's bin directory.

The OV Event Builder also relies on MySQL tables in order to access information about the number of USB streams and PMT boards it expects to find in the data. It also writes diagnostic information to MySQL tables every time it finished successfully writing an output

file to disk in order to track its own progress in the event of a crash. Finally, information such as pedestals, thresholds, and topological cuts are stored to allow the low-level data manipulations performed in the OV Event Builder to be tracked run by run.

This dependence on MySQL manifests itself in 2 ways. First, the mysqlclient and mysqlpp packages must be properly installed on the OV Event Builder machine in order for the OV Event Builder to compile. And second, a MySQL database must be properly configured in order for OV Event Builder to communicate with the MySQL server at run time. The MySQL database connection information is assumed to be located at `config/DCDatabase.config` in the top-level directory of the DC online software repository.

Finally, the OV Event Builder has a dependence on the local system configuration. It assumes that data disks are mounted under `/data1` and `/data2` and that both `OVDAQ/DATA` and `OVDAQ/REP` exist on both partitions. The `dconline` user should have write permission for these directories. Furthermore, as described in Sec. B.1, it assumes that the OV DAQ binary data is accessible via `/${OVDAQHost}/data${disk}/${DataFolder}`, where `/${OVDAQHost}` is the mount point for the OV DAQ computer (`/dcfovdaq` as currently configured).

B.5.1 Execution and Command-line Arguments

The OV Event Builder software is located in the `DCOV/EBuilder` subfolder of the DC online software repository top-level directory. After compilation, an executable named `EventBuilder` is created in the `EBuilder/bin` directory. Invoking `./EventBuilder` results in the following output:

```
Usage: ./EventBuilder -r <run_number> [opt args]
For help: ./EventBuilder -h
```

Typing `./EventBuilder -h` gives the following:

```
Usage: ./EventBuilder -r <run_number> [-d <data_disk>]
    [-D <use_DOGSifier>] [-s <semaphore_filename>]
    [-t <offline_threshold>] [-T <offline_trigger_mode>] [-R <run_type>]
```

```
    [-H <OV_DAQ_data_mount_point>] [-e <EBuilder_output_disk>]

-r: specify expected run number for incoming data
-d: disk number of OV DAQ data to be processed    [default: 2]
-D: whether to run in online mode with DOGSifier  [default: 1]
-s: file name to generate DOGSifier semaphore     [default:
                                                  /var/tmp/OV_EBuilder.txt]
-t: offline threshold (in ADC counts) to apply    [default: 73]
-T: offline trigger mode (0: NONE, 1: OR, 2: AND) [default: 2]
-R: OV run type (P: physics, C: calib, D: debug)  [default: P]
-H: OV DAQ mount path on EBuilder machine         [default: dcfovdaq]
-e: disk number of OV EBuilder output binary data [default: 1]
```

B.6 Data Validation

Low-level checks on the data before and after the OV Event Builder are required to validate the performance of the OV Event Builder as well as the data integrity after the low-level data manipulations it performs.

The OV Event Builder algorithm described in Sec. B.3 should guarantee that the following conditions hold in OV Event Builder output data passed to the DOGSifier:

1. The OV events are time-ordered.

2. There is no gap longer than 3 clock cycles between hits built into the same OV event.

3. There is no gap shorter than 4 clock cycles between the end of one OV event and the beginning of the subsequent OV event.

4. If an OV Event Builder threshold is applied in the single-layer mode, at least one hit in a μ-like double in each OV event exceeds the threshold value. If an OV Event Builder threshold is applied in double-layer mode, two hits in a mu-like double in each OV event exceed the threshold value.

5. The output of the OV Event Builder has exactly the same hit distributions as the OV DAQ raw data, as long as the OV Event Builder is configured to apply a threshold lower than the 1/3 PE (roughly 10 ADC counts) hardware threshold applied in the OV PMT board firmware. In particular, the number of hits in a given time period is the same before and after the OV Event Builder; i.e., no hits are lost or duplicated in the OV Event Builder.

In order to verify this behavior, code was written to analyze the data before and after the OV Event Builder. To analyze the raw output of the OVDAQ, the raw binary data was decoded and histograms of the following distributions were made:

- Hits per OV PMT board
- Hits per OV data packet per OV PMT board
- Time difference between subsequent OV data packets for each OV PMT board
- Time difference between subsequent OV data packets for each USB daisy chain

Additionally, the data output from the OV Event Builder was analyzed and histograms of the following distributions were made:

- Hits per OV PMT board
- Hits per OV event
- Number of modules per OV event
- Time difference between subsequent OV events
- Time difference between subsequent hits within an OV event
- Time elapsed within an OV event
- Number of hits per OV event above the OV Event Builder threshold

These histograms provide sufficient information to verify conditions 1–4 above. Additional code was written to verify condition 5, which counts all hits occurring between two user-specified 62.5 MHz clock counts in the OV raw data and counts hits occurring between the same 62.5 MHz clock counts in the data output by the OV Event Builder.

B.6.1 Results of Validation Tests

The validation code described in Sec. B.6 was run on several sets of OV data. All conditions were successfully verified. Results for a representative run are summarized below.

B.6.1.1 Condition 1

The histogram of the time difference ΔT between packets OV data packets (see Fig. B.3) reveals that some OV data packets are out of order in the raw output of the OV DAQ. ΔT is defined as the clock count of one OV data packet minus the clock count of the subsequent OV data packet, so entries with negative ΔT correspond to out-of-order pairs.

The histogram of ΔT between hits within an OV event (see Fig. B.4) and the histogram of ΔT between OV events output by the OV Event Builder (see Fig. B.5) show that the OV Event Builder corrects these misorderings. In all cases, ΔT between hits within an OV event (defined as the clock count of a hit minus the clock count of the subsequent hit) and ΔT between OV events (defined as the clock count of the last hit in an OV event minus the clock count of the first hit in a subsequent OV event) are greater than zero.

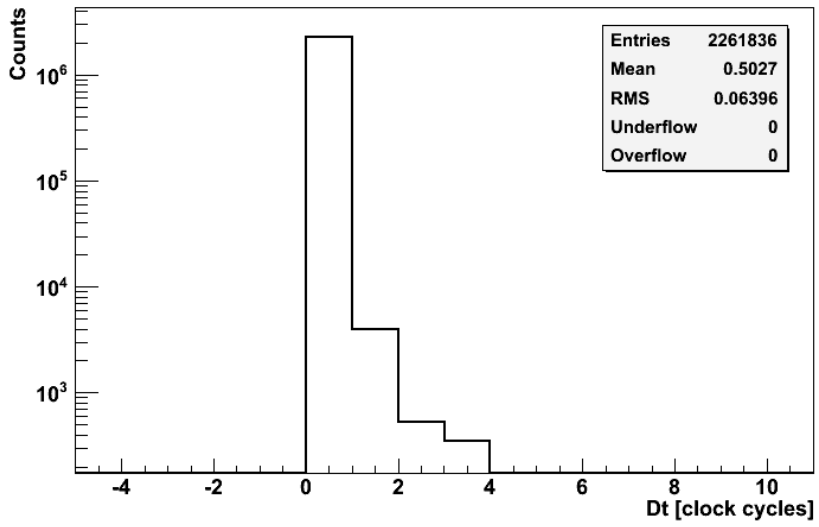

Figure B.4: ΔT between subsequent hits in an OV event, after the OV Event Builder.

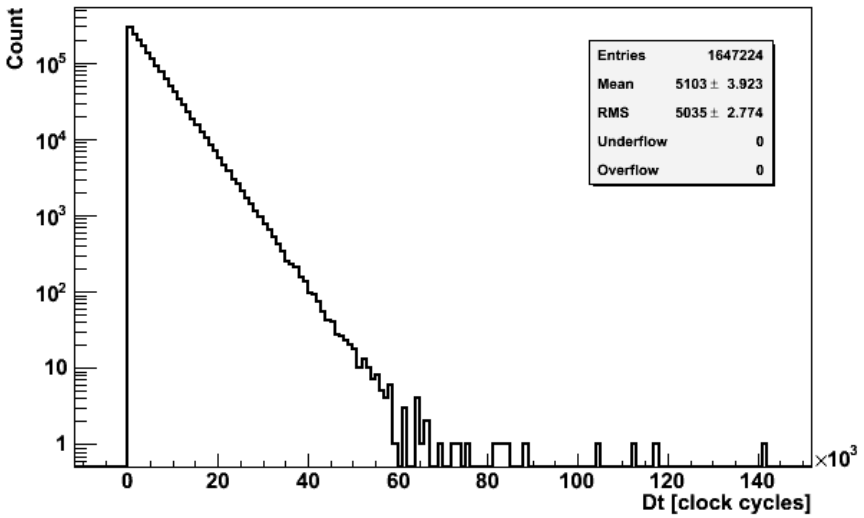

Figure B.5: ΔT between subsequent OV events, after OV Event Builder.

B.6.1.2 Condition 2

The histogram of ΔT between hits in an OV event (see Fig. B.4) shows that there are no gaps greater than three clock cycles built into the same OV event.

B.6.1.3 Condition 3

The histogram of ΔT between subsequent OV events (see Fig. B.6) shows that there are no gaps shorter than four clock cycles between OV events.

B.6.1.4 Condition 4

When a single-layer threshold of 73 ADC counts is applied in the OV Event Builder, at least one—but often exactly one—hit exceeds the threshold in every OV event. The histogram of above-threshold hits per OV event (see Fig. B.7) shows that at least one hit exceeds the threshold for each OV event. A separate script verified that at least one of these above-threshold hits is part of a μ-like double.

When a double-layer threshold of 73 ADC counts is applied in the OV Event Builder, at least two hits exceed the threshold in every OV event. The histogram of above-threshold

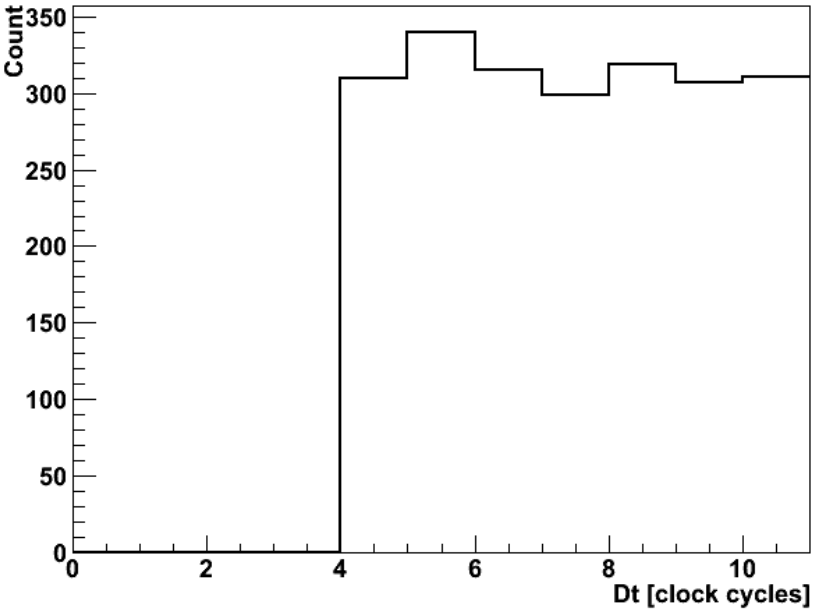

Figure B.6: ΔT between OV events zoomed in on short ΔT.

hits per OV event (see Fig. B.8) shows that at least two hits exceed the threshold for each OV event. A separate script also verified that at least two of these above-threshold hits form a μ-like double.

B.6.1.5 Condition 5

Finally, the number of hits occurring between two randomly chosen clock counts was counted in the OV DAQ raw data and in the OV Event Builder output when no threshold was applied. The counts agree, demonstrating that no hits are lost or duplicated in the OV Event Builder.

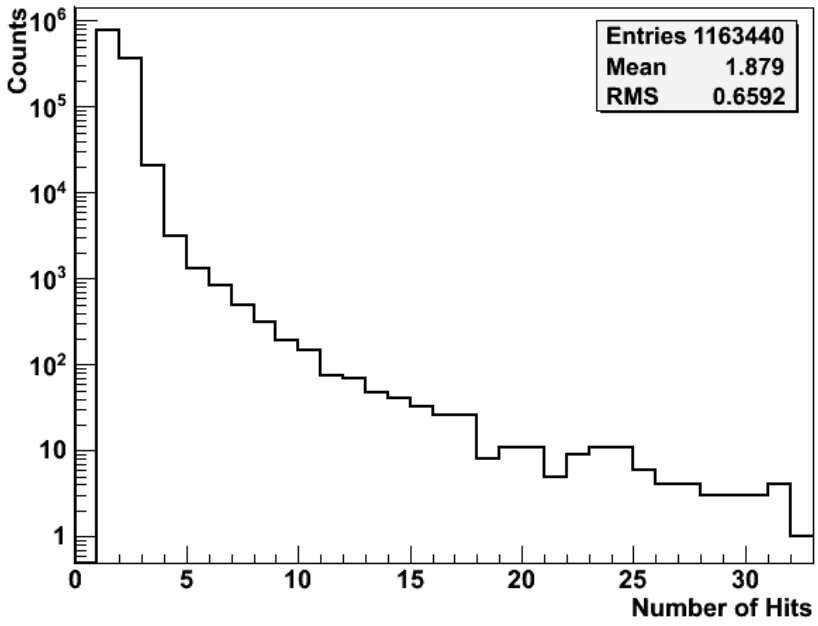

Figure B.7: The number of hits exceeding the 73 ADC count threshold in each OV event after applying a single-layer threshold in the OV Event Builder.

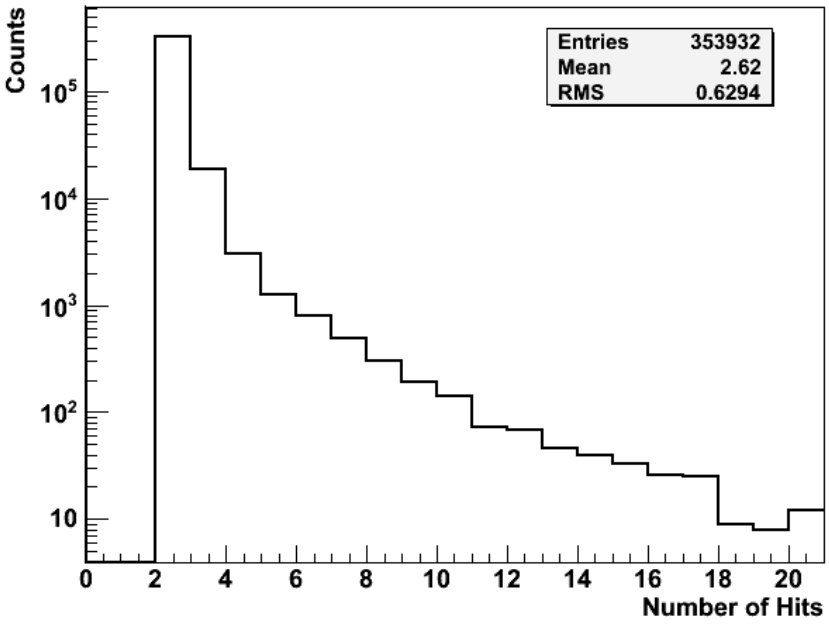

Figure B.8: The number of hits exceeding the 73 ADC count threshold in each OV event after applying a double-layer threshold in the OV Event Builder.

Appendix C

OV Data Merging

The OV data merger is designed to identify events coincident between the outer veto data acquisition system (OV DAQ) and the inner detector/inner veto data acquisition system (ν-DAQ). The time alignment of the data streams generated by these two independent DAQs is accomplished via a common 62.5 MHz master clock distributed by the DC trigger system. When each DAQ writes an event to disk, the status of a 32-bit clock counter is also recorded. Vertical muons are used to measure the time offset between the ν-DAQ and OV DAQ clock counters, which arises due to cable and logic delays in each system. Once this offset has been determined, muons crossing both the OV and ID/IV can be identified and reconstructed.

C.1 Signal Propagation

The DC trigger system distributes a 62.5 MHz master clock to both the ν-DAQ and the OV DAQ. In addition, the DC trigger system distributes a clock reset (sync) signal to the OV. The sync signal is synchronous with the DC master clock and is generated each time the DC trigger system's internal 32-bit clock counter reaches an integer multiple 2^{29} clock counts. Fig. C.1 is a histogram of the arrival times of the OV sync pulse in terms of the internal 32-bit clock counter of one of the OV trigger boards for a 10.76 h data-taking run. All 4507 sync pulses arrive at the expected clock count value of $2^{29} - 1$.

Both the clock and sync signals are fanned out by OV NIM fan-out modules and prop-

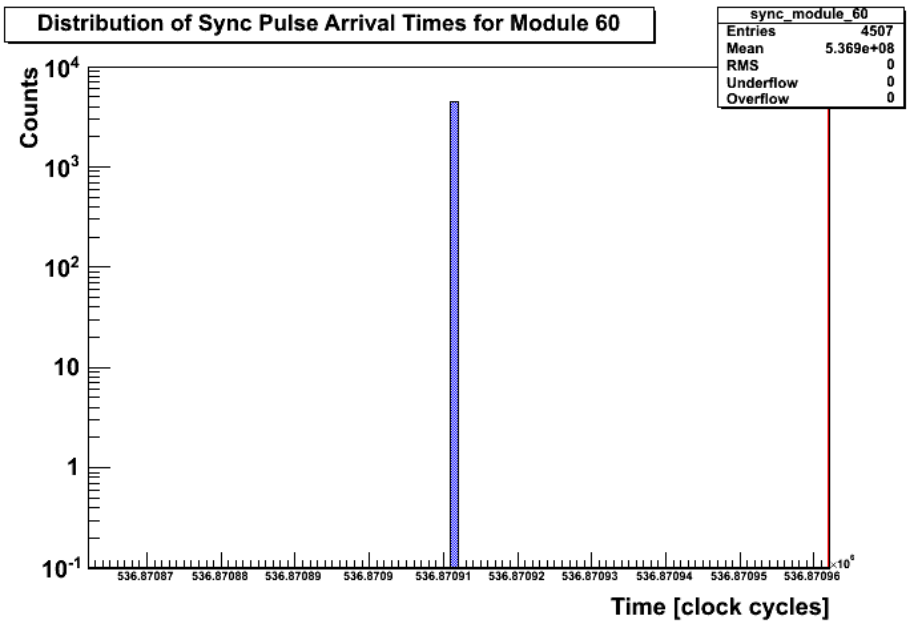

Figure C.1: Histogram of the arrival times of the OV sync pulse for a 10.76 h data-taking run. All 4507 sync pulses arrive at the expected clock count value of $2^{29} - 1$.

agate to OV trigger boards located near groups of OV modules. As described in App. B, these trigger boards distribute the clock and sync signals to each of the OV PMT boards. Time stamps are generated based on the value of 32-bit clock counters for data from both the trigger boards and the PMT boards. Fig. C.2 gives a block diagram of the propagation of the clock and sync signals to the OV.

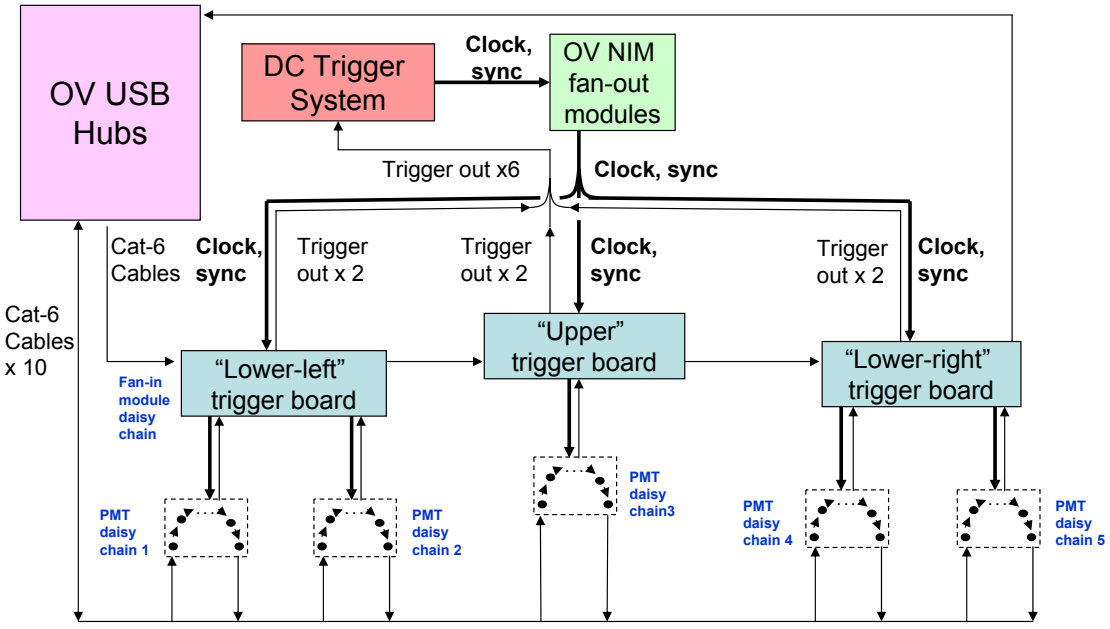

Figure C.2: Block diagram of the propagation of the clock and sync signals to the OV.

C.1.1 OV Signal Propagation and Delay

Due to logic and cable delays in the propagation of the sync signal from the DC trigger system to the OV, the value of the OV clock counters are offset from the value of the clock counters in the DC trigger system at any given time. More specifically, the delay in the propagation of the sync signal to the OV PMT boards comes from the sum of the following

contributions:

1. Signal transit time from the DC trigger system to the OV NIM fan-out module
2. Signal processing time in the OV NIM fan-out module
3. Signal transit time from the OV NIM fan-out module to the OV trigger boards
4. Signal processing time in the OV trigger boards
5. Signal transit time from the OV trigger boards to the OV PMT board for each module
6. Signal processing time in the OV PMT boards

The contributions to the signal delay are dominated by items 3–6 above. For example items 1–2 contribute ~ 32 ns to the total delay, whereas the signal processing times in the OV trigger boards and OV PMT boards (items 4 and 6 above) contribute 22×16 ns $= 352$ ns and 4×16 ns $= 64$ ns to the total delay, respectively. Furthermore, cable delays (items 3 and 5 above) contribute a large amount to the overall signal delay.

RG58 coaxial cable was used to connect the OV NIM fan-out module to the OV trigger boards. The signal delay of the RG58 cables installed for the OV was measured to be 1.4 ns/ft with a signal degradation over the required distance of ~ 100 ft that was found to be acceptably small. On the other hand, RG174 coaxial cable was used to connect the OV trigger boards to the OV PMT boards because its smaller diameter and greater flexibility allowed it to be routed more easily to each OV module. The signal degradation over the RG174 cable for these shorter $\sim$50–60 ft distances was also found to be acceptably small, and the signal delay of the RG174 cables installed for the OV was measured to be 1.57 ns/ft.

For the lower plane of OV modules, the cables connecting the NIM fan-out module and the OV triggers boards are 110 ft long, and the cables connecting the trigger boards to the PMT boards are all 50 ft long. Therefore, the total delay for the lower plane of OV modules due to items 3 and 5 above is 110 ft $\times$ 1.4 ns/ft + 50 ft $\times$ 1.57 ns/ft = 233 ns[1]. Thus, the

[1]Although the upper plane of OV modules uses different cable lengths, they are chosen such that the total signal propagation delay remains the same. Specifically, the upper plane of OV modules uses 97.5 ft RG58 cables and 61 ft RG174 cables.

total difference in the simultaneous value of the clock counters of the OV PMT boards and the DC trigger system is ~ 680 ns.

On the other hand, the difference in the simultaneous value of the clock counters of the OV trigger boards and the DC trigger system is less than this. First of all, items 5–6 are irrelevant for OV trigger boards. Furthermore, although it takes the OV trigger boards 22 clock cycles to transmit clock and sync signals to the OV PMT boards, it only takes 19×16 ns $= 304$ ns for an incoming sync signal to be processed by the OV trigger board internally. Therefore, the difference in the simultaneous value of the clock counters of the OV trigger boards and the DC trigger system is only ~ 490 ns.

C.1.2 OV DAQ Time Stamps

When the readout of an OV trigger board or OV PMT board is triggered, the time stamp associated with the event is given by the value of the 32-bit clock counter. However, there are delays between the clock cycle in which the signal first arrives and the clock cycle in which the value of the 32-bit clock counter is recorded.

The firmware logic in the OV PMT boards assigns a time stamp to its data 9 clock cycles (144 ns) after the signal first arrives at the OV PMT board. On the other hand, the firmware logic in the OV trigger boards assigns a time stamp to its data only 6 clock cycles (96 ns) after the signal first arrives at the OV trigger board. As described in App. B, while the data associated with each OV PMT board involves strip-level hit information, the data associated with the OV trigger boards involves only module-level hit information. The module-level hit information is sent from each OV PMT board to the OV trigger boards via a hardware trigger signal over a 50 ft[2] RG174 cable. This hardware signal is generated 9 clock cycles (144 ns) after the signal arrives at the OV PMT boards.

Based on the clock counter offset between the OV trigger boards and the OV PMT boards, the different delays in assigning time stamps to OV trigger board data and OV PMT board data, and the hardware trigger signal propagation delay, we can estimate an offset in the time stamp assigned to OV strip-level and module-level data for a given OV

[2]This is 61ft in the case of the the upper OV plane of modules.

DAQ event to be

$$\Delta T = \underbrace{(680\text{ ns} - 490\text{ ns})}_{\text{clock counter offset}} - \underbrace{(144\text{ ns} - 96\text{ ns})}_{\text{difference in time stamp assignment}} + \underbrace{(144\text{ ns} + 50\text{ ns} \times 1.57\text{ ft/ns})}_{\text{signal propagation delay}}$$

$$\sim 365\text{ ns (22–23 clock counts)}$$

C.1.3 ν-DAQ Time Stamps

There is also a delay in the ν-DAQ between the time at which a muon signal arrives at the ID/IV PMTs and the time at which the 32-bit DC trigger system clock counter is recorded for the event. The delay is due to the sum of the following contributions:

1. Signal transit time from ID/IV PMTs to FEE
2. FEE processing time for signal path to DC trigger system
3. DC trigger system trigger evaluation time

The total cable length (RG58) from the ID/IV PMTs to the FEE is $\sim$ 50 m. This corresponds to a total cable delay of $\sim$ 230 ns[3]. The FEE processing time for the signal path which goes to the DC trigger system is $\sim$ 50 ns. Finally, the DC trigger system trigger evaluation time is 156–188 ns. Therefore, a ν-DAQ event receives a time stamp $\sim$ 468 ns after the signal arrives at the ID/IV PMTs.

C.1.4 OV DAQ/ν-DAQ Time Offset

The total offset in the value of the time stamps assigned to vertical muon events coincident in the OV and ID/IV can be estimated based on the clock counter offset between the DC trigger system and the OV PMT boards and the different delays in assigning an event a time stamp in the OV DAQ and the ν-DAQ. Therefore, we estimate the total offset to be 680 ns + 468 ns − 144 ns $\sim$ 1 μs.

[3]RG58 cable has a delay of 1.4 ft/ns—see Sec. C.1.1.

C.2 Timing information

Both the OV DAQ and ν-DAQ data streams contain global (absolute) timing information for each event based on unix time stamps, which have a precision of ± 1 s. In addition, both data streams contain local (relative) timing information for each event based on the value of a 32-bit clock counter incremented by a common 62.5 MHz master clock. The 32-bit clock counters record the time of each event to a precision of 16 ns. These clock counters reset (at least once) every $2^{32} \times 16$ ns $= 68.7$ s and therefore do not uniquely specify the absolute time of an event. However, if the 32-bit clock counters are reset with a precisely known and fixed frequency and if the timing offset between the OV DAQ and ν-DAQ is known, then the relative time of each event in a data-taking run can be known to a precision of 16 ns.

C.2.1 OV DAQ Timing Information

There are two pieces of timing information associated with each OV DAQ event: a 32-bit unix time stamp and a 32-bit clock count. The unix time stamp provides absolute timing for each OV DAQ event with a precision of ± 1 s, whereas the 32-bit clock count provides relative timing information for each OV DAQ event with a precision of 16 ns.

As described in Sec. C.1, a sync signal sent by the DC trigger system to the OV resets the OV trigger board and OV PMT board clock counters every 2^{29} clock counts (~ 8.6 s). However, the number of times the OV clock counters have been reset during a given data-taking run can be computed from the unix time stamps. Therefore, the relative timing of each OV DAQ event can be reconstructed to a precision of 16 ns based on these two pieces of timing information.

Sec. C.2.1.1 describes the OV data format, which contains the OV DAQ timing information for each OV event and is stored as a ROOT tree (OVHitInfoTree).

C.2.1.1 OV DAQ Data Format

Data type	Variable Name	Description
unsigned int	fChNum	OV global DC channel number
short int	fStatus	OV data packet type (ADC, latch, trigger box)
double	fQ	ADC value (or 1 for latch, trigger box packets)
double	fTime	62.5 MHz clock count
double	fTimeUnix	Last unix time stamp preceding signal

C.2.2 ν-DAQ Timing Information

There are three pieces of timing information associated with the ν-DAQ relevant for merging the OV DAQ and ν-DAQ data streams:

1. A unix time stamp, which is recorded at the beginning of each data-taking run.
2. The number of 62.5 MHz clock cycles elapsed in a data-taking run since the first triggered event, which is recorded for each event.
3. The value of the trigger master board's 32-bit clock counter, which is recorded for each event.

The sum of the run start time (`fRunStartTime` in RunInfoTree) and the time elapsed since the first triggered event (`fTrigTime` in GlobalInfoTree) can be used to compute the absolute time of a ν-DAQ event to a precision of ± 1 s. This can be compared to unix time stamps associated with each OV DAQ event to determine the absolute time difference between OV DAQ and ν-DAQ events to a precision of ± 1 s.

The DC trigger system sends a sync signal to reset the OV trigger board and OV PMT board clock counters every 2^{29} clock counts. The value of the trigger master boards's 32-bit clock counter (`fClkCounter` in TriggerDiagnosisTree) can therefore be used to predict the value of the OV clock counters for events coincident between the OV DAQ and ν-DAQ after time offset corrections have been applied.

Fig. C.3–C.4 give cartoons illustrating the relationship between the trigger master board's 32-bit clock counter and the OV clock counters. After correcting for the OV DAQ/ν-DAQ time offset measured with vertical muons, the trigger master board clock

counter and the OV clock counters will be equivalent modulo 2^{29}, and the number of OV sync pulses since the beginning of the run can be determined from unix time stamp data.

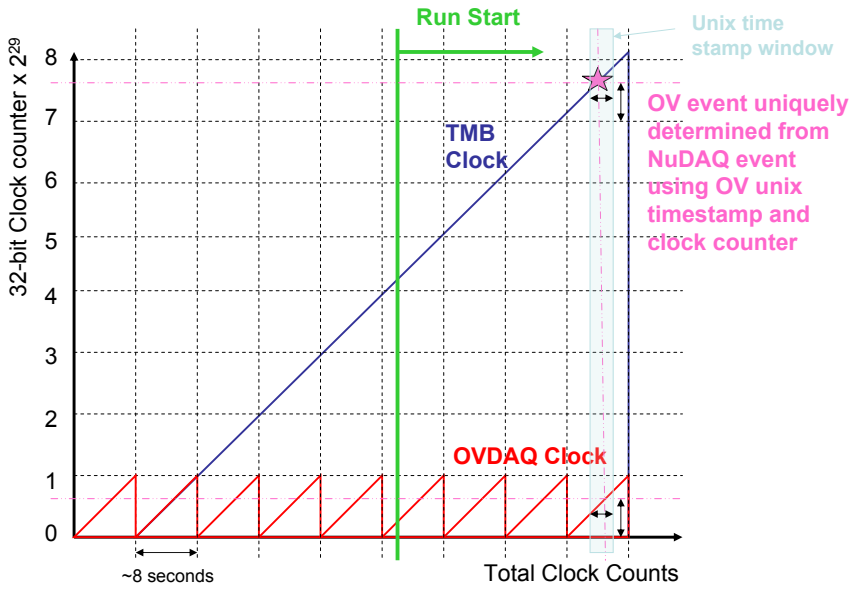

Figure C.3: Cartoon illustrating the time alignment of the OV DAQ and the ν-DAQ assuming no time offset. The trigger master board clock counter and the OV clocks counters are equivalent (modulo 2^{29}).

C.3 Description of Algorithm

The OV DAQ and ν-DAQ data streams are completely independent. They assign trigger IDs to each event independently and have very different event rates. The OV DAQ has an event rate of $\sim$ 2.7 kHz, and the ν-DAQ has an event rate of $\sim$ 120 Hz. Since the OV is a muon veto, we are primarily interested in identifying the last OV DAQ event which occurred prior to each ν-DAQ event. The OV data merging algorithm is therefore designed to find the last OV DAQ event for each ν-DAQ event and determine whether or not the timing of the OV DAQ event is such that the events should be considered "coincident", as in the case of vertical muons. Fig. C.5 gives a cartoon illustration of the timing structure

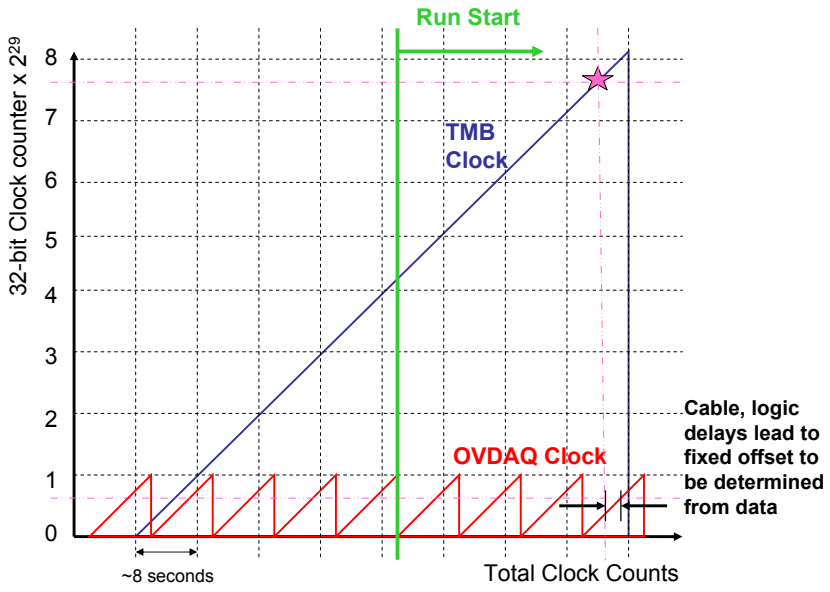

Figure C.4: Cartoon illustrating the time alignment of the OV DAQ and the ν-DAQ with an assumed time offset. The trigger master board clock counter is offset from the OV clocks counters (modulo 2^{29}) by an amount to be determined from data.

of events in the independent OV DAQ and ν-DAQ data streams.

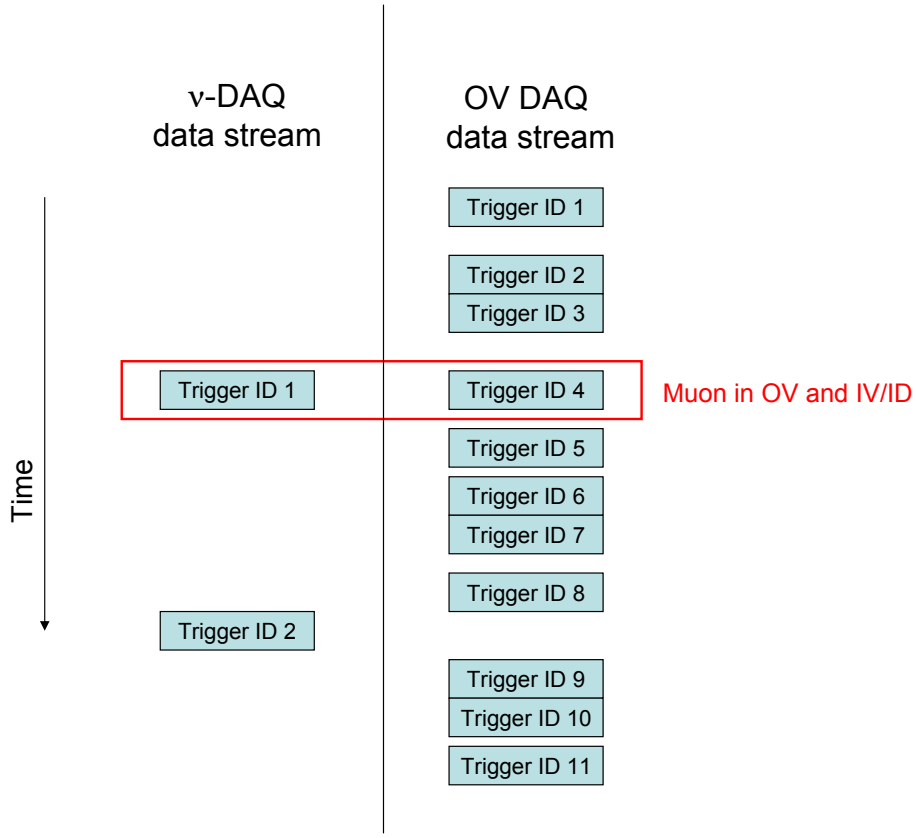

Figure C.5: Cartoon illustrating the timing structure of events in the independent OV DAQ and ν-DAQ data streams.

The OV data merging algorithm consists of first loading both OV DAQ and ν-DAQ data files into memory[4]. Next, for each ν-DAQ event, we step forward in time through each OV DAQ event starting with the OV DAQ event immediately preceding the previous ν-DAQ event and compute the time difference between the trigger master board and OV clock counters. As we move forward in time, the time difference between the ν-DAQ event and the OV event should monotonically decrease. Finally, the OV DAQ event with the smallest,

[4]A file catalog must be used to load the data from the two DAQs into memory because all other data access methods are declared as static. If, however, FileDB is used to access the data, this is handled internally using FileDB's MakeCatalog member function. Otherwise, a file catalog must be specified explicitly.

nonnegative time difference is the last OV DAQ event preceding the ν-DAQ event.

In order to compute the time difference between an OV DAQ and a ν-DAQ event, the unix time stamp associated with each OV DAQ event is first compared to the sum of the ν-DAQ run start time and the ν-DAQ event trigger time[5]. If the OV DAQ event occurs more than 2 s before the ν-DAQ event, the algorithm immediately moves to the next OV DAQ event[6]. Otherwise, the time difference between the OV clock counter and the trigger master board clock counter (modulo 2^{29}) is computed[7]. If the time difference between the OV DAQ event and the ν-DAQ event is negative, then the last OV DAQ event processed is the OV DAQ event immediately preceding the ν-DAQ event.

When computing the time difference between the trigger master board and OV clock counters, a correction must be applied to account for the offset between the time stamps assigned by the OV DAQ and the ν-DAQ to coincident events, e.g. vertical muons. This offset can be measured once and for all by looking for a correlation peak due to vertical muons in the distribution of the time differences between each ν-DAQ event and the last preceding OV DAQ event with no time offset correction applied.

Fig. C.6 shows the distribution of the time differences between each ν-DAQ event and the last preceding OV DAQ event with no OV DAQ/ν-DAQ time offset correction applied. There is a clear peak at time differences below $\sim$ 50 μs due to correlated OV DAQ/ν-DAQ events and a long exponential tail due to uncorrelated OV DAQ/ν-DAQ events[8].

Fig. C.7 shows the distribution of the time differences between each ν-DAQ event and the last preceding OV DAQ event for time differences of less than 100 clock counts. There are two clear peaks indicating two classes of OV DAQ events correlated with ν-DAQ events.

---

[5]Due to inconsistencies in how daylight savings time is handled in the OV DAQ and the ν-DAQ, an offset of two hours is applied to the ν-DAQ run start time. This offset is decreased in one hour increments until the absolute time difference between the first OV DAQ event and the first ν-DAQ event is less than 30 minutes.

[6]Due to the high OV DAQ event rate, the probability that this event is the last OV DAQ event preceding the ν-DAQ event is negligible.

[7]If the magnitude of this time difference is larger than $\sim$ 4 s, then the algorithm assumes that a sync pulse must have occurred between the OV DAQ event and the ν-DAQ event and corrects for this effect.

[8]The time constant associated with the exponential tail is consistent with the OV DAQ event rate.

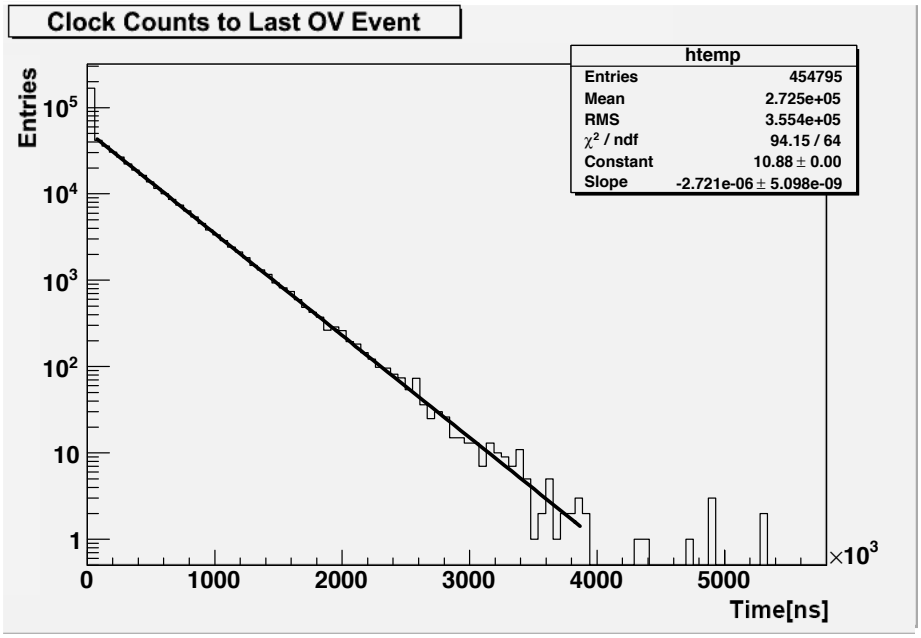

Figure C.6: Distribution of the time differences between each ν-DAQ event and the last preceding OV DAQ event. No OV DAQ/ν-DAQ time offset correction applied. The time constant associated with the exponential fit is consistent with the OV DAQ event rate.

The first, smaller correlation peak consists of OV DAQ trigger board data packets, and the second, more pronounced correlation peak consists of OV PMT board data packets. The offset between the two peaks is $\sim$ 22 clock counts, consistent with the value computed in Sec. C.1.2.

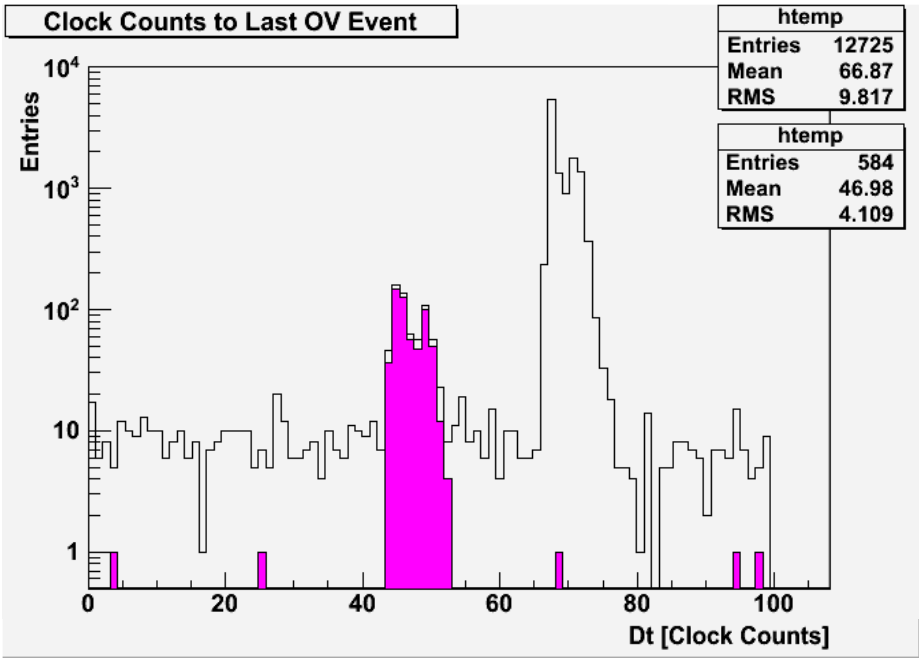

Figure C.7: Distribution of the time differences between each ν-DAQ event and the last preceding OV DAQ event for time differences of less than 100 clock counts. No OV DAQ/ν-DAQ time offset correction applied. Time differences corresponding to OV trigger board data packets are shown in pink.

Fig. C.8 shows the distribution of the time differences between each ν-DAQ event and the last preceding OV DAQ event after correcting for the 22 clock count offset between the OV DAQ trigger board data packets and the OV PMT board data packets in the OV Event Builder (see App. B). The smaller correlation peak has now been merged with the more pronounced correlation peak.

In fact, the more pronounced correlation peak actually consists of two, overlapping distributions. Fig. C.9 shows the distribution of the time differences between the last OV

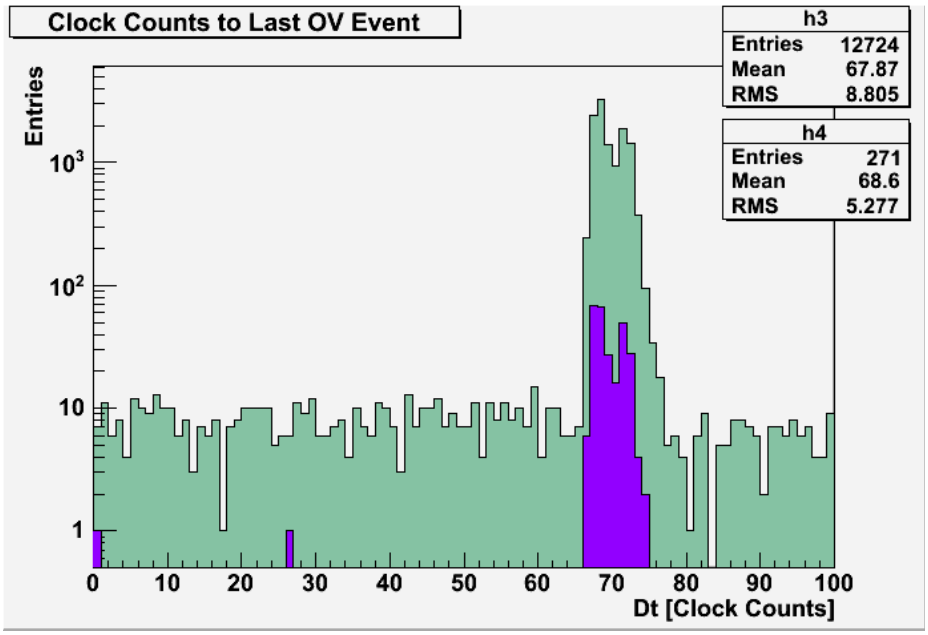

Figure C.8: Distribution of the time differences between each ν-DAQ event and the last preceding OV DAQ event after correcting for the 22 clock count offset between the OV trigger board and OV PMT board data packets. No OV DAQ/ν-DAQ time offset correction has been applied. Time differences corresponding to OV trigger board data packets are shown in purple. Time differences corresponding to all OV data packets are shown in green.

DAQ event and ID-triggered ν-DAQ events and IV-triggered ν-DAQ events separately. The first peak corresponds to ID-triggered ν-DAQ events and occurs at time differences of $67 - 68$ clock cycles ($\sim 1.07\ \mu$s), roughly consistent with the offset computed in Sec. C.1.4. The second peak occurs $\sim 3 - 4$ clock cycles later and corresponds to IV-triggered ν-DAQ events. The difference is a real electronics effect and can be compensated for in the firmware of the DC trigger system.

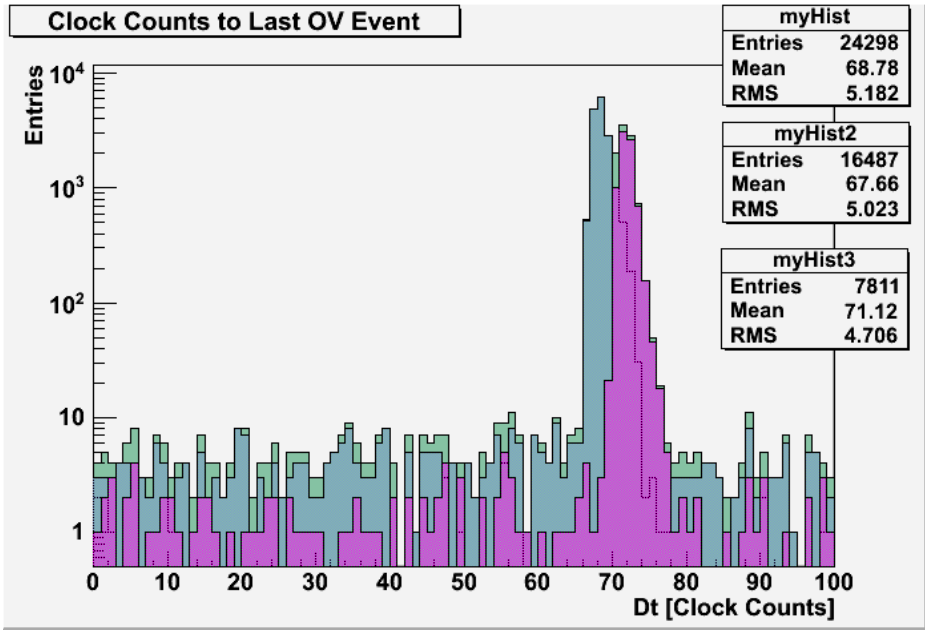

Figure C.9: Distribution of the time differences between the last OV DAQ event and ID-triggered ν-DAQ events and IV-triggered ν-DAQ events separately. No OV DAQ/ν-DAQ time offset has been applied. The histogram of ID-triggered ν-DAQ events is shown in blue. The histogram of IV-triggered ν-DAQ events is shown in purple. There is a $\sim 3 - 4$ clock count offset between these two classes of events. The histogram of all ν-DAQ events is shown in green.

Based on the offset measured in Fig. C.9, the OV data merging algorithm applies a correction conservatively set at 64 clock counts to the OV DAQ/ν-DAQ time difference. Fig. C.10 shows the distribution of the time differences between each ν-DAQ event and

the last preceding OV DAQ event after this correction has been applied. To conservatively include all events in the correlation peak, OV DAQ events with time differences of less than 14 clock counts (224 ns) with respect to ν-DAQ events are considered "conincident".

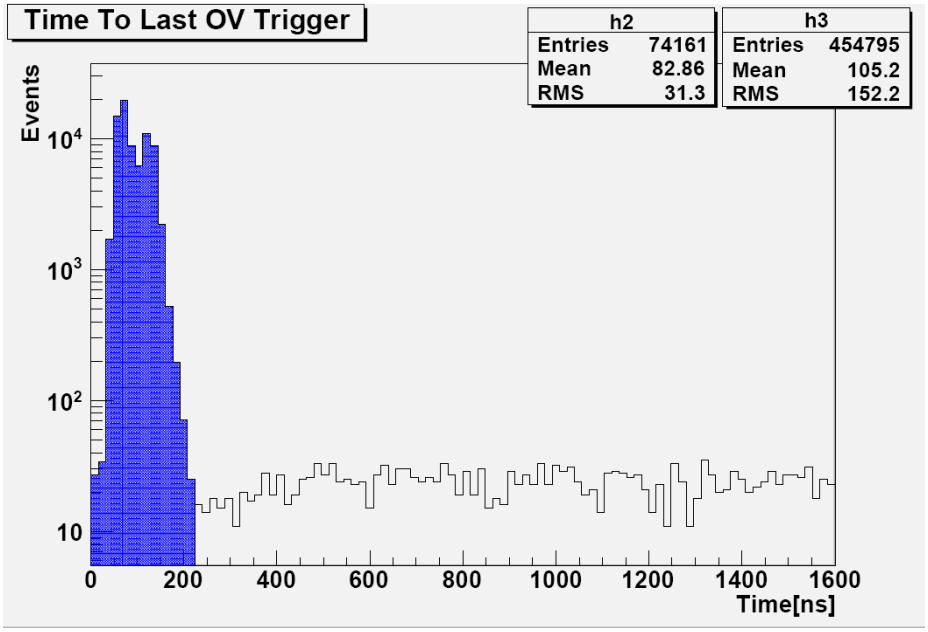

Figure C.10: Distribution of the time differences between each ν-DAQ event and the last preceding OV DAQ event after correcting for the measured OV DAQ/ν-DAQ time offset. Events in blue are defined as "coincident" between the OV DAQ and the ν-DAQ.

C.4 Results

Fig. C.11–C.13 show the reconstructed OV X and Y positions for OV DAQ muon events, which have hits in at least two overlapping modules and are coincident with certain classes of ν-DAQ events. The radial outlines of the target, γ-catcher, buffer, and IV volumes are indicated on each plot.

Fig. C.11 shows reconstructed OV position for all OV DAQ muon events coincident with ν-DAQ events. These events are clearly centered above the ID/IV volume with a slight offset coming from the average muon angle in the far detector hall. The areas with

no OV hits at the center and lower-left corner of the plot are regions of the detector that currently do not have any OV coverage[9]. The fact that there are fewer hits along the Y axis of the OV is a reconstruction artifact and not an indication of lower efficiency[10].

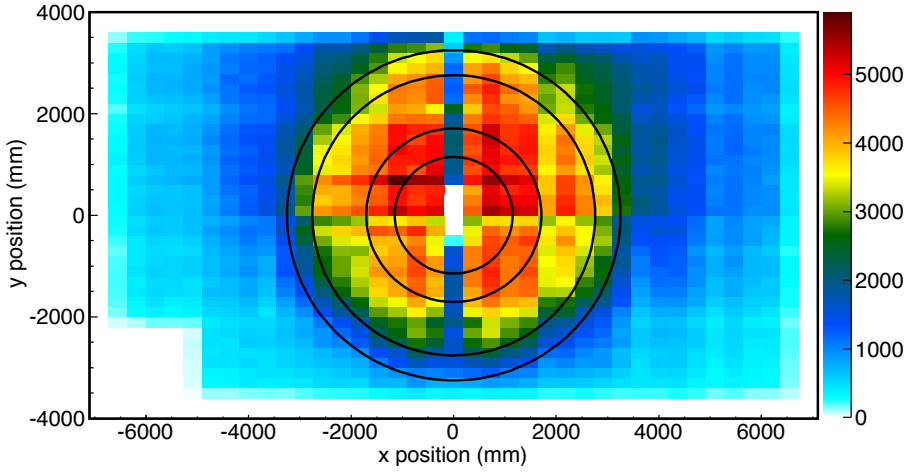

Figure C.11: Reconstructed OV position for all OV DAQ muon events coincident with ν-DAQ events.

Fig. C.12 shows the reconstructed OV position for OV DAQ muon events, which are coincident with ν-DAQ events that have no charge deposition in the ID. The shadow of the ID is clearly visible and has the correct size. A similar offset is observed as was seen in Fig. C.11.

Finally, Fig. C.13 shows the reconstructed OV position for OV DAQ muon events, which are coincident with ν-DAQ events that deposit more than 1.1×10^6 DUQ ($\sim$ 550 MeV) in the IV. The IV cut selects muons which have a very long path length in the IV. The reconstructed OV positions of these events form a ring centered above the radial portion of the IV extending beyond the outer radius of the ID, consistent with muons traveling straight down the sides of the IV.

[9]Once installed, the upper plane of OV modules will cover the central axis of the detector, above the chimeny.

[10]Most of the lower plane of OV modules consists of two layers of modules oriented in orthogonal directions. However, along the Y axis the lower plane of OV modules consists of two layers of modules oriented in antiparallel directions. The reconstruction currently treats this in an overly stringent way.

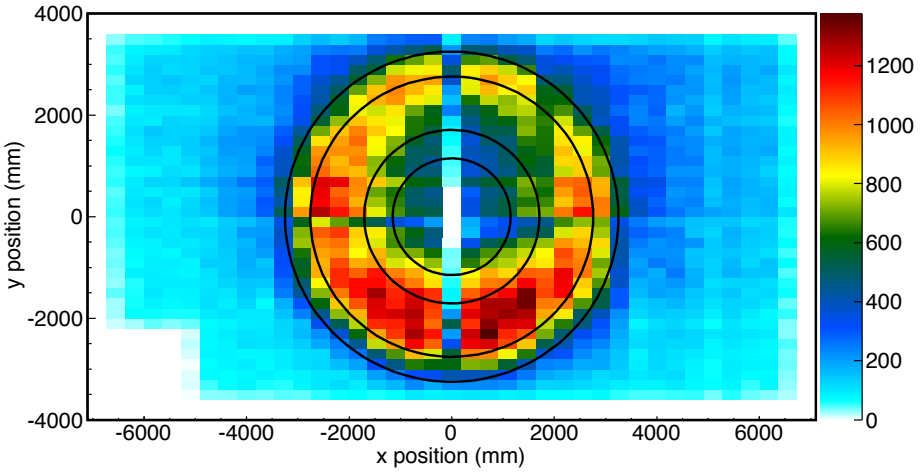

Figure C.12: Reconstructed OV position for OV DAQ muon events, which are coincident with ν-DAQ events that have no charge deposition in the ID.

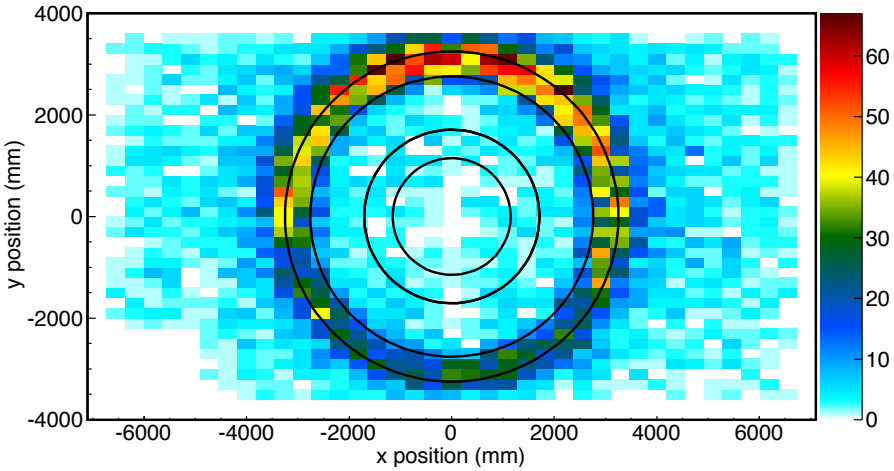

Figure C.13: Reconstructed OV position for OV DAQ muon events, which are coincident with ν-DAQ events that deposit more than 1.1×10^6 DUQ ($\sim$ 550 MeV) in the IV.